Virtual Fabrication of Full Size Welded Steel Plate Girder Specimens

János Néző

Submitted for the degree of Doctor of Philosophy

Heriot-Watt University
School of Engineering and Physical Sciences

March 2011

“Prima sapientiae clavis definitur, assidua scilicet seu frequens interrogation...
Dubitando enim ad inquisitionem venimus; inquirendo veritatem percipimus.”

“Constant and frequent questioning is the first key to wisdom...
For through doubting we are led to inquire, and by inquiry we perceive the truth.”

“A bölcsesség kulcsa a szüntelen kérdezés...
A kételkedés kérdéshez vezet, a kérdezés által pedig feltárul az igazság.”

“La primera llave de la sabidura está en plantear continua y frecuentemente cuestiones... Al examen llegamos por la duda, y por el examen se llega a la verdad.”

by French scholastic philosopher and theologian Peter Abelard (1079 – 1142)

Abstract

The use of virtual experiments of welded steel plate girders are commonplace in modern structural research. One key factor in the success of using such numerical analysis is the availability and reliability of input data including imperfections such as initial deformations and residual stresses. In this research a methodology combining experimental and numerical work is developed in order to use virtually fabricated welded specimens, which include the imperfections as a result of the manufacturing process, in virtual experiments.

A series of experiments are performed to calibrate and validate the numerical models. Temperature measurements are conducted in a steel structure factory during the welding of plate girders. The measurement methodology developed combines two types of measurements using an infrared thermometer without disturbing the fabrication process itself. The residual stresses are measured using a modified hole drilling method. Geometrical imperfection measurement results are also available from other related projects.

For the numerical simulation of welding a mixed time integration scheme is proposed. For the modelling of the heat source of welding an "equivalent prismatic heat source model" is developed, which is very robust and allows for very simple calibration. Both thermal and thermal stress analyses of the welding process are performed including a large number of parametric studies. The residual stress measurements are also numerically investigated and calibration tables are developed to evaluate the measurements considering inaccuracies in their execution.

The fabrication of full size plate girders is simulated. The calculated and measured web deformations are compared and reasonable agreement is found. Finally, to demonstrate and summarise the achievements of this research, a virtual specimen is used in a virtual experiment in which the ultimate behaviour of a plate girder is studied.

Acknowledgements

I thank Prof. László Dunai from Budapest University of Technology and Economics for his continuous support from a very early stage of my university studies all the way to finishing this thesis. He has always believed in me and my work and it is thanks to his vision that this project originally started and now has been completed.

I thank Prof. Barry H.V. Topping for recognising the importance of this project and giving me the opportunity to complete this research at Heriot-Watt University. I also thank the members of the Department of Mechanical Engineering and the members of my research group for their support.

The experimental investigation of this project could not have taken place without the support of Lindab Building System Ltd. and the support of the OTKA T049305 project of the Hungarian Scientific Research Fund. Special thanks are due to the people at the structural laboratory of Budapest University of Technology and Economics, especially to Miklós Kálló and László Kaltenbach for their dedicated work. I also thank the members of the Department of Structural Engineering, Budapest University of Technology and Economics, especially Gábor Jakab and László Gergely Vigh, for their help in the execution and the evaluation of the experimental investigations.

I also would like to thank Prof. John A. Goldak from Carleton University for his invaluable advice and opinion on the numerical modelling strategy developed in this project.

Finally, I would like to especially thank my family for their never ending support and always being there for me along this journey.

Contents

Chapter 1

Introduction

1.1 Background

In a collaboration between the Budapest University of Technology and Economics (BME) and Osaka University a research project was conducted with the aim of investigating the effects of new structural details required for the fabrication of plate girders by robotic welding [1, 2, 3, 4, 5, 6, 7]. To improve the use of robotic welding gaps at the ends of the stiffeners of the web were introduced. This gap significantly reduced the complexity of the welding path around the stiffeners and allowed for a much more efficient fabrication process.

The research involved both laboratory experiments and numerical analyses of the girders using advanced non-linear three-dimensional shell models. The experimental work included measurement of geometrical imperfections of the girders and their ultimate load tests. The numerical aspect of the project focused on the ultimate behaviour of the girders taking into account the effects of the size of the stiffener-end-gap, geometrical imperfections and the use of high-performance steel materials.

It was during this extensive work that the idea of using virtually fabricated specimens in virtual experiments emerged.

1.2 Objectives

The long term objective of the current research project is to include the simulation of the fabrication process into the design and analysis of welded steel structures. Simulation of the fabrication (virtual fabrication) would allow researchers and en-

gineers to build better numerical models for their structural analyses. Nowadays performance based design is more and more widespread but for creating more realistic numerical models that include imperfections the analysts generally still rely on the recommendations of design codes or other simplified approaches. This mainly arises from the complexity of the welding simulation and the very high computational cost that such realistic models involve. This work focuses on the development of an efficient numerical analysis technique to calculate the imperfections (residual stresses and distortions) in full size welded plate girders.

Advanced numerical analysis (a virtual experiment) of structures has been commonly used in research (e.g. [8, 9]) for a significant period of time and more recently they have also become an integral part of the everyday design process: modern design codes includes guidance and recommendations on how such models can be and should be used [10, 11].

A virtual experiment can be described with the following three components:

$$INPUT \Rightarrow PROCESS \Rightarrow OUTPUT$$

Naturally the results ($OUTPUT$) obtained by virtual experiments are highly dependent on both the input data ($INPUT$) and the methodology ($PROCESS$) used by the analyst. In this work the term "input data" is used in a very general sense. It not only refers to the quantitative aspects of data (e.g. the actual numerical values of certain parameters such as material properties) but also to the whole decision making process of including or excluding certain characteristics of the structure studied (e.g. what imperfections should be considered). This is the most important and most difficult task the analyst has to face. Building the actual model, running the analysis and evaluating the results is a relatively straightforward process once all the decisions concerning the modelling strategy have been made. In this research the main focus is on the $INPUT$ of virtual experiments.

Even if it seems trivial, the single most important question that needs to be answered before one can start the development of any numerical model is: What are the aims of the analysis? The objectives need to be very clearly defined in order to work out what simplifications can be applied without risking the usability of the result (*i.e.* what is the most efficient way to achieve the aims). The need for simplifications is not a question in itself. It is a necessity for many reasons and often it is driven not only by the aims. Ideally the aims dictate what information

is necessary to perform the analysis, however, the availability of this information is often very limited and assumptions need to be made.

In brief, the objective of this research is to find efficient ways to provide sufficient reliable input data for conducting virtual experiments of welded steel plate girders by investigating the complete life cycle of the girders from fabrication to destruction using both laboratory experiments and numerical analyses.

When a specimen is brought into the structural laboratory and prepared for the experiment or when a structural member is assembled into a more complex structure on the construction site, it has already undergone a transformation (the fabrication) process that has greatly influenced its present physical state. Stresses and deformations build up in the girder long before it is put to work in its intended structural role. This state of the girder is rather different from the perfect one that was designed on the drawing table. These differences are the main subject of this work. To find out how they can be calculated efficiently and what are their importance the following three phases are considered in the life cycle of a welded plate girder:

- fabrication (transient state),
- post-fabrication (static state), and
- structural role (transient state).

The first phase is the fabrication. It is a transient state where the input (the base material: the individual steel plates) through a specified process (welding) is transformed into the output (the welded plate girder). Of course those individual plates (input from the fabrication point of view) are the result (output) of another processes (e.g. hot rolling, plasma cutting). It would be possible to keep going back in time and analyse all the preceding processes and their input and output. For example in [12] the effects of initial imperfections on out-of-plane deformation and residual stress produced by welding is studied. However, such investigation is beyond the scope of the present research. Only the process that directly precedes the experiments, the fabrication, is studied as it is shown in Figure 1.1.

The second, post-fabrication phase is a static state during which the physical state of the girder is unchanged. At this point all the effects of the fabrication process are "locked" into the girder but it still has not been subjected to other

external effects (e.g. the loading of an experiment). Using relatively simple methods certain characteristics of this constant physical state can be "extracted", *i.e.* the imperfections of the girder can be measured.

The final phase is the one that the girder is designed for: to fulfil its structural role. In the present work the girders are designed for conducting a series of experiments to study their behaviour. These ultimate load tests represent another transient state where the input is the girder in its post-fabrication state, the process is the gradual application of external loads and the output is the structural response of the girder to those loads. The three phases are summarised in Figure 1.1.

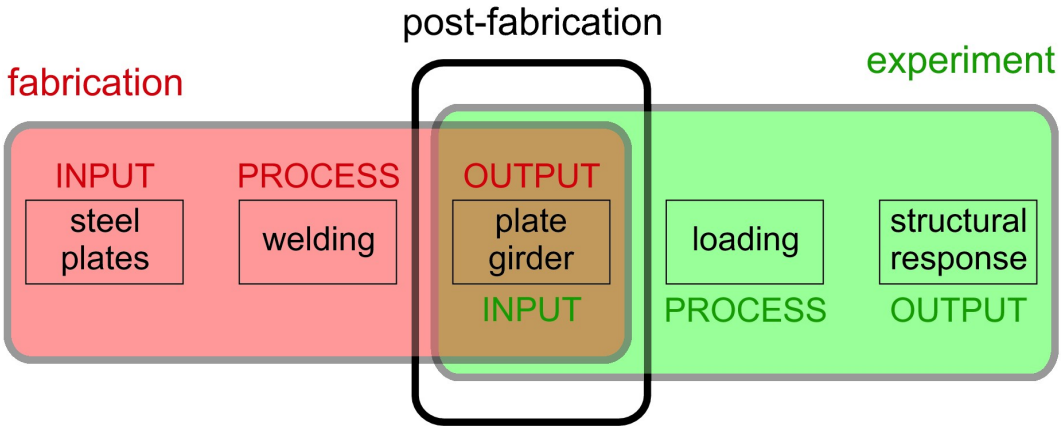

Figure 1.1: Phases in the life cycle of a welded plate girder.

In the view of the definition of the above phases the main objectives of the research can be refined:

- To find efficient ways to describe the post-fabrication state of welded plate girders by investigating the effect of the fabrication process using both laboratory measurements and numerical analyses.
- To determine an easy-to-follow approach for manufactures and analysts to improve their fabrication and analysis process by considering the post-fabrication state of welded structural members.

Reaching the above goals by being able to simulate the fabrication of welded plate girders would open up a wide range of new possibilities in the numerical analyses of welded steel structures. Eventually it could bring performance based design to a new level where the effects of the fabrication can also be accounted for.

Numerical simulation of welding has a long history in the field of mechanical engineering. Computational welding mechanics (CWM) is used for both studying the welding process itself and the effects of welding on specimens. One major difference in the application of CWM in mechanical engineering and civil engineering is the scale of the specimens. In the former usually the size of the welds and the size of the welded specimens are comparable, they have a similar order of magnitude. However, in the latter a weld seam of a few millimetres in size joins plates that can be easily of several meters long. That is a huge leap in terms of overall model size but the details of the weld zone cannot be scaled up to match the scale of the model. Details in the weld must be kept at the millimetre scale since the structural response is governed by what is happening in those few millimetres of the weld. While CWM has been used for small scale problems (e.g. studying fillet welded lap joints [13]) it is yet to leave a significant mark in civil engineering. Nevertheless, it has been widely used in a somewhat similar field: shipbuilding. The main focus of the research in shipbuilding in terms of welding simulation is on the analysis of stiffened plates. The achievements of those works in shipbuilding could be almost directly applied for example to orthotropic decks in steel bridge structures. However, when it comes to the simulation of the fabrication of plate girders there is still a big gap. The present research aims to contribute to the filling in this gap.

An extensive experimental program is developed in cooperation with a steel structure manufacturer in Hungary and the structural laboratory of the Budapest University of Technology and Economics. The experimental program consists of five main phases:

- measurements of temperature in the steel factory during the fabrication of the specimens,
- measurements of distortions in the structural laboratory,
- measurements of residual stresses in the structural laboratory,
- ultimate load tests in the structural laboratory, and
- dissection of specimens to obtain weld seam cross-sections in a contracted external laboratory.

It has been already emphasised that the aim of this work is to find efficient solutions to the problems outlined above. Therefore it is important to mention that to achieve efficiency the measurements are designed with simplicity in mind. The methodology used in this research is such that it can be easily reproduced, either completely or partially, in any similar future projects if necessary at relatively little cost.

Parallel to the experimental investigation several numerical models are also developed:

- thermo-mechanical analysis of the welding process,
- simulation of the residual stress measurement process for better evaluation of the measurements, and
- virtual experiments (load bearing tests) on a virtually fabricated specimen.

In a similar fashion to the measurements, the objective with the numerical work is to find a relatively simple and efficient way for the numerical simulation of welding.

Although the main aim of the research is to provide input data for virtual experiments, it is evident that this investigation also provides valuable information for manufacturers of similar welded structures. The manufacturer involved in this research often finds itself in a difficult situation caused by the distortions of welded plate girders. The distortions can be so severe that the automatic welding equipment cannot complete its task. If there is a relatively simple methodology, both experimental and numerical, to study the imperfections the manufacturer can more easily fine tune its fabrication process to avoid such costly disruptions of the production line.

1.3 Structure

In Chapter 2 the extensive experimental program and its objectives are discussed. There are several research projects that are interconnected by some of the experiments. Representative results of the measurements conducted as part of other related projects but with relevance to this work are also presented here.

Chapter 3 focuses on the welding process, its thermomechanical effects and its numerical simulation. The discussion on the effects of welding include uneven tem-

perature distribution, metallurgical changes, distortions and residual stresses. A literature review on the numerical simulation of welding is also presented here. The main difficulties of computational welding mechanics and the different simulation strategies are discussed with special attention to the common ways of simplifications and their shortcomings. Finally the explicit and implicit time integration schemes are evaluated briefly with respect to the welding simulation.

In Chapter 4 the use of mixed time integration is proposed for the simulation of welding in large models. The stability of the explicit time integration method is discussed in detail and the use of mass scaling is studied in an attempt to reduce the excessive computational times. Simple guidelines are also established to determine the optimal time to switch from explicit to implicit time integration.

In Chapter 5 the development of a temperature measurement methodology and some results are presented. The methodology is based on the combination of two different measurement types in order to address different aspects of the welding process and provide sufficient data for the calibration of the numerical model of welding.

In Chapter 6 the thermal analysis of welding is presented. A modified welding heat source model based on prescribed temperatures is proposed and used in a number of parametric studies. The most important parameters to influence the temperature distribution in the welded plates are identified for the calibration of the numerical model. The calibration is based on the temperature measurements conducted during the fabrication of the specimens.

In Chapter 7 the residual stress measurements are presented. High resolution photographs are used to determine the range of the inaccuracies present in the measurements. A numerical model is developed to evaluate the effect of those inaccuracies. The numerical model is also used to develop calibration tables for the measurement method.

In Chapter 8 the thermal stress analysis of welding is presented. The modelling strategy is discussed in detail and a series of parametric studies are presented on a small scale model. Models of full size girders (of length of $3000mm$ and $6000mm$) are also investigated and a technique to speed up the analysis is also studied. The calculated deformations in the specimens are compared to the measured ones.

One specimen is selected from the experimental program and its complete life cycle is simulated, in Chapter 9, from its virtual fabrication to its failure in a virtual

experiment. All the lessons learnt in the steps of the development of the numerical model in the previous chapters are put together here and presented as a step-by-step guide.

Chapter 10 summarises the most important results and achievement of this challenging project. Possible further directions of the research are also established here.

Chapter 2

Experimental program

2.1 Introduction

An extensive experimental program has been developed to study the interaction of fabrication technology, imperfections and experimental behaviour of welded plate girders with single-sided fillet welds between the web and the flanges [14]. The structures investigated are the frame components of the Lindab Building Systems. The applied fabrication technology and the resulting imperfections (geometrical out-of-plane imperfections and residual stresses) are studied by factory on-site and laboratory measurements on thirty full-scale test specimens. In order to study different behaviour modes the specimens are designed with a range of different design parameters:

- lengths of 3m and 6m,
- uniform and tapered shape,
- different section parameters (web b/t ratio, web-to-flange ratios), and
- single- and double-sided fillet welds.

The primary aims of the experimental program:

- investigation of the effect of the single-sided fillet weld on the geometrical imperfections and different behaviour modes, and
- providing the experimental background for the development of computer based fabrication simulation (virtual fabrication) and load-bearing test simulation (virtual testing).

The programme is completed in three phases and starts with on-site measurements in the factory of Lindab Building Systems Ltd.. During the welding procedure the temperature distribution is measured using a radiation (infrared) thermometer. The temperature data is the verification base of the advanced finite element model which simulates the welding process using thermomechanical analysis.

The second phase of the experimental research is continued in the Structural Laboratory of the Department of Structural Engineering, Budapest University of Technology and Economics (BME): the geometrical imperfections are measured by a special device developed for this purpose and the residual stresses are determined on selected specimens by a modified hole drilling method.

Finally the experimental behaviour of the specimens is investigated in simply supported test arrangements, applying different ratios of bending and shear, as well as local concentrated loads. A wide range of behaviour modes are studied: local flange/web buckling, shear buckling, crippling, distortional buckling, lateral torsional buckling and their interaction. The results are evaluated on the bases of the fabrication process, the design method of the Eurocode 3 standard and the numerical analyses completed alongside the experiments.

Several research projects ([15, 11] have been brought together to take advantage of the results of this extensive program. In the present work only the parts of the program that are more relevant to the virtual fabrication of the specimens are presented in detail in separate chapters, however, a brief summary of the other parts is given in this chapter.

2.2 Plate girder specimens

The main characteristics of the plate girder specimens are summarised in Table 2.1. There are two groups of specimens: large specimens (from L1 to L11) that are subjected to geometrical imperfection measurements and load-bearing tests, and small specimens (from S1 to S4) some of which are used for residual stresses and geometrical imperfection measurements while others are also used for load-bearing tests in other projects studying different arrangements of web stiffeners. The table shows four small specimens but actually more than one specimen of each type is fabricated in order to provide sufficient number of specimens for other projects.

Preliminary calculations according to Eurocode 3 (2003) are completed to deter-

Specimen	Flange	Web	Weld	Length
L1	150x6	250x4	Single	5970
L2				
L3		600x4		
L4				
L5	200x10			
L6				
L7		250-600x4		
L8				
L9	150x6	600x4	Double	
L10	200x10	600x4-8	Single	
L11		600x4		
S1	150x6	600x4	Single	2970
S2			Double	
S3		250x4	Single	
S4	200x10	600x4		

Table 2.1: Plate girder specimens (all units in mm).

mine the basic sizes of the large specimens: length, flange and web sizes, as detailed in Table 2.1. The geometry of the small specimens is based on the geometry of the large specimens (*i.e.* same cross-sections). The material grade of the specimens is S355 ($f_y = 355MPa$). On the bases of the preliminary calculations, the large specimens are fabricated in the factory with stiffeners only at the end supports. Additional longitudinal and/or vertical stiffeners are welded in the workshop of the Structural Laboratory of BME before the load-bearing tests in order to investigate different failure modes. The final design of the specimen used for load-bearing tests, in particular the position of additional stiffeners, is completed using advanced finite element analysis.

2.3 Tests and measurements

2.3.1 Fabrication: on-site temperature measurements

During welding a highly concentrated heat source moves along the joint of the plates melting the base material and generating an uneven temperature distribution in the structure. For numerical modelling purposes the amount of heat introduced into the structure needs to be known. Welding is a very complex phenomena and the direct measurement of the actual heat input is not feasible. However, an indirect evaluation of the heat input by measuring the temperature of the base material at specific locations and times is possible. Using this temperature data the numerical model can be calibrated and an artificial heat input, which has the same effect on the base material as the actual one, can be determined. Details of the different types of measurements (fixed and moving) and the results are presented in Chapter 5.

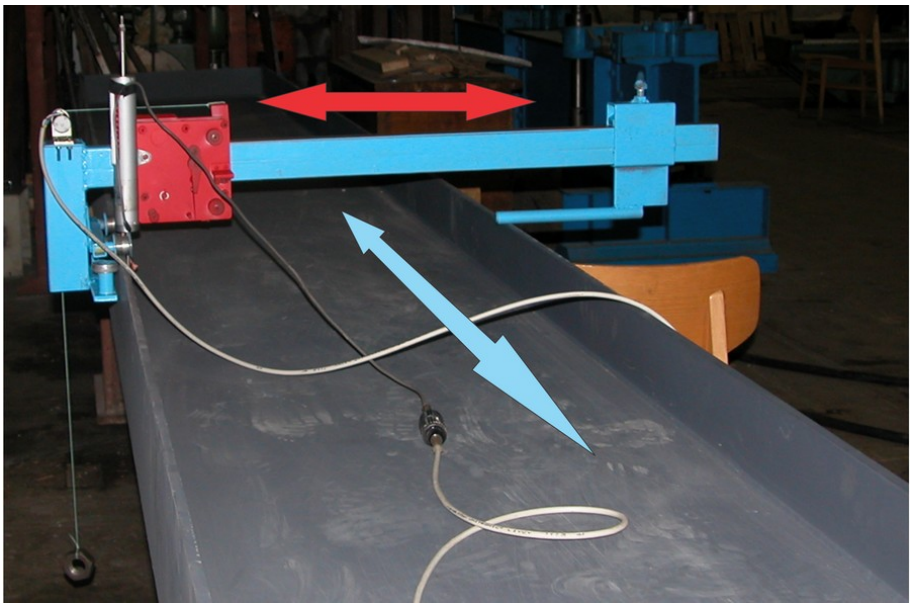

Figure 2.1: Device for imperfection measurement.

2.3.2 Material properties

Plates of different thicknesses are used to build up the girders as shown in Table 2.1. Tensile tests have been performed on each different plate size to determine the yield strength and the ultimate tensile strength of the material of the plates. These are the actual material properties that are used in the numerical models of the specimens.

The results are summarised in Table 2.2 [14, 10].

Plate	Grade	f_y [MPa]	f_u [MPa]
150 x 6	S355	374	484
200 x 10	S355	373	474
600 x 4	S355	479	587

Table 2.2: Tensile test results.

2.3.3 Geometrical imperfections

The imperfections of the web are measured by using a half-automatic device developed for this purpose, as shown in Figure 2.1 [16]. The shape of the web is measured with a transducer in a transverse direction using the flange edges as reference bases. The position of the transducer and the measured value are registered. The range of the transducer measuring perpendicular to the web is +/- 15 mm, with a sensitivity of 0.01 mm. The measured data is recorded with a sample rate of 100 Hz using a HBM SPIDER 8 device connected to a computer. In the longitudinal direction the distance of the measured cross-sections ranges from 50 to 100 mm. Only the results that are used later in this work are presented here.

Figures 2.2 and 2.3 show the measurement results of a specimen of type S1 in Table 2.1. The former shows the out-of-plane deformations (UY) in the web at different sections of the height of the web (b) and the latter shows the full web. In Figure 2.2 the origin of the horizontal axis corresponds to the centre of the specimen.

Figure 2.4 shows the measurement of the out-of-plane deformations (UY) in the web of specimens L3 and L4 in Table 2.1. Even though the characteristics of the two specimens and their fabrication conditions are identical, the deformations at the end of the girder (right side of the graph) are quite different.

2.3.4 Residual stresses

Residual stresses in the flanges of the specimens are measured by a modified hole-drilling method that uses a single uniaxial strain gauge. A hole is drilled directly next to each gauge at both sides of it. Both the placement of the gauges and the execution of the drilling are very prone to inaccuracies. Using high resolution digital photographs the relative location of the holes and the gauges and the exact

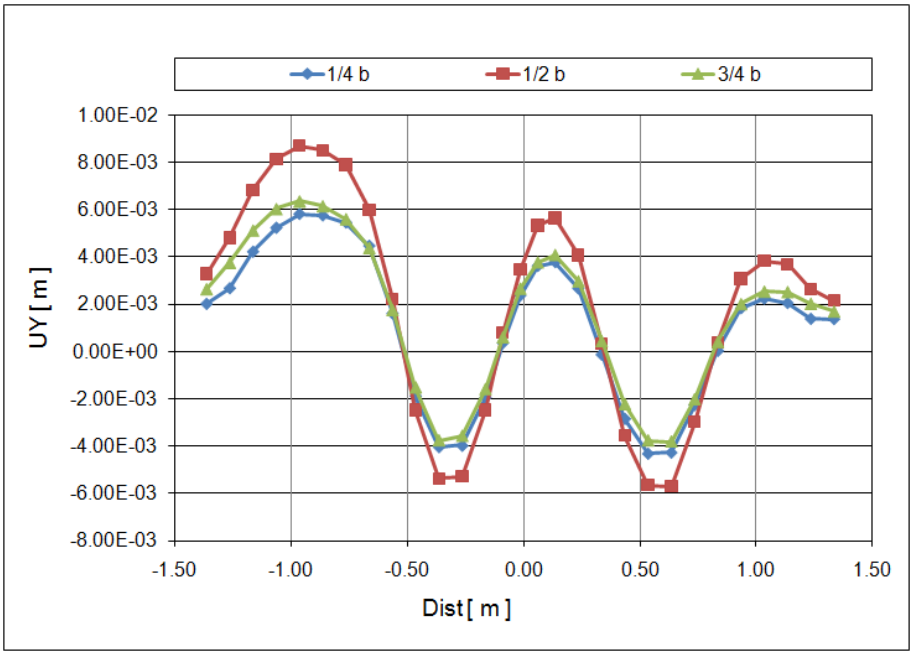

Figure 2.2: Web imperfections of type S1 specimen (b - height of web).

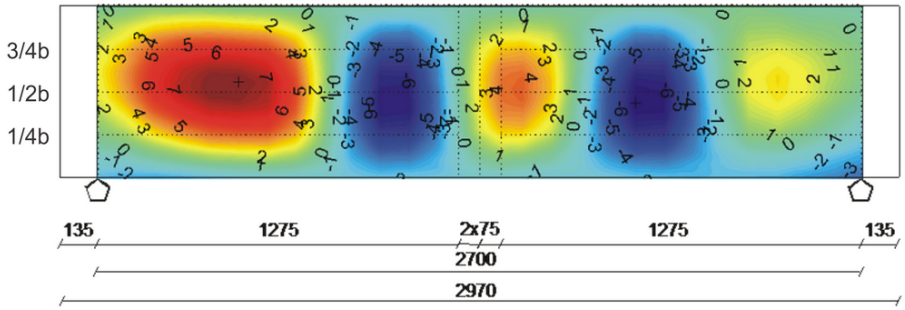

Figure 2.3: Web imperfections of type S1 specimen (isosurface).

orientation of the gauges can be estimated with high accuracy. The results of the measurements are evaluated with the help of numerical simulation of the actual measurements considering all the inaccuracies observed during the execution of them. A thorough parametric study is also performed to understand how those accuracies influence the readings of the strain gauges and to develop calibration tables to be used in the evaluation of future measurements. The measurements are performed in two specimens, one with a single-sided and one with a double-sided fillet weld in order to evaluate how the two fabrication methods influence the development of residual stresses. Details of the measurements, their results and the numerical investigation are presented in Chapter 7.

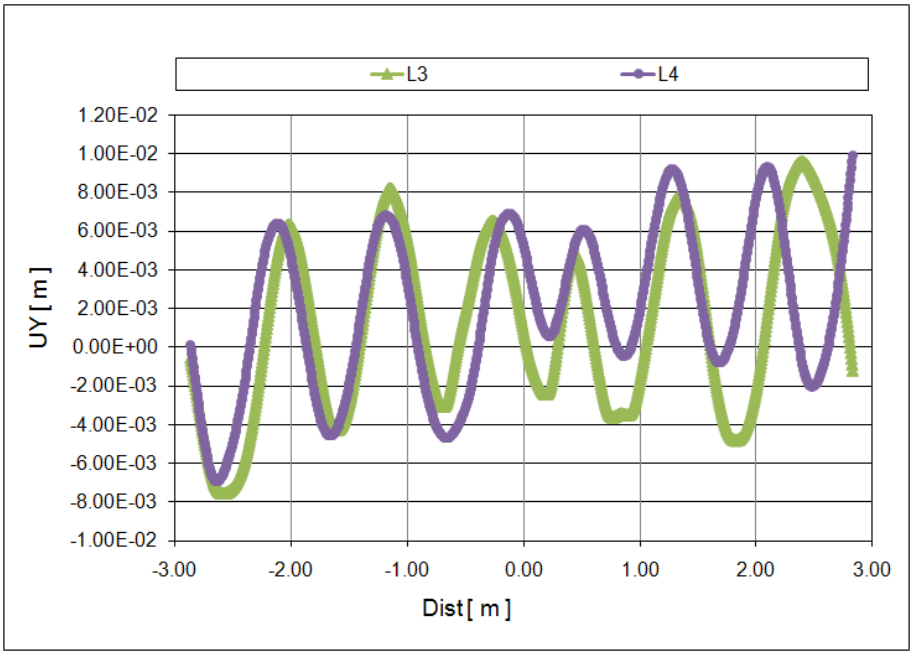

Figure 2.4: Web imperfections of specimens L3 and L4.

2.3.5 Load-bearing tests

The load-bearing tests are performed in three and four point bending arrangements on both long and short specimens. According to the aim of the research the load-bearing tests covered a wide range of failure modes. In general the observed experimental behaviour is an interaction of stability and strength phenomena. The observed phenomena are local, distortional and global stability failure modes: web crippling, distortional buckling and lateral-torsional buckling [15].

Unfortunately the available test results are from ultimate load tests performed on plate girders with additional stiffeners. The simulation of the welding of additional stiffeners is beyond the scope of this research. Nevertheless, there are numerical test results in [17] that can be used as a reference in this project. Those analyses were performed on three dimensional shell models of plate girders with the geometry of specimens L3 and L4 in Table 2.1 and with a test set-up similar to the actual experiments but no additional stiffeners were considered.

The four point bending test set-up is shown in Figure 2.5. The span for the long specimen is 5700mm. The end supports on the lower flange and the lateral supports of the upper flange provide a hinged fork support for the specimen. The load in the experiments is applied by two hydraulic jacks above the web of the specimen using thick plates to distribute the concentrated force.

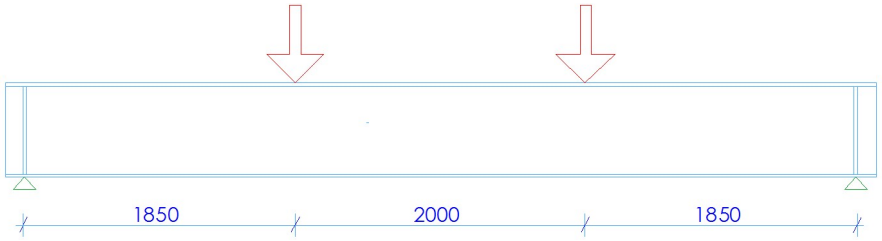

Figure 2.5: Four point bending test set-up.

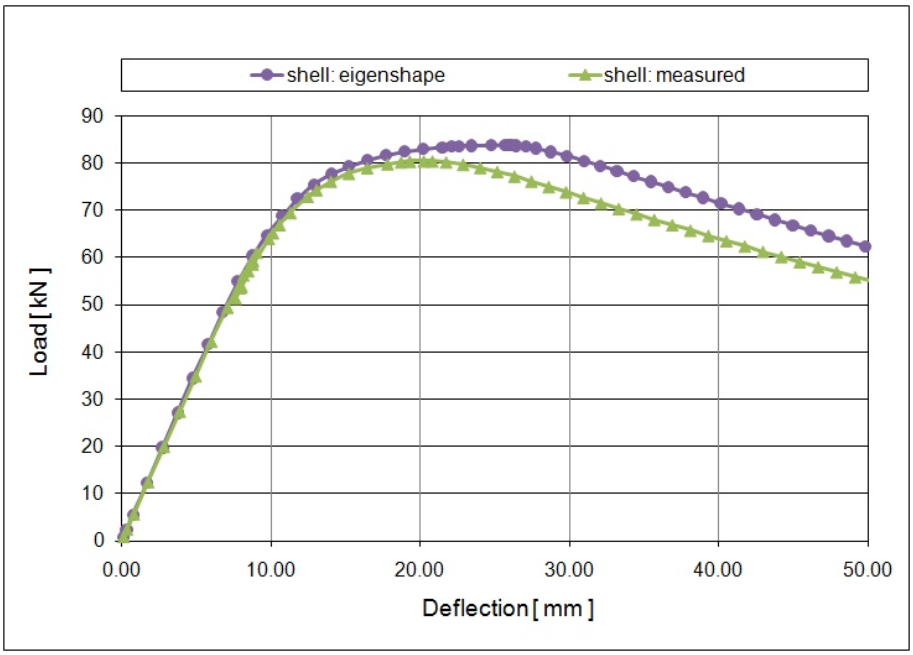

Figure 2.6: Calculated load-deflection curves considering different initial imperfections.

Figure 2.6 shows the calculated load deflection curves. The deflection is measured at the bottom of the cross section at mid-span. In the analyses the initial imperfections were also considered. In one of the model the imperfections are based on the eigenshape of the model. In the other model the actual imperfection measurement results of specimen L4 shown in Figure 2.4 were used. No residual stresses are considered in the analyses. The calculated load bearing capacities of the two numerical models are $83.8kN$ and $80.5kN$, respectively.

The next chapter gives a general introduction of the thermomechanical effects of fusion welding and a review of the available strategies for the numerical simulation of welding.

Chapter 3

Thermomechanical effects of welding

3.1 Introduction

In this chapter the main difficulties in the numerical simulation of welding and the available strategies to deal with those difficulties are reviewed and evaluated. For this it is necessary to analyse the welding process itself and its thermomechanical effects on welded structures. This is followed by a review of the numerical strategies employed to simulate welding which also includes the discussion of the complexity of welding and the different ways of simplifications used by researchers. These simplifications are necessary in order to be able to perform welding simulations in a reasonable time frame. Finally the main spatial and time discretisation methods are reviewed with respect to the welding simulation.

3.2 Welding process

In this section the fusion welding method used in the fabrication of the specimens of this research is introduced very briefly. This is followed with a detailed discussion of the effects of the welding process. First, using an example developed in the early stages of this research, the uneven temperature distribution of welding is analysed. After that the metallurgical effect and the development of residual stresses and deformations are discussed as well.

3.2.1 Welding types

The joining processes for metals can be classified into five main categories [18]:

- fusion welding,
- resistance welding,
- solid phase welding,
- liquid-solid joining, and
- adhesive bonding.

In fusion welding the metal parts are heated beyond their melting temperature with or without additional filler material. Once this molten pool solidifies the previously separated parts become one. Examples of fusion welding include arc welding, gas welding, electron beam welding and laser welding [18]. For large welded structures the most common welding methods are shielded metal arc welding (manual covered electrode welding), gas metal arc welding and submerged arc welding. The specimens of this research are fabricated using automatic submerged arc welding. Nevertheless the discussion of this chapter can be applied to other forms of arc welding.

3.2.2 Temperature distribution

In the early stage of the research a three dimensional explicit finite element code was developed to be used for the analysis of the temperature distribution during welding. Apart from being a very good training for the work ahead, the purpose of this development was to analyse the main characteristics of the temperature distribution both in time and space. This information was then used to determine the direction of a much more advanced numerical model development based on commercially available software packages. The developed software has limited features that prevent drawing quantitative conclusions from the results, however, it provides a sufficiently capable tool to analyse the overall thermal process of welding and to draw qualitative conclusions. The software has the following main features:

- Element type:
    - 8-node isoparametric thermal hexahedral finite element

- Boundary conditions:
  - prescribed nodal temperatures,
  - moving prescribed nodal temperatures (to model welding heat source),
  - convection on element surfaces,
  - heat flux on element surfaces, and
  - internal heat generation
- Constitutive model:
  - temperature independent linear thermal properties
- Solver:
  - explicit time integration
- Mesh generation:
  - Lagrangian mesh,
  - use of rectangular building blocks to construct more complex geometry such as a plate girder with stiffeners, and
  - biased mesh towards the edges
- Visualization:
  - output to be processed by Open Visualisation Data Explorer (OpenDX) [19].

The following two examples are the results of this early work [20]. The images are created with the Open Visualisation Data Explorer [19].

In the first example a 400mm long section of a 20mm thick and 400mm wide steel plate with bead-on-plate welding is analysed. Only one half of the plate is modelled; the heat source consists of sixteen nodes of three consecutive hexahedral elements held at 1500°C and it moves at the speed of 5mm/sec (a typical speed for covered electrode welding [21]). Figure 3.1 shows the temperature distribution on the top surface of the plate at the time when the heat source has nearly reached the end of the plate (isothermal lines at 25°C, 50°C, 100°C, 200°C, 400°C, 700°C, 1000°C and 1300°C). It has to be noted that even at such a low welding speed only a small area of the plate near the heat source is affected by large temperature changes.

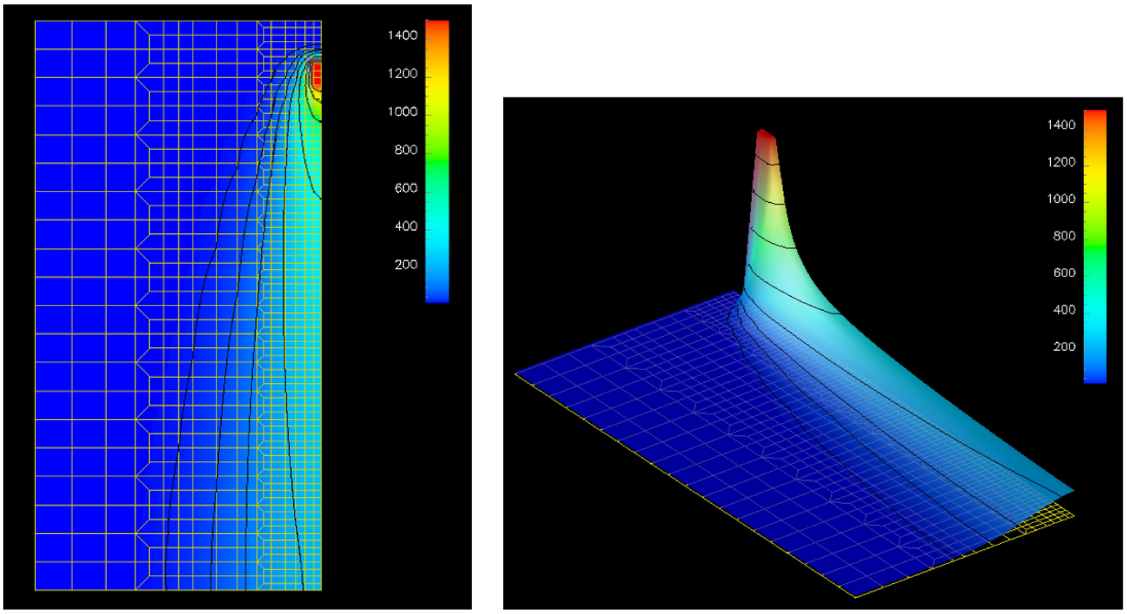

Figure 3.1: Temperature distribution in plate during welding: the heat source has nearly reached the end of the plate.

In the second example an 800mm long section of a steel plate girder with vertical stiffeners on the web is studied as shown in Figure 3.2. The web is 600mm high and 6mm thick. The flanges are 300mm wide and 10mm thick and the stiffeners are 84mm wide and 6mm thick. The numbered arrows in Figure 3.2 show the sequences and directions of welding (in the example the consecutive sequences are conducted continuously without any break between them). The welding heat source consists of two consecutive nodes held at the temperature of 1500°C. This heat source moves along the nodes joining the web to the flanges and the stiffeners to the web at a speed of 15mm/sec (a typical welding speed for gas metal arc (GMA) welding [21]).

Figure 3.3 shows the temperature distribution in the plate girder during welding and cooling. The right side of each image shows the finite element mesh while the left side is transparent making the isothermal lines (at 25°C and 200°C in the left image, at 41.75°C, 48.5°C and 51.3°C in the right image) more distinguishable.

In Figure 3.2 four locations are marked on the girder with numbered dots and Figure 3.4 shows the thermal histories of these locations. It has to be noted how rapidly the temperature changes at nodes in the welds (locations 1 and 2). Immediately after the high temperature heat source passes these nodes their temperature drops significantly. However, after reaching a relatively low temperature it takes a very long time to cool down further and eventually to reach the ambient temper-

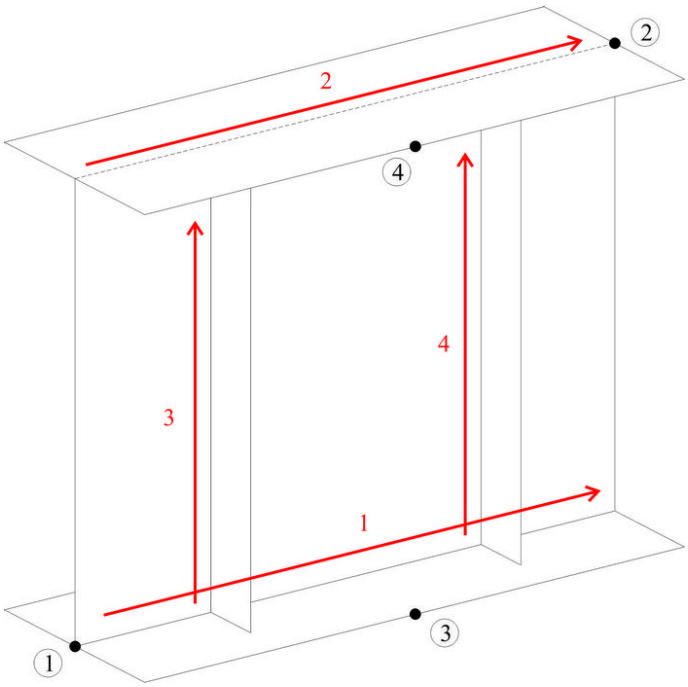

Figure 3.2: Plate girder with vertical stiffeners.

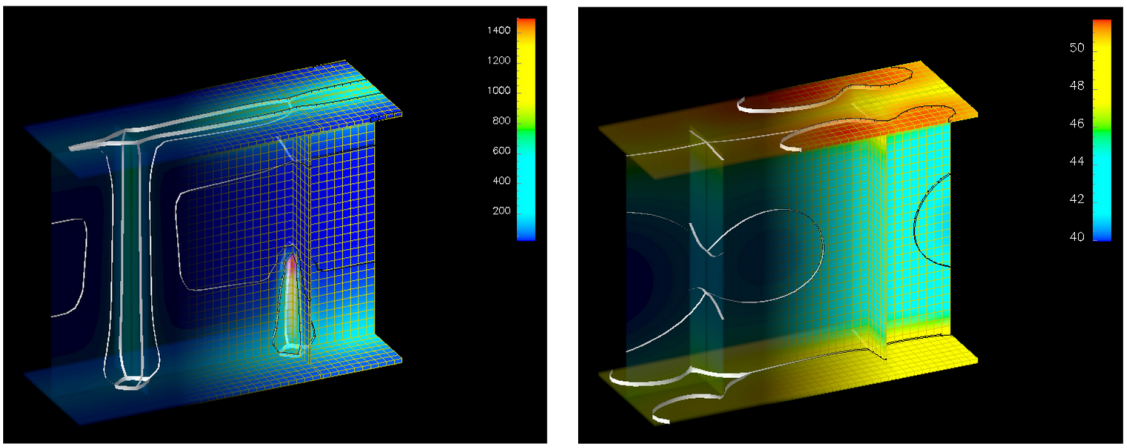

Figure 3.3: Temperature distribution in plate girder during welding and cooling.

ature (which is not shown in the graph). The other two curves (locations 3 and 4) show that far from the weld the temperature changes are relatively small and after the sharp drop in the other two curves all the four curves remain in the same temperature region for an extended period of time.

The first example demonstrates how the characteristic of the analysis changes in space while the second one demonstrates these different characteristics both in time and space. The key question in the further development of the numerical model

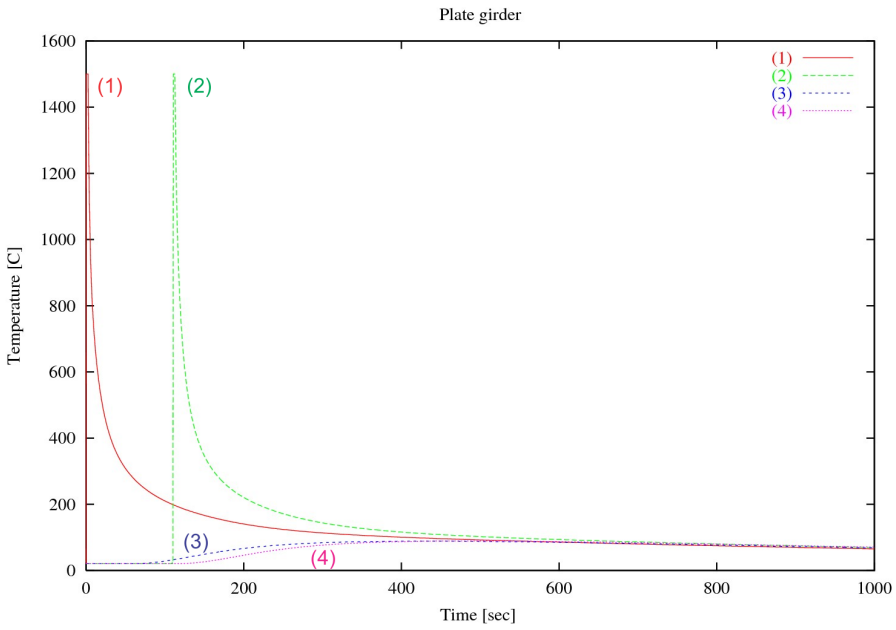

Figure 3.4: Temperature history.

is to find a way to exploit these special features of welding analysis of large scale structures in order to make the simulation as efficient as possible. This is discussed in detail in Section 3.3.

These examples demonstrate how the numerical modelling process of welding can be divided into two clearly distinguishable parts both in space and time. In space: in the welds and in their close vicinity the temperature gradient is very high demanding a high density of finite elements while in the rest of the model a relatively coarse mesh is sufficient. In time: the welding itself is a relatively fast and rapidly changing process while the cooling of the whole structure is a time-consuming and much slower changing process. These special features of welding simulation influence the selection of the numerical methods. During welding and close to the welds the temperatures are changing rapidly in a very wide range and the material behaviour is very complex. These characteristics suit the explicit method as discussed in the next section. However, during cooling and far from the welds the temperatures are changing much slower in a narrower range and the material behaviour is simpler. These characteristics suit the implicit method. Therefore the efficiency of the numerical simulation can be improved by combining the two methods and applying them when and where they are most efficient.

3.2.3 Metallurgical effect

During welding the microstructure of the material changes in the weld and in the heat affected zone, which results in changes in the material properties. Volume changes of the base material caused by phase transformation in the weld pool introduces additional stresses.

The subject of metallurgical changes caused by welding is one of the most complex aspects of welding simulation and therefore it is often ignored as discussed in Section 3.3.

3.2.4 Distortion and residual stresses

As a result of the highly concentrated heat input an uneven temperature distribution develops in the welded components resulting in the development of additional stresses and deformations. Figure 3.5 shows a schematic representation of the temperature and thermal stress distribution during bead-on-plate welding [18]. The high tensile stresses near the weld, which can reach the yield limit, may reduce the strength of the structure and increases the chances of fatigue crack development. The compressive stresses, which maintain equilibrium with the tensile stresses in the unloaded structure, reduce the buckling strength of the structure. Figure 3.6 shows the most common modes of distortion observed in welded components. These deformations can be very significant and beside their unfavourable effects on the strength of the structure they also make the assembly of the structure more difficult [18, 21].

Since residual stresses and deformations may seriously affect the behaviour of welded structures they have to be taken into consideration during their design. Current design practice uses semi-empirical methods based on extensive experimental studies. In everyday practice the most common case for engineers to come across the problem of imperfections is when they are using the relevant column buckling curve based on the type of section. It is very rare that even an idealised distribution of residual stresses, which can be obtained from the recommendation of most design codes, or initially deformed shapes of structural components are considered during design. Even in numerical studies used for research purposes it is not uncommon to see models that are based on the assumption that the structural components are without any imperfection. While this tendency is changing very rapidly in research,

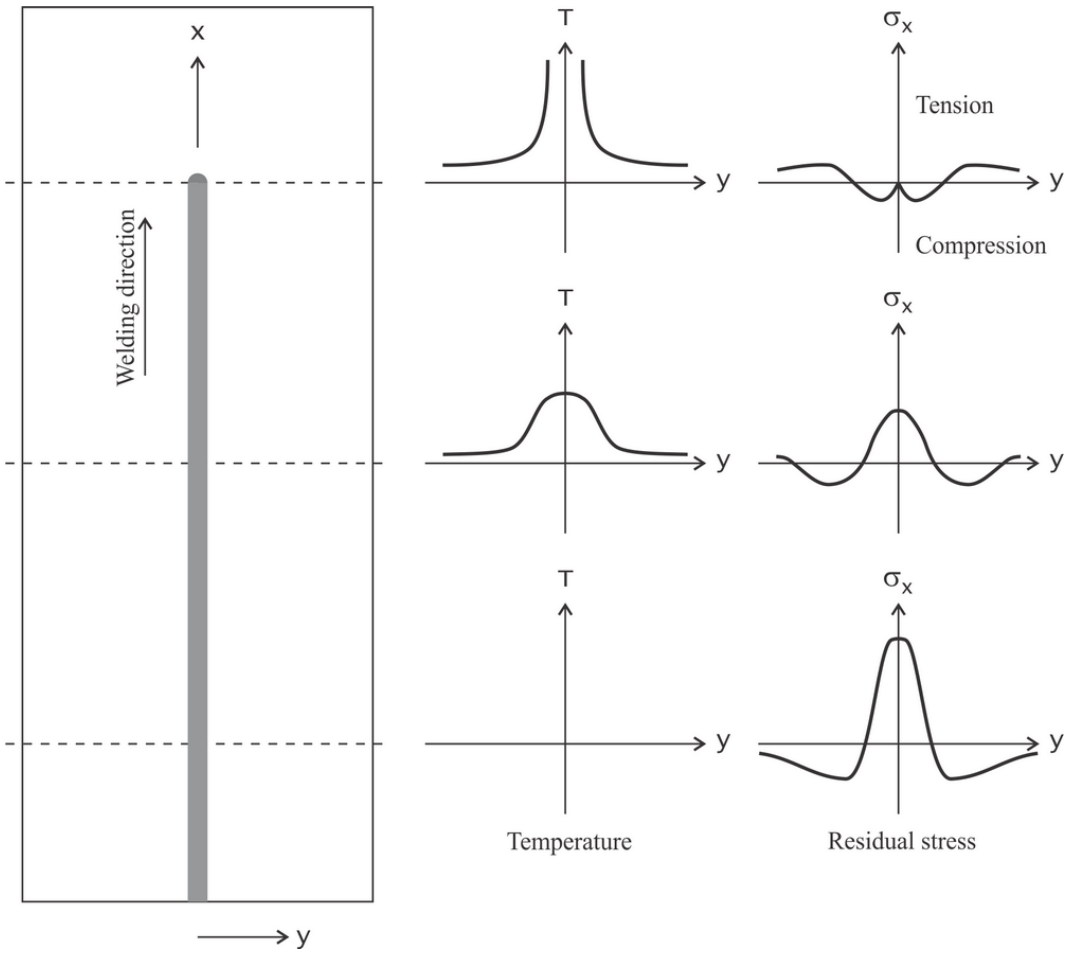

Figure 3.5: Temperature and thermal stress distribution during welding.

in everyday design further progress must be made before the use of more advanced numerical models can be considered as common practice.

3.3 Numerical simulation

3.3.1 State of the art

The main focus in most of the past work done in the field was on the understanding of the welding process itself. Very complex numerical models were developed that required such high computational power and time that industrial application of them was simple impossible. Research concentrating on practical application of welding simulation on geometrically complex structures appeared only in the last two decades. However, in the majority of the works still simplified models (e.g. two dimensional models) or models of very limited size are analysed.

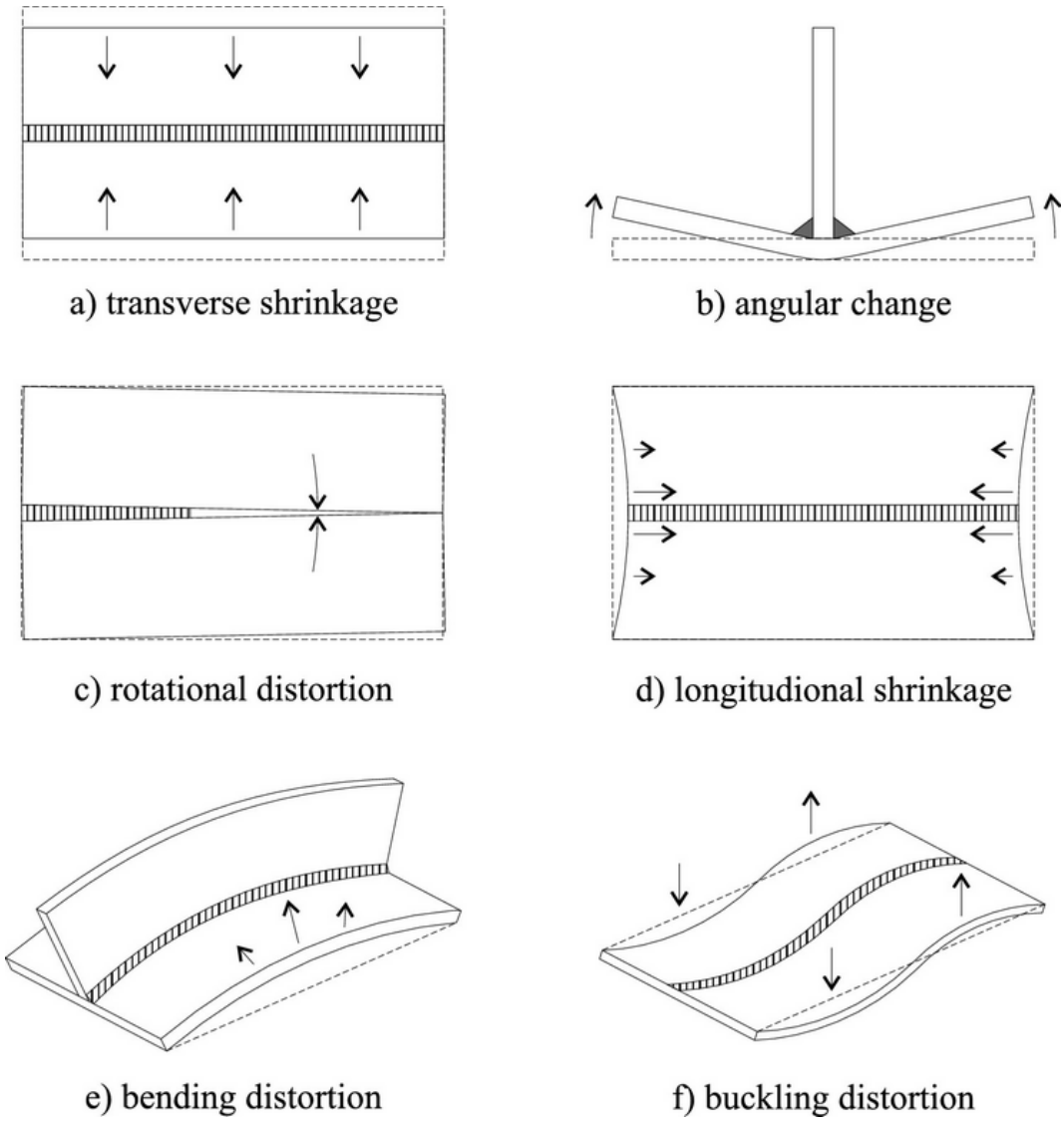

Figure 3.6: Common types of weld distortion.

Below there is a list of quotations about the state-of-the-art of welding simulation from papers published in the year showed above the quotes.

1994

" ... it is best to adopt a fully three-dimensional model but such models are usually **very costly and time consuming** so simplified models have to be used for welding problems" [22]

1995

"Even on current supercomputers, some relatively small problems can be **intractable**." [23]

1996

“ Even using today’s most powerful computers, a complete analytical simulation of residual stresses and distortion produced during welding fabrication of complex weldments commonly used for actual, complex structures is **impractical, if not impossible**.” [24]

“ ... a three dimensional problem requiring **large computer time and effort**.” [25]

1997

“ ... the use of a fully three-dimensional model to perform the thermomechanical weld simulations of complex structures is **impractical and computationally prohibitive**.” [26]

“The multiple thermal cycles and sequence effects make analysis of real structures a **challenge**.” [27]

“ ... three dimensional, nonlinear FEM analysis of girth welds with moving heat source is **computational intensive** and sometimes **cost prohibitive**” [28]

“Unfortunately, even with the latest advances in computer architecture and software, it is **not possible** to model all the relevant phenomena without incurring **excessive computational costs**” [29]

1998

“The calculations have to be done on a computer, but the **storage requirements** and **computation times** for solving realistic problems can become **prohibitive**.” [30]

1999

“In thermal elastic-plastic analysis, the analysis time becomes **enormous**” [31]

“ ... welding ... modelling techniques ... **too complex and labour intensive** to be applied industrially” [32]

2000

“In recent years three-dimensional models in analysis of welding have become more frequent but still geometrical **complex structures are rarely, if ever, seen**.” [33]

"Although the finite element method has emerged as one of the most attractive approaches for computing residual stresses in welded joints, its application to practical analysis and design problems has been **hampered by computational difficulties**." [34]

2001

" ... three-dimensional simulations demand a **large computing power** if good resolution is to be obtained." [35]

2002

"The type of model used and the sophistication of the analysis has often **hinged** on the accuracy required and the type of **computational resource** available to solve the problem." [36]

2003

"One reason why welding simulation is not used in "everyday practice " is of course the **required computational capacity** ... Still three-dimensional analyses are **restricted** to plates, pipes and similar simple structures." [37]

2004

" ... particularly computational issues **impeding** the use of FEA to model a sequence of manufacturing processes." [38]

2005

" ... the transient aspect and the highly non-linear behaviour assumed in these models make the analyses **computationally inefficient**, and hence they are not widely used in an industrial context. ... The **highly complex, massive, three-dimensional structures** often found in fabrication industries are **not well-suited** to full multi-physics welding simulations based on three-dimensional models." [39]

2006

"Although the numerical method might simulate a welding process, a **limit** exists due to the **enormous computational size of any practical problem** resulting primarily from a three dimensional modelling of the process." [40]

" ... a 3-D analysis is simply **not feasible** in a realistic time frame" [41]

2007

"Welding models using 3-D elements are generally very slow, which makes them **less suitable** for extensive research." [42]

2008

" ... thermal elastic plastic finite element analysis is the most general method to predict welding residual stress and distortion. While this method can be used to predict welding residual stress and distortion for small or medium welded structures, it is **not applicable** enough to simulate the welding distortion for large welded structures because of a **large amount of computational time and a huge storage**." [43]

2009

"Although the capability of the personal computer has been largely improved, simulating thermo-mechanical behaviour based on a full 3-D model for a multi-pass welded joint is still **time-consuming** work." [44]

2010

" ... the implementation of FEA is **complex**, needs expert knowledge and can be **expensive in computational costs.**" [45]

"Numerical simulations of welding processes are **complex** and **computationally expensive**." [46]

The numerous papers published in the field of welding simulation show that there have been significant improvements made in the last decades. However, the above quotes also clearly show that despite the fast development of computer hardware and numerical methods even nowadays practical applications of welding simulation are still not considered feasible by many, especially when it comes to large scale complex welded structures. The intense interest of researchers also underlines the need for a numerical tool that allows for such simulations in a computationally efficient way.

While it is very easy to compile such list of quotes pointing to the high computational cost and therefore the impracticality of welding simulations there have been a significant advancement in the size and complexity of structures studied in

the last few years. Some consider that nowadays the computing cost is not a serious limitation any more in welding simulation [47]. What really limits the practical use of computational welding mechanics is the lack of experimental data that could reduce the uncertainties involved in the simulations.

3.3.2 Complexity

Complexity of the model

Welding is an extremely complex process. It involves a wide range of fields of science including thermodynamics, continuum mechanics, fluid mechanics, material sciences, etc. It is currently impossible to include all the phenomena related to welding into one complex model. There are different levels of modelling, however, there is not a sharp border between them. At one end there are the oversimplified models such as two dimensional plane strain models, while on the other end there are the highly sophisticated ones that might end up eventually in subatomic models in the future.

Two basic ways of modelling strategy can be distinguished [32]:

- "process understanding", and
- "process simulation".

The first approach is applied to study the physics of welding and to understand the driving phenomena of it. Such sophisticated models allow researchers to investigate the welding process itself (e.g. to improve welding quality, efficiency). Certainly these models could be used to simulate any process involving welding with high accuracy. Only the limitations of our resources make it necessary to develop another modelling strategy for the same problem.

The final aim of developing a tool for welding simulation must be clearly defined in order to determine the required complexity of the welding model employed. It should include all the phenomena having strong influence on the "final product" (e.g. residual stress) of the tool but on the other hand phenomena with a relatively small influence should excluded because of the high computational cost. Not only the "final product" but also the size and complexity of the investigated welded structure should be considered. There might be big differences between a model developed to investigate the residual stresses in the weld and in its close vicinity and

another model developed to estimate the residual stresses and distortions in large scale engineering structures. It could lead to a very costly calculation if the first model were used for the second problem. While in the first case certain phenomena might have strong influence on the shape of the weld and stresses in the weld, it can be that the same phenomena have much less effects on the stresses developed far from the weld in a structure several orders of magnitude larger (100...1000 times larger) than the weld itself. The complexity of the welding model should be in agreement with the aimed results and the analysed structure.

Consideration about the minimally required complexity of the model is certainly not equal to oversimplification. It is hard to determine in advance which phenomena are essential and which are not. It is always advisable to start from a more complex model and simplify it gradually if the results show that the effects of certain phenomena are negligible. The strategy of the development should aim at using the most complex and sophisticated model that can be still handled by the available computational resources within an acceptable time frame. The alternative strategy would be to include as few physical phenomena as possible and then to evaluate the acceptability of the accuracy of the results. This, however, would not serve well the long-term aims of a research project.

Fortunately the rapid development of computational technology narrows the gap between the two modelling strategies and today researchers have to face much fewer limitations than they had to in the past.

3.3.3 Main difficulties

The basis of welding simulation is a standard transient thermomechanical analysis of solids. The thermal analysis should include the basic ways of heat transfer such as conduction inside the body as well as convection and radiation to the surrounding air. Knowing the temperature changes in the solid the thermal stresses and deformations can also be calculated. In the stress analysis both geometric and material nonlinearity are present. Since distortion can be large in the structure, the assumption of small deformations can results in serious errors in the analysis. Although the basis of welding simulation seems quite straightforward there are some major difficulties that should be considered.

Experiments

Relatively little experimental data is available. The main reasons for this are the difficulties that arise when measurements should take place in an environment with extremely high temperatures. Most of the available data is based on measurements that were taken after the welded structure had cooled down. The lack of data during welding makes the verification of numerical methods more challenging since only the results of the final step can be compared.

Material behaviour

In welding processes the temperature varies in a very wide range: from room temperature to beyond melting point. With such an extreme condition the material properties are also seriously affected. Some properties maybe reduced even to or close to zero which introduces numerical difficulties. For example the yield strength of the material approaches zero as the temperature reaches to the melting point. Material becomes so soft that it cannot resist any stress and the deformations become so large that it can lead to the failure of the calculation [27].

Contrary to pure materials that have a single melting point, alloys have a complex phase diagram resulting in a range of temperatures where the melting takes place. It also makes more difficult to consider the effects of phase transformation on material properties which can be very significant. In addition the material properties depend not only on the current temperature and phase of the material but on the entire history of temperature and microstructure changes. To include all these effects in the welding simulation a coupled thermal, metallurgical and mechanical analysis has to be conducted. There are only few examples of such analyses in the literature [35, 48, 49].

Heat source and weld pool

Accurate modelling of the heat source involves arc physics and fluid mechanics. This problem is characterised by Goldak [50] as a "fascinating area of research with more questions than answers". The molten material is subjected to many forces (Marangoni force, buoyancy, etc.) and the interaction between the arc and the weld pool is very strong making the analysis very complex.

There are significant losses of heat during welding and in the analysis only the

net heat input should be applied. The efficiency of the heat source depends on the applied welding method. Since at the present it is not possible to calculate the heat input only by means of numerical analysis it has to be specified by measurement of temperature and observation of weld pool size and shape [35].

The temperature gradient is extremely high at the heat source. This requires very fine mesh in the area close to the heat source. A large number of elements increases the computational load and the small size of the elements significantly reduces the critical time step size for explicit solution methods which can lead to very long calculation time.

Interaction of welds

Welded structures such as plate girders in a bridge are built up from many parts. Beside the main parts of the girder (two flanges and the web) there are many other components such as stiffeners and gusset plates that are welded to the main structure. The interaction of the numerous welds results in a complex distribution of residual stresses and deformations in the structure.

3.3.4 Simplifications

Because of the difficulties in numerical simulation of welding and the computationally demanding nature of the problem there have been many attempts to simplify the numerical approach and at the same time significantly reduce the computational cost.

Decoupled thermal and stress analyses

The heat generated by mechanical deformation of the material is several orders of magnitude less than the heat generated by welding. Assuming that the heat generated by the deformations has a negligible effect on the temperature distribution, the thermal analysis and the stress analysis can be conducted separately. First a thermal analysis has to be completed to calculate the thermal history of the structure throughout welding and cooling. This thermal history (thermal load) is the basis for the stress analysis to determine the residual stresses and deformations.

In a so called staggered method the thermal and stress analyses are not completely separated. At each time step, first the temperature distribution is calculated,

then the stresses and deformations are determined and finally the geometry of the model is updated. Thus the thermal analysis is done always on the geometry of the previous time step. If required it can be improved by iterating between the thermal and the stress analyses [35].

The temperature distribution and the deformation of the structure can also be calculated simultaneously. This require the solution of unsymmetric system of non-linear equations which increases the computational cost without giving more valuable results since the coupling is weak. However, using an explicit solution method this difficulty of the computation do not arise [35].

The conditions for decoupling the two analyses are not always satisfied. There are welding methods such as friction welding where the coupling is so strong that it cannot be neglected. Fortunately for welding methods that are considered in this research such as arc welding this decoupling can be applied and it is widely used by researchers.

Two dimensional models

The computational cost of full three dimensional models is very high. Therefore the use of three dimensional models in published papers [46, 51, 39, 52, 53, 54, 55, 40, 56, 57, 36, 37, 58, 59, 29, 33, 60, 61] are limited to only small problems. For thin plates three dimensional shell models [28, 57, 58] may also be used. Reducing the domain of the problem from three dimensional to two dimensional can decrease the computational cost very significantly on the other hand its usage is limited. There are three types of two dimensional models:

- plane strain model,
- axisymmetric model, and
- plane stress model.

In plane strain models a cross-section of the welded plate perpendicular to the path of the welding is analysed. It is assumed that in the welding (longitudinal) direction heat flow and deformation are zero. The later means that the model behaves in such a way as if it were fixed in the welding direction. Using of generalized plane strain or generalized plane deformation theory improves the models [35]. Such models are used in references [62, 63, 64, 65, 25, 66, 22].

Similarly to plane strain models in axisymmetric models a cross-section of the axisymmetric structure (e.g. welded pipe) perpendicular to the path of the welding is analysed. Such models are used in references [51, 31, 67]. The main drawback of these two models are that they are not capable of handling longitudinal changes for example at the beginning and the end of the welds.

In plane stress models the middle plane of a plate is analysed. The welding heat source is assumed to move in the plane. It is also assumed that through the thickness everything is constant and the stresses perpendicular to the plane are zero. It can be used for welding of thin plates, however, the lack of effects of thickness and the fact that a real weld is not located in the middle plane of the plate limit its usage. Plane stress models are used in references [62, 68, 69, 70, 71, 67, 72].

To overcome the limited geometry of problems that can be analysed by two dimensional models there have been attempts to combine two dimensional and three dimensional models without conducting a fully three dimensional analysis. Michaleris and DeBiccari [26] combined two dimensional plane strain welding analysis and three dimensional eigenvalue analysis to predict buckling in stiffened plates used in shipbuilding. From the two dimensional welding analysis they obtained a 'weld load'. Applying this weld load in the weld would have about the same effects on the structure as the real thermal load has. They used three dimensional eigenvalue analysis to determine the critical buckling load. Comparing the critical load to the weld load they could predict if buckling due to welding occurs in the plates. This approach reduced the computational cost very significantly but on the other hand the results are rather qualitative (buckling occurs or not) than quantitative (e.g. residual stress distribution in the structure). In addition the use of two separate finite element models in two steps seems impractical and the presented problem is realistic but still not a complete built–up structure. In welding simulation of complex structures the use of full three dimensional analysis is unavoidable.

Simplified material modelling

One reason for simplification in material modelling is the lack of data for material properties at elevated temperatures. If correct material properties are not available the use of a very sophisticated material model would be inappropriate. Another reason is the numerical difficulty that occurs at very high temperatures. As the

temperature approaches the melting point the material properties are dramatically changed and conventional material modelling is not suitable. Fortunately stresses that develop at high temperatures have much less an effect on the final residual stresses than stresses that develop during cooling down [27]. Therefore one solution is to ignore everything above a certain temperature. This can be improved by using a series of temperature cut-offs ignoring certain phenomena above certain temperature. For example in the case of steel up to ∼900°C there is no difficulty. Above ∼900...1100°C deviatoric stresses are set to zero as if the yield strength was zero and thermal strains are calculated only up to ∼1000...1200°C [27].

Phase transformations affect residual stresses by volume changes of the material and by its effects on material properties. Most commonly the effects of phase transformation are ignored and it is assumed that material properties depend only on temperature. If this assumption is acceptable or not depends on the type of base material. If the yield strength is relatively high at the temperature where phase transformation takes place then the effects of phase transformation are significant [21]. For example the effects of phase transformation may be ignored in the case of austenitic steels while it might play an important role in the case of ferritic steels. Nevertheless, even in the second case it is ignored by many researchers [73].

The material modelling is also influenced by the aims of the numerical simulation. If the weld and its close vicinity are of interest then a more complex material model is recommended. If the overall residual stress distribution in the structure is of interest then a simplified material model will also give satisfactory results [35].

Other ways of simplification

In welding and in other joining methods the primary aim is to join two separated components. Although it seems obvious there are surprisingly few simulations where the separated nature of components is taken into account. It is rather common that the components are handled as a single body which might introduce further errors since the distortion due to the movement of the free components can be very large [24].

If experimental data is available that should otherwise be calculated in a simulation then the computational cost can be reduced. Such data can be the shape of the fusion zone in which the developed thermal contraction is the main reason for

distortion. In reference [32] a so-called shrinkage volume (the fusion zone) is used to predict distortion in welded plates. Their results are very promising although they showed that this method is very sensitive to the actual shape of the shrinkage volume. The problem with such an approach where very specialised input data are used is that it is hard, if it is possible at all, to generalise the method. If the numerical model needs to be validated for every new problem then its application in everyday practice is questionable.

There are many ways of simplifications to cope with the high computational demand of welding simulation. Hoverer, no papers have been published concerning real complex welded structures built up from several components joined together by several welds.

3.3.5 Spatial discretisation

There are two main ways of spatial discretisation: Lagrangian and Eulerian meshes. The main difference between them is the way they handle the relation among the mesh, space and material.

Lagrangian reference frame

The main features of Lagrangian meshes can be summarised as follows [74, 75]:

- the mesh nodes represents points of the material and the mesh moves with the material,
- element integration points remain coincident with material points,
- boundary nodes remain on the boundary,
- nodes on the interface between two materials remain on the interface,
- elements deform with the material and the mesh can become severely distorted, and
- because of accuracy only limited deformations can be modelled with a Lagrangian mesh.

In a welding simulation using a Lagrangian mesh the heat source moves while the mesh is fixed to the material. In the view of welding process the advantages of Lagrangian meshes are that they can handle [50, 27]:

- starting and ending transient (*i.e.* the start and the end of the weld),
- a highly curved welding path,
- intermittent or intersecting welds, and
- changing geometry along the weld.

Considering the wide range of welded structures, using a Lagrangian mesh provides the analyst with much more freedom, on the other hand such a mesh usually requires more computational resources.

Eulerian reference frame

Main features of Eulerian meshes can be summarised as follows [74, 75]:

- the mesh nodes represents points in the space and the material flows through the mesh,
- material point at a given element integration point changes with time and complicates the treatment of path (e.g. stress history) dependent materials,
- boundary conditions must be applied at points which are not nodes,
- nodes on the interface between two materials do not remain on the interface,
- elements are unchanged by the deformation of material,
- no degradation in accuracy because of material deformation, and
- the mesh must be large enough to enclose the material in its deformed state.

In a welding simulation using Eulerian reference frame the mesh and usually the heat source are fixed in space. This makes the modelling of the heat source and weld pool easier and more accurate. However, the use Eulerian meshes is limited to the cases of [50, 27]:

- quasi-stationary steady state in the middle of the weld, and
- constant geometry along the weld.

Eulerian analyses are usually faster than Lagrangian ones but the difficulties with boundary condition definition and the limited geometry makes Lagrangian meshes more attractive for welding simulation. Therefore Eulerian meshes are much less frequently used in the literature.

Arbitrary Lagrangian Eulerian (ALE)

The main features of ALE meshes can be summarised as follows [74, 75]:

- the formulation of ALE methods is close to that of Eulerian methods,
- nodes of the mesh can be programmed to move arbitrarily to exploit the advantages of both methods,
- nodes on the boundary can remain on the boundary, and
- interior nodes can move to minimise distortion.

The ALE mesh description combines the advantages of Lagrangian and Eulerian meshes and eliminates most of their disadvantages. However, it requires much more programming effort to implement a method based on ALE meshes. ALE meshes are widely used for the analyses of geometrically complex structures subjected to very severe deformations. One example is the crash test simulation in the car industry.

Features of mesh used for welding simulation of large structures

The domain of the problem can be divided into two different parts. One is the weld seam and its close vicinity (all the welds if there are more than one in the structures, which is very likely) and the other one is the rest of the structure. At the weld seam the temperature gradient is very high and so very fine meshes are required. One could say that the rest of the structure is there just to provide correct boundary conditions for the numerical simulation. It means that only a relatively coarse mesh is needed in most parts of the model. This special feature of the model might be exploited when it comes to the selection of solution strategies. Because of the different characteristic of these two parts of the model two different solution technique may be applied on them. Thus the most suitable procedures can be used without compromises.

The temperature gradient is even higher very close to the moving welding heat source and the mesh requires further refinement. Moving adaptive mesh refinement can be used to omit an unnecessarily high density of elements along the whole length of the weld.

Eulerian and ALE meshes are useful to describe problems that either involves significant movement of the material or where the deformation of elements is so

severe that it significantly affects the accuracy of the analysis. In welding such large deformations are very unlikely to develop therefore Lagrangian meshes are appropriate and, because of the other advantages mentioned above, Lagrangian meshes seem to be more suitable for welding simulation.

3.3.6 Time discretisation

In the case of transient problems not only the space domain but also the time domain needs to be divided into a series of discrete points. The approximate results are calculated only at these points of time. There are two main types of time discretisation: explicit and implicit methods.

Explicit and implicit methods

The fundamental difference between the two time integration techniques is that with explicit methods the unknowns of the equation system can be expressed explicitly therefore there is no need to solve an assembled system of equations. In implicit methods for nonlinear problems the unknowns are present on both sides of the equations therefore the solution of the system of equations must be carefully considered. The main features of explicit and implicit time discretisation methods are summarised below.

The characteristics of explicit algorithms are:

- computationally more economical per time step,
- numerical stability limits the length of the time steps,
- low memory requirements, and
- these methods can more easily handle complex material laws.

The solution of the problem with explicit methods is very straightforward and easy to implement. Since there is no need to solve a system of equations there is also no need to assemble global matrices. This results in a very fast solution of one time step and in very low memory requirements which makes explicit methods very attractive to solve problems with very large numbers of elements. On the other hand the main drawback of the method is its conditional stability. The critical time

step can be extremely small which makes the method suitable mainly for rapidly changing phenomena only.

The characteristics of implicit algorithms are:

- the computation is more expensive per time step,
- larger time steps are possible, and
- with a direct solver the memory requirement is large as a result of the large global matrices (an iterative solver can reduce the memory requirement).

Implicit methods can generally handle much greater time steps than explicit methods which makes them more suitable for long-lasting phenomena. On the other hand the solution of one time step is much slower and the larger memory requirements may limit the size of the problem. There are iterative solution methods such as conjugate gradient methods [76] which eliminate the need for global matrices saving large amounts of memory.

The selection of the time discretisation method is not an easy task. There are only guidelines and not ultimate solutions to help the analyst in the decision making. The following needs to be considered for parabolic problems such as heat conduction [74]:

- usually implicit methods are used,
- in explicit methods the stable time step decreases by a factor of four each time the element size is halved, and
- in complex heat conduction problems it is often impossible to take advantage of the large time step permitted by implicit methods.

Implicit methods are often restricted, because of the accuracy, to a time step that is only a small multiple of the one used for explicit methods [77].

Time discretisation in the view of welding simulation

Let us consider a plate girder with a length of $10m$. Using fillet welds on both sides of the web results in a total of $40m$ of welds. It can be assumed that the two welds on the same side of the web are welded simultaneously in an automated process which reduces the welding time by half. The total time required to complete the

welding of this girder using the highest speed for common welding methods [21] given in Table 3.1.

Welding method	Max. speed [mm/s]	Time [min]
Covered electrode	5	66.667
Gas metal arc	15	22.222
Submerged arc	25	13.333
Laser beam	150	2.222

Table 3.1: Welding speed and time.

It is very likely that in a real structure there are horizontal and vertical stiffeners on the web. The welding of these stiffeners might double the above welding times. The analysis has to follow not only the welding process itself but also the cooling down. The cooling under normal conditions is driven by natural convection to the surrounding air. Depending on the size of the welded structure and the total length of welds, *i.e.* the total heat input, the cooling process can last for as long as several hours.

Because of the long lasting nature of the welding process it is questionable if an explicit time integration scheme can be efficiently used as a result of its strict restriction on the time step size (a very small critical step). On the other hand the rapid changes in the temperature close to the heat source suggests that even with an implicit method the time step may be very small during welding. However, in the case of an implicit method, during the cooling phase the time step size may be increased significantly.

Although in the literature the implicit method is employed almost exclusively, there are also a few examples that use explicit method [35, 78]. The ability of an explicit method to handle complex material behaviour with relative ease makes it attractive for welding simulation in which, because of the wide range of temperatures, the materials exhibit complex behaviour. The explicit method also has the advantage that it is more suitable for parallelisation than the implicit method.

Considering the advantages of both implicit and explicit time integration and how their characteristics suits the different phases (welding and cooling down) of welding simulation, a mixed time integrations scheme is proposed for the simulation

of large welded structures [79]. In a mixed time integration solution the analysis starts by using the explicit method during the welding phase. At some point during the cooling down phase, when the rate of the temperature change is sufficiently low to make the implicit method more efficient, the time integration scheme is switched to implicit. The proposal is presented in detail in the next chapter.

Chapter 4

A mixed time integration scheme for virtual fabrication

4.1 Introduction

In the simulation of sheet metal forming it is common practice to use a combination of explicit and implicit time integration as a result of the special characteristics of the procedure: the first part of the process is stamping which is then followed by a phenomenon called springback. Stamping is a rapid process and involves a high degree of non-linearity and contact. On the other hand springback, which occurs during unloading, is a relatively slow process during which the sheet metal part (the blank) undergoes further dimensional changes arising from the release of elastic strain energy accumulated in it during stamping [80]. Since explicit time integration is more suitable for phenomena such as stamping and implicit time integration is more suitable for phenomena such as springback it seems natural to combine the two and employ them where they perform best.

The simulation of welding can also be divided into two very distinguishable parts: the welding itself and the cooling down that follows. This was demonstrated in Section 3.2.2 using an early example [20]. The general characteristics of the two time integration methods were presented in Section 3.3.6. In this chapter special attention is paid to the stability of the explicit method which is conditionally stable and requires a strict limit on the time step size. In Section 4.2 it is also discussed how this limit can be improved to avoid very computationally costly analysis using a technique called mass scaling.

Several examples of increasing size are presented to demonstrate how a mixed time integration scheme could reduce the high computational cost of welding simulations. The optimal time to switch from an explicit to an implicit method is also investigated in Section 4.6.

4.2 Stability of explicit time integration

In the case of implicit time integration, since the solution will converge with any time step, the step size is limited by the accuracy of the solution. As a general guide the time step is determined by limiting the temperature change in one step to around a few tens of degrees. In the welding phase of the analysis this would result in rather small steps, however, in the cooling phase the step size can be significantly increased.

As it is pointed out in the previous chapter, the main drawback of explicit time integration is that it is conditionally stable and the small time steps required for stability are often prohibitive in practical applications. In this section the focus is on the factors that influence this critical time step and how it can be improved to make explicit time integration an attractive option for welding simulation.

In a coupled thermo-mechanical analysis ABAQUS/Explicit [81] uses the central-difference integration rule to integrate the equation of motion and the forward-difference integration rule to integrate the heat transfer equation.

In the integration of the equation of motion the stability limit [76, 74, 81] for an undamped structure depends on the highest frequency (ω_{max}) of the system according to:

$$\Delta t \leq \frac{2}{\omega_{max}} \tag{4.1}$$

The time step stability limit can be approximated [74] by the smallest transit time of the dilatational wave across the smallest element in the mesh according to:

$$\Delta t \approx \frac{L_{min}}{c_d} \tag{4.2}$$

where

$$c_d = \sqrt{\frac{E(1-\nu)}{(1+\nu)(1-2\nu)\rho}} \tag{4.3}$$

is the dilatational wave speed for solid elements of isotropic, elastic material and L_{min} is the smallest element size in the model, while E, ν and ρ represent the Young's modulus, Poisson's ratio and density of the material, respectively.

In the integration of the heat transfer equation the stability limits [81] depends on the largest eigenvalue (λ_{max}) in the system of equations of the thermal solution response according to:

$$\Delta t \leq \frac{2}{\lambda_{max}} \tag{4.4}$$

The time step stability limit can be approximated [81] using thermal diffusivity (α) of the material according to:

$$\Delta t \approx \frac{L_{min}^2}{\alpha} \tag{4.5}$$

where

$$\alpha = \frac{k}{\rho c} \tag{4.6}$$

and k, ρ, and c represent the thermal conductivity, density, and specific heat of the material, respectively.

Since both thermal and mechanical solutions need to be stable the smaller of the two stable time steps [81] is used in the analysis:

$$\Delta t \leq \min(\frac{2}{\omega_{max}}, \frac{2}{\lambda_{max}}) \tag{4.7}$$

Using the properties, specified in the example of the next section, of steel at room temperature results in the following values of c_d and α:

$$c_d = 5.93 \cdot 10^3 \frac{m}{s} \qquad \frac{1}{c_d} = 1.686 \cdot 10^{-4} \frac{s}{m} \tag{4.8}$$

$$\alpha = 1.817 \cdot 10^{-5} \frac{m^2}{s} \qquad \frac{1}{\alpha} = 5.503 \cdot 10^4 \frac{s}{m^2} \tag{4.9}$$

It can be concluded that practically independent of the element size the mechanical solution's stable time step size is always several magnitudes smaller than that of the thermal solution in the case of a steel-like material.

According to Equations 4.3 and 4.6 both limitations are influenced by the density (ρ) of the material. A technique called "mass scaling" [74, 78] takes advantage of this

by artificially increasing the density of the material in order to increase the stable time step and so reducing the number of steps to complete the analysis. The thermal solution's stable time step is a linear function of the density, while the mechanical solution's stable time step is a function of the square root of the density. As a result of the large difference between the stable time step limit of the mechanical and thermal solution (Equations 4.8 and 4.9), in the rest of the chapter the focus will be on the mechanical solution as the use of mass scaling is being investigated.

Changing the other parameters (E and ν) that influence the stable time step would significantly alter the properties of the structure and thus the results of the analysis. Of course this can also be said about the mass of the model in the case of a dynamic analysis. However, welding simulation can be considered as a quasi-static (*i.e.* the dynamic effects are very limited) even if an explicit dynamic code is used to solve the problem. On the other hand, by no means can the mass of the system be changed arbitrarily as demonstrated in the example of the next section.

Another technique to tackle the problem of limited time step size in an explicit time integration is to artificially speed up the physical process that is analysed, in this case the welding process. This so called "velocity scaling" [78] requires the adjustment of the thermal properties of the model. Otherwise simply increasing the welding speed in the analysis would result in solving a completely different problem to the original. Velocity scaling is not discussed here in more detail.

4.3 Three-dimensional solid rod model

The rod model is often used [18, 82] to demonstrate the principles of residual stress development in welded plates. In its simplest implementation it is a rod that is supported at both ends while the temperature of it is gradually increased and decreased. As the temperature starts to increase, the compressive axial stress develops in the bar. As a result of the increasing temperature the stress starts to decrease as the material softens and eventually when the temperature reaches the melting point the rod returns to a stress free state. During the following cooling process tensile stress develops in the rod and this stress remains in the rod when it returns to its original temperature. Even though it might seem like an oversimplified approach the same principles have also been successfully applied in complex cases such as multipass welding [82].

In this work the simple rod model is reproduced using solid finite elements. Solid elements have been chosen because in the more complex problems of this research solid elements will also be used. However, the principles of mass scaling could be demonstrated equally well using other element types.

Figures 4.1 and 4.2 show the temperature dependent mechanical (Young's modulus (E), Poisson's ratio (ν), yield stress (σ) at $\epsilon_p = 0$ and $\epsilon_p = 0.01$ plastic strain levels) and thermal properties (thermal expansion coefficient (α), density (ρ), conductivity (λ) and specific heat (c)) of the steel material considered in the analysis [21, 82].

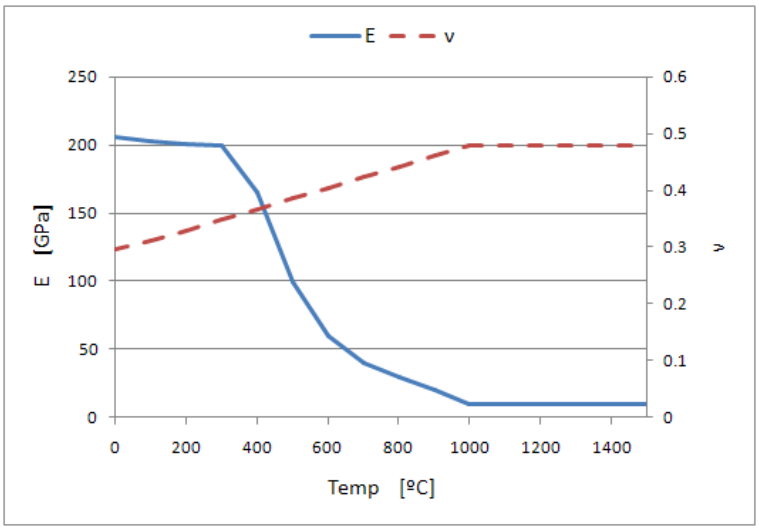

(a) Variation of the Young's modulus and Poisson's ratio with temperature

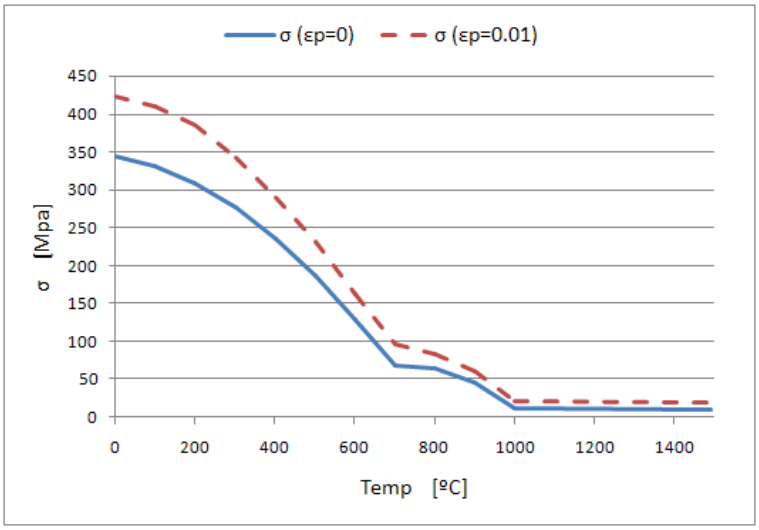

(b) Variation of the yield stress with temperature

Figure 4.1: Variation of mechanical properties with temperature [21, 82].

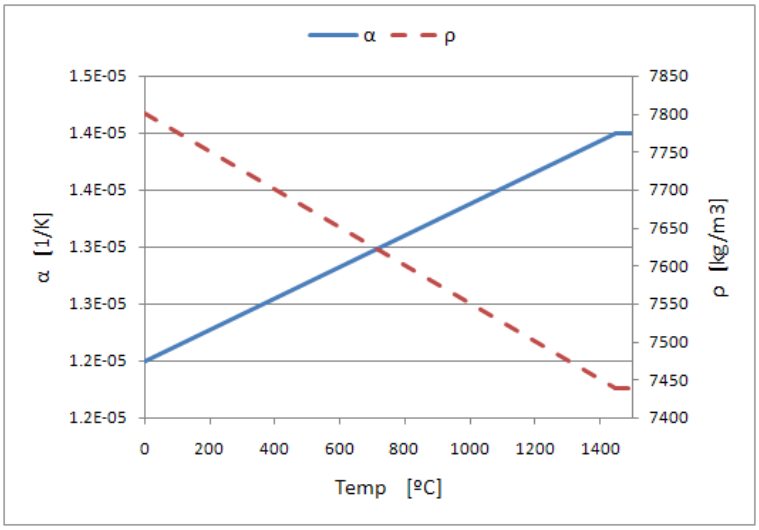

(a) Variation of the thermal expansion coefficient and density with temperature

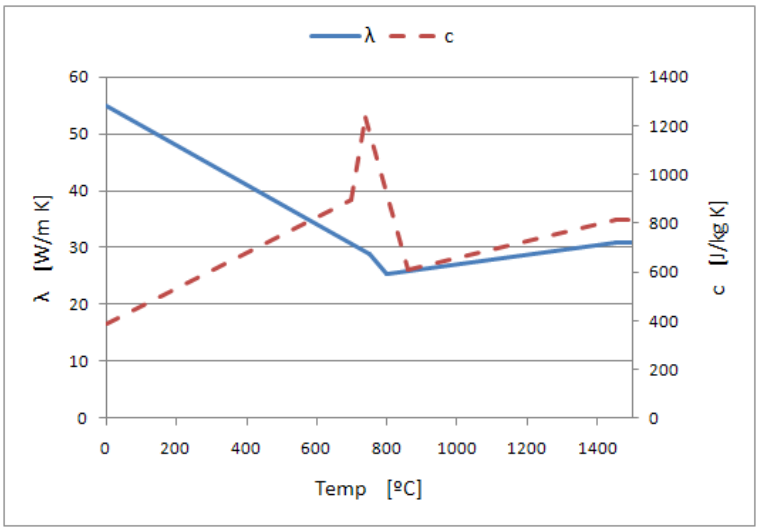

(b) Variation of the conductivity and specific heat with temperature

Figure 4.2: Variation of thermal properties with temperature [21, 82].

The finite element model is shown in Figure 4.3. The cross-section is 20mm by 20mm and the length is 200mm. The model consists of ten C3D8T elements. It is an eight-node coupled temperature-displacement element with four degrees of freedom (DOF) at each node: three translational and one temperature DOF. The rod is supported at both ends to restrict the axial deformation but it is free to expand in the plane of the cross-section.

Since the overall stable time step is determined by the mechanical analysis in this example the thermal analysis is practically suppressed by explicitly defining a temperature history shown in Figure 4.4. During the first second of the analysis the

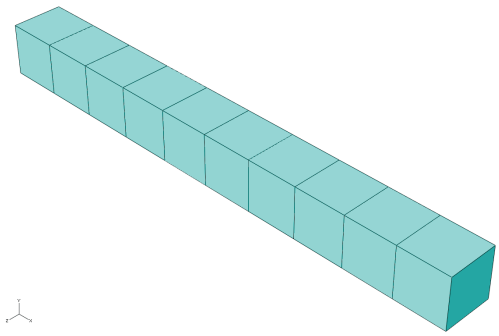

Figure 4.3: Finite element mesh (Model #1) of the solid rod model.

temperature of the entire model is increased from 0°C to 1500°C, approximately the melting point of steel, and during the second second of the analysis the model is cooled down to the original 0°C. As mentioned in Section 4.2, to ensure the accuracy of the implicit analysis the temperature change within one increment is limited to 20°C which results in 76 increments in both load steps. A similar limitation is applied to all the examples presented in this chapter. For explicit analysis, however, such a limitation is not necessary due to the extremely small stable time steps that would practically never result in temperature changes anywhere near 20°C.

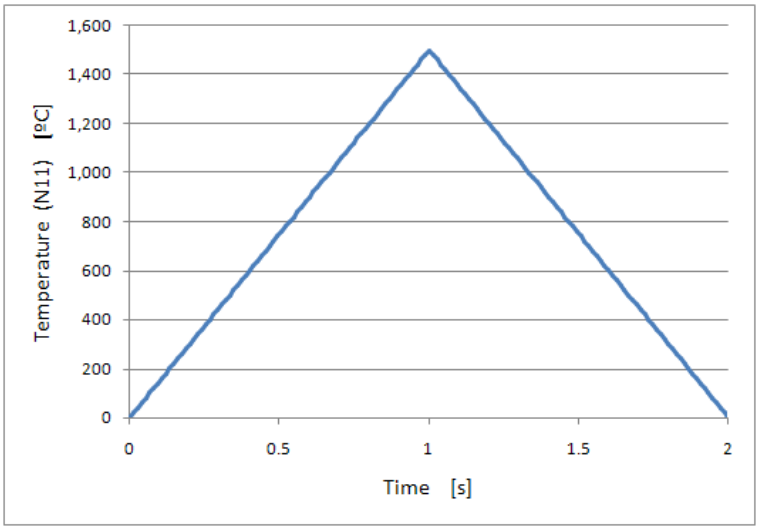

Figure 4.4: Temperature history for the solid rod model.

One important aspect of welding simulation is the effect of melting. For the purpose of this study only the effect on the development of plastic strains is considered. In the model, as the temperature increases, the compressive axial stress starts to develop and eventually reaches the plastic range. When the metal melts,

at the end of the first second of the analysis, the plastic strains in the material are reset to zero. This can be taken into account in ABAQUS in both the explicit and implicit analysis by defining an annealing temperature in the material model. Figure 4.5 shows the equivalent plastic strain (PEEQ) and the axial stress (S11) of the implicit analysis (using ABAQUS/Standard [81]) for two cases: with and without the annealing effect. When annealing is ignored the plastic strains are not reset at the melting temperature which means that during cooling when the tensile stresses get into the plastic range and the material goes through hardening the final residual stresses reach a higher level.

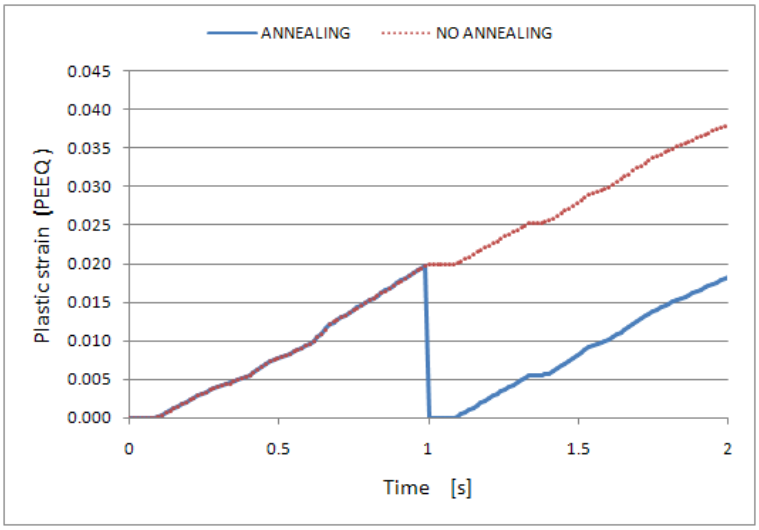

(a) Equivalent plastic strain (PEEQ)

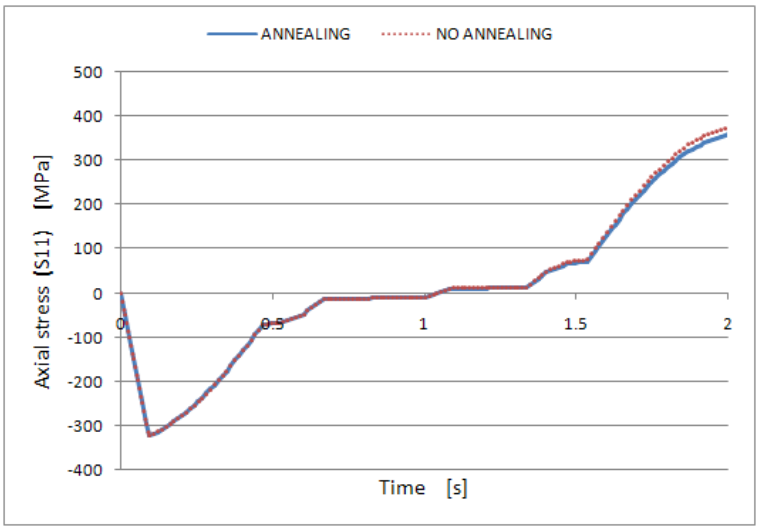

(b) Axial stress (S11)

Figure 4.5: Results of the implicit analyses of the simple rod model.

Using ABAQUS/Explicit the same example considering the effect of annealing

is recalculated with and without mass scaling. A mass scaling factor in the range of 10^3 to 10^8 is considered. This means that the stable time step of the analysis is increased by a factor in the range of $\sqrt{10^3}$ to $\sqrt{10^8}$ according to Equations 4.2 and 4.3. The results of the explicit analysis with a mass scaling factor of 10^3, 10^4 and 10^5 are identical therefore the former two cases are not presented here. Figure 4.6 shows that the development of the axial stress during the heating and cooling of the model is identical in the implicit method and in the explicit method without mass scaling and with a mass scaling factor of 10^5.

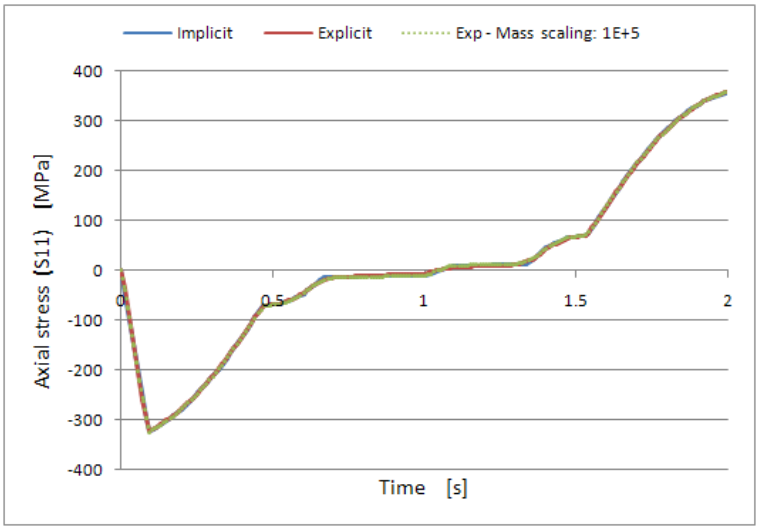

Figure 4.6: Results of the implicit analysis and explicit analyses with no mass scaling and mass scaling of 10^5 of the simple rod model.

Figure 4.7 shows the results of the explicit analyses with greater mass scaling factors. It was found that a mass scaling factor of 10^6 causes only a negligible variation in the stress development (not shown). However, a factor of 10^7 results in a strong disturbance at the beginning of the cooling phase but the final remaining residual stress in the rod is not influenced by this. After increasing one step further the mass scaling factor to 10^8, the results show a very significant oscillation.

It is important to point out that as a result of the rigid constraints at both ends of the rod the displacements of the model are restricted and therefore there are no dynamic effects. Therefore very high mass scaling factors can be applied without the loss of accuracy. In the presence of dynamic effects the results would be very strongly influenced by such a level of mass scaling.

The reason mass scaling would be used in a model is to reduce the calculation

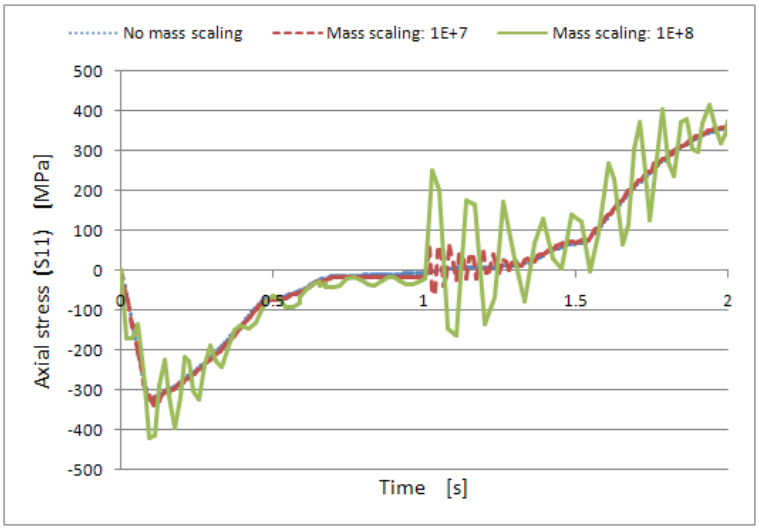

Figure 4.7: Results of the explicit analyses with no mass scaling and mass scaling of 10^7 and 10^8 of the simple rod model.

time by increasing the stable time step size. To see how in this simple example the calculation time is affected by mass scaling two other meshes, shown in Figure 4.8, are included in the study since the model shown in Figure 4.3 has only ten solid elements and therefore can be solved in such a short time that makes any comparison meaningless. In the Model #2 the number of elements is increased to $10 * 2^3 = 80$ while in Model #3 it is increased to $10 * 4^3 = 640$.

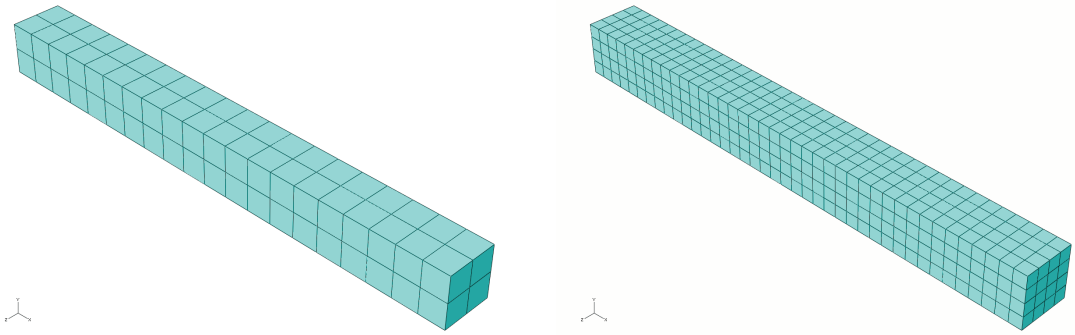

(a) (b)

Figure 4.8: (a) Model #2 and (b) Model #3 of the solid rod model.

Table 4.1 shows the element size of the model, the stable time step calculated using Equation 4.2 with material properties at initial temperature and the initial time step size used by ABAQUS/Explicit. The CPU time shown in Table 4.2 is given in the output of the calculation. The latter two data items are given for the

different levels of mass scaling including the case where no mass scaling is applied.

			Mass scaling factor			
			0	1E+03	1E+04	1E+05
Model	L_{min} [mm]	L_{min}/C_d [s]	Initial time step [s]			
#1	20	3.37E-06	1.83E-06	5.80E-05	1.83E-04	5.80E-04
#2	10	1.69E-06	9.17E-07	2.90E-05	9.17E-05	2.90E-04
#3	5	8.43E-07	4.58E-07	1.45E-05	4.59E-05	1.45E-04

Table 4.1: Initial time step size: rod model.

	Mass scaling factor			
	0	1E+03	1E+04	1E+05
Model	CPU time [h:m:s]			
#1	0:06:53	0:00:12	0:00:04	0:00:02
#2	1:04:56	0:01:56	0:00:31	0:00:14
#3	19:07:08	0:37:53	0:12:46	0:04:06

Table 4.2: CPU time for different levels of mass scaling: rod model.

The initial time step size used by ABAQUS/Explicit is always smaller than the stable time step calculated using Equation 4.2. This is because the value that Equation 4.2 gives is just an approximation and it is often not a conservative one. Therefore, depending on the dimensionality of the problem, ABAQUS/Explicit applies an additional factor of value less than 1.0 when it determines the initial step size. The stable step size is then constantly reviewed in the course of the analysis to ensure that it never gets into an unstable region even if there are significant changes in the state of the model compared to its initial state.

The results of Model #3 show two important facts. First it demonstrates that explicit analysis is not generally efficient in solving static or quasi static problems without the use of mass scaling or other techniques to speed up the analysis. Even in the case of this relatively simple problem and small model the analysis runs for more than 19 hours as a result of the extremely small stable time step. This would be clearly unacceptable for any practical problem. However, more importantly, it also shows what a difference the use of mass scaling can make. As shown in Table 4.2,

a factor of 10^5 reduced the calculation time to just 4 minutes without any loss of accuracy of the results.

Figure 4.9 shows the computational time as a function of the mass scaling factor for all the three models. When there is a larger number of small elements, as is the case of Model #3, the use of mass scaling results in a much more significant reduction in the computational cost.

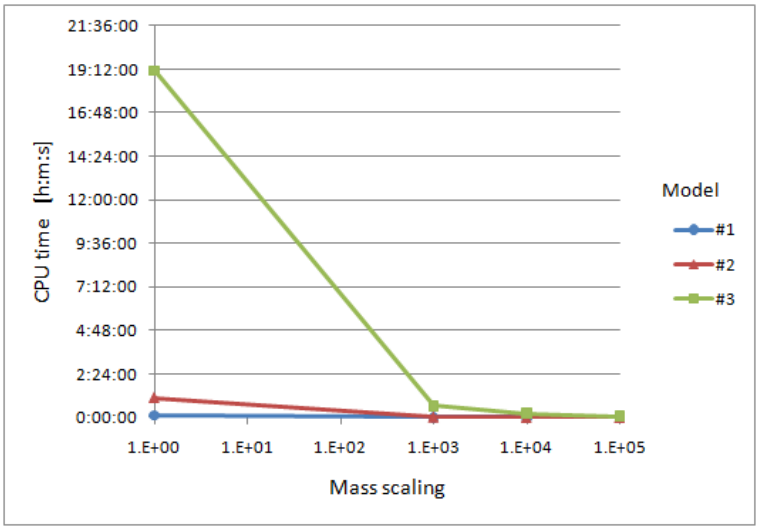

Figure 4.9: CPU times for the three rod models #1, #2 and #3.

It should be pointed out that the maximum value of the mass scaling factor that does not alter the results (in the present example it is 10^5) is independent of the number and size of the elements. The three models represent the same physical problem even if the mesh has been changed therefore an increase of the overall mass of the model would have the same effect in all the models. Of course the stable time step size depends on the size of the mesh, and the overall solution time depends on the number of elements as well, therefore the efficiency of mass scaling is different in the three models while the limit for the mass scaling factor remains the same.

In the examples presented here the results of an explicit analysis are compared to that of an implicit analysis. However, in practice very often such a comparison is not available for checking the validity of the results. A simple and general strategy to evaluate the results is to compare the internal energy history to the kinetic energy history in the analysis. Mass scaling can be successfully applied to welding because it is a quasi-static process with very limited dynamic effects. To consider a problem quasi-static the ratio of kinetic energy to internal energy should remain

low. Additionally, any significant oscillation of the results and the kinetic energy is an indication that the level of mass scaling applied to the model might negatively influence the accuracy of the output.

4.4 Three-dimensional solid plate model

The above simple example demonstrates the concept behind the use of mass scaling but does not provide a basis to decide if this technique would really make explicit analysis an attractive option for the simulation of welding. In this and the next sections more realistic examples are presented to investigate this issue.

The next model is one half of a 150mm long section of a butt welded steel plate. The thickness of the plate is 20mm and its width is 200mm. Figure 4.10 shows the mesh of the model. The model consists of 330 C3D8T elements and 576 nodes. In Figure 4.10 the highlighted elements represent the weld seam, while in Figure 4.11 the elements used to present some results later in this section are highlighted and numbered.

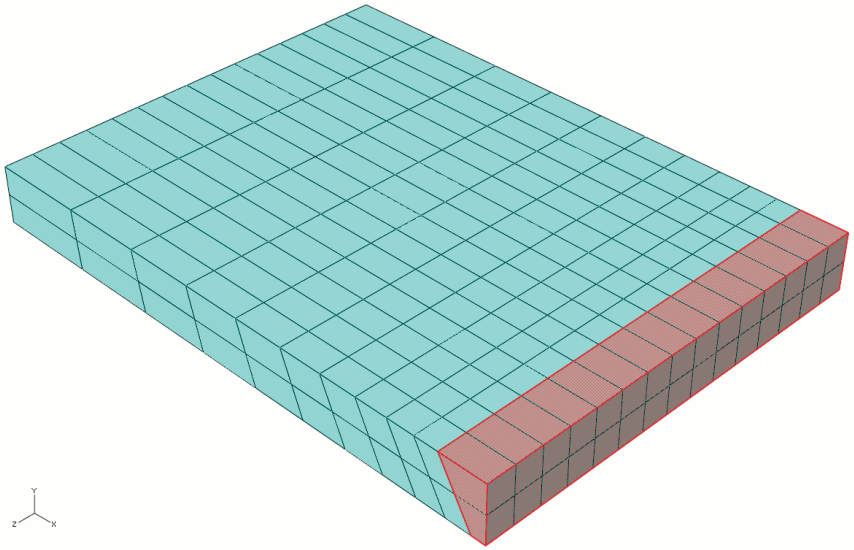

Figure 4.10: Finite element mesh for the plate model: plate and weld seam.

The following mechanical boundary conditions are applied to the plate: symmetry boundary conditions at the centre plane, vertical support at the two corners opposite to the weld and an axial support at the node located at the bottom of the weld seam at the centre of the plate. To simplify the analysis the welding along

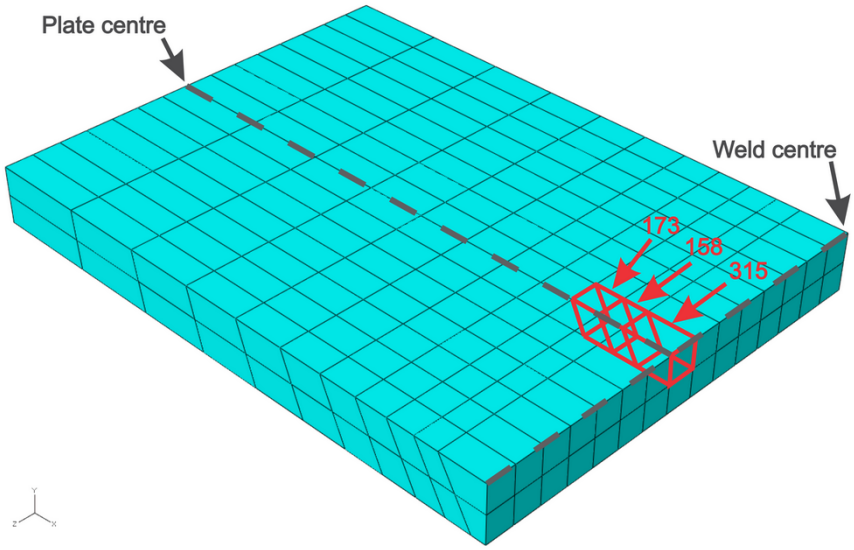

Figure 4.11: Finite element mesh for the plate model: path and elements used in postprocessing.

the centre line of the plane is modelled in one instance for the whole length of the weld: during one second the elements highlighted in Figure 4.10 are heated up to 1500°C using prescribed temperatures (in a similar manner to what is used in the rod model example). The cooling down phase, however, is modelled by defining convective boundary conditions on all surfaces of the model apart from the plane of symmetry. The temperature independent convective heat transfer coefficient of $\alpha_c = 30W/m^2K$ is used. The temperature dependent material properties are identical to the ones defined in the previous section.

Figure 4.12 shows the complete temperature history of a node in the weld seam. It takes about 10,000s for the entire model to return to its original temperature. However, it is worth pointing out that the temperature change in the last 8,000s is only about 30°C which means that most of the temperature change occurs in the initial part of the analysis. To illustrate this better Figure 4.13 shows the rate of temperature change as a function of time up to 200s. In the first 20s the curve is very steep and this is the zone that would probably be the most suitable for explicit time integration. Beyond 50s the rate is so low that it would be certainly unsuitable to use the explicit method beyond this time. In the present work the explicit solution is studied up to 50s. Similarly to the rod model example, different levels of mass scaling are compared using factors of 10^3, 10^4 and 10^6. Further studies presented

in the next section help to determine the optimal time to initiate a change from explicit to implicit method in a mixed time integration solution.

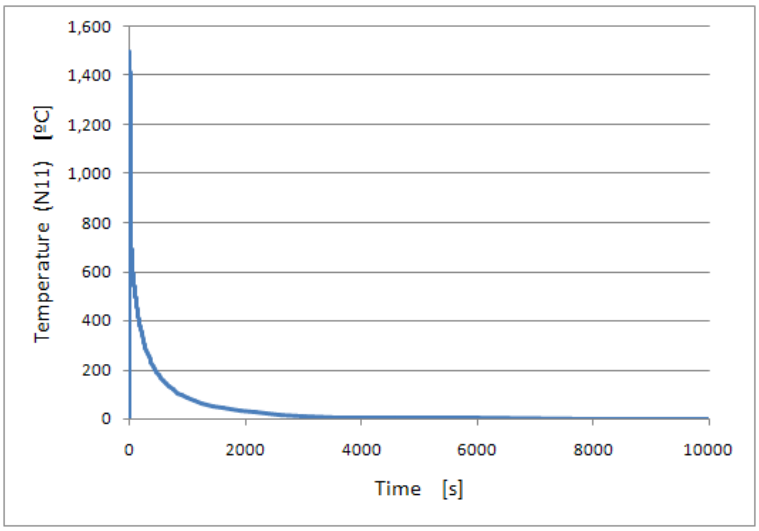

(a) Up to 10,000s.

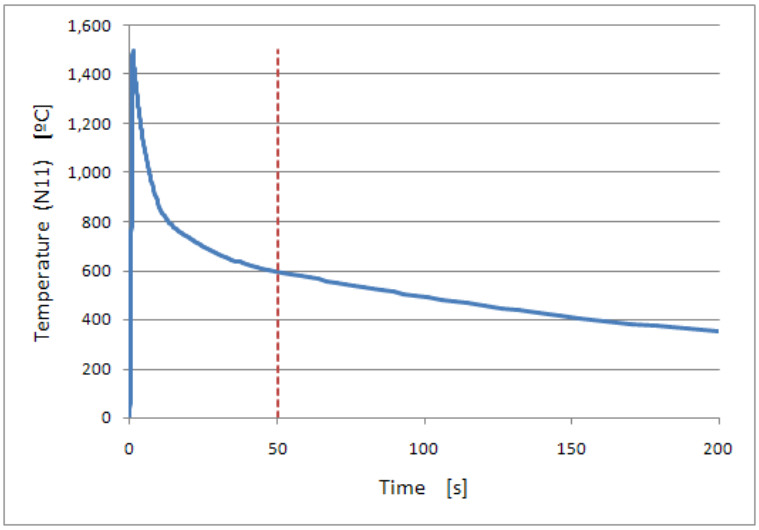

(b) Up to 200s.

Figure 4.12: Temperature history for the steel plate shown in Figure 4.10.

Figure 4.14 shows the displacement time history in the middle of the top of the weld seam. In all three cases the explicit analysis seems to underestimate the displacements calculated with the implicit method but it is only in the case of the highest mass scaling factor where oscillation of the results can be observed. This could be improved by using a more restricted mass scaling strategy at the very beginning of the analysis and gradually increasing the mass scaling factor during the course of the simulation. Damping could also be considered to make the explicit solution smoother. However, the use of such techniques is beyond the scope of this

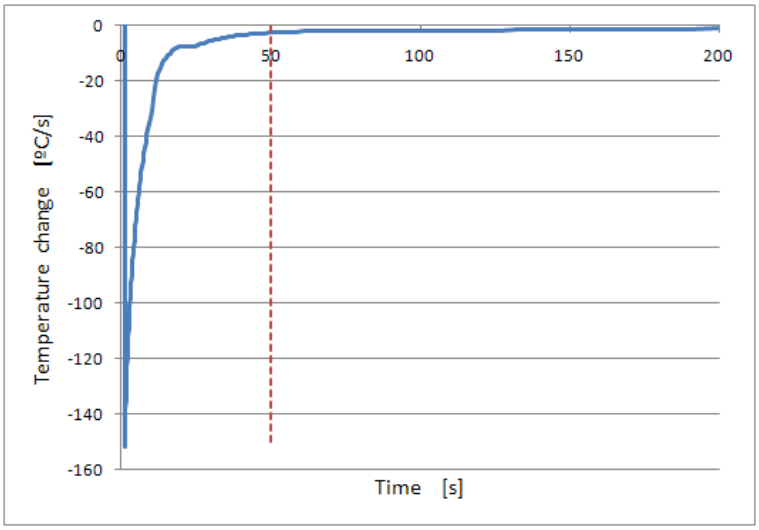

Figure 4.13: Temperature change rate for the steel plate shown in Figure 4.10.

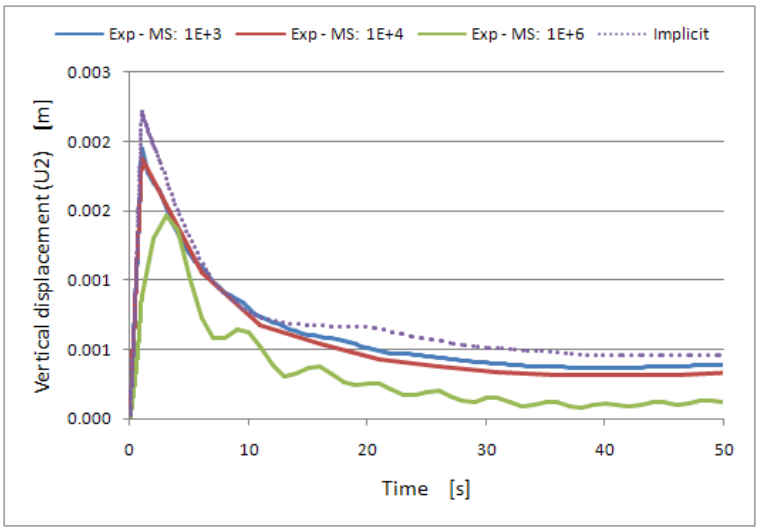

Figure 4.14: Displacement history for the steel plate shown in Figure 4.10 using an explicit analysis with three levels of mass scaling (10^3, 10^4 and 10^6) and an implicit analysis.

work.

Despite these differences in the displacement histories, the stress histories in the elements highlighted in Figure 4.11 show a high degree of similarity. The longitudinal stress (in the direction of the welding) history in the centroid of the elements are compared in Figures 4.15 and 4.16. In elements 173 and 315 the stress histories are indistinguishable in the three explicit cases and they are practically equal to that

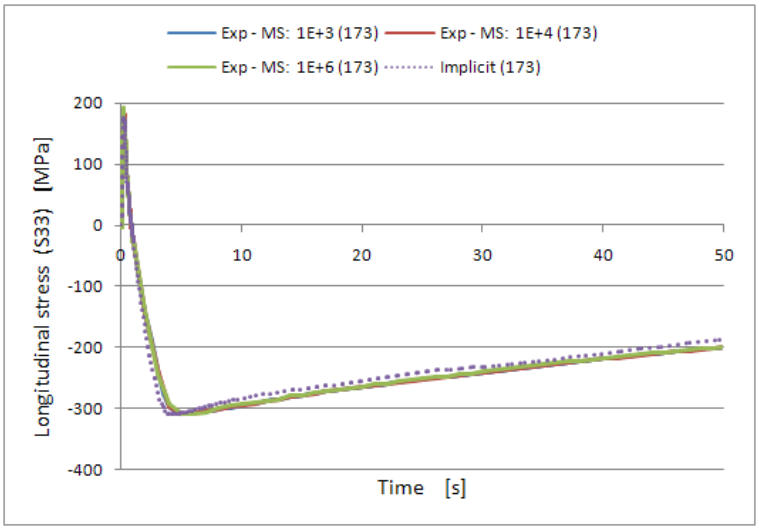

(a) Stress history of element 173.

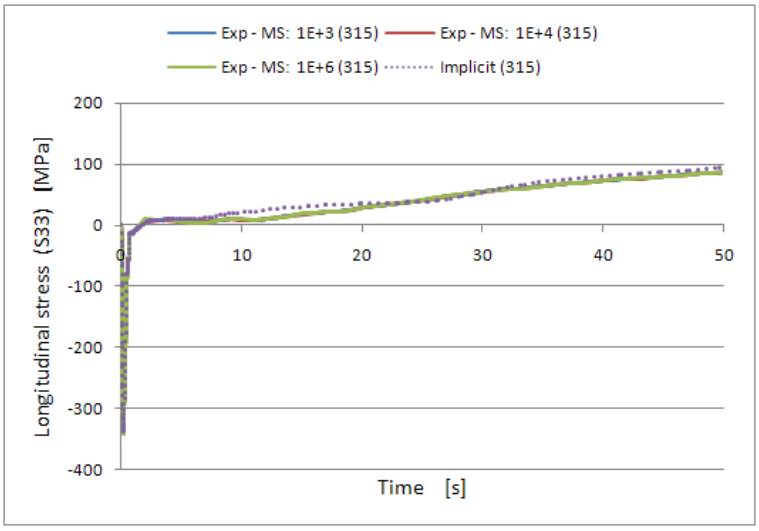

(b) Stress history of element 315.

Figure 4.15: Stress history of (a) element 173 and (b) element 315 using an explicit analysis with three levels of mass scaling (10^3, 10^4 and 10^6) and an implicit analysis.

of the implicit analysis. Again in element 158 (location shown in Figure 4.11) the stress histories are indistinguishable in the three explicit analyses. However, in the first 20s the results of the implicit method are slightly different. Nevertheless at the end of the analysis, at 50s, the results converge to the same value. To demonstrate that these differences in the first seconds of the analysis do not influence the final residual stress distribution in the model an explicit analysis using a mass scaling factor of 10^6 is performed up to 4,000s. Of course this is not an efficient solution and it is not recommended that an explicit analysis is used for such a long period.

This analysis is performed solely to compare the accuracy of implicit and explicit methods for a long run and to evaluate the effects of the differences in the results.

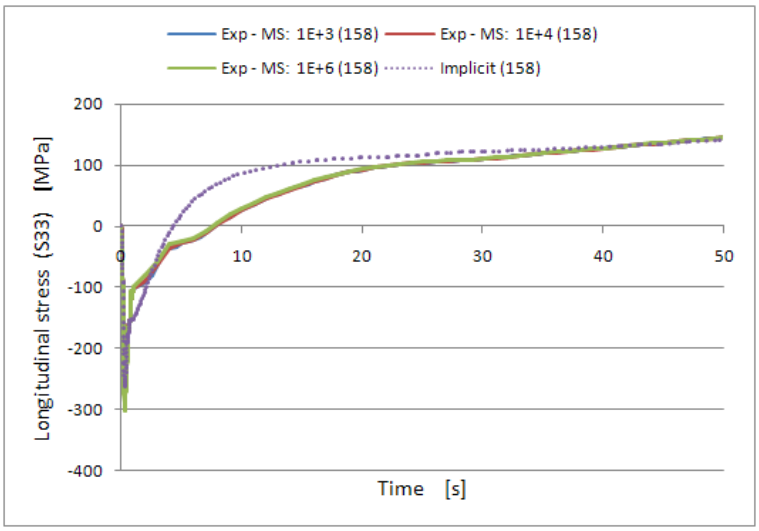

Figure 4.16: Stress history of element 158 using an explicit analysis with three levels of mass scaling (10^3, 10^4 and 10^6) and an implicit analysis.

Figure 4.17 shows the stress distribution at 3650s along the two lines on the top face of the plate defined in Figure 4.11. Figure 4.17(a) shows the longitudinal stresses at the plate centre line while Figure 4.17(b) shows the transverse stress distribution along the weld centre line. In both cases there are practically no differences between the results of the explicit and implicit analyses.

Mass scaling factor	Init step [s]	CPU time [h:m:s]
1.00E+03	2.56E-05	3:07:53
1.00E+04	8.11E-05	1:03:01
1.00E+06	8.11E-04	0:05:34

Table 4.3: CPU time for explicit analysis up to 50s with three levels of mass scaling (10^3, 10^4 and 10^6): plate model.

Finally, in Table 4.3 a summary of the CPU times is given for the explicit analyses up to 50s with different levels of mass scaling. As seen in the rod model example, the computational times can be reduced very significantly by increasing the mass scaling. When using a mass scaling factor of 10^3 a CPU time of more than 3 hours is

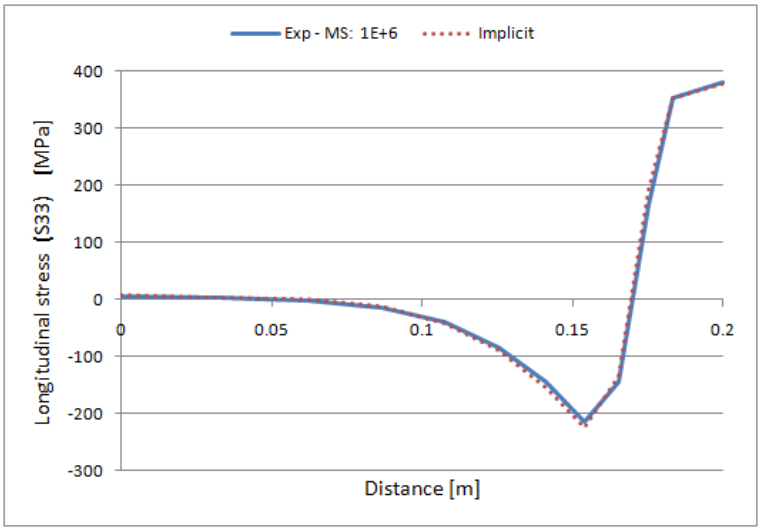

(a) Longitudinal stress distribution along the plate centre.

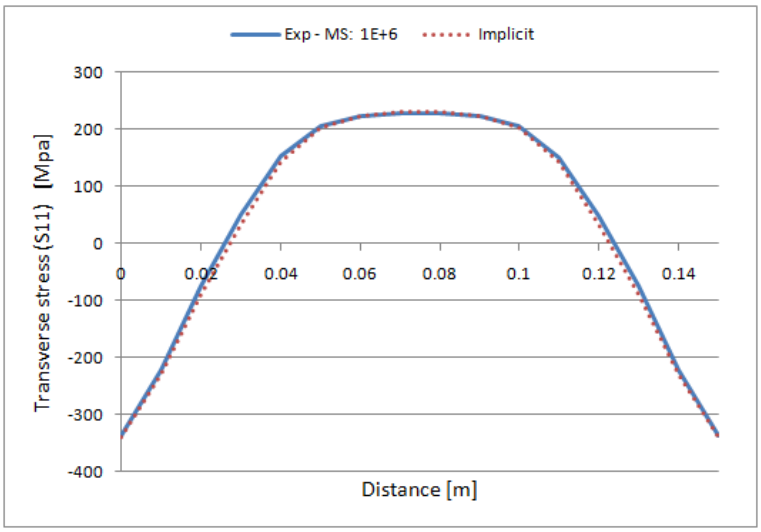

(b) Transverse stress distribution along the weld centre.

Figure 4.17: (a) Longitudinal and (b) transverse stress distribution at time=3650s for both an implicit analysis and an explicit analysis with mass scaling of 10^6.

required whereas the CPU time is reduced to only 5 minutes (similar to the implicit analysis) when the mass scaling factor is increased to 10^6. It is expected that with larger finite element models, as demonstrated with the rod model example, this time saving would be even more significant.

4.5 Three-dimensional plate girder model

The third and last example is a segment of a plate girder with single-sided deep penetration fillet welds connecting the web with the flanges. Figure 4.18 shows the finite element mesh of the model: the vertical plate is the flange (thickness: 6mm) and the horizontal one is the web (thickness: 4mm). The length of the model is 100mm, while both the width of the flange and the half-width of the web are 200mm. Unlike in the previous cases, a moving heat source of welding is also considered in this example. Since the objective of this research project is to bring virtual fabrication into the design process of steel structures it is important to keep the simulation simple enough because details of the fabrication are frequently unavailable at the time of the design. Moreover, designers of steel structures do not usually get involved with the fabrication itself. They define the geometry of the plates and the weld size to fulfil the structural requirements but normally they do not even know exactly what type of welding will be used for the fabrication, let alone the welding parameters. However, the designed weld size and the required penetration is always known and can be used as a good approximation for the welding simulation. It can be assumed that at the border between the weld seam and the base material the temperature is equal to the melting temperature of the base material. Therefore if the cross-section of the weld seam is known the welding heat input can be easily estimated by simply defining prescribed temperatures equal to the melting temperature of the base metal at the nodes of the weld seam in the finite element model.

The first image (from the left) of Figure 4.19 shows the cross section of the single-sided deep penetration fillet weld of the plate girder studied while the second shows the comparison between the idealised and the actual weld seam cross-section. The last two images show the ideal geometry only and the finite element mesh near the weld seam. Even though the actual weld is not perfectly symmetric it has approximately the same area as the idealised weld therefore using the idealised geometry in the analysis to apply the prescribed temperature is an acceptable approximation of the welding heat source. This allows analysts to conduct an approximate welding simulation without knowing the exact parameters such as voltage, amperage and efficiency of the welding heat source. Nevertheless, the welding speed is a parameter that needs to be included in the analysis and should be approximated by typical welding speeds of the given type of structure if no further details are

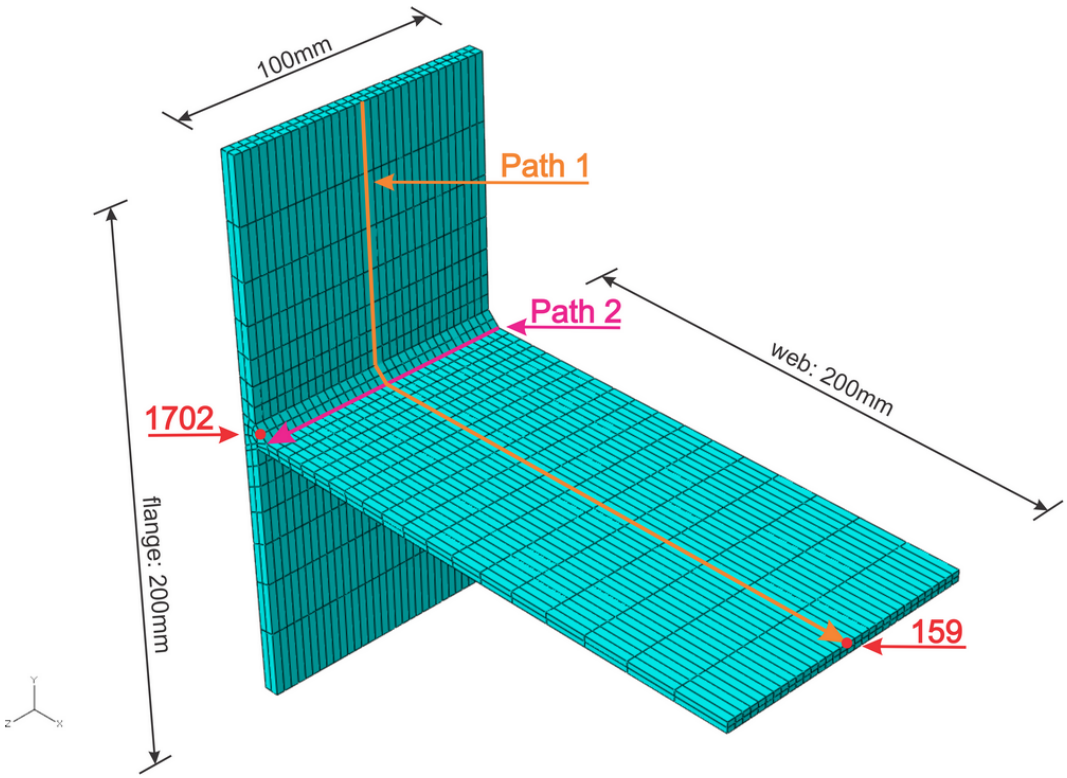

Figure 4.18: Finite element mesh for the plate girder model.

available. More details of such a heat source model, called the "equivalent prismatic heat source model", is presented in Chapter 6.

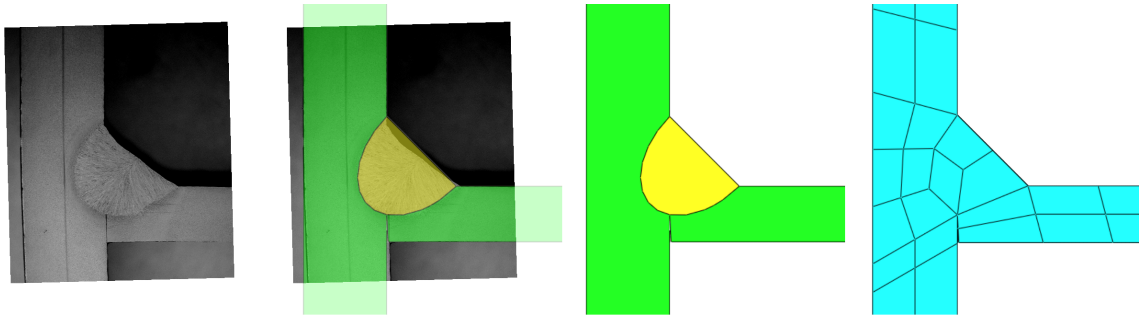

Figure 4.19: Weld seam cross-section for the plate girder model.

In the present example a melting temperature of 1500°C and a welding speed of 25mm/s is assumed which results in a total of 4s of welding time. The full length of the weld is assumed to be done in eight welding load steps in the analysis. Figure 4.20 shows the sets of elements highlighted that represent each step of the welding process. It is important that the melting temperature is not applied instantaneously to the

nodes of those elements but the temperature is increased gradually over a short period of time (0.01s in the example). Figure 4.21 shows the prescribed temperatures for the first four welding steps of the analysis. At the beginning of each step the temperature is increased gradually, then it is maintained constant until the end of the step. By the end of the current step the nodes of the next step have already reached the melting temperature to assure a smooth evolution of the welding heat input. Increasing the number of welding load steps would make the process even smoother but at the same time it would also increase the computational cost significantly.

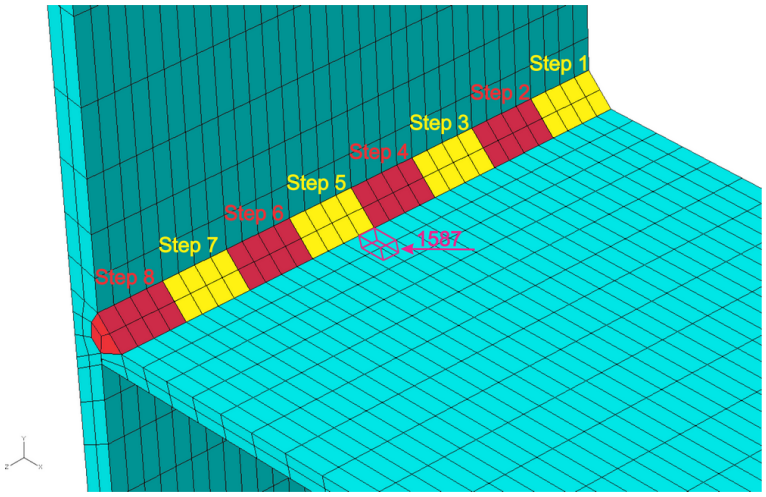

Figure 4.20: Welding steps for the plate girder model.

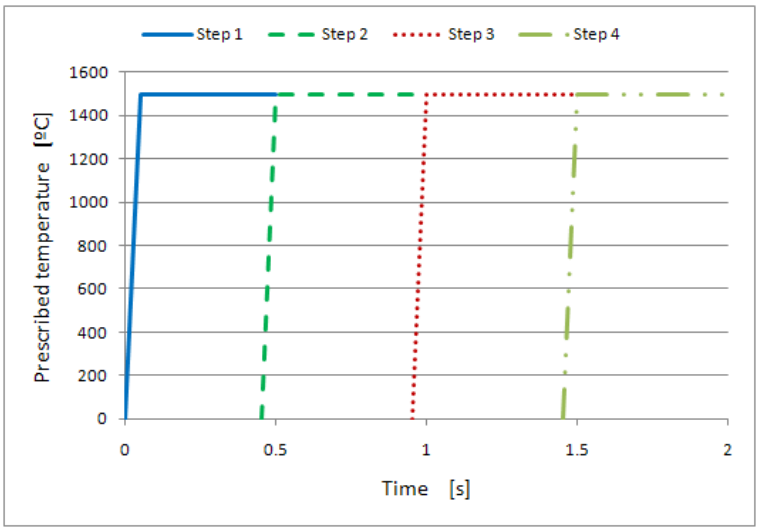

Figure 4.21: Prescribed temperature heat input for the plate girder model.

The material properties and the convective boundary conditions are the same as

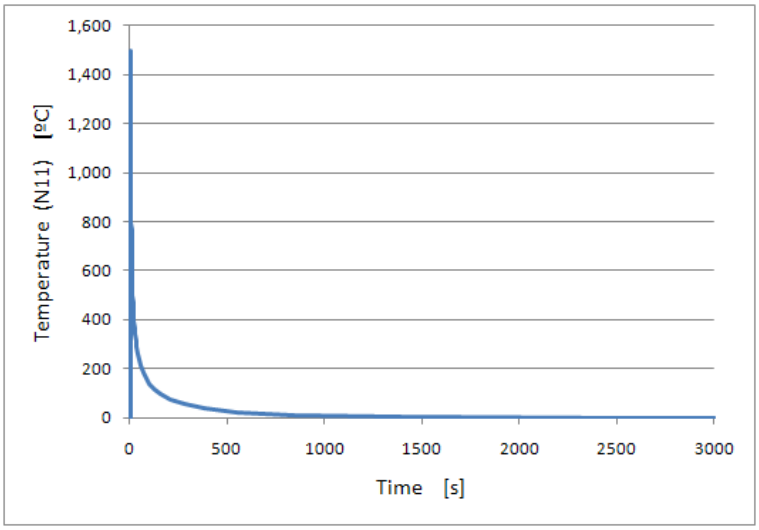

(a) Up to 3,000s.

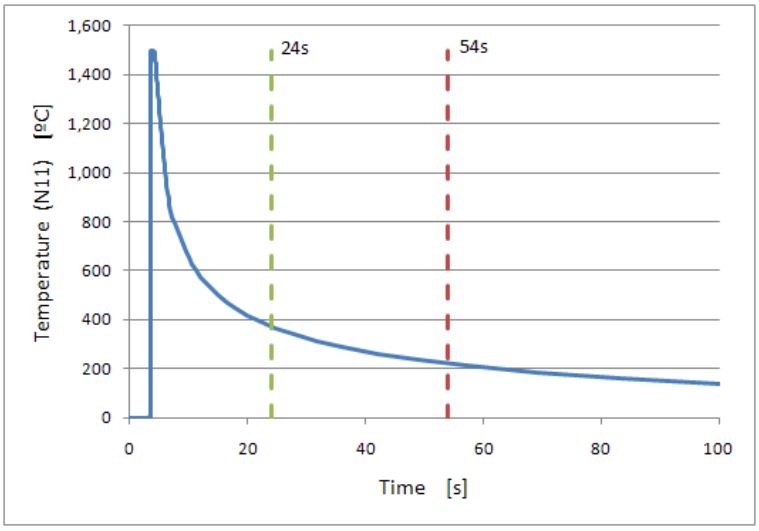

(b) Up to 100s.

Figure 4.22: Temperature history for node 1702 (shown in Figure 4.18) of the plate girder model.

in the previous example. The following mechanical boundary conditions applied to the model: symmetry boundary condition at the centreline of the web, vertical support at the bottom extreme of the flange, transverse (perpendicular to the welding direction) horizontal support along the two vertical edges of the outside face of the flange and longitudinal (in the direction of the welding) horizontal support at the middle of the centreline of the web. These boundary conditions closely resemble the actual support conditions in an automatic welding machine of plate girders at a discreet point in time. As the plate girder advances inside the machine these conditions change. This continuous change of boundary conditions, however, is not reflected

in the model since only a short segment of the girder is studied to demonstrate the use of different numerical methods.

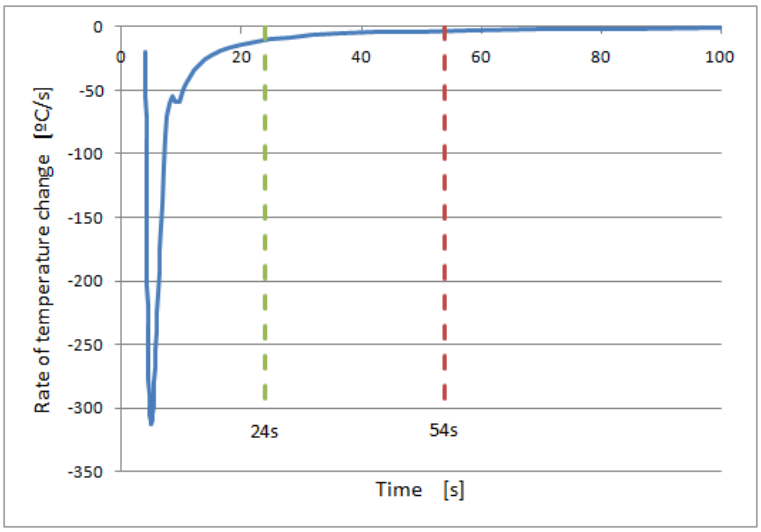

Figure 4.23: Rate of temperature change for node 1702 (shown in Figure 4.18) of the plate girder model.

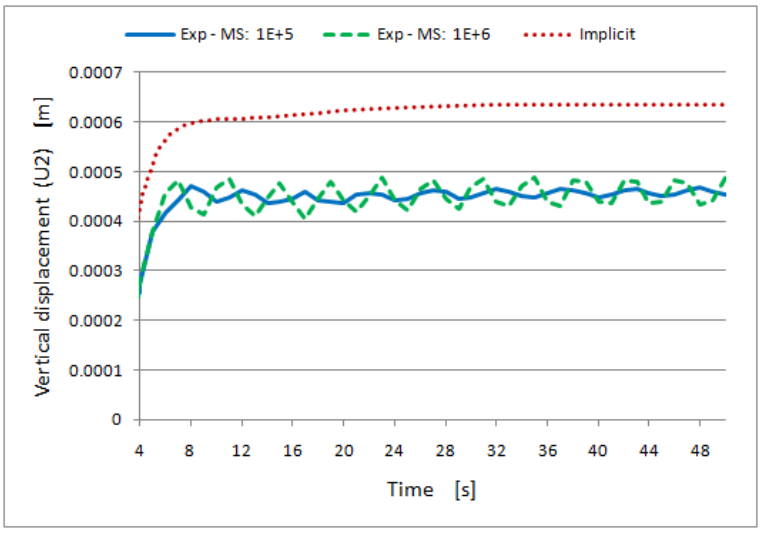

Figure 4.24: Displacement history of node 159 (shown in Figure 4.18) of the plate girder model during an implicit analysis and an explicit analysis with mass scaling of 10^5 and 10^6.

Figure 4.22 shows the complete temperature history of node 1702 located at the very end of the weld seam as shown in Figure 4.18. It takes about 3,000s for the entire model to return to its original temperature but in the last 2,500s the

temperature change is only about 20°C. Figure 4.23 shows the rate of temperature change as a function of time up to 100s. Up to 20s of cooling (*i.e.* 24s of total time) seems to be very suitable for explicit analysis since the curve is very steep but beyond 20s the rate becomes too low to use such a solution method. Nevertheless, similar to the previous example, the explicit analysis is studied up to 50s of cooling (*i.e.* 54s of total time) with mass scaling factors of 10^5 and 10^6.

Figure 4.24 shows the displacement time history of node 159 located in the middle of the centreline of the web as shown in Figure 4.18. The results are similar to that of the plate example: the explicit analyses appears to underestimate the displacements calculated with the implicit method and the higher mass scaling factor produces stronger oscillations.

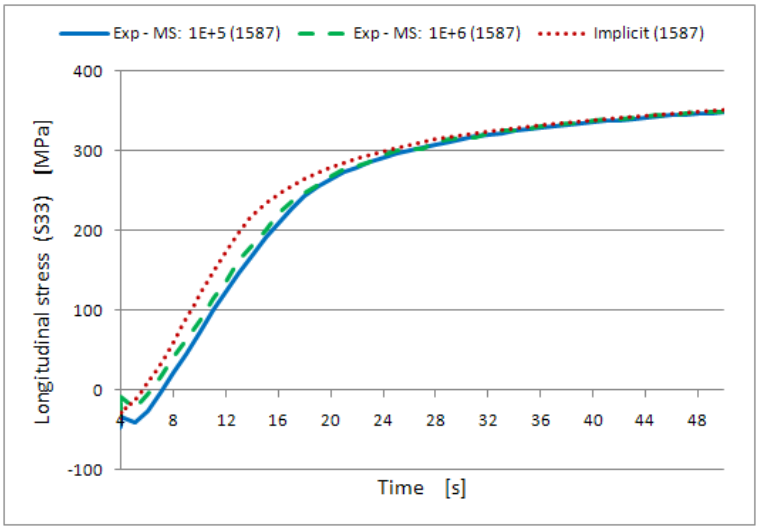

Figure 4.25: Stress history of element 1587 (shown in Figure 4.18) of the plate girder model during an implicit analysis and an explicit analysis with mass scaling of 10^5 and 10^6.

During the cooling phase the longitudinal stress (in the direction of the welding) history at the centroid of element 1587 (highlighted in Figure 4.20) once again displays a better agreement of the results. Figure 4.25 shows that in the first 20s of cooling the explicit analyses slightly underestimate the stress calculated using the implicit method but around 30s they are in agreement. This is also illustrated in Figures 4.26 and 4.27 where the stress distributions are shown at 20s and 50s of cooling. Figure 4.26(a) and Figure 4.27(a) show the longitudinal stress distribution along Path 1 shown in Figure 4.18 while Figure 4.26(b) and Figure 4.27(b) show

the longitudinal stress distribution along Path 2 of Figure 4.18. There is a good agreement between the results of the implicit and explicit analyses.

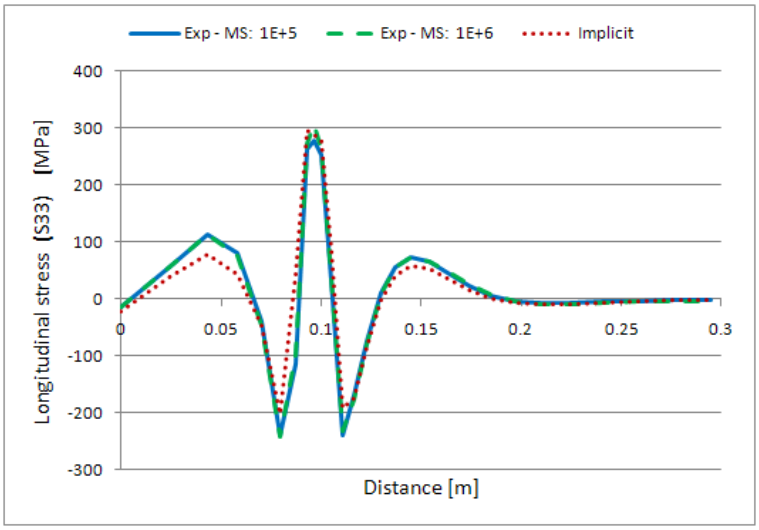

(a) Longitudinal stress distribution along Path1 shown in Figure 4.18.

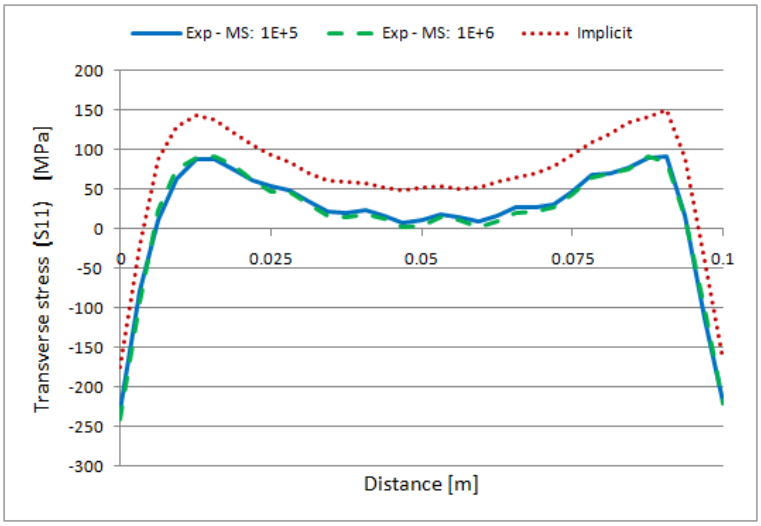

(b) Transverse stress distribution along Path2 shown in Figure 4.18.

Figure 4.26: (a) Longitudinal and (b) transverse stress distribution at cooling time of 20s in the plate girder model during an implicit analysis and an explicit analysis with a mass scaling of 10^5 and 10^6.

Table 4.4 shows a comparison of the calculation times for the three different analyses. Table 4.5 gives the times as percentages of the time required for the implicit analysis. The time interval from 0s to 4s corresponds to the welding phase of the analysis, while the interval from 4s to 54s corresponds to the investigated short portion of the cooling phase. The 24s designates the estimated time limit identified in Figure 4.23 beyond which explicit analysis is very inefficient. It is

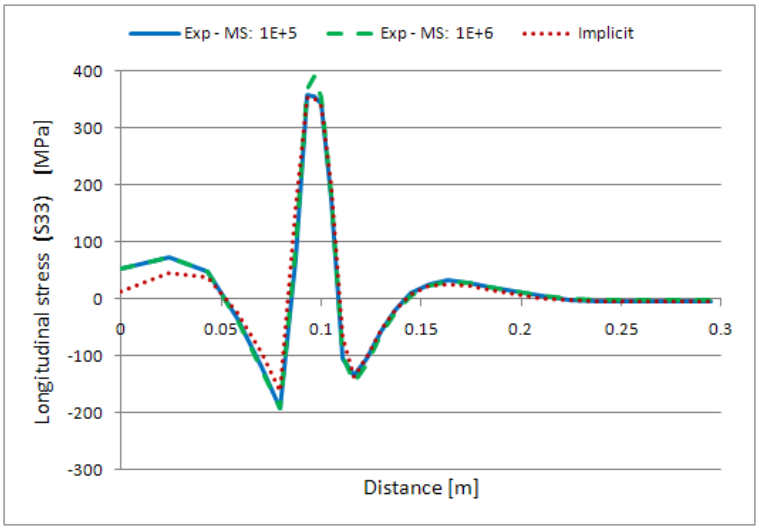

(a) Longitudinal stress distribution along Path1 shown in Figure 4.18.

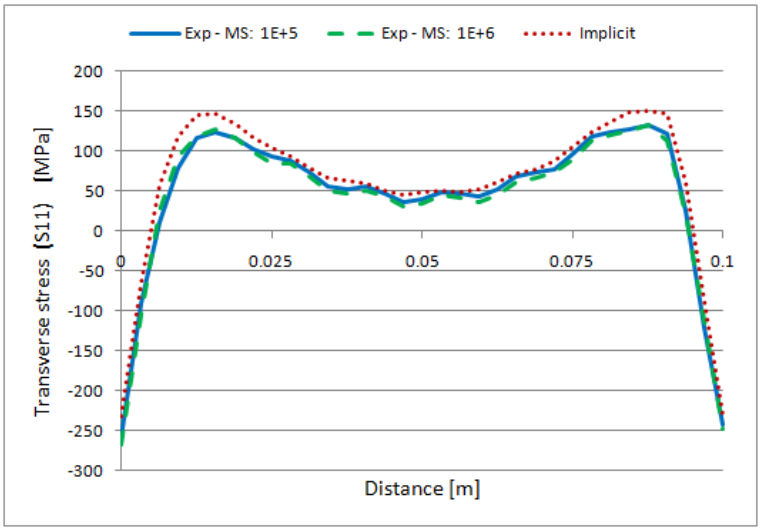

(b) Transverse stress distribution along Path2 shown in Figure 4.18.

Figure 4.27: (a) Longitudinal and (b) transverse stress distribution at cooling time of 50s in the plate girder model during an implicit analysis and an explicit analysis with a mass scaling of 10^5 and 10^6.

evident that a longer welding phase is severely punishing for the implicit analysis because of the limited 20°C temperature change per increment. In a large model not only would there be even more welding steps but also much many elements that can result in a very costly analysis. On the other hand explicit analysis shows its potential even more under such circumstances. Already in this small example the explicit analyses with a mass scaling factor of 10^6 requires 81% less time for the welding phase of the simulation. In a larger model this difference would be even

more pronounced. However, this tendency quickly turns around as the simulation gets into the cooling phase. The implicit analysis can accommodate its time step control to the changing circumstances and keeps increasing the time step size as the temperature change rate decreases. The time step size of the explicit analysis is governed by the stable time step size of the model and cannot take advantage of the decreased temperature change rate which results in unacceptably long solution times. It seems that the larger the model and the longer the welding phase is, the more efficient the explicit analysis is during welding and the more efficient is the implicit analysis during cooling.

		Implicit		Explicit			
				Mass scaling: 1E+5		Mass scaling: 1E+6	
Time interval		CPU time [h:m:s]		CPU time [h:m:s]		CPU time [h:m:s]	
start	end	per interval	accum.	per interval	accum.	per interval	accum.
0s	4s	1:45:02	1:45:02	0:59:07	0:59:07	0:20:11	0:20:11
4s	24s	0:11:05	1:56:07	4:52:14	5:51:21	1:26:48	1:46:59
24s	54s	0:01:11	1:57:19	7:18:05	13:09:26	2:14:42	4:01:41

Table 4.4: Plate girder model: CPU time for an implicit analysis and an explicit analysis with mass scaling of 10^5 and 10^6.

		Implicit		Explicit			
				Mass scaling: 1E+5		Mass scaling: 1E+6	
Time interval		CPU time [%]		CPU time [%]		CPU time [%]	
start	end	per interval	accum.	per interval	accum.	per interval	accum.
0s	4s	100	100	56	56	19	19
4s	24s	100	100	2636	303	783	92
24s	54s	100	100	36878	673	11339	206

Table 4.5: Plate girder model: relative CPU time for an implicit analysis and an explicit analysis with mass scaling of 10^5 and 10^6.

4.6 Optimal time to switch from the explicit to implicit method

As a result of the enormous differences in the calculation costs of the two phases (welding and cooling) of the simulation and the two solution methods it is critical to determine the optimal moment for switching from explicit to implicit analysis in order to maximise the benefits of a mixed time integration solution.

For this it is necessary to study the relation between the CPU time and the load step time intervals of the analysis, *i.e.* the time of the process (in this case welding and cooling) being analysed. Figure 4.28 shows this relationship for the implicit analysis and the two explicit analyses with mass scaling of 10^5 and 10^6 up to 54s in the analysis (the complete cooling phase would last about 3,000s as shown in Figure 4.22). The curves of the explicit analyses are practically straight lines since the time step size of the calculation is governed by the critical time step size, which is practically independent of the evolution of the process studied and nearly constant for the whole analysis. Nevertheless there is a slight difference in the slope of the two parts of the curve corresponding to the welding and cooling phase of the analysis. The explanation for this comes from the way ABAQUS/Explicit handles the critical time steps as it is explained in Section 4.3. The welding phase is modelled as a series of short load steps (eight load steps in the present example). At the beginning of each load step ABAQUS/Explicit starts with a conservative estimation of the critical time step size and within the same load step it tries to relax it. As a result of this, the slope of the curve represents an average value of the continuously revised critical time step approximation. The same applies during the cooling phase of the analysis which is just one very long load step. However, after the initial conservative value of the critical time step is revised it can be maintained for a much longer period then previously during the load steps of the welding phase. This is why the CPU vs load step time curve has two segments with slightly different slopes, with the second segment always having the smaller slope. The difference in the slopes is also influenced by the mass scaling factor since the difference between the first conservative estimation of the critical time step size and its revised value is also magnified.

An implicit algorithm, unlike an explicit, can adapt itself to the changing process and can speed up the analysis very significantly during the cooling phase. The lack

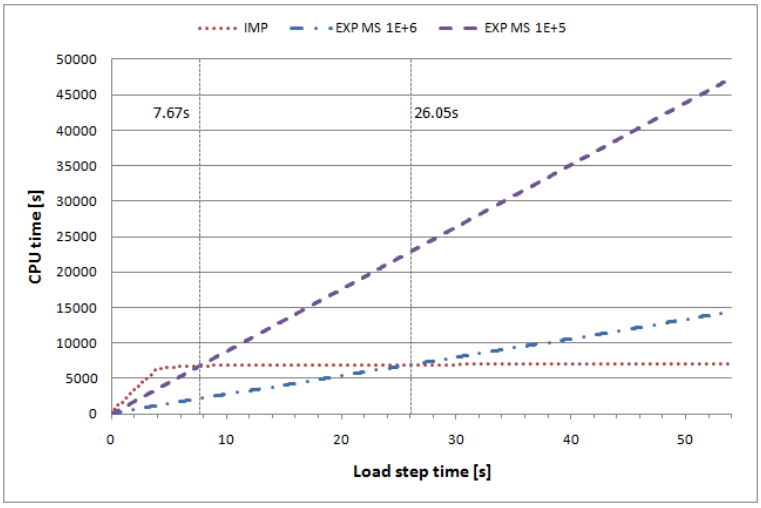

(a) Up to 54s.

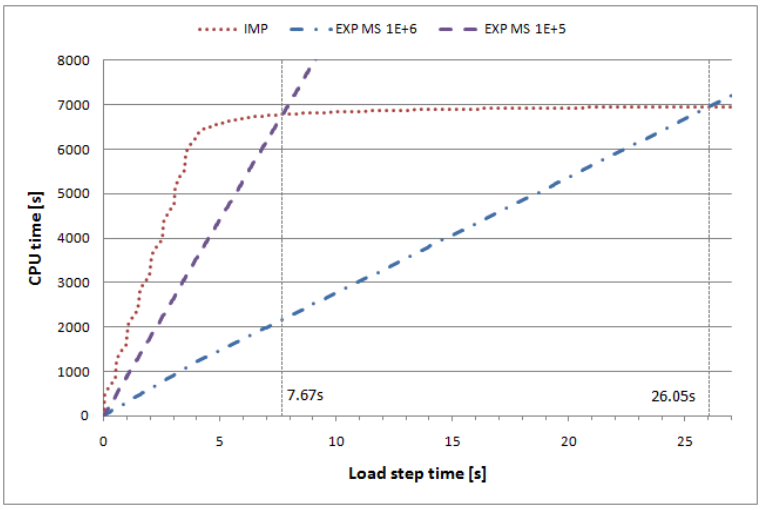

(b) Up to 27s.

Figure 4.28: CPU time vs Load step time of the plate girder model during an implicit analysis and an explicit analysis with mass scaling of 10^5 and 10^6.

of such an ability in the explicit method makes it very inefficient for the cooling phase which is well illustrated in the figure where the lines of the explicit analysis go well beyond that of the implicit analysis.

Since the slope of the implicit curve approaches zero during the cooling phase of the analysis, the upper time limit for the explicit-implicit switch is defined by the intersection of the explicit lines and the implicit curve. As shown in Figure 4.28, the intersection times are 7.67s and 26.05s for the analyses with mass scaling factor of 10^5 and 10^6, respectively. Switching to implicit methods beyond these times would result in CPU times longer than that of a pure implicit analysis.

The total CPU time of a mixed explicit-implicit time integration scheme can be easily determined from the data presented in Figure 4.28 using the following expression:

$$CPU_{mix}(T) = CPU_{exp}(T) + CPU_{imp}(T_{max}) - CPU_{imp}(T) \tag{4.10}$$

where $CPU_{mix}(T)$ is the total CPU time of the mixed solution if the switch takes place at time T, $CPU_{exp}(T)$ is the CPU time of the explicit analysis up to time T, $CPU_{imp}(T)$ is the CPU time of the implicit analysis up to time T and $CPU_{imp}(T_{max})$ is the total CPU time of a pure implicit analysis. Figure 4.29 shows the two curves determined by the above expression for the analyses with mass scaling factor of 10^5 and 10^6 named *MIXED MS 1E+5* and *MIXED MS 1E+6*, respectively. The minimums of these curves indicate the ideal time to initiate the change from the explicit to the implicit method in order to achieve a minimum CPU time to the complete simulation. In the present example the total CPU times can be reduced by up to 41% and 74% in the case of mass scaling of 10^5 and 10^6, respectively.

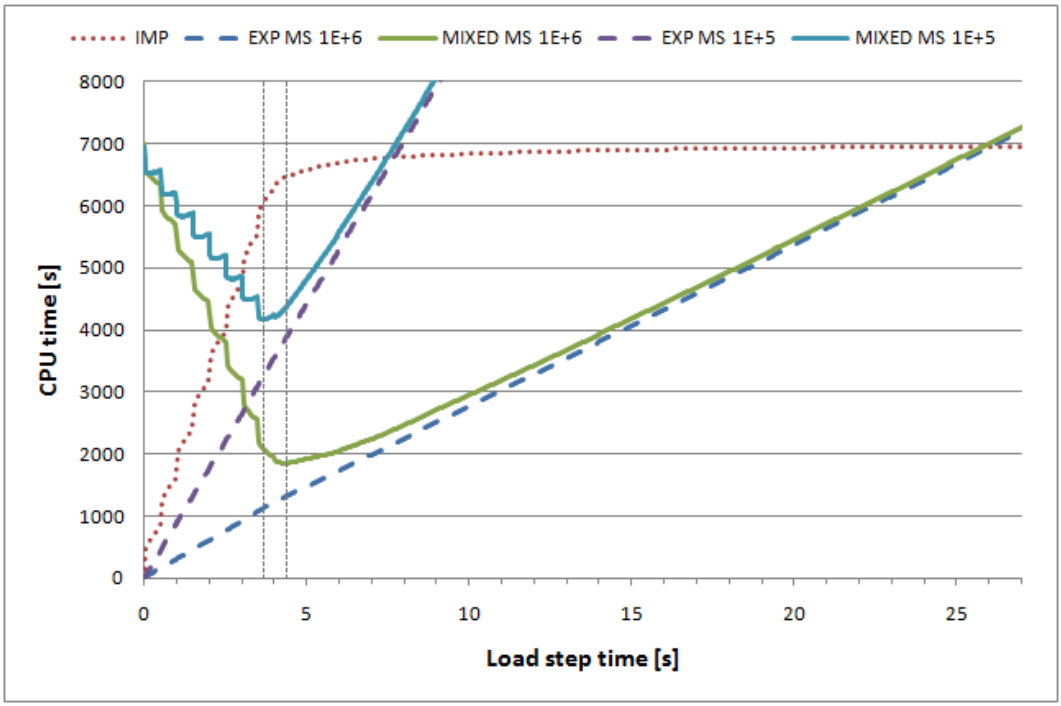

Figure 4.29: Variation of CPU time of the plate girder model with mixed time integration solution (combination of implicit method and explicit method with mass scaling of 10^5 and 10^6).

It is evident that the minimums of both curves are in the very close vicinity of

the end of the welding phase (4s). Basically what this result shows is that in the cooling phase the implicit method is so much more efficient than the explicit method that in order to achieve minimum calculation (CPU) time the best strategy is to switch to implicit method as soon as the welding phase is over.

In all the examples presented it has been observed that the stresses calculated using the explicit analyses tend to differ from that of the implicit analysis at the beginning of the calculation but with time they converge to the same solution. This means that while switching from explicit to implicit method immediately at the end of the welding phase would result in the least expensive calculation, it might not be the ideal strategy considering the accuracy of the results. Therefore it is useful to find a way to estimate the upper limit of the time for the explicit-implicit transition.

Figure 4.28 shows that this limit is where the curve of the explicit analysis crosses that of the implicit analysis. However, usually these curves are not available and a good approximation of them is needed to establish the "time window" for the explicit-implicit switch. As discussed earlier and shown in Figure 4.28 the relationship between the CPU time and the load step time is close to linear in the case of the explicit analysis. Therefore performing an analysis of only one welding step (in the present example that corresponds to 0.5s as shown in Figure 4.21) a good approximation of this linear relationship can be established. Looking at Figure 4.28 it is apparent that the curve of the implicit analysis can also be well approximated using a bilinear relationship as a result of the great difference between the two portions of the curve during the welding phase and the consecutive cooling phase. The slope of the line corresponding to the welding phase can be estimated in the same way as that of the lines of the explicit analyses by performing an analysis of a single welding step. For the line that corresponds to the cooling phase, using a horizontal plateau starting from the end of the welding phase is a reasonably good and at the same time a conservative assumption as shown below.

The estimated (marked with *EST*) and the original curves are shown in Figure 4.30 for the implicit analysis and the two explicit analyses with mass scaling factors of 10^5 and 10^6. In the case of 10^6 mass scaling there is a noticeable difference between the original and the estimated curve. This is because the slope of the estimated curve is calculated from the data of only one load step at the beginning of the welding phase which results in a higher slope than in the cooling phase of the analysis as explained above. Since the estimated curve always has a higher slope than the

real curve, this difference always results in a conservative value of the upper limit of the "time window". Moreover using the horizontal plateau for the approximation of the cooling phase of the implicit analysis brings the upper limit further down making it even more conservative. In the present example these conservative estimated upper limits are 7.4s and 21.8s for mass scaling of 10^5 and 10^6, respectively. These values are to be compared to the exact values of 7.67s and 26.05s, respectively. Since the higher level of mass scaling results in a greater difference between the slopes of the two segments (welding and cooling) of the CPU vs the load step time curve, it is expected that the estimated upper limit is closer to the exact value in the case of the analysis with the smaller mass scaling factor.

The results of the plate girder example presented in this section show that using a mixed time integration solution strategy can result in very significant reduction of computational cost even in a small scale example like the one shown. The lower limit of the "time window" to switch from an explicit to an implicit method can be estimated to be equal to the end of the welding phase, while the upper limit of it can be estimated using time data from the analyses of a single welding step. The decision about the time to switch between the methods comes down to the eternal dilemma of speed vs accuracy. While using the lower limit would result in the least expensive analysis, the more the time of the switch is postponed the closer the results of the explicit and implicit phases of the analysis get.

4.7 Summary and conclusions

In this chapter the use of a mixed time integration method for welding simulation is proposed with special attention to explicit time integration and the mass scaling technique to speed up the explicit analysis.

In Section 4.2 it is demonstrated that for typical steel material properties the critical time step, *i.e.* the stable time step limit, of an explicit coupled thermo-mechanical analysis is governed by the mechanical part of the problem. With mass scaling, during which the mass of the structure is artificially increased, the critical time step can be significantly increased and the larger the model the more the calculation time can be reduced. Applying excessive mass scaling, however, can alter the accuracy of the results by introducing artificial dynamic effects that make the response of the numerical model oscillate.

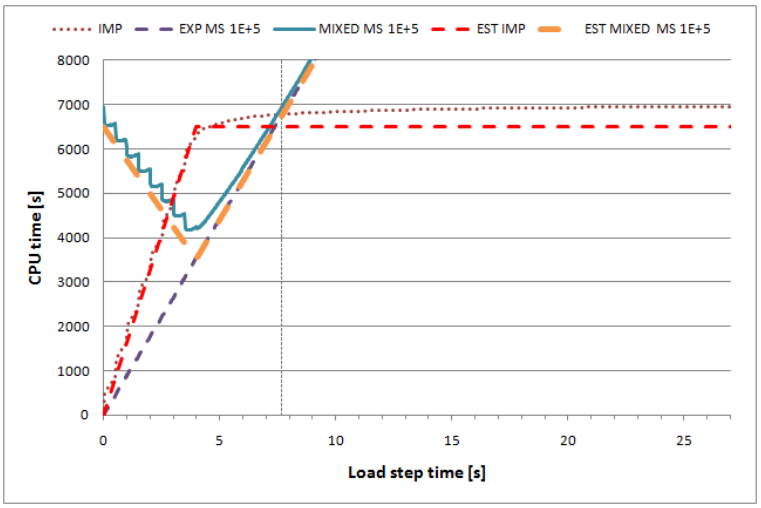

(a) Mass scaling factor of 10^5.

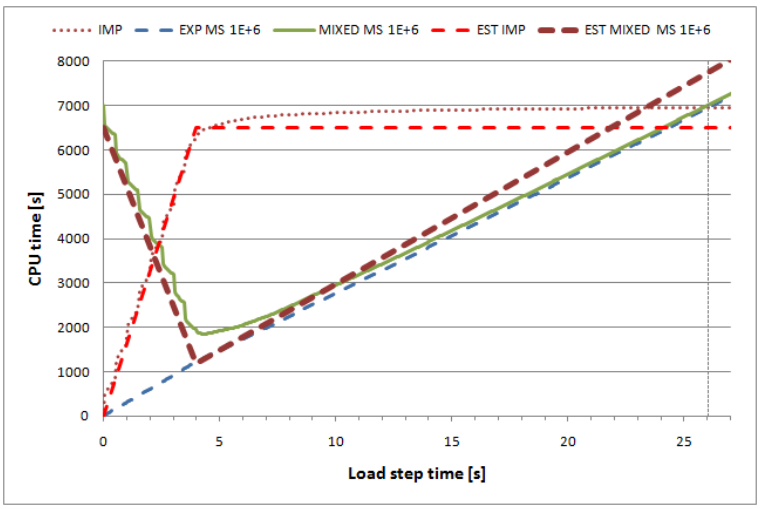

(b) Mass scaling factor of 10^6.

Figure 4.30: Variation of CPU time of the plate girder model with mixed time integration solution using estimated CPU times (combination of implicit method and explicit method with mass scaling factor of 10^5 and 10^6).

During the welding phase and at the beginning of the cooling phase of the simulation using the explicit method with mass scaling can result in a more efficient solution than when using the implicit method. However, with the temperature change rate continuously dropping during cooling, the efficiency of the explicit method is also diminishing very rapidly. Therefore below a certain temperature change rate an implicit method needs to be employed. In fact, the results obtained from the small scale example given in Section 4.6 show that switching to implicit method as early as the end of the welding phase of the analysis can result in near minimum

computational cost.

If the aim of the simulation is to determine residual stresses in welded structures then the small errors introduced by an explicit analysis with mass scaling at the beginning of the analysis might be ignored since they seem to have little influence on the final results. If distortions are also of interest, however, more caution needs to be taken as it seems that the discrepancies in the results in the early stages of the analysis are carried on until the end of the analysis as seen in the examples of Sections 4.4 and 4.5.

Choosing the time to switch from explicit to implicit method can also be influenced by the fact that letting the explicit analysis run longer brings the explicit results closer to that of the implicit method therefore lowering the likelihood that any error from the explicit phase of the analysis is carried over to the implicit phase. Nevertheless there is an upper limit for switching from one method to the other, since there is a moment when it becomes more efficient to run a pure implicit analysis. This upper limit can be easily estimated using a small sample of data collected from conducting preliminary analyses of a single welding step with both explicit and implicit methods.

Although the examples of this chapter are of a small scale, they demonstrate the potential of using mixed time integration for efficient welding simulation.

The next chapter presents the temperature measurements conducted in a steel structure factory during the fabrication of welded plate girders. Both the methodology and the results are discussed in detail.

Chapter 5

Temperature measurements during fabrication

5.1 Introduction

In this chapter the temperature measurements conducted during the fabrication of the welded plate girders are presented. The objective of the measurements is to obtain temperature data that can be used for the calibration of the numerical model to simulate the welding process. Both the methodology and the results of the measurements are discussed in details. Finally, recommendations are provided for future measurements of this kind.

5.2 Temperature measurement methodology

The main objective of the temperature measurements is to collect experimental data that can be used to calibrate the numerical model for welding simulation. The actual heat input and the heat loss to the surroundings are two parameters of the numerical model that cannot be measured directly. However, if the temperature histories of certain points of the welded plate girder are known those unknown parameters can be adjusted by matching the calculated temperature histories with the measured ones.

For the measurements a Land UNO stand alone radiation (infrared) thermometer (model: U2 300/1100CS) [83] with a temperature range of 300°C to 1100°C was used. When choosing the thermometer the following assumptions were made:

- The melting temperature of steel is around 1500°C. The welding process used for the fabrication of the specimens is submerged arc welding. The weld seam is covered by powder along a length of approx. 300-400mm in front of the welding head. Measurements can take place only outside of that distance which means that by the time the plate girder travels that distance the temperature of the weld seam is considerably lower than the melting point of steel. Therefore the 1100°C upper measurement limit of the infrared thermometer seems sufficiently high for the purpose of this experiment.

- The relatively high lower limit of the thermometer's range means that the measurement locations are limited to an area near to the weld seam since only in a that zone around the weld is it expected that the temperatures reach and go beyond 300°C. Nevertheless, this should be sufficient for the purpose of this research.

- Since several specimens of the same geometry were fabricated one thermometer could be used to measure at different locations of the same type of specimens.

Two different kinds of temperature measurements are devised to provide sufficient temperature data for the calibration of the heat source model and the boundary conditions between the welded plates and the surroundings. While these two parameters of the numerical model cannot be completely separated since they are simply two different characteristics of the same physical process, the two measurement types should provide an insight into these different aspects of the process. The two measurement types are:

- FIXED temperature measurement and

- MOVING temperature measurement.

The notion "fixed" and "moving" refers to the point of measurement on the specimen and its relative position to the welding arc (*i.e.* welding head). The welding heads of the automatic welding machine are fixed and the plates to be joined are pushed through the machine.

FIXED measurement: The infrared thermometer is placed on a fully adjustable tripod on the floor next to the specimen being welded and therefore it is stationary, as shown in Figure 5.1. The instrument focuses on a point at a fixed distance from

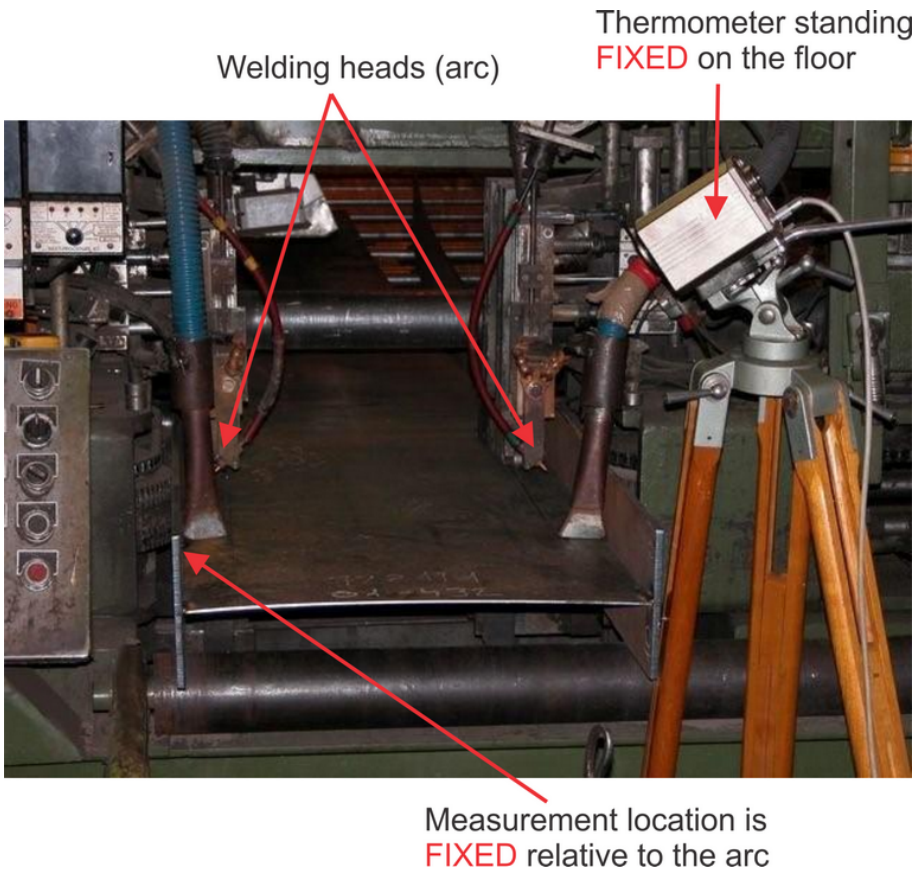

Figure 5.1: FIXED measurement setup.

the welding arc. The measured point is fixed relative to the welding arc but continuously changing relative to the specimen. The traditionally used method based on thermocouples would not permit such a measurement since using thermocouples attached to the specimen would only provide results similar to that of the MOVING measurements, which is discussed below. The expected result from the FIXED measurement, shown in Figure 5.2, is such that after a very short initial period a constant temperature should develop, assuming that the welding process is steady and the geometry of the welded plates are also constant. Figure 5.3 shows an example of the actual results. The scatter of the data is caused by the constant attempt to keep the weld seam clean of slag. The slag is periodically removed manually with a metal hand tool. As a result of that the thermometer's view is often blocked by the tool which is recorded as a relatively low temperature. The highest temperatures are recorded when the thermometer is measuring the temperature of the slag before it is removed from the weld. However, there is a clearly distinguishable narrow range of nearly constant temperatures which represent the data that the measurement is

designed for: the temperature of the surface of the weld seam.

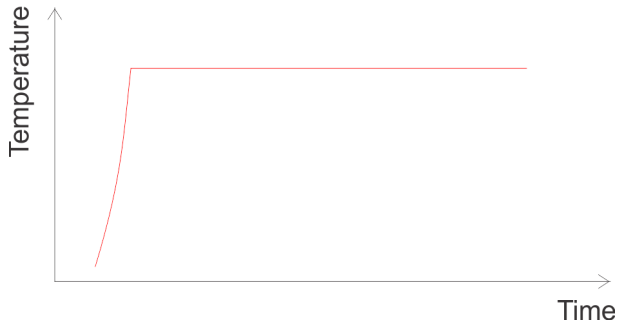

Figure 5.2: Expected FIXED measurement result.

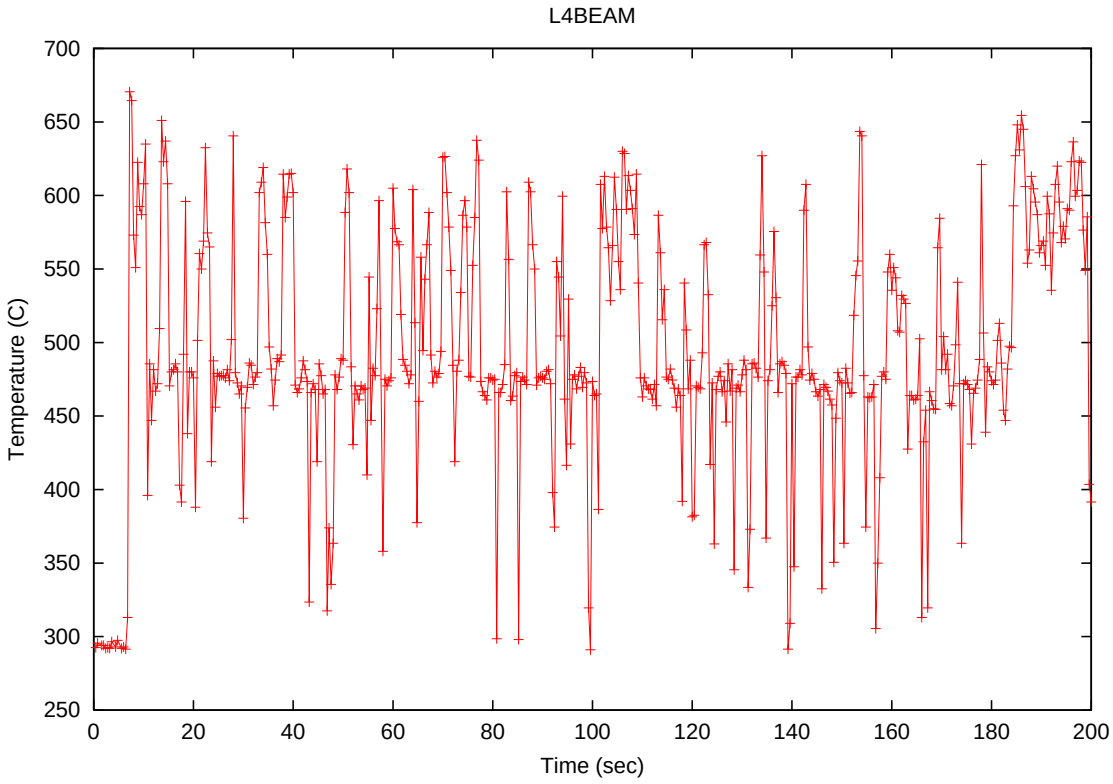

Figure 5.3: FIXED measurement result sample (specimen L4).

MOVING measurement: The infrared thermometer is placed on the web of the welded specimen itself, as shown in Figure 5.4. In this way the instrument travels with the girder and it focuses on a point of the girder that is moving relative to the welding arc but it is fixed relative to the specimen. The expected result from this kind of measurement, shown in Figure 5.5, is such that after the point reaches its peak temperature during a very short initial period there is a steep drop in the

temperature followed a very slow cooling down process. Figure 5.6 shows an example of the actual results. At the beginning some scatter of the data can be observed that is also caused by the removal of the slag. However, once the weld is clean the curve remains relatively smooth. It can be seen that the slope of the curve is constantly decreasing, *i.e.* the cooling rate is constantly dropping. Below 300°C, the lower limit of the thermometers range, the cooling rate drops even further and a relatively long cooling time follows.

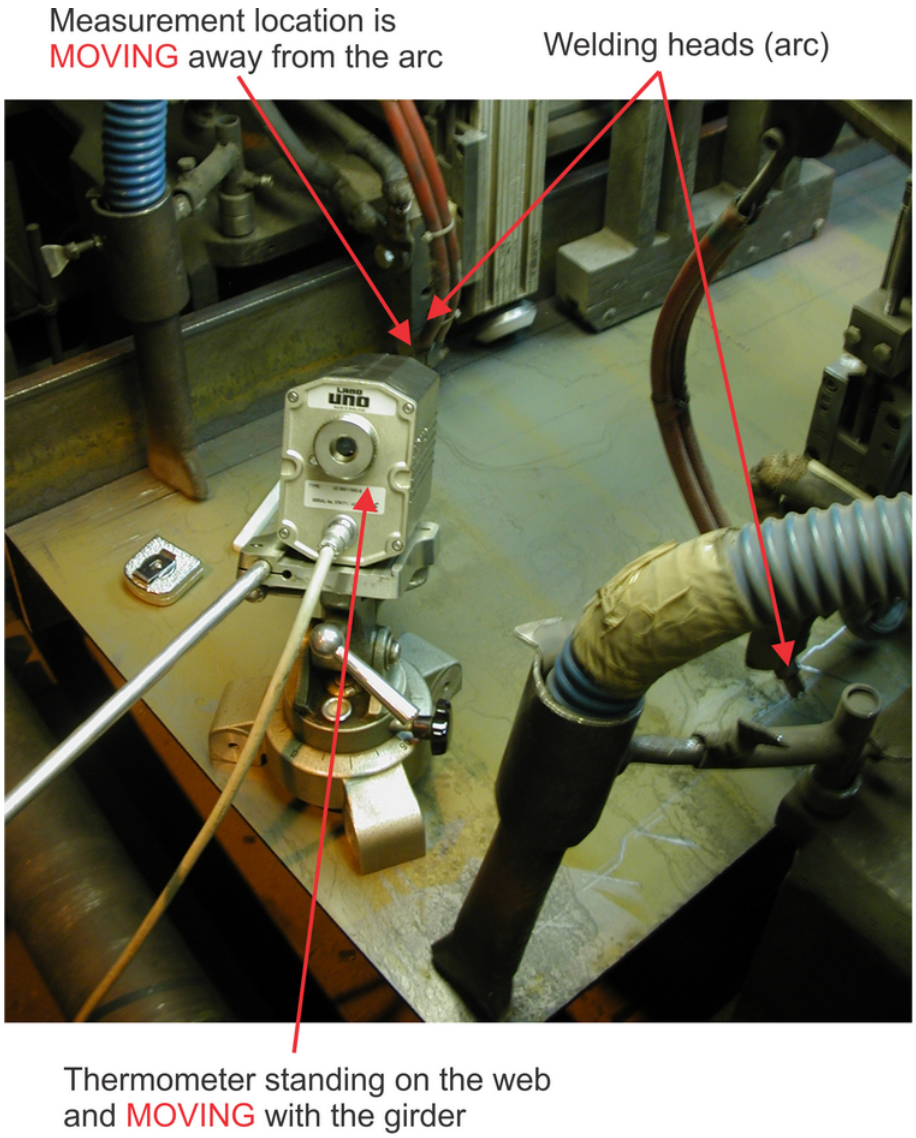

Figure 5.4: MOVING measurement setup.

In the next section a summary of the measurement results and their analyses is presented.

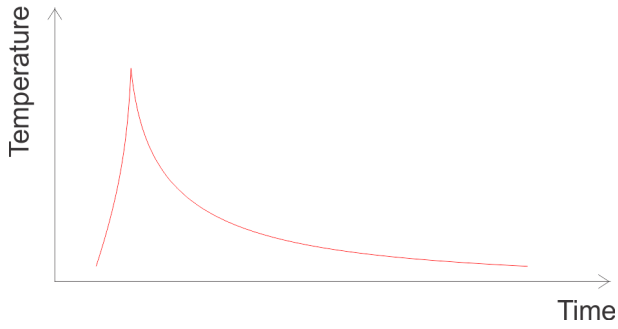

Figure 5.5: Expected MOVING measurement result.

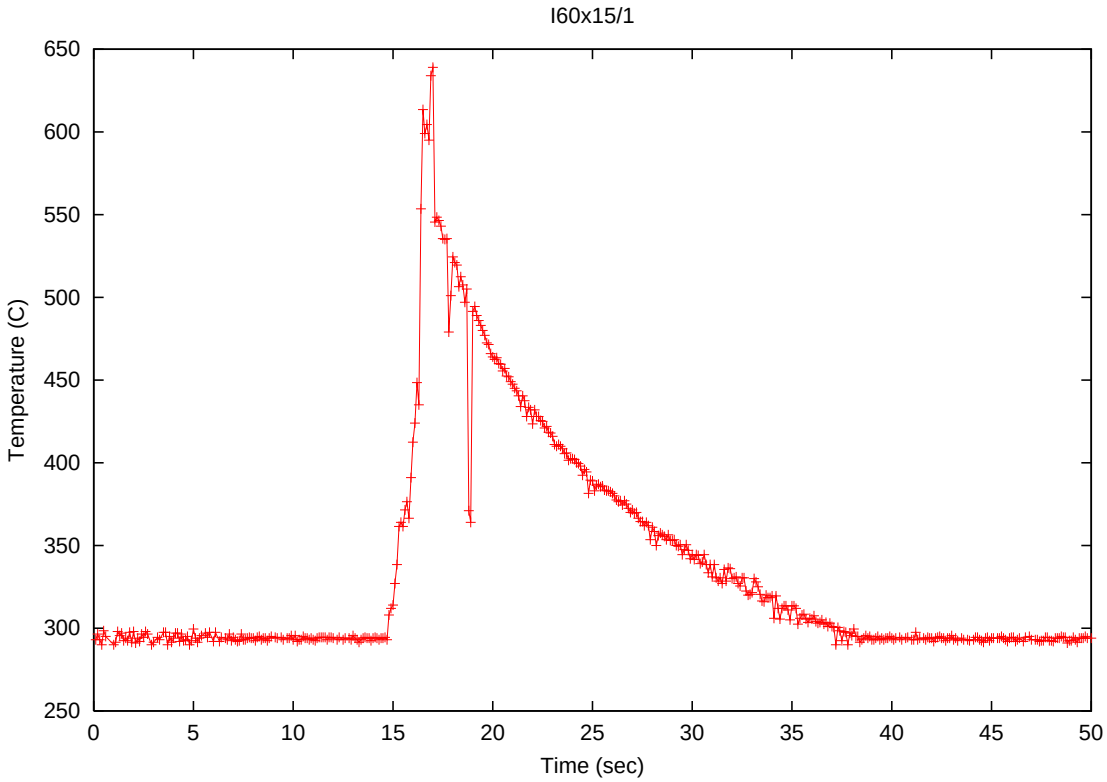

Figure 5.6: MOVING measurement result sample (specimen S1_a).

5.3 Temperature measurement results

Most of the specimens in the experimental program were fabricated with flanges of 150x6mm, with a web of 600x4mm and with single-sided fillet welding. In the temperature measurements these girders were the main focus as well. Two long girders, specimens L3 and L4 with a length of 5970mm, were fabricated with this cross-section and both were used to perform FIXED temperature measurements. Both girders were fabricated with preheating. According to the documentation

available to the operator of the welding machine, the aim of the preheating was to increase the temperature of the web to about 130°C to 150°C in the cross-section at the position of the welding head. Since these values are below the range of the thermometer it was not possible to confirm the actual temperature of the web and therefore the efficiency of the preheating. However, the welding engineer of the factory has confirmed that in their experience the temperature of the plates never actually reaches the documented values. In fact once they measured it and it stayed well below that temperature around 70°C to 90°C, and in the case of thicker plates even reaching 50°C was a challenge.

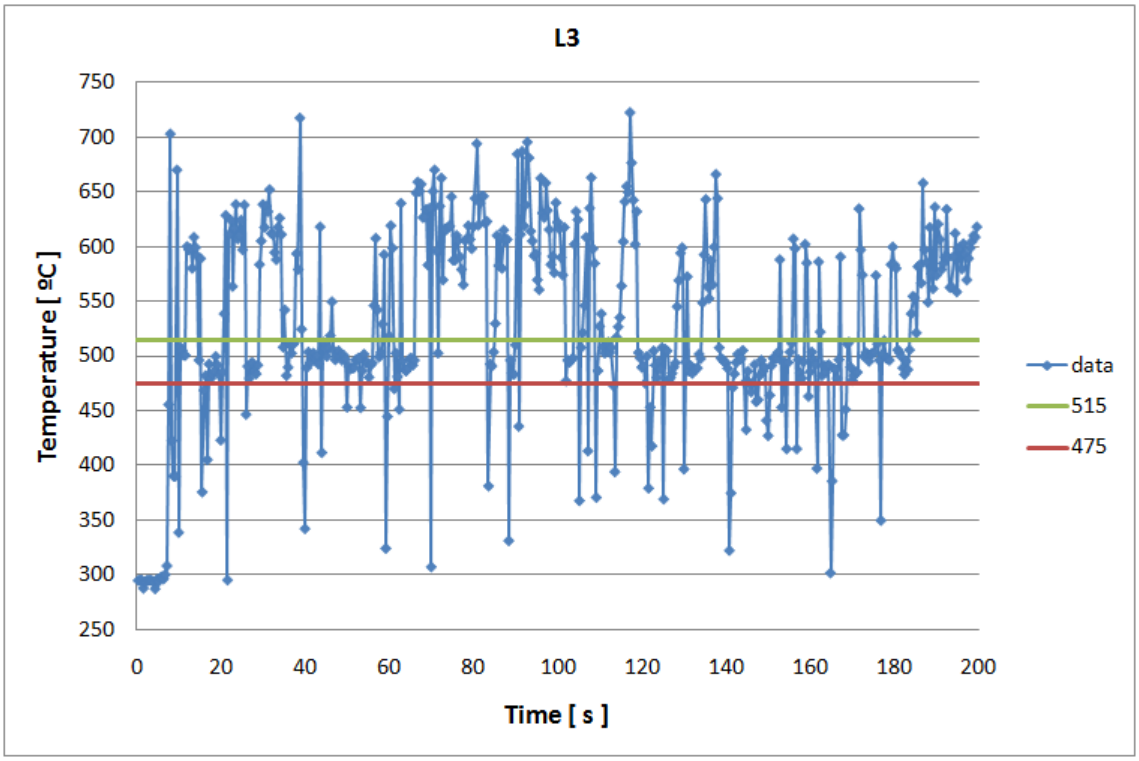

Figure 5.7: FIXED measurement result of specimen L3.

The results of the FIXED measurements of specimen L3 and L4 are shown in Figures 5.7 and 5.3, respectively. These measurements took place at 380mm distance from the welding head. In the figures a narrow range of temperatures around 500°C (specimen L3) and around 470°C (specimen L4) can be observed. Somewhere in that range lies the temperature of the surface of the weld seam that needs to be determined in order to calibrate the numerical model. One possible way to obtain a single weld surface temperature is to take all those points within a fixed range

and calculate their average value. In Figure 5.7 one possible range is marked with two horizontal lines. Calculating the average of all the temperature points between 475°C and 515°C gives a weld surface temperature of 494°C. However, changing the range slightly to from 470°C to 510°C results in an average temperature of 492°C. While this does not seem to be a significant difference, choosing the temperature limits for this way of calculating the weld surface temperature is rather subjective and a question of interpretation. It is also important to point out that this variation of the temperature is not a naturally occurring process during the fabrication but is provoked by irregular human intervention in an attempt to keep the weld surface clean of slag. Therefore a simple average of the temperature values might not be the best way to determine the weld surface temperature.

It can be assumed that after the temperature measurement is disturbed by fragments of hot slag or the hand tool used to remove the slag the temperature reading returns to the actual weld surface temperature. Determining the frequency of the temperature reading values gives a temperature distribution the peak of which is a good indication of the actual weld surface temperature. The histograms of the temperature readings for specimens L3 and L4 are shown in Figure 5.8. Clear peaks can be observed in the two sets of data at 496°C and 475°C. The two specimens are identical and were fabricated one after the other with the same welding parameters and preheating. Therefore from the manufacturing point of view there is no reason for the temperature distribution to be so different. It is very likely that the differences in the temperature values are the result of inaccuracies in the measurement itself. The infrared thermometer's target area from a distance of $790mm$, the measuring distance of the FIXED measurements, is $7.9mm$. Assuming a fillet weld with legs of 5.2mm, the average weld size observed in the macrographs of the weld sections, the width of the surface of the weld seam is $7.35mm$. If the thermometer is not perfectly pointing at the weld seam the target area might include a relatively big portion of the flange or web which would reduce the measured temperature. This can be caused not only by not setting up the thermometer accurately but also by the movements of the girder as it travels through the welding machine. The manufacturer pointed out that during the fabrication they often experienced that girders become slightly curved. Such deformation could alter the position of the weld seam relative to the target area of the thermometer to an extent that would notably effect the outcome of the measurement. Since any inaccuracy in the measurements

would result in a reduction of the measured temperatures, the higher temperature of the two is chosen to represent the average weld seam surface temperature and to calibrate the numerical model developed to simulate the fabrication process.

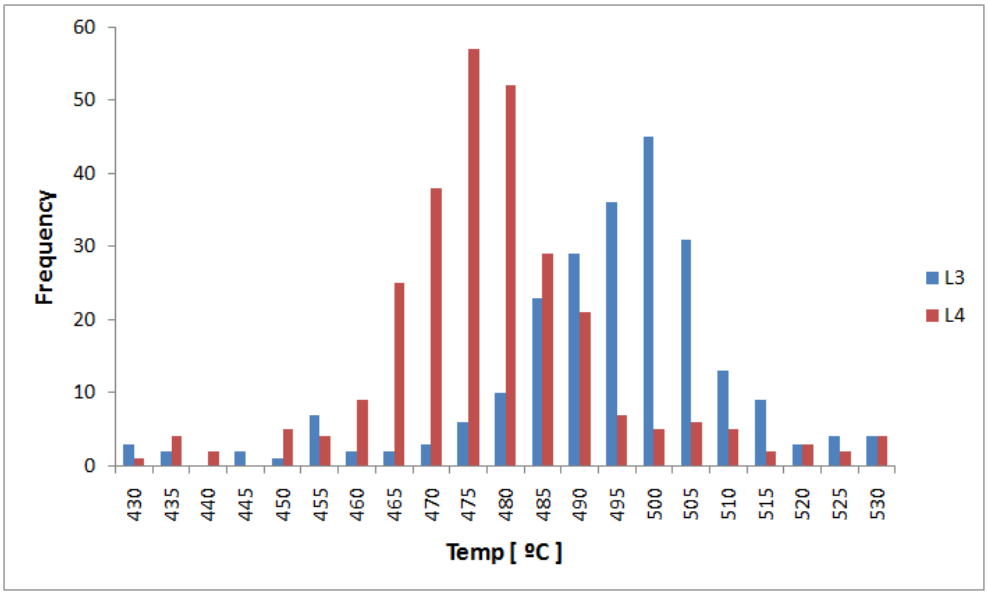

Figure 5.8: Histogram of measured temperatures in specimens L3 and L4.

Several short girders (specimen type S1) with a length of 2970mm and with the same cross-section as specimens L3 and L4 were also fabricated and some of them were the subject of MOVING temperature measurements. Figure 5.9 shows three sets of results, one of which (S1_a) is the same as the one shown in Figure 5.6. Specimens S1_a and S1_b were fabricated without preheating while in the case of S1_c preheating was applied. The purpose of preheating is to reduce the cooling rate which can be observed well comparing the curves. It can also bee seen that while curves S1_a and S1_b are close to each other there is a clear difference between them and that difference would be even more obvious if S1_b had more data points in the 450°C to 550°C temperature range. Similarly to the case of long specimens L3 and L4 there is no reason for them to be different since they are identical and they were fabricated under the same conditions. However, the difference cannot be explained in the same way as for the FIXED measurements. During the MOVING measurements the thermometer is placed on the web of the girder as shown in Figure 5.4 therefore the distance between the thermometer and the weld seam surface is much smaller, around 400mm. This makes the diameter of the target area 4mm and therefore the measurement is less sensitive to errors in the aiming of the thermome-

ter's optic. Furthermore even if the girders become curved during welding it has no effect on the measurement since the thermometer is attached to the girder therefore the relative position of the girder and the thermometer is fixed unless, as a result of the movements and vibrations, the thermometer is slightly displaced. While this is a possibility there is no evidence to support that this caused the differences between the measurements.

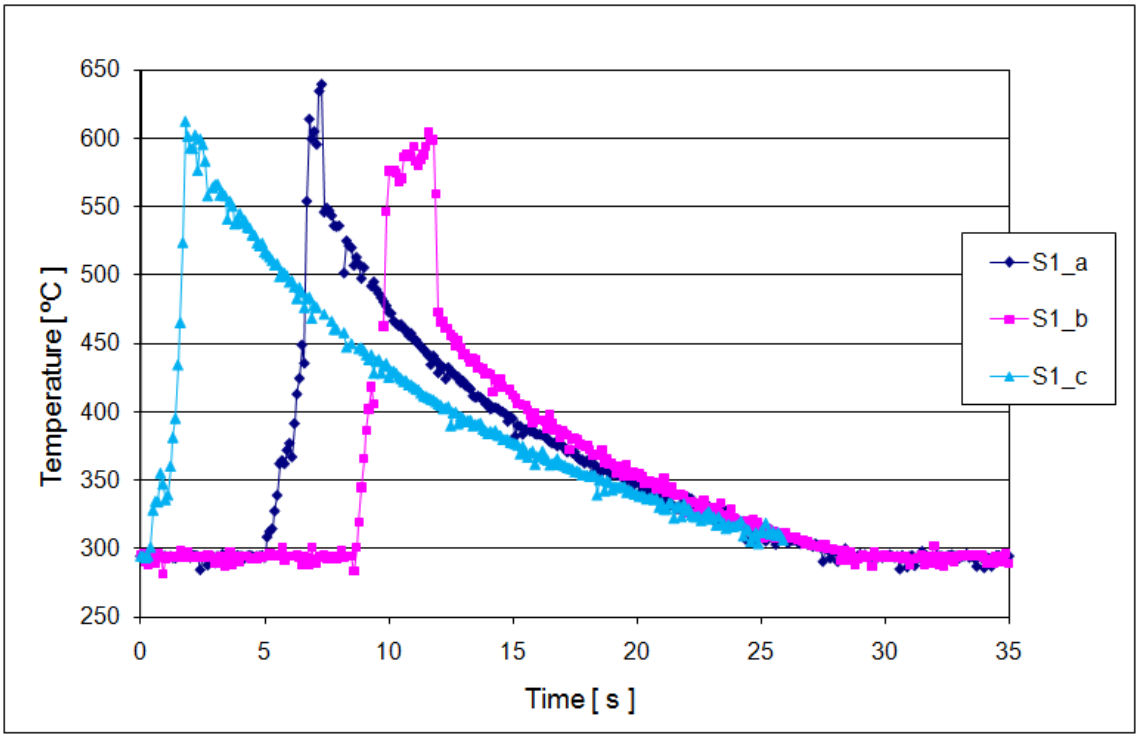

Figure 5.9: MOVING measurement result of several S1 specimens.

There is a much simpler explanation. It can be seen in Figure 5.4 that the thermometer is aimed at a point somewhere very near the welding head. Actually there are very few options when positioning the thermometer. Right behind the welding head there is a series of rollers. Their role is to keep the plates in place but at the same time they also block the view of the edge of the web pushed against the flange where the thermometer needs to aim. Since the thermometer is travelling with the specimen it is not possible to adjust its position once the welding has started, it has to be done beforehand. Moreover, unlike in the case of the FIXED measurements, the thermometer needs to be re-positioned for every single measurement which also adds to the uncertainty of the exact location of the target area. These uncertainties probably would not cause much trouble if the measurement took place somewhere

far from the start of the weld where the temperature flow becomes relatively steady as it can been seen in the results of the FIXED measurements. However, because of those rollers behind the welding head there is only a short gap where the thermometer can aim at it. So close to the start of the weld the temperature variation is far from steady as it will be demonstrated by numerical analysis which means that even a small difference in the distance between the measurement target area and the start of the weld can result in rather different temperature history curves.

5.4 Summary and conclusions

It needs to be pointed out that the measurements did not take place in a controlled laboratory environment. In fact one of the aims of the experiments was to design a series of measurements that are easy to execute, requires a limited pieces of equipment and can be set up in a factory with minimal disturbance to the normal production process. Keeping this in mind, based on the experience of these measurements the following conclusions and recommendations can be made about the experimental set-up to assist future measurements of this kind:

Thermometer:

- The thermometer's upper measurement limit of 1100°C proved to be sufficient for the purpose of these experiments.
- The relatively high lower limit of 300°C reduces the possible measurement locations to a very narrow zone around the weld seam. In fact several measurements of this study had been unsuccessful because the selected measurement location was outside of this zone.
- The efficiency of preheating with an estimated max. preheating temperature of 150°C was also outside the range of the thermometer.
- While the assumption that a single thermometer can be used in several measurements on the same type of specimens would stand in a fully controlled laboratory environment, the results show that even when exactly the same kind of measurement is repeated there might be significant differences (see the measurements of specimens L3 and L4 in Figure 5.8).

Practically all of these problems could be addressed by including in the experimental set-up a second thermometer with a lower measurement range of approx. 0°C to 500°C. The low temperature range would allow measurements to be performed at any point of the specimen far from the weld seam. It would also allow the effect of preheating to be measured accurately. Additionally it would give the option to follow the complete cooling down of the specimen to ambient temperature.

Having two thermometers would make sure that two measurements that take place at different locations of the specimens are directly related and can be evaluated together without the need of relying on separate measurements on identical specimens. Probably the most important advantage of using two thermometers would be that the two measurement types could be mixed by using the thermometer with the higher temperature range for the FIXED measurement near the welding head and the other one for the MOVING measurement travelling on top of the specimen away from the welding head.

Execution of the measurements:

- For the FIXED measurements the thermometer was supported by a tripod placed next the specimen. Since the height of the web of the specimens is $600mm$ there is no way to place the thermometer close enough to the weld seam in order to reduce significantly the target area diameter. From that distance the target area diameter is approximately the same as the width of the weld seam surface therefore even a small inaccuracy in the aiming of the thermometer can result in lower temperature readings as a result of including larger parts of the flange or the web in the target area.

- The MOVING measurements were used to record the temperature history at a location very near to the start of the weld. Close to the start of the weld even a small difference in the distance between the measurement location and the start of the weld can result in significantly different temperature histories, as demonstrated later in the numerical studies, which makes the evaluation of the measurement results rather difficult.

Reducing the target area diameter of the FIXED measurements would greatly improve the consistency and therefore the accuracy of the measurements. This could

be achieved optically with additional lenses or a fibre optic extension (these solutions could require a different thermometer model to the one used in this research). Another option would be to devise an alternative solution to the use of a tripod next to the specimen. Depending on the welding machine it might be possible to hang the thermometer and bring it closer to the weld seam but it could make the aiming less convenient since somebody needs to be able to look through the lens of the thermometer therefore it has to be accessible easily. This however, might go against the principle of keeping the measurement set-up as simple and easy to manage as possible.

For the MOVING measurements it is important to perform it far enough from the start of the weld where practically any point would have the same temperature history and therefore the exact position of the measurement location would not influence the outcome of the measurement.

Using two thermometers at the same time would not significantly increase the complexity of the set up and execution of the measurement. In fact it would simplify it since the FIXED measurement would need to be set up only once and would require only slight adjustments before each measurements. The MOVING measurements would require the exact same effort as using only one thermometer.

The proposed combination of FIXED and MOVING measurement methods are easy to set up in a factory environment with very limited disturbance of the normal fabrication process and they provide sufficient temperature measurement data for the calibration of the numerical model. This calibration and the development of the numerical model to simulate the thermal process of welding is the subject of the next chapter.

Chapter 6

Thermal analysis of plate girder fabrication

6.1 Introduction

In this chapter the development and calibration of the numerical model for the thermal analysis of welding is presented. The equivalent prismatic heat source model is proposed to simulate the welding heat input. A series of studies is performed to investigate the effects of the governing parameters of the analysis. Finally, the numerical model is calibrated with the temperature data presented in Chapter 5.

6.2 Numerical model

Three dimensional solid finite element model using ANSYS [84] is developed to simulate the welding process and to calculate the temperature history in the specimens. The calculated temperature histories can be compared to the measurement results and the governing parameters of the numerical model can be adjusted (calibrated) by matching the numerical and experimental temperature data. Before attempting to reproduce the measured temperatures, however, a thorough numerical study is conducted to determine the importance of the parameters of the numerical model.

The eight-node three dimensional thermal SOLID70 element is used to construct the model. The element has a single degree of freedom (temperature) at its nodes and can be used in steady-state or transient thermal analysis. The full finite element model is shown in Figure 6.1. During the fabrication there was always a gap at

both ends of the specimens between the end of the girder and the end of the weld seam. The size of the gap varied but it was always around $300mm$. This gap is also considered in the numerical model but with a reduced length of $60mm$. Numerical results presented later in this chapter (Figure 6.22) show that this has little influence on the weld surface temperature. The single-sided fillet weld has a length of $500mm$. While the length of the specimens were $2970mm$ and $5970mm$ the numerical model only has a total length of $560mm$. The results presented later in this chapter demonstrate that this is sufficiently long to allow for the development of a constant weld surface temperature at a given distance from the welding arc which means that a longer model would not give different result, in fact the length could be further reduced. This is because in welding the heat transfer in the direction of the welding is almost negligible compared to the heat transfer in the transverse direction [82]. This is, however, not the case at the two extremes of the weld seam which is why two dimensional models work well only in the internal portion of the weld and ignore any disturbances at the start and end of it. The flange width is $150mm$ and the plate thickness is $6mm$. The web of the specimens is $600mm$ wide but here only half of the model is considered. The thickness of the web plate is $4mm$.

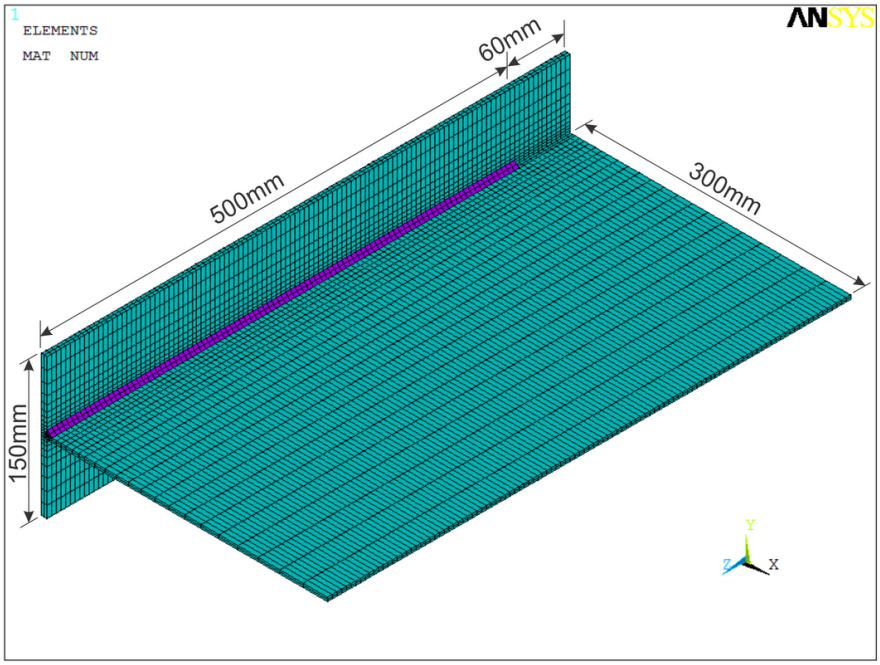

Figure 6.1: Finite element model of the plate girder.

Figure 6.2 shows the mesh and the dimensions of the idealised fillet-weld with the shape of an ellipsis. Unless otherwise stated the legs of the weld seam are $5mm$ long, the throat is 1.1 times the leg length (*i.e.* $5.5mm$) and the angle of the weld surface relative to the web is 45°. These dimensions correspond to the designed weld size of the plate girder specimens of dimension given above. The dimensions of the weld cross-section are to be revised for the simulation to reproduce the temperature measurements since the macrograph images of the weld seams reveal some differences to these idealised dimensions. The nodes below the root of the weld seam (marked with circles in the figure) are not connected. There the face of the flange plate and the end of the web plate are separated in the same way as in a real girder with a single-sided fillet weld. The effect of this is investigated later in this chapter.

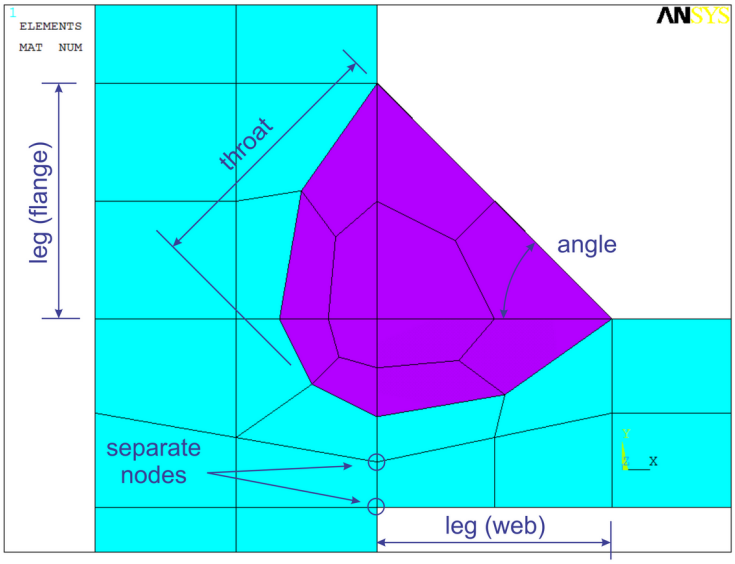

Figure 6.2: Mesh of the weld section.

One of the major difficulties in computational welding mechanics is the limited availability of material properties at elevated temperatures. The standard Eurocode 3, Part 1-2, EN 1993-1-2: Structural Fire Design [85] provides mechanical and thermal properties of carbon steel up to a temperature of 1200°C. In the analyses of this research it is assumed that the material properties remain constant above 1200°C. This is an acceptable assumption since it is an often employed technique to introduce a cut-off temperature above which any changes in the material properties are ignored. For steel the cut-off temperatures used in other studies are in a range from 600°C to 1200°C [86, 87]. This is justified by the fact that the cooling process below

half of the melting point of the material plays the most important role in the development of residual stresses because it is in this range where the yield limit of the material steeply increases [82]. The thermal material properties of steel (c - specific heat, λ - thermal conductivity) defined in Eurocode 3 are shown in Figure 6.3.

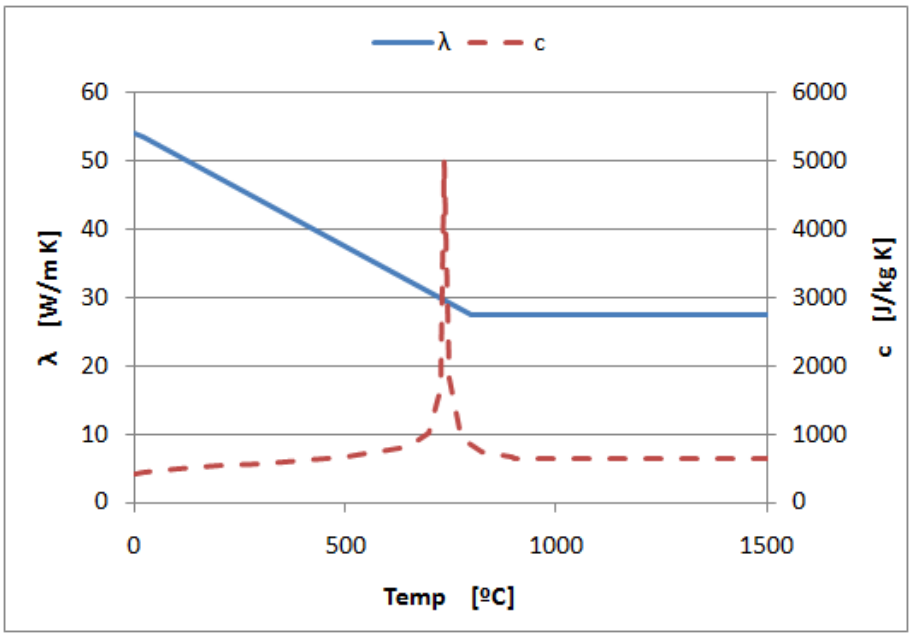

Figure 6.3: Thermal material properties of EC3.

The welding heat source is modelled using prescribed temperatures and known weld pool shape [86, 87]. If the temperature history outside of the molten weld pool is of interest then the heat source can be accurately modelled with an equivalent heat source model [82] that consists of the melting temperature of the base material being specified at the liquid-solid interface separating the solid base metal and the molten weld pool. A schematic representation of the longitudinal section of the liquid-solid interface is shown in Figure 6.4. This model cannot give any information about the thermodynamic behaviour of the weld pool itself therefore it is required that a fictitious temperature distribution is also prescribed within the weld pool region in order to be able to calculate the cooling of the weld region as well. It is recommended that either the melting temperature or a parabolic increase in the temperature is prescribed within the volume enclosed by the liquid-solid interface [82].

One commonly used heat source model is the double-ellipsoidal volume heat source [86]. This is constructed from two ellipsoid quadrants, a shorter one in the front and an elongated one in the back. While this model has been successfully used

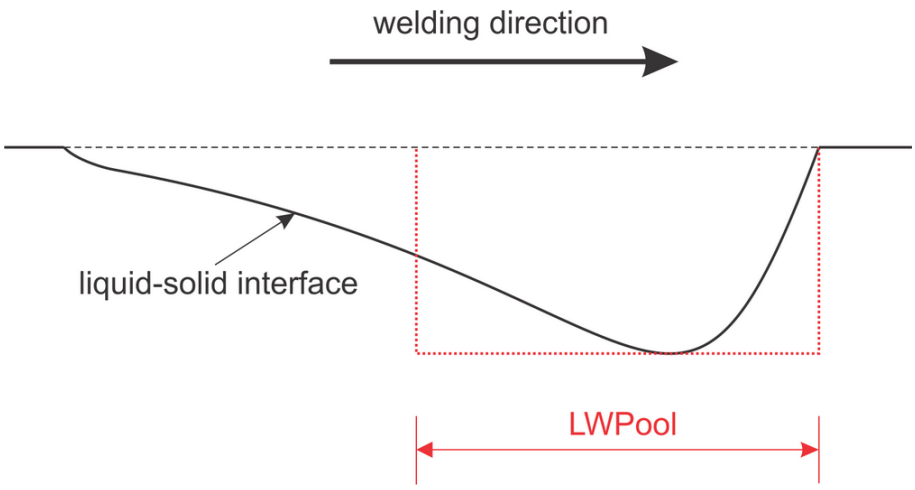

Figure 6.4: Schematic liquid-solid interface of the weld pool [82] and the fictitious prismatic weld pool (red line).

in welding simulation, it requires not only the knowledge of the characteristic size of the weld pool [87] but also the welding parameters including welding arc efficiency. The efficiency of submerged arc welding is the highest among the common welding methods and suggested values vary from 0.91 to 0.99 [87]. Since no exact values of the data (geometry, efficiency) required by double ellipsoid can be obtained, in this research a further simplification is introduced in the heat source model with known weld pool shape. Instead of trying to estimate the real geometry of the weld pool a fictitious prismatic weld pool shape is assumed. A somewhat similar idea is used in reference [88] where three heat source models were studied:

- Gaussian heat source model over an ellipsis area,
- conical heat source model over a circular area, and
- prismatic heat source model over a rectangular area.

It is found in [88] that as long as the net total heat input was the same, the shape of the heat source had little effect on the calculated temperature field. Taking this idea one step further a prismatic volume with a constant cross-section can be used in the prescribed heat source model. The red line in Figure 6.4 shows the longitudinal sections of the prismatic weld pool where the parameter LWPool is the length of this fictitious weld pool. However, this is not just a way to simplify the heat source model. By introducing a parameter that can be freely adjusted

has actually created a very robust model. The length of the prismatic pool can be easily calibrated with the available temperature measurement results. When the weld pool length that reproduces the measurements is found, all the simplifications and uncertainties that are part of the numerical model are compensated for. Not only the unknown weld pool shape is replaced by an equivalent prismatic shape but also the unknown temperature distribution inside the weld pool is accounted for. Also the uncertainties in the material properties become less important as long as the use of this artificial heat source is able to reproduce the temperature history of the actual fabrication process. The proposed name for this model is "equivalent prismatic heat source model".

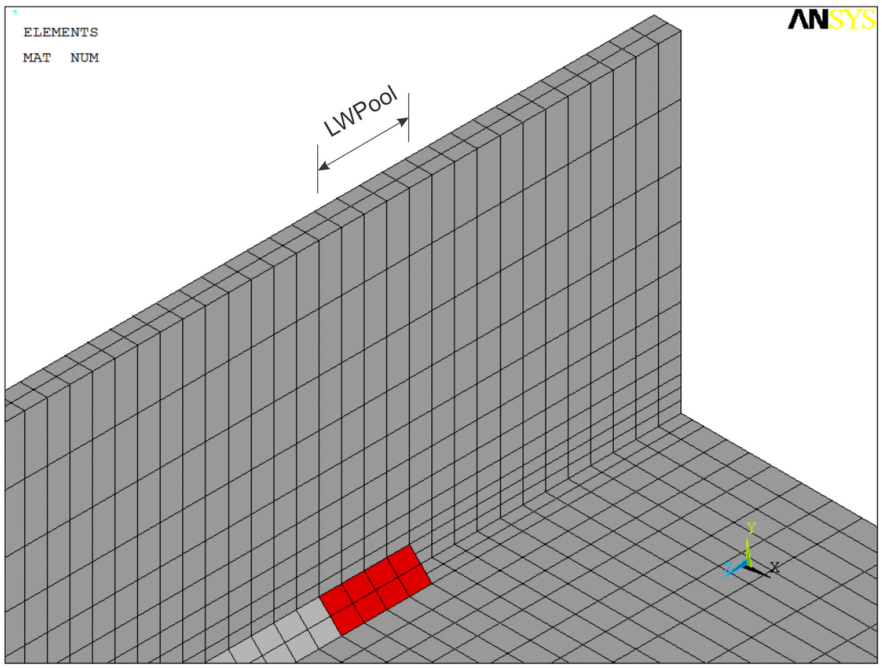

Figure 6.5: Mesh at the start of the weld. The highlighted elements represent the welding heat source.

Figure 6.5 shows the finite element mesh at the beginning of the model. The highlighted elements represent the surface of the prismatic weld pool. In the following parametric studies the LWPool parameter is set to $20mm$ if not stated otherwise. Figure 6.6 shows the process of applying the prescribed temperature in the first three steps of the analysis. At the beginning of the first step the temperature of the nodes of the elements of the weld pool highlighted in Figure 6.5 is gradually increased to the weld temperature of 1520°C (equal to the liquidus temperature of mild carbon

steel) during a short initial period of $0.01s$ (the *temperature increasing phase* of the welding step). This temperature is then maintained during the time determined by the welding speed and the weld pool length (the *temperature maintaining phase* of the welding step). The prescribed temperatures at this point are removed from the nodes and they are allowed to cool down freely. By the end of the first welding step the nodes corresponding to the elements of the next welding step need to reach the welding temperature. Therefore at the time equal to the time at the end of the first time step minus $0.01s$ the temperature of these nodes is gradually increased to 1520°C. It is now that the prescribed temperatures of the nodes of the first welding step are removed and the nodes of the second step are kept at the welding temperature. The same procedure is repeated until the end of the weld seam is reached. From that moment no prescribed temperature is applied to any of the nodes of the entire model and it is allowed to cool down according to the global thermal boundary conditions of the model.

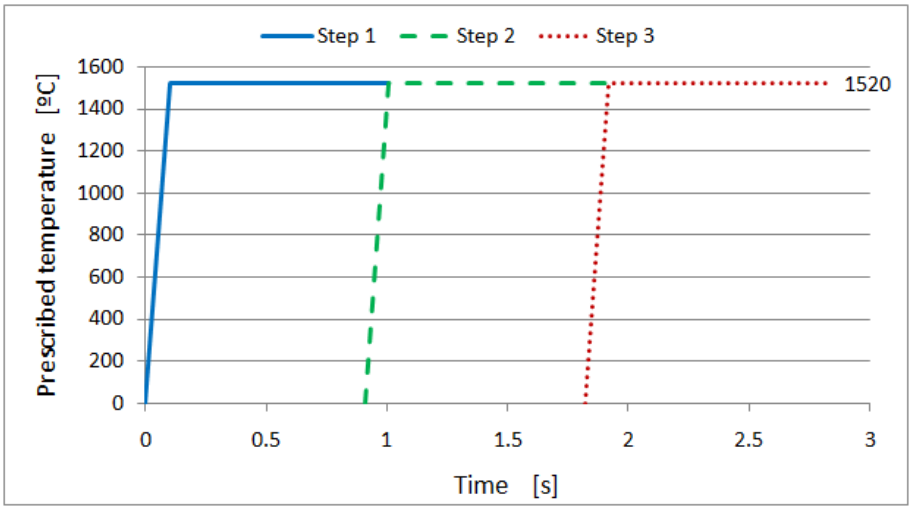

Figure 6.6: Prescribed temperatures of the first three welding steps.

The heat in the plates is transferred to the surroundings by convection and radiation. Radiation boundary condition leads to a non-linear solution and since radiation is dominant only at very high temperatures it is usually either ignored or included in a combined heat transfer coefficient that accounts for both convection and radiation. The latter solution is applied in this work. Convective boundary conditions are applied to all external surfaces of the model including the end faces of the plates, the surface of the weld seam and the two faces at the start and the end

of the weld seam. A wide range of combined heat transfer coefficient definition can be found in the literature. Three options are selected for this study to determine their influence on the calculated temperature history of the welded specimens. The simplest method is to use a constant combined heat transfer coefficient; a value of $h_c = 30W/m^2K$ is considered here. The other two options take into account that the coefficient is temperature dependent. They are shown in Figure 6.7 along with the constant coefficient. Curve Var_1 is taken from [89] and calculated using the following equation:

$$h_c = 24.1 \cdot 10^{-4} \varepsilon T^{1.61} \tag{6.1}$$

where $\varepsilon = 0.9$ is assumed as recommended for hot rolled steel [89]. Curve Var_2 is taken from [59] and calculated by the following equation:

$$h_c = h + \varepsilon\sigma(T + T_{amb})(T^2 + T_{amb}^2) \tag{6.2}$$

where h is the thermal convection coefficient ($8W/(m^2K)$), ε is the radiation emissivity (the average value for hot rolled steel: 0.51 [59]), σ is the Stefan Boltzman constant ($5.67 \cdot 10^{-8}W/(m^2K^4)$) and T_{amb} is the ambient temperature. Since only half of the plate girder is modelled, at the face of the web plate in the plane of symmetry an adiabatic boundary condition is applied.

The first parameter to be investigated in a series of studies is the combined heat transfer coefficient itself. The results are evaluated in a similar way to the experimental measurements. Even though these results can not be compared directly to the measurements, knowing how the parameters of these studies affect the outcome of the results obtained in a similar way to the measurements helps to understand how a given parameter can help in the calibration of the numerical model in order to match the experimental results which is discussed in the next chapter.

Figure 6.8 shows the results similar to that of the FIXED measurements (this is indicated by the word FIXED at the end of the caption). In all of the studies in this chapter the temperature of the surface of the weld seam at a distance of $200mm$ from the front of the weld pool are analysed. As the welding progresses at some point the weld pool (*i.e.* the equivalent prismatic welding heat source) will have travelled this distance and the temperature data collection can start. The data is collected up until the last welding step when the weld pool reaches the end of the weld seam. It is expected that, similar to the FIXED measurements, a constant weld seam surface

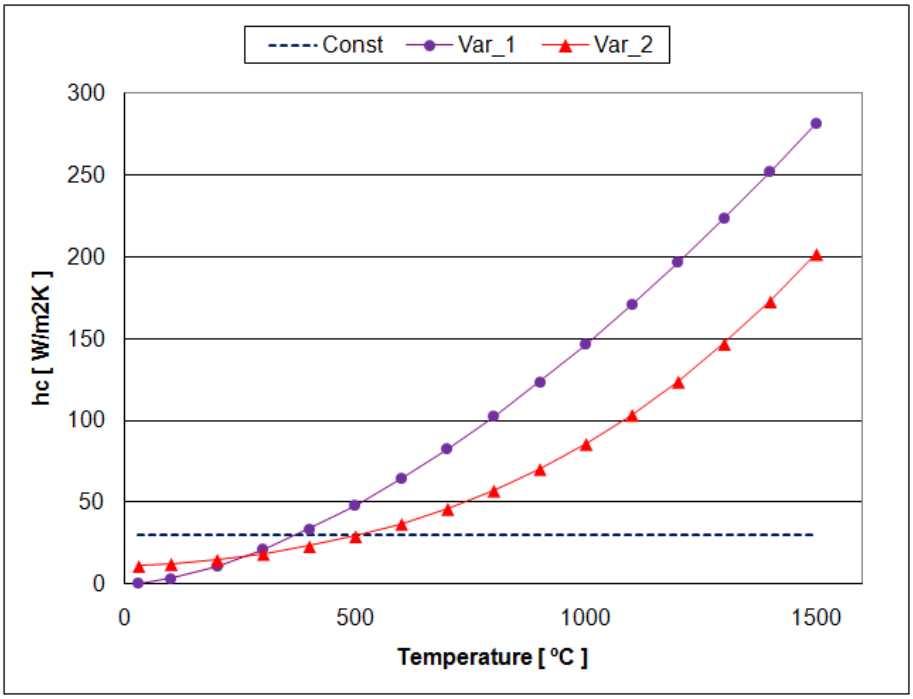

Figure 6.7: Combined heat transfer coefficients.

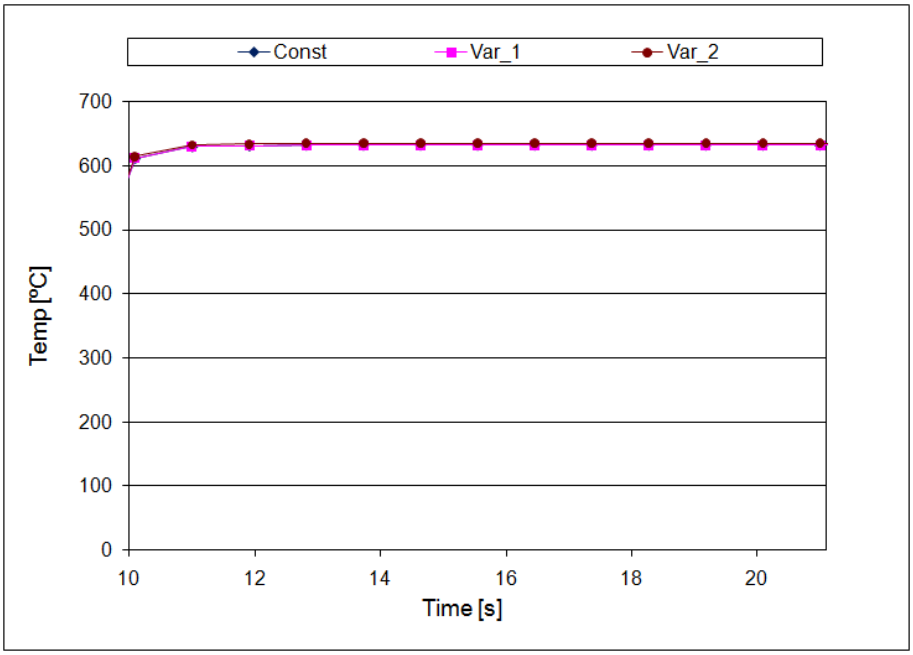

Figure 6.8: Effect of different combined heat transfer coefficients on the weld surface temperature (FIXED).

temperature develops at a constant distance behind the heat source. Only at the very start of the welding is it expected to see a slightly different temperature as a result of that $60mm$ distance between the start of the weld and the plates. This

makes the very first nodes of the weld seam to cool down faster then the rest of the nodes. Both the development of the constant temperature and the lower temperature at the start of the weld can be clearly observed in Figure 6.8. Each point in the chart represent the weighted average of the temperatures of the three nodes across the surface of the weld seam which can be seen in Figure 6.5. The weight of the node in the centre of the weld seam surface is double of the weight of the nodes on the two edges of the weld seam. The use of average temperature instead of simply using the temperature of the node at the centre of the weld is necessary in order to be able to compare the calculated temperatures to the measured ones later in the calibration of the model since the target area of the thermometer is approximately equal to the size of the weld seam (see Section 5.3). The comparison of the analyses with the three different combined heat transfer coefficients shows that the results are practically identical and the influence of the coefficient is negligible at this high temperature range.

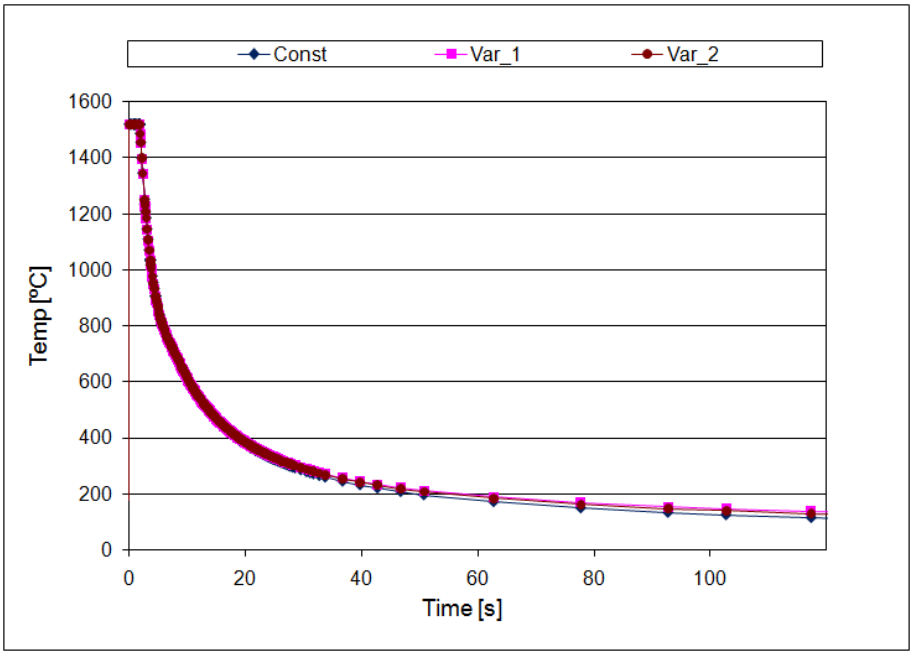

Figure 6.9: Effect of different combined heat transfer coefficients on the weld surface temperature (MOVING).

Figure 6.9 shows the numerical results that correspond to the MOVING temperature measurements. A fixed location is selected on the weld seam surface (in this case it is one weld pool length distance from the start of the weld) and the weighted average of the three nodes of the weld is calculated throughout the anal-

ysis. As seen in the FIXED results the heat transfer coefficient has no influence on the temperature history in the high temperature range. However, in the lower temperature range it is clear that the constant coefficient produces the lowest temperatures. It is because in this temperature range the constant coefficient is much higher than the variable ones as shown in Figure 6.7 which results in higher cooling rate. Similar tendency cannot be observed in the high temperature range even though the differences among the coefficient are much more significant. This is because at high temperatures the heat transfer in the plates are dominated by heat conduction within the plates and not by heat transfer into the ambient. On the other hand when the plates cool down considerably this tendency changes and the differences on the heat transfer coefficient becomes the governing factor of the final stage of the cooling down process.

No significant computational cost saving has been observed as a result of using a constant coefficient since the evaluation of the temperature dependent coefficient is a straightforward fast process. For the rest of the numerical analyses the temperature dependent combined heat transfer coefficient Var_2 (see Figure 6.7) is selected because in the lower temperature range it provides more reasonable cooling time unlike Var_1 that results in very low cooling rates near the ambient temperature.

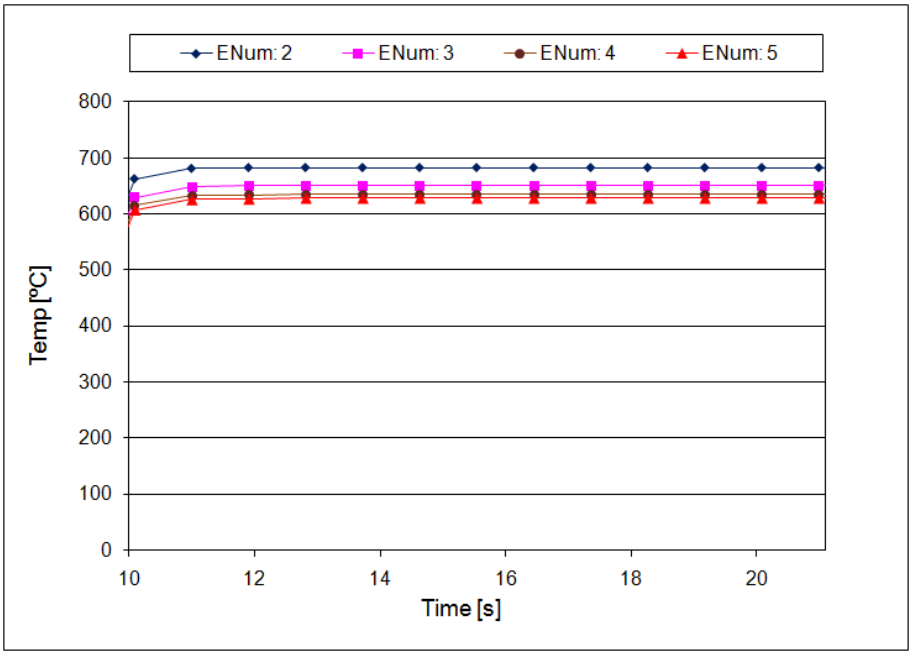

Figure 6.10: Effect of number of elements (ENum) along the weld pool length on the weld surface temperature (FIXED).

The mesh inside the weld pool shown in Figure 6.5 consist of four elements in the welding direction. Figure 6.10 shows the effect of the number of element divisions inside the weld pool region. Increasing the element number from four to five results in small difference in the weld surface temperature while the number of elements in the model is increased by 20%. Therefore four elements per weld pool length are used in the rest of the analyses.

Figure 6.2 shows that the nodes of the web and the flange under the weld root are not connected as is the case in the actual plate girders. If they are not connected there is no direct heat transfer from one plate to the other. Those faces are considered as free surfaces and convective boundary conditions are applied to them with the same combined heat transfer coefficient as the rest of the outer surfaces of the model. Figure 6.11 shows the temperature distribution at the end of the weld soon after the welding is finished. As expected, the temperatures are not equal in the flange and in the web just under the weld root since the elements are not connected therefore no heat conduction can take place between them. While it is true that those plates are not actually connected as if they were one material, in the welding machine rollers on both sides of the girder are applying pressure on the flanges that pushes them against the web and contact can develop depending on how smooth the edges of the web plates are.

To estimate how a perfect contact between the plates would affect the temperature distributions another analysis is performed where those nodes under the weld root are connected to allow for heat conduction between the plates. The result shown in Figure 6.12 demonstrates how much the heat transfer in the plates is dominated by heat conduction at this high temperatures. By connecting the two plates more heat can flow out of the weld pool and therefore it can cool down faster as it can be seen from the smaller red zone that represent the highest temperature zone in the model.

Figure 6.13 shows the comparison of the weld surface temperature $200mm$ behind the weld pool for both cases with merged and separated plates. There is a difference of about 10°C which is not very significant. The real thermal contact between those plates lies somewhere between these two extremes therefore it can be concluded that using the separated model the temperature is overestimated by less then 10°C at the given distance from the weld head. Not only this is a very small difference considering all the uncertainties in computational welding mechanics but using the

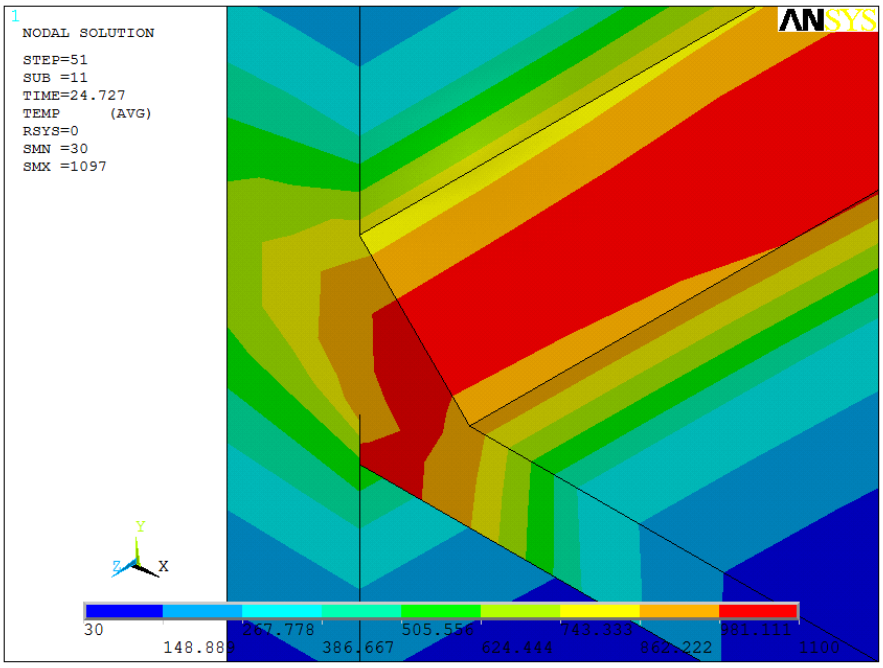

Figure 6.11: Separated flange and web.

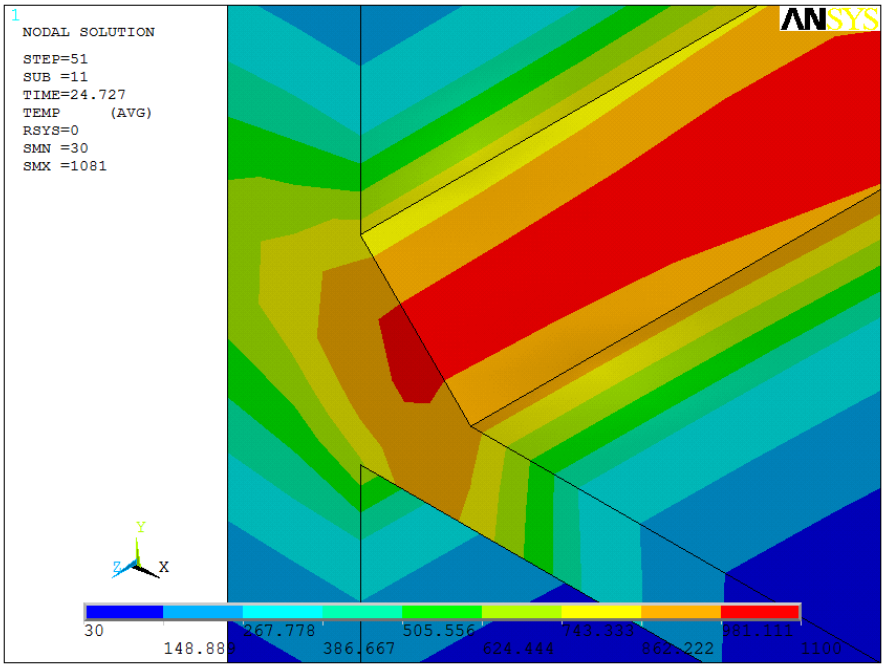

Figure 6.12: Merged flange and web.

equivalent prismatic heat source model means that this phenomena can also be compensated for by adjusting the length of the weld pool to match the measurement data. This is what makes this heat source model so robust despite its relative

simplicity.

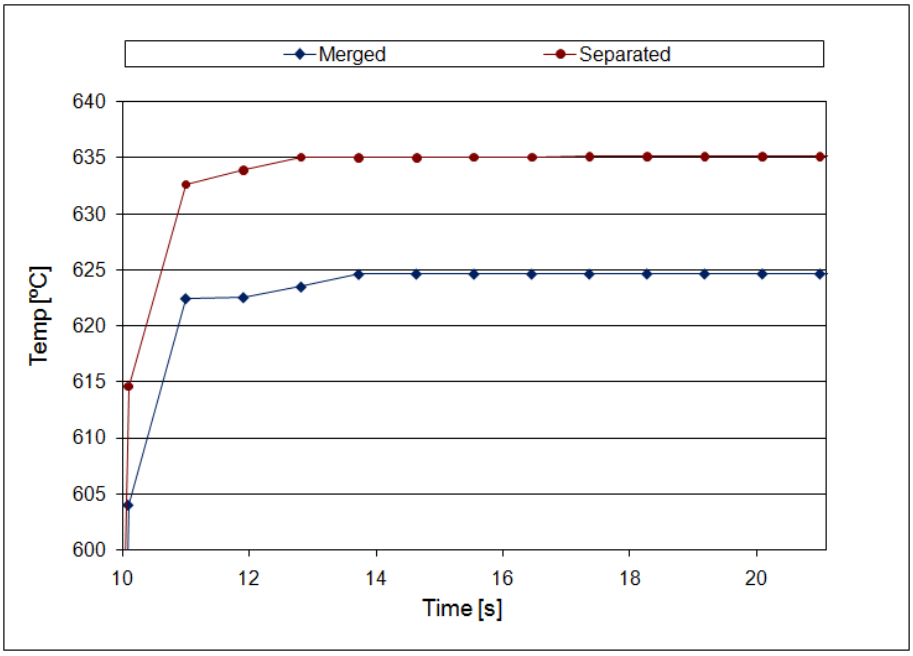

Figure 6.13: Effect of web-flange connection on the weld surface temperature (FIXED).

The next in the line of parameters investigated is the weld pool length itself. Figure 6.14 shows that increasing the weld pool length while maintaining the weld cross section can very significantly alter the temperature field in the weld. A $10mm$ increase in the weld pool length from $20mm$ to $30mm$ increased the weld surface temperature by more than 50°C and an additional $10mm$ results in a further increase of about 60°C. It is easy to see that this parameter alone gives a lot of room for the calibration of the model. Small changes in the weld pool length are translated into important changes in temperature that can be successfully exploited in the calibration process presented in the next chapter.

Figure 6.15 shows how the welding speed influences the weld surface temperature. These results are somehow misleading since higher a welding speed seems to result in higher temperatures. The explanation for this is that the curves represent temperatures at a fixed ($200mm$) distance behind the heat source. A higher welding speed means that the heat source travels this distance in a shorter period of time which leaves less time for the nodes to cool down.

Figure 6.16 shows a similar chart but instead of collecting temperature data at a fixed distance behind the welding heat source, the time that the heat source travels

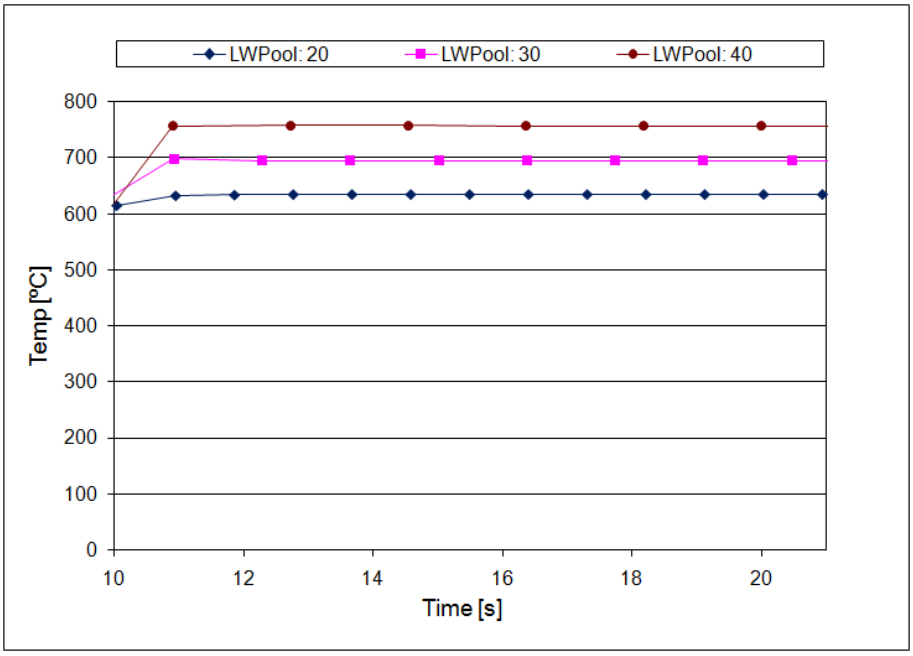

Figure 6.14: Effect of the length of the weld pool on the weld surface temperature (FIXED).

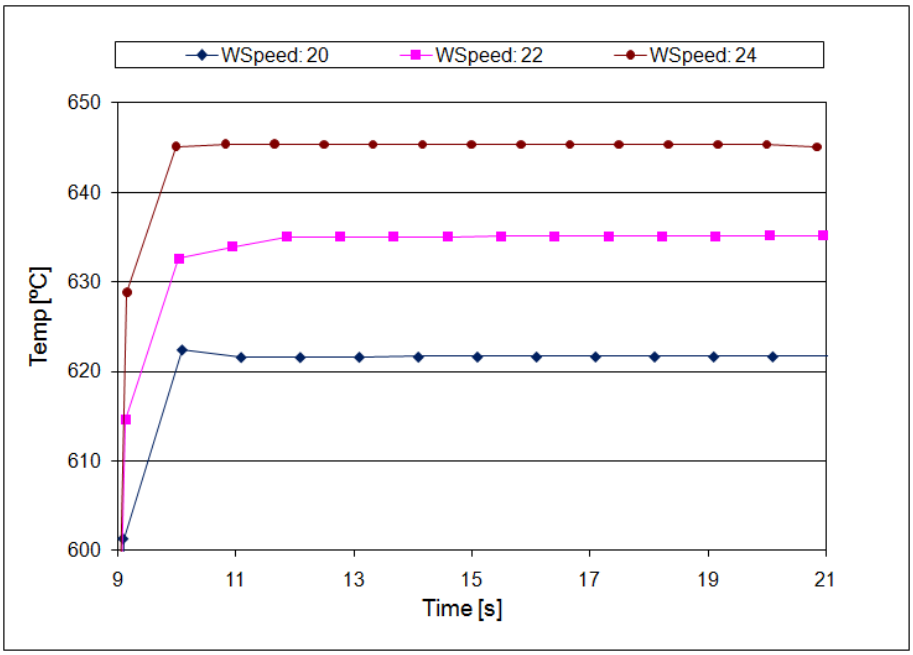

Figure 6.15: Effect of welding speed on the weld surface temperature (FIXED).

is fixed. Now, as expected, the highest temperature values come from the analysis with the slowest welding speed.

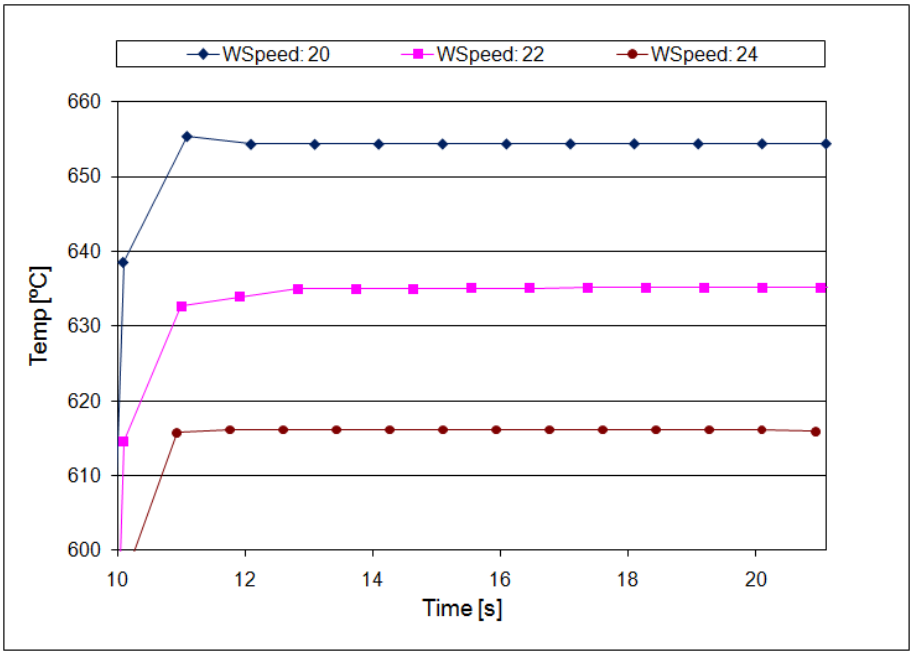

Figure 6.16: Effect of welding speed on the weld surface temperature (FIXED) - corrected.

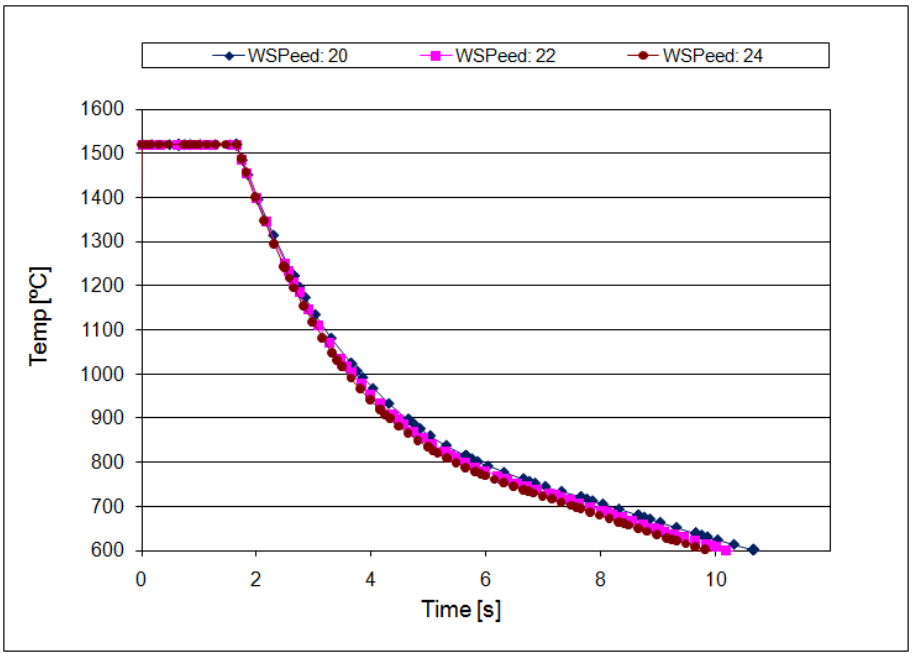

Figure 6.17: Effect of welding speed on the weld surface temperature (MOVING).

Figure 6.17 demonstrates well the effect of the welding speed on the temperature history of the weld seam. The temperatures are taken at one weld pool length

distance from the start of the weld. The curves have been shifted along the horizontal axis (time) to make sure that the cooling down starts at the same time in order to make the comparison more accurate. It is clear that the higher welding speed results in a higher cooling rate.

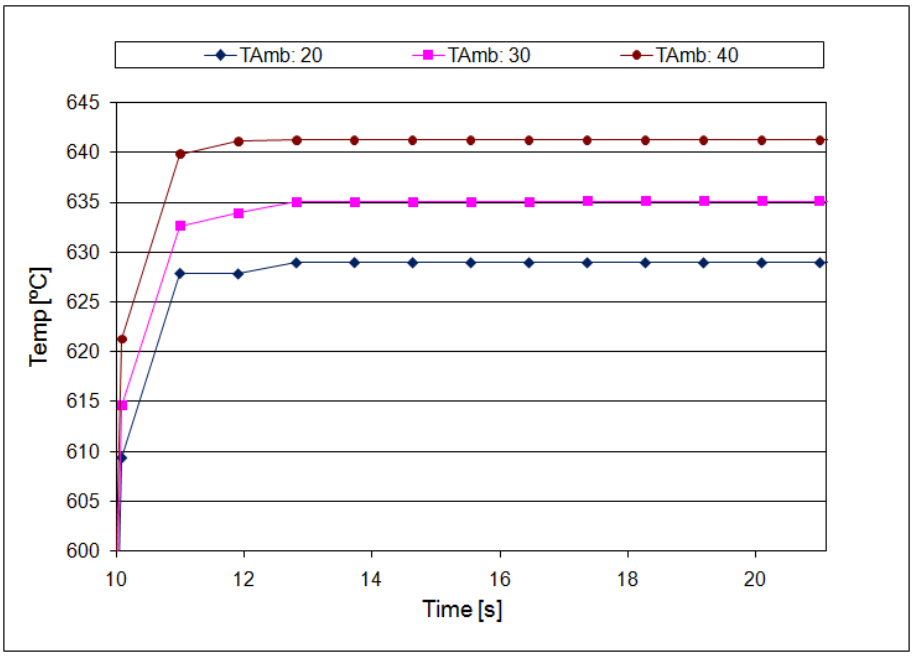

Figure 6.18: Effect of the ambient temperature on the weld surface temperature (FIXED).

While the ambient temperature is not a parameter that can easily be changed it is useful to check how it influences the temperature history of the specimens especially since during the fabrication an ambient temperature of 30°C was recorded which is higher than the 20°C usually quoted in the numerical analyses seen in the literature. As expected, a higher ambient temperature brings down the cooling rate and the weld surface temperature increases. This is also a good indication of how preheating affects the temperature history which is the next parameter to be studied.

Unfortunately no experimental data is available to check the efficiency of the preheating during the fabrication. What is known is that the aim of the preheating was to increase to temperature of the web in the section of the welding head to about 130°C to 150°C. While travelling through the welding machine the plate of the web is subjected to a stream of hot air before it reaches the welding heads. Choosing the upper limit of the target temperature range (150°C) and assuming an even distribution of that temperature on the surface nodes of the web is probably

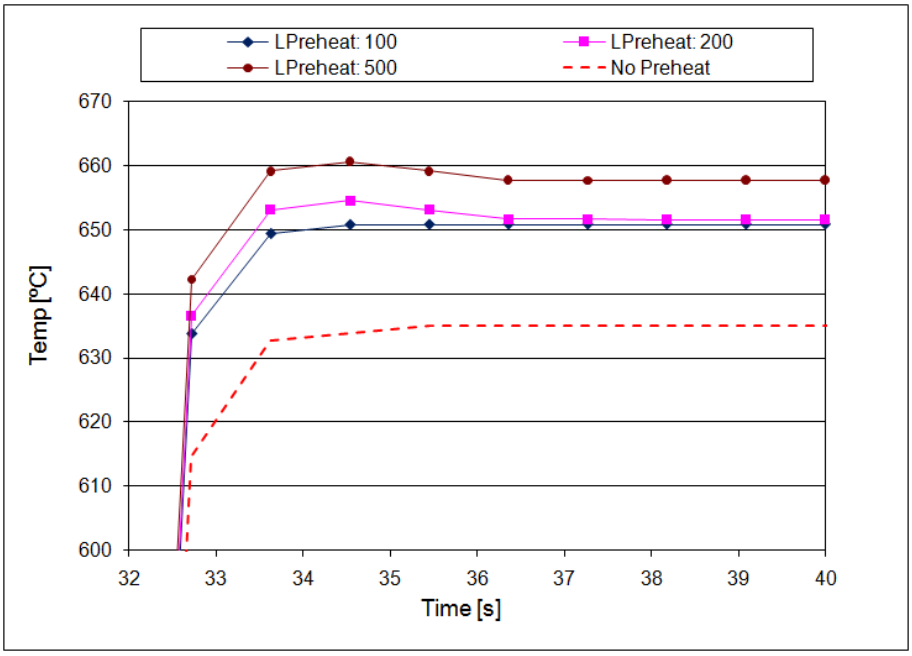

Figure 6.19: Effect of the length of the preheated zone on the weld surface temperature (FIXED).

an optimistic assumption of the effectiveness of the applied preheating. (According to the welding engineer of the factory the target temperatures of preheating are never actually achieved. See Section 5.3 for more details.) By studying two extreme cases, one without preheating and another one assuming an efficient preheating, it is likely that the real case would lie somewhere in between. It is also necessary to define the length of the portion of the web along which the preheating temperature is maintained in the nodes of the web surface before the plates arrive at the welding head. Figure 6.19 shows the weld surface temperature 200mm from the welding head considering 100mm, 200mm and 500mm for the preheating length. The longer the preheating is applied the more efficient it is. The results demonstrate that by applying preheating along a distance of 100mm increases the weld surface temperature by 15°C, an additional 100mm adds another 1°C and 500mm of preheated web surface results in a total of 22°C increase. Whenever preheating is applied in the rest of the numerical analyses it is assumed that the preheating temperature (150°C) is maintained along 200mm in the web. Preheating is not directly applied to the flanges of the specimens.

The remaining parameters to study are all related to the geometry of the weld seam: angle of the weld seam surface, cross-section area of the weld seam and the

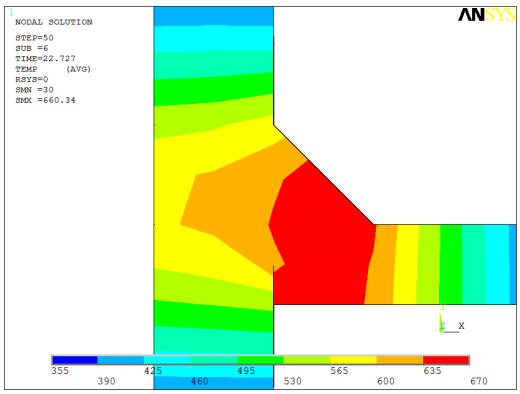

(a) Angle: 45°

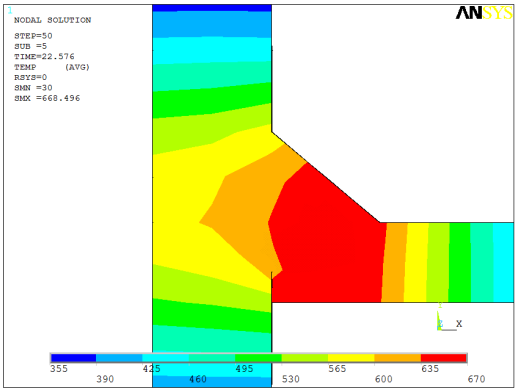

(b) Angle: 40°

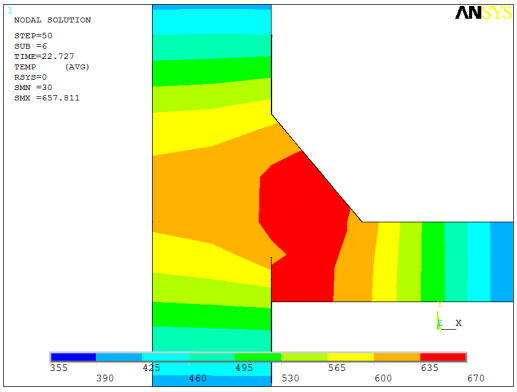

(c) Angle: 50°

Figure 6.20: Effect of the angle of the weld seam surface.

distance between the start of the girder and the start of the weld. The weld section shown in Figure 6.2 with the following dimensions has been used in all the previous analyses: both legs of the weld seam are $5mm$ long and the throat is 1.1*leg (*i.e.* $5.5mm$).

To study the effect of the angle between the web and the weld surface, the weld cross section shape is maintained, *i.e.* the length of the weld surface and the throat kept constant. The legs, however, are recalculated according to the angle that takes the values of 40°, 45° and 50°. The weld surface temperatures at $200mm$ behind the heat source are almost identical (hence are not shown here) in the three cases therefore no conclusions can be drawn from their comparison. However, if the cross-sections of the weld zone at the same location and at the same time in the welding process are compared in the three cases the effect of the angle of the weld seam surface can immediately be seen as shown in Figure 6.20. The three images feature the same temperature scale therefore the areas of the zones with the same colour

can be compared. The smallest red zone belongs to the case of a 50° angle and it is because the larger angle means that the weld seam is more oriented towards the flange. Since the thickness of the flange is greater than that of the web more heat is transferred from the weld seam towards the flange by heat conduction. In the case of a 40° angle the opposite happens and more heat is trapped near the weld seam resulting in a larger red zone. The case of a 45° angle is somewhere in between.

Once all the experimental investigation had been completed some of the specimens were sliced up in order to produce macrograph images of the actual weld cross-sections. The macrographs reveal that the weld sections are not constant and change slightly from one specimen to another and in general their dimensions are larger than the designed values. Therefore it is necessary to investigate how the size of the weld seam influences the calculated thermal history. The legs of the weld seam are shortened and lengthened by 10% relative to the initial $5mm$ which results in an approximate variation of 20% in the area of the weld cross-section. The three cases with their dimensions are listed in Table 6.1.

Leg $[mm]$	Throat $[mm]$	Area $[mm^2]$
4.5	4.95	49.48
5.0	5.5	61.09
5.5	6.05	73.92

Table 6.1: Weld section dimensions.

Figure 6.21 shows that the size of the weld seam, which directly influences the equivalent prismatic heat source model, can significantly change the weld surface temperature. While the variation in the weld geometry observed in the macrograph images are far less than in the three studied weld sections, it is important to know that, apart from the length of the weld pool, this is an important parameter of the model that needs to be carefully chosen when the numerical model is calibrated with the experimental data.

In all the previous analyses the distance between the start of the girder and the start of the weld seam has been assumed to be $60mm$ (see Figure 6.1) which is far less than the actual $300mm$ distance observed during the fabrication. In this last study the effect of this gap is investigated to demonstrate that reducing its length, and therefore reducing the size of the model significantly, is justified. Three cases

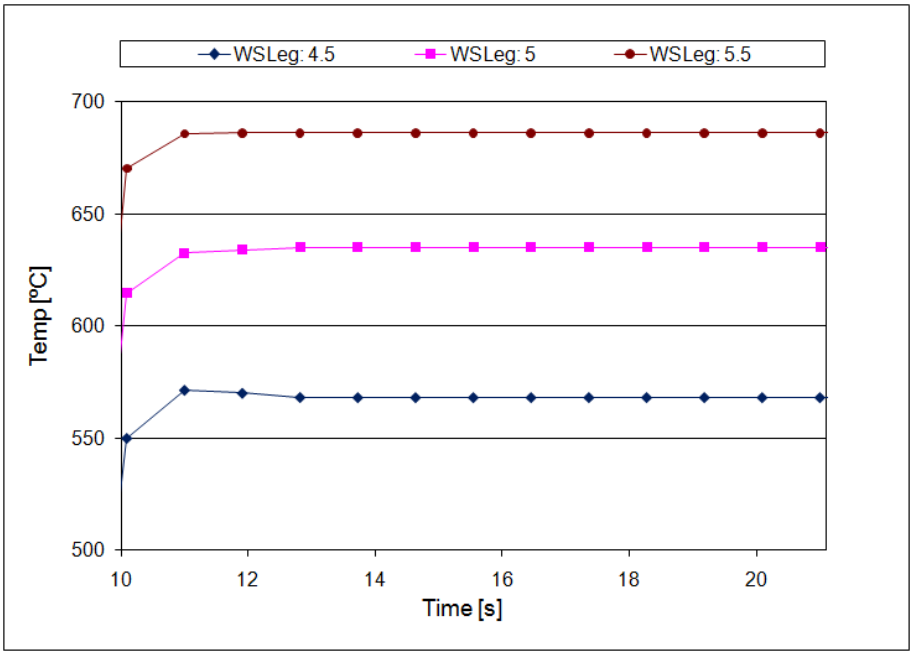

Figure 6.21: Effect of the area of the weld seam cross section on the weld surface temperature (FIXED).

are studied: in the first one there is no gap, *i.e.* the weld starts at the start of the girder, while in the other two cases the gap is $60mm$ and $120mm$ long. Figure 6.22 shows the results and the only difference that can be observed is the temperature of the very first point of the curves. This point represents the weld surface at the very start of the weld seam. As it has been discussed before, the heat transfer near the weld at high temperature is dominated by heat conduction. In the two cases with a gap at the start of the weld a much larger amount of material surrounds the weld than in the case without a gap. This is why the latter two cases produce lower temperature values at the start of the weld. Apart from this, however, the results are identical therefore all the previous analyses with a gap of $60mm$ are valid.

As a conclusion of this parametric study the following characteristics of the numerical model are fixed before the experimental calibration of the simulation:

- combined heat transfer coefficient: variable, calculated by Equation 6.2,
- number of elements within the weld pool: 4,
- the nodes of web and the flange under the weld root kept separated and convective boundary conditions are applied to the free surfaces,
- welding speed: $22mm/s$ (actual welding speed used during fabrication),

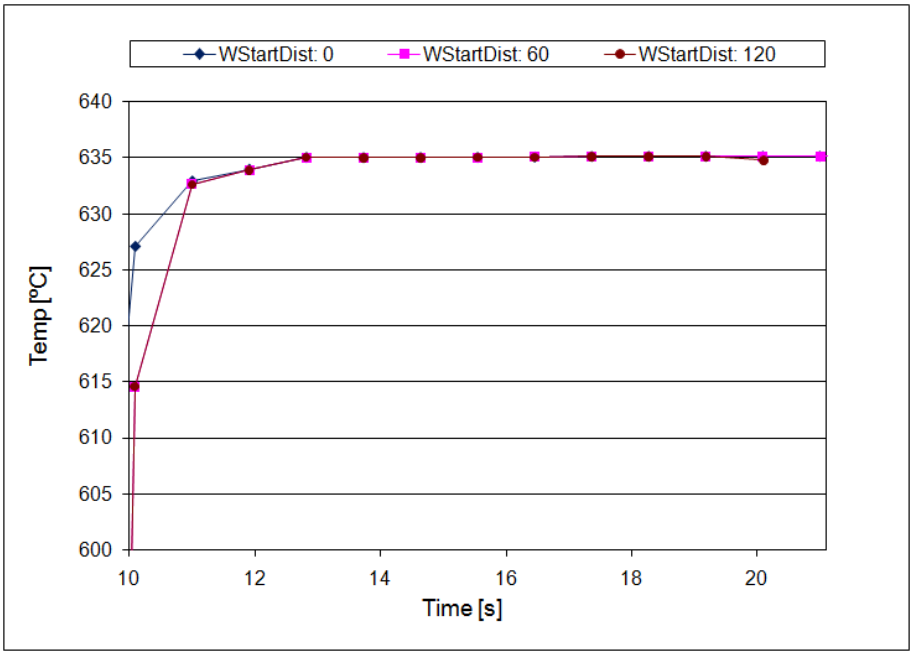

Figure 6.22: Effect of the distance between the end of the girder and the start of the weld on the weld surface temperature (FIXED).

- ambient temperature: 30° (actual ambient temperature recorded during fabrication),
- preheating temperature: 150° (upper limit of the aimed temperature range during fabrication),
- preheating length: $200mm$, and
- distance between the start of the girder and the start of the weld: $60mm$.

The weld dimensions will be adjusted according to the macrographs obtained after the experiments. After that the only parameter that remains undefined is the length of the artificial weld pool, *i.e.* the length of the equivalent prismatic heat source model.

6.3 Calibration of the numerical model

The calibration is performed for two different weld sections. The dimensions of one of them corresponds to the designed weld size, *i.e.* the legs are equal to $5mm$ and the throat is assumed to be $5.5mm$. The other section is an average section based on

the macrograph images of three weld sections. One of them is shown in Figure 6.23. The image includes the results of the measurements prepared by the Digimizer [90] image analysis software.

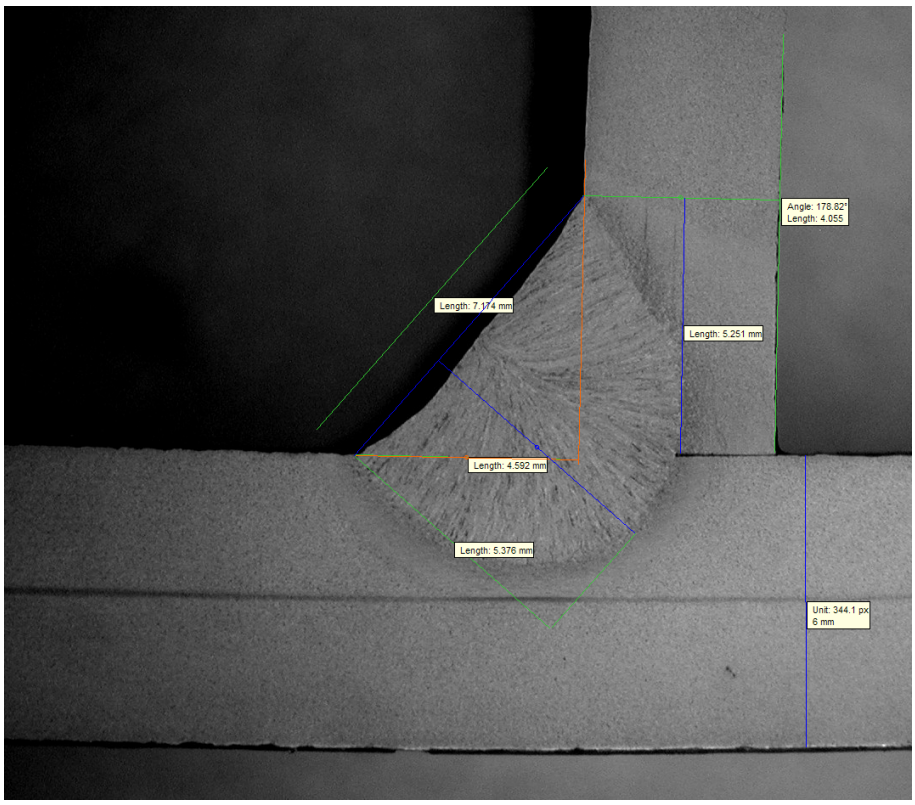

Figure 6.23: Weld section macrograph image with measurements.

Table 6.2 gives a summary of the dimensions of the three sections including the average dimensions of them, the dimensions chosen for the finite element model to reproduce the experiments and in the last row the design values of the ideal weld section. The dimensions chosen for the numerical model are slightly different from the actual average values. In the one hand it reflects that there is a certain degree of inaccuracy in the measurements since in the macrographs there is not a very sharp line that marks the edge of the weld pool. On the other hand there is not a clear tendency regarding which leg of the weld seam is larger. In two cases the leg on the web side is larger but in one case the leg on the flange side is significantly larger than in the other cases. For this reason equal leg dimensions are chosen for both sides of the weld section.

During the FIXED temperature measurements the distance between the measurement location and the welding head was $380mm$. The length of the numerical

No.	Leg (flange) $[mm]$	Leg (web) $[mm]$	Throat $[mm]$	Area $[mm^2]$
1	5.045	5.419	5.723	66.559
2	5.607	5.120	5.313	63.368
3	4.592	5.251	5.376	58.906
Average:	5.081	5.263	5.471	62.944
EXP FE Model:	5.2	5.2	5.5	63.533
Design:	5.0	5.0	5.5	61.089

Table 6.2: Average weld section dimensions based on three macrograph images; the weld section used in the finite element model; the design values of the weld section dimensions.

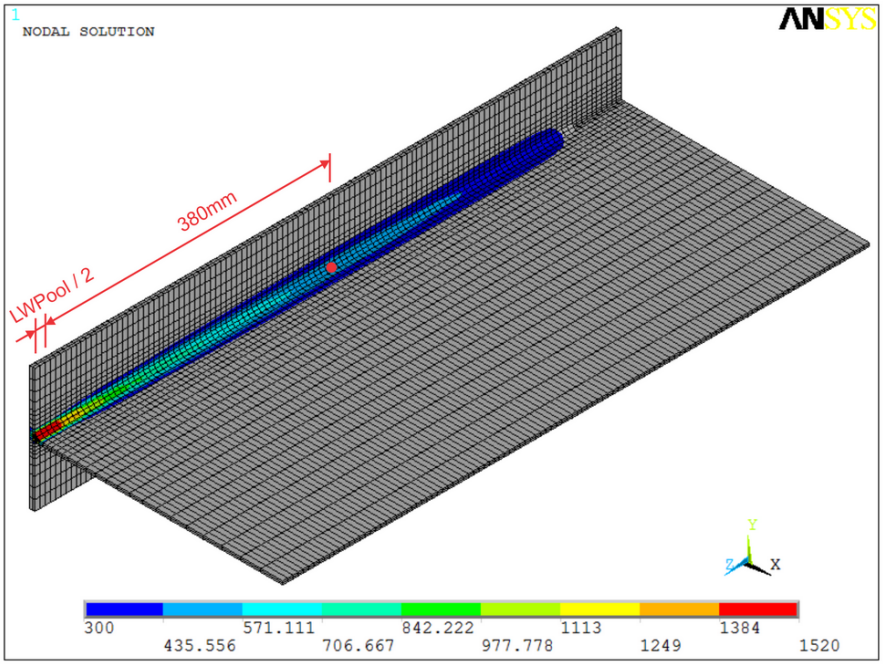

Figure 6.24: Simulation of the FIXED temperature measurement for the calibration of the numerical model.

model used in the previous parametric studies is increased to $700mm$ in order to reproduce such data. Figure 6.24 shows the model with the increased length. In the model it can happen that there are no nodes at a distance of $380mm$ from the centre of the weld pool, in which case a linear interpolation is performed between the nodes just before and just after the $380mm$ distance. As in the previous studies

the weld surface temperature is estimated as a weighted average of the three nodal temperatures across the weld surface as explained in Section 6.2. Figure 6.24 also demonstrates the difficulties caused by the relatively high lower limit of the temperature range of the thermometer. The figure shows the temperature distributions at the last step of the welding. Only temperatures greater than 300°C are displayed. The zone where the given thermometer can be used is a very narrow one indeed. Practically no measurements can take place outside of the welding zone. This is the reason why a number of measurement attempts failed even if the target area was only 1-2 *cm* away from the weld seam.

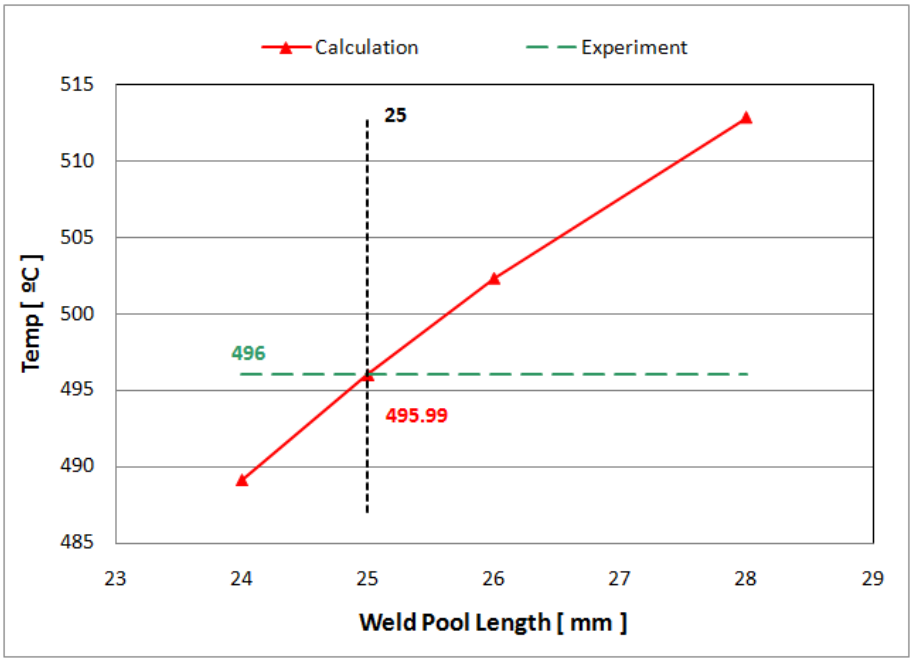

Figure 6.25: Calibration of the numerical model without preheating.

The first step in the calibration process is to arbitrarily select different weld pool lengths, perform the analyses and compare the calculated weld surface temperatures to the measured value of 496°C (horizontal line in Figure 6.25). The lengths of $24mm$, $26mm$ and $28mm$ are selected for the analyses without preheating. Linear interpolation between the values of $24mm$ and $26mm$ gives the approximate weld pool length of $25mm$ with which the analysis is repeated and the results are also displayed in the figure. The calculated weld surface temperature is 495.99°C which is very close to the measured temperature. The same procedure can be followed for the model considering preheating. The result of this calibration is shown in Figure 6.26. With the calibrated weld pool length of $21.6mm$ the calculated weld

surface temperature at a distance of $380mm$ behind the welding heat source is 495.88°C which is also in very good agreement with the measured value.

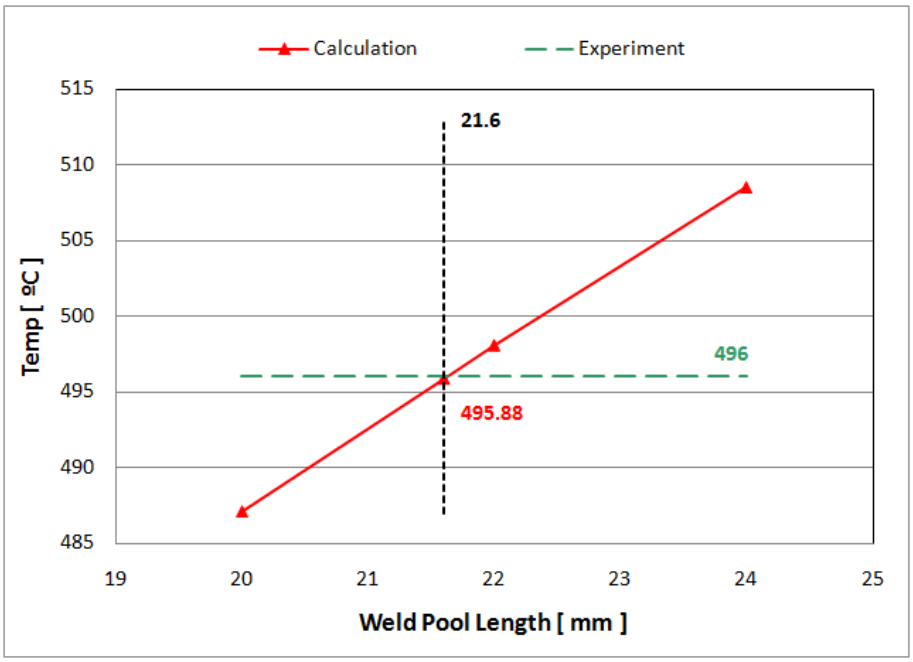

Figure 6.26: Calibration of the numerical model with preheating.

All these steps can be repeated considering the weld section with the design value of the leg size of the weld ($5mm$) instead of the $5.2mm$. Table 6.3 gives a summary of the calibrated prismatic weld pool lengths and the calculated weld surface temperatures for both cases of preheating and for both weld dimensions. The slightly longer weld pool lengths in the case of the weld seam with the smaller leg compensates for the difference between the designed weld geometry and the actual geometry.

Weld leg $[mm]$	No preheating	Preheating
$5.2mm$	$25.0mm$ (495.99°C)	$21.6mm$ (495.88°C)
$5.0mm$	$26.4mm$ (496.04°C)	$23.0mm$ (496.21°C)

Table 6.3: Calibrated prismatic weld pool lengths (and the calculated weld surface temperatures).

Using the adjustable equivalent prismatic heat source model the results of the FIXED measurements can be reproduced accurately. The purpose of the MOVING measurements was to provide a "second opinion", a way to check if the calibrated

model can reproduce the cooling down history of the specimens as well. The measurement locations of the MOVING measurements were just behind the welding head. Close to the start of the weld even a small difference in the measurement location could affect significantly the results as it is demonstrated with the help of the results of the numerical analysis. In Figure 6.27 the curve labelled WDist_1 shows the cooling down of the nodes at the start of the weld seam. As before, it represents the weighted average of the three nodal temperatures in the starting section of the weld seam surface. The second (WDist_2) and the third (WDist_3) curve belong to the nodes of the surface of the weld seam at one and two weld pool length distance from the start of the weld, respectively. No other results are shown because practically there are no changes as the distance from the start of the weld increased further. Within twice the length of the weld pool (in this case $50mm$) the temperature history is changing from curve WDist_1 to curve WDist_3. This is the reason why aiming the thermometer near the welding head can introduce a lot of uncertainties in the evaluation of the measurements.

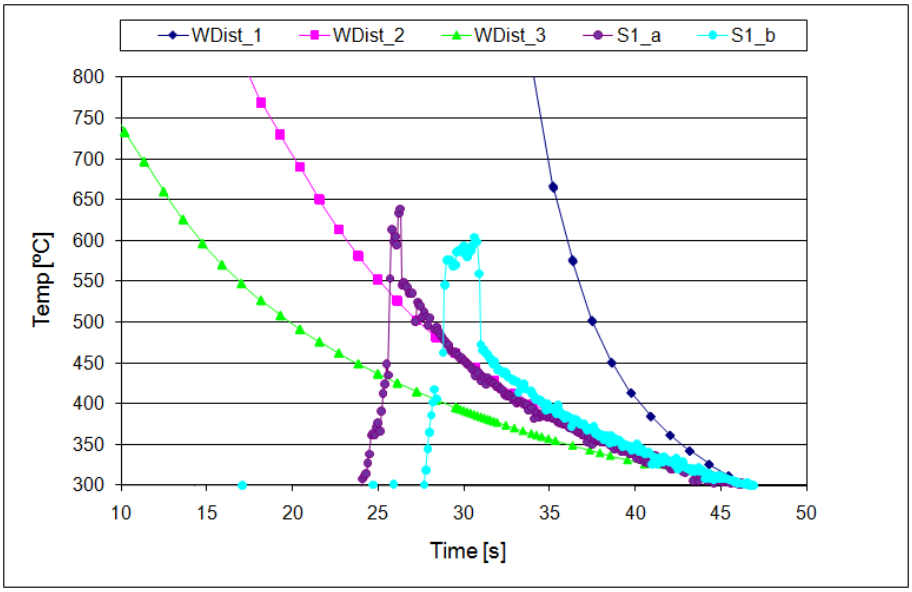

Figure 6.27: Comparison of MOVING measurements (S1_a and S1_b) with numerical results at the start of the weld (WDist_1), at a distance of one (WDist_2) and two (WDist_3) weld pool lengths from the start of the weld. No preheating is considered (Weld leg=$5.2mm$).

The three curves have been shifted along the time axis in such a way that they

come together at 300°C, the lower limit of the thermometer's temperature range. This makes the comparison with the measurements easier. In the same figure the two MOVING measurement results without preheating (S1_a and S1_b) are also displayed. It can be seen that they fit well within the area defined by the two extreme curves of the numerical results. Since there is no reliable information about the exact location of the measurement target area behind the welding head, this is the best result that can be extracted from the available data.

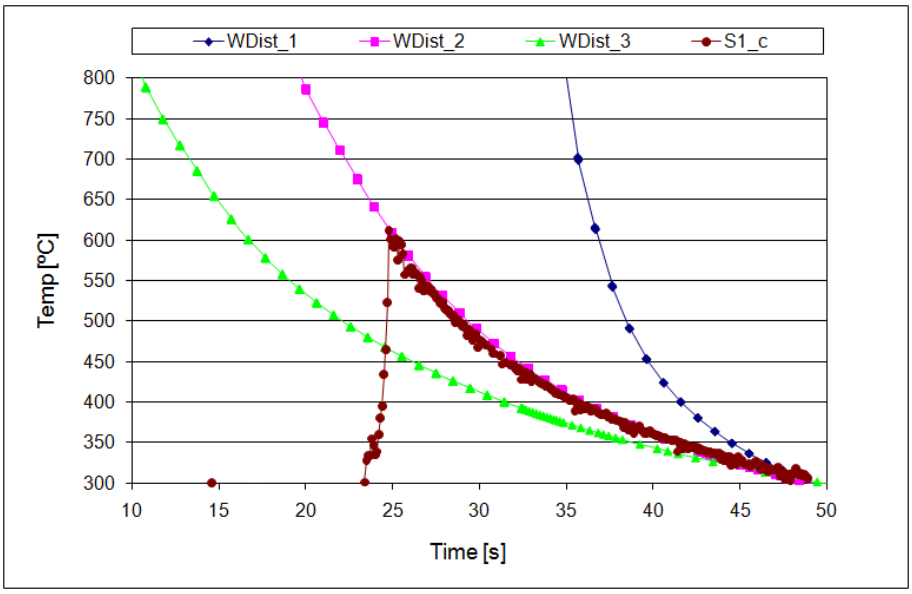

Figure 6.28: Comparison of MOVING measurement (S1_c) with numerical results at the start of the weld (WDist_1), at a distance of one (WDist_2) and two (WDist_3) weld pool lengths from the start of the weld. Preheating is considered (Weld leg=5.2mm).

Figure 6.28 shows the same kind of chart created for the analyses with preheating and the measurement result of the specimen with preheating (S1_c). The measurement data again fits nicely within the curves of the numerical results. While no quantitative conclusions can be drawn from these two figures because of the reasons mentioned before, it is interesting to point out that all the three experimental curves are very close to curve WDist_2. This suggest that the measurements took place close to each other and that the numerical simulation captured well the cooling down process of the weld seam.

The same evaluation is repeated with the numerical analyses based on the weld section with a 5mm weld leg size. Figures 6.29 and 6.30 show the results without

and with preheating, respectively. Very similar conclusions can be drawn from these figures.

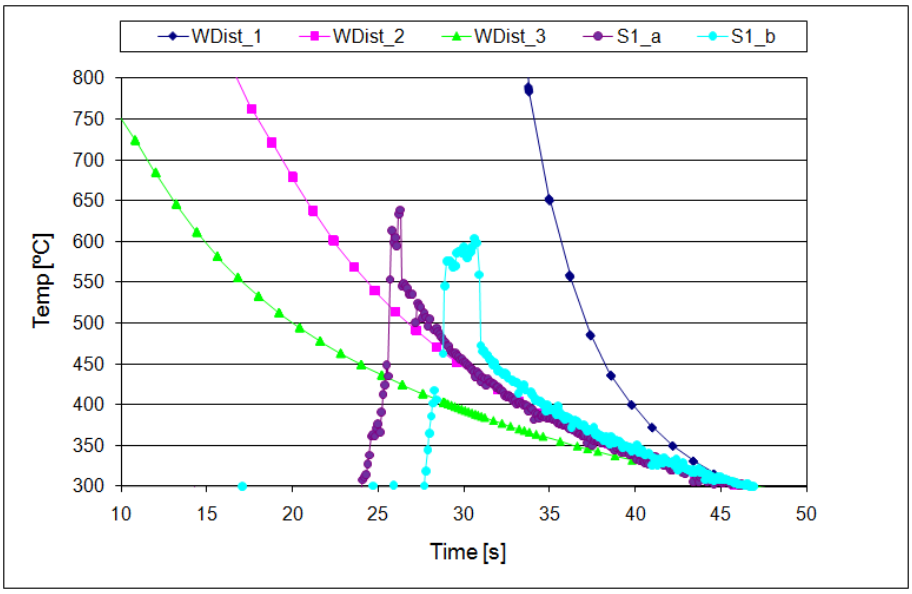

Figure 6.29: Comparison of MOVING measurements (S1_a and S1_b) with numerical results at the start of the weld (WDist_1), at a distance of one (WDist_2) and two (WDist_3) weld pool lengths from the start of the weld. No preheating is considered (Weld leg=5.0mm).

Comparing all the results, in Figure 6.28 an almost perfect match between one of the numerical curve and the experimental curves can be observed. While this is very reassuring it cannot be said that the numerical model with the larger weld section and with preheating reproduces the experimental results better than any of the other models. The reason for this that between the two extreme curves (WDist_1 and WDist_3) many other curves could be drawn at different locations within two weld pool length distance from the start of the weld. Certainly one of them would produce a perfect match with the experimental result in all the other figures as well. What is important is that such a perfect match can be found among the numerical results. This suggest that the numerical model can reasonably well reproduce the experimental measurements.

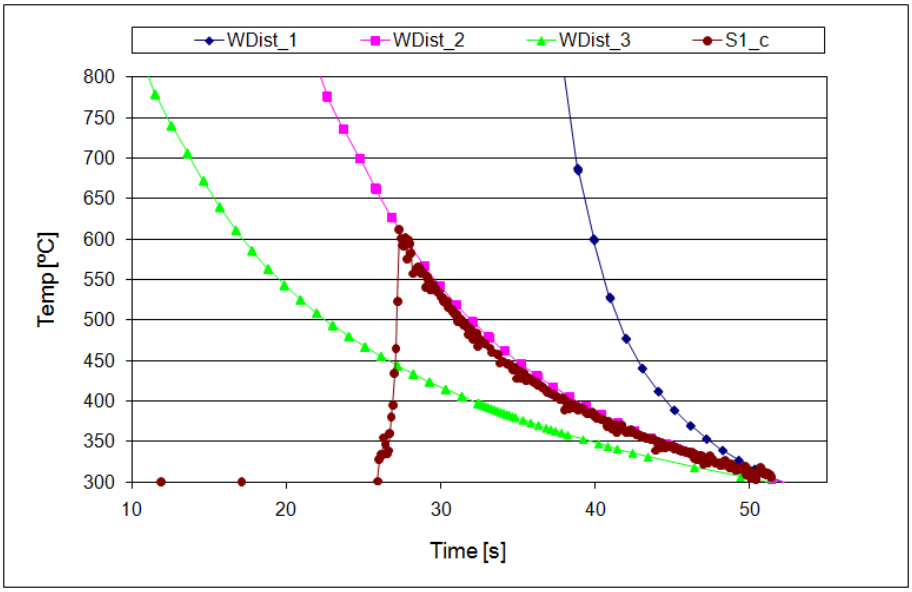

Figure 6.30: Comparison of MOVING measurement (S1_c) with numerical results at the start of the weld (WDist_1), at a distance of one (WDist_2) and two (WDist_3) weld pool lengths from the start of the weld. Preheating is considered (Weld leg=5.0mm).

6.4 Summary and conclusions

The development of a three dimensional numerical model to reproduce the temperature measurements and its successfully calibration has been presented. Based on the equivalent heat source model that uses prescribed temperatures at the known liquid-solid interface of the weld pool, a so called equivalent prismatic heat source model with adjustable length is developed. The cross-section of the heat source model is determined by the actual weld seam cross section that is either known from macrograph images of the weld or approximated by the design values of the weld dimensions. The length of the heat source model can be freely adjusted which provides a very efficient way to calibrate the model and to compensate for any uncertainties present in the analysis.

It is demonstrated that as a result of the simplicity and robustness of the equivalent prismatic heat source model the calibration of the numerical model based on the FIXED temperature measurement data can be done in very few steps with great accuracy. As a result of the given uncertainties regarding the MOVING measurements, the additional verification of the calibrated numerical model cannot be fully

evaluated quantitatively. Nevertheless, the comparison of the numerical and experimental temperature histories of the cooling process suggests very good agreement. The successful calibration demonstrates that the combination of the equivalent prismatic heat source model with the FIXED and the MOVING temperature measurements provides a powerful yet simple set of tools to create a virtual fabrication environment based on in-situ factory measurements.

The following general guidelines are recommended for consideration when developing and calibrating a numerical model to simulate the fabrication of plate girders:

- The equivalent prismatic heat source model has a single variable parameter which greatly simplifies the calibration process without sacrificing accuracy.
- The difference between the actual weld section and the designed weld section can be assumed to be small enough to be compensated for by the equivalent prismatic heat source model.
- A single reliable temperature data can be sufficient to calibrate the model. The FIXED temperature measurements used in this research are easy to execute without interfering with the fabrication and provide a large amount of data of the same physical property (weld surface temperature) over a period of time that improves the reliability of the data.
- A second measurement of a property that varies over time, such as the weld surface temperature history of a fixed point of the weld seam provided by the MOVING temperature measurements of this research, can provide a "semi-independent" control data for the revision of the calibration.

The last step to complete the development of the numerical model for the virtual fabrication of plate girder specimens is the thermal stress analysis of welding, which is the subject of Chapter 8. The next chapter presents the results of the residual stress measurements and an extensive numerical study in order to develop calibration tables for the employed measurement method.

Chapter 7

Residual stress measurements

7.1 Introduction

In this chapter a series of residual stress measurements in the flanges of plate girders are presented. The main objective of the measurements is the comparison of the longitudinal residual stresses in plate girders with single-sided and double-sided fillet welds. A simple measurement method based on the hole drilling method is used. In the execution of the measurements some inaccuracies have been observed. To evaluate the influence of those inaccuracies, the measurements are also simulated with finite element models. As a result of the numerical investigation, calibration tables are developed that can be used in the evaluation of future measurements using the same methodology.

7.2 Residual stress measurement methodology

The hole-drilling method is one of the most widely used techniques to measure residual stresses. The method is based on drilling a hole in the stressed material and measuring the stresses that are relaxed as a result of removing part of the material. The procedures for the measurement have been standardized by using the ASTM Standard Test Method E 837 [91] and it involves a three-element strain gauge rosette (shown in Figure 7.1) and it is performed in three main steps [92, 93]:

- drilling a small shallow hole (blind hole) at the centre of the rosette (Figure 7.2),
- measuring the deformations near the hole, and

- calculating residual stresses.

Figure 7.1: Typical strain gauge rosette for residual stress measurement by the hole-drilling method manufactured by Vishay [93].

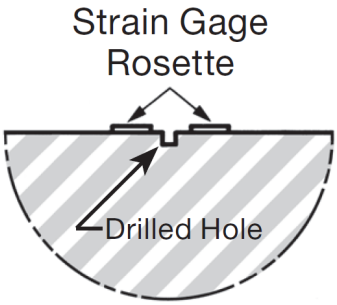

Figure 7.2: Blind hole at the centre of the strain gauge rosette [93].

The technique is considered semi-destructive since the size of the blind hole is usually small enough not to cause any significant structural damage. The accuracy of the measurement largely depends on the alignment of the hole at the centre of the rosette. For example in the case of rosette 062RE manufactured by Vishay, which is shown in Figure 7.1, the typical whole diameter is 1.5mm to 2.0mm. To limit the error of the calculated stresses to 3% the eccentricity of the blind hole should not exceed 0.025mm [93]. To achieve such precisions it is necessary use a milling guide, an example of which is shown in Figure 7.3.

The main advantage of this method is its semi-destructive nature. However, the severe requirements of precision and therefore the need to use special equipment to execute the measurement makes it impractical for the present project. The specimens for this research are eventually destroyed in ultimate load tests therefore

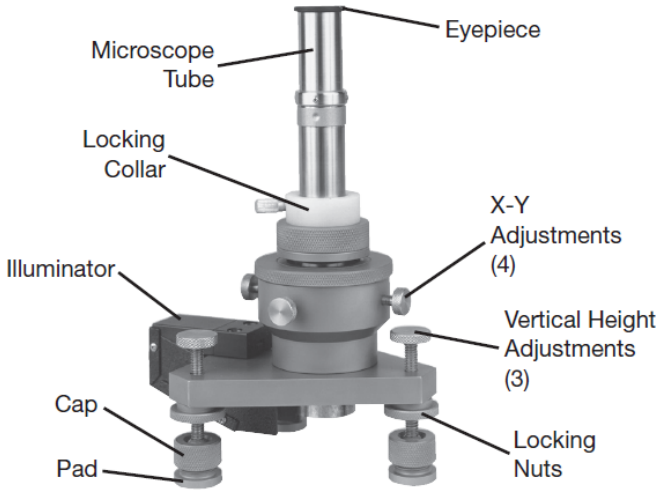

Figure 7.3: RS-200 milling guide of Vishay [93].

using a non-destructive or semi-destructive method for the measurements of residual stresses have low priorities. Another method based on the same principal of stress relaxation but with much easier execution is employed.

At each point of interest a single uniaxial strain gauge is placed on the specimens and two through-holes are drilled on both sides of the strain gauge as shown in Figure 7.4.

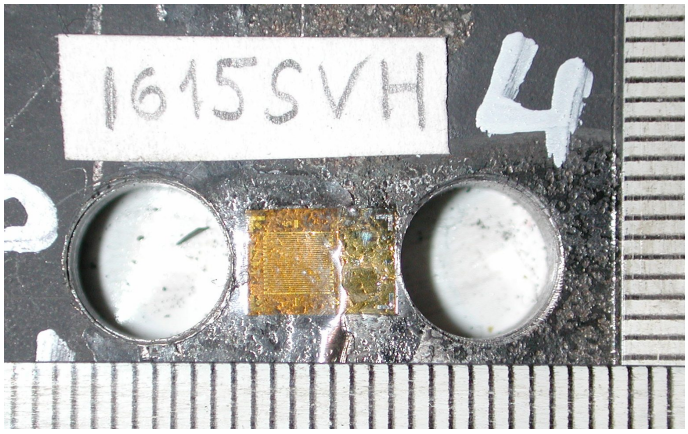

Figure 7.4: Single strain gauge and through holes in the flange of a plate girder.

Using this method means that a considerably larger amount of material is removed from the specimens, and therefore a larger amount of residual stress is freed (relaxed). As a result of this the measurement is much less sensitive to any inaccu-

racies of the execution as is demonstrated by the numerical analyses in Section 7.3. This also means that relatively simple equipments can be used to drill the holes as shows in Figure 7.5.

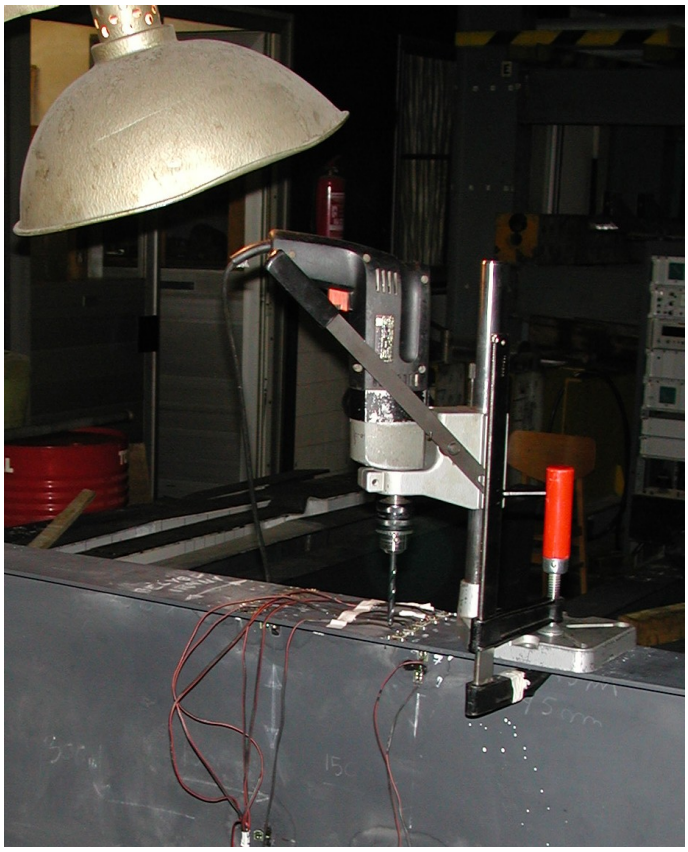

Figure 7.5: Drilling stand and drilling machine used in the measurements.

The primary interest of this investigation is to compare the longitudinal residual stress distribution in plate girders with single-sided and double-sided fillet welds. This objective also justifies the use of a simplified measurement method since the focus is on the comparison of the two fabrication methods and not on the exact residual stress values. Using the same methodology gives results of the same quality and therefore they can be compared even if the individual measurements are not of the highest accuracy. Nevertheless in Section 7.3 the accuracy of the method itself is also investigated to allow for better evaluation of the measurements.

When a strain gauge rosette is used the strains are measured in three directions that allows the calculation of the principal stresses and their angle, *i.e.* the complete stress state. When a single uniaxial strain gauge is used only the strain in the direction of the gauge can be determined. In welded plate girders the dominant residual stresses are the longitudinal stresses. The transverse residual stresses reach only a

fraction of the longitudinal ones [18] therefore using a single uniaxial strain gauge can give very good qualitative information about the stress state of the specimens.

Figure 7.6 shows the cross-section at the centre of a plate girder and the arrangement of six gauges in the flange of the girder. The image shows only the case of the single-sided fillet weld but the same gauge locations are used for the plate girder with a double-sided fillet weld. Figure 7.7 shows the flange of a plate girder with all the six measurement locations after all the through-holes have been drilled.

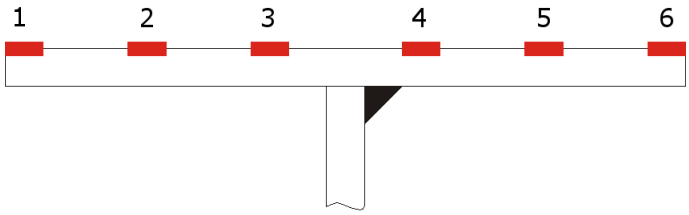

Figure 7.6: The strain gauge arrangement is shown the cross-section of a plate girder.

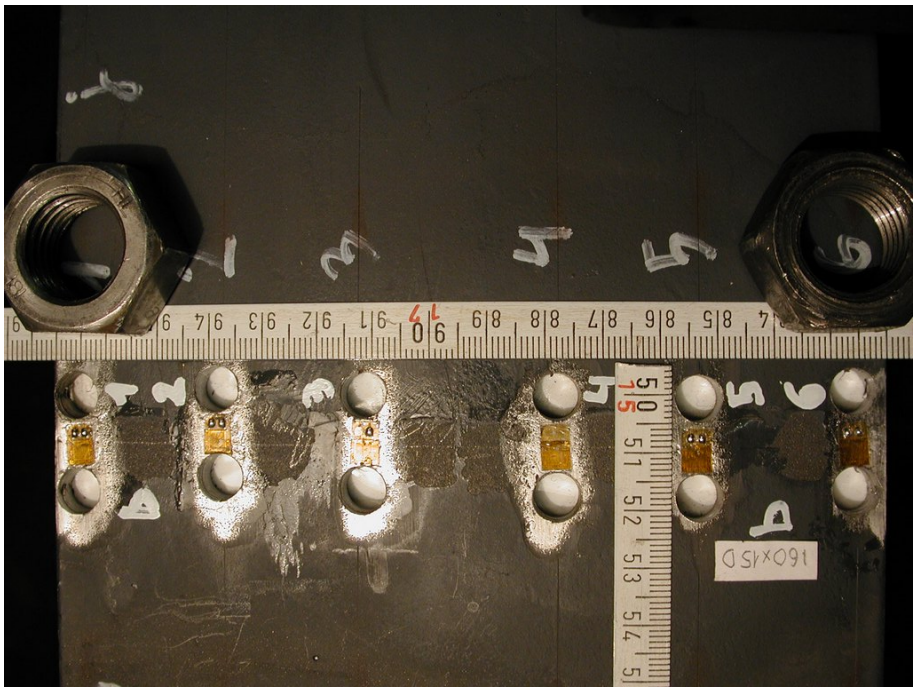

Figure 7.7: Strain gauge arrangement in the flange of a plate girder.

Two specimens are selected from the plate girders of the experimental programme for the residual stress measurements. The only difference between the two selected plate girders is the fillet weld between the web and the flanges as shown in Table 7.1.

Specimen	Flange	Web	Weld	Length
S1	150x6	600x4	Single	2970
S2			Double	

Table 7.1: Plate girder specimens selected for residual stress measurements (all units in mm).

Based on the measured strains in the flanges of the two girders the residual stresses can be estimated by simply multiplying those strain values by the Young's modulus of the material. The residual stresses calculated are shown in Figure 7.8. As expected, the residual stress level in the girder with single-sided fillet weld is significantly lower and the distribution of the residual stresses show a lower degree of symmetry.

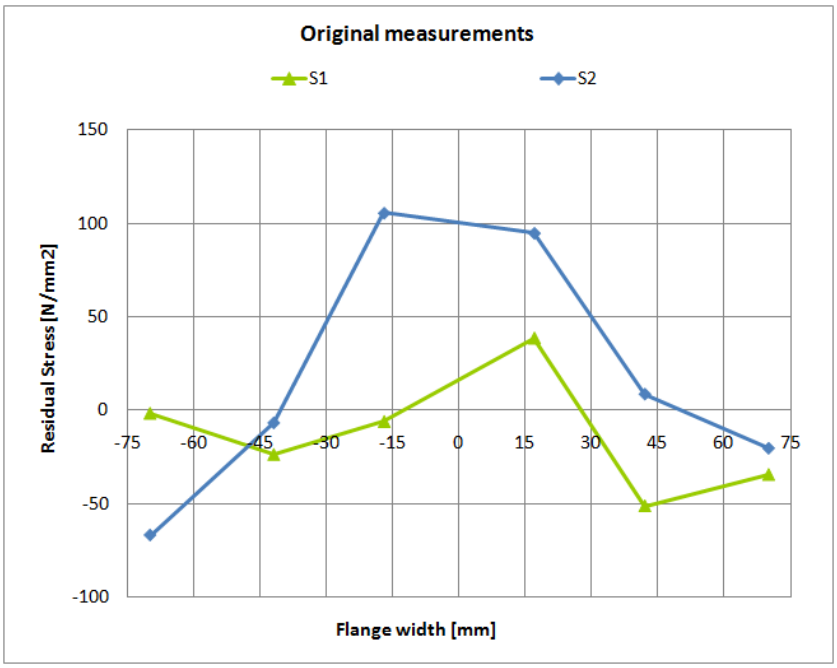

Figure 7.8: Residual stress measurements results calculated directly from the measured strains.

While these results seem to correspond well to the expected results, further investigation is required to determine how reliable these values are and to see if a more accurate evaluation of the measured strains leads to the same conclusions. The studies presented in Section 7.3 were designed to answer these questions.

7.3 Measurement sensitivity

7.3.1 Measurement inaccuracy

The centre of the strain gauge and the centre of the through-holes shown in Figure 7.4 are well aligned along a straight line. Unfortunately not all the measurements are executed with such accuracy as shown in Figure 7.9.

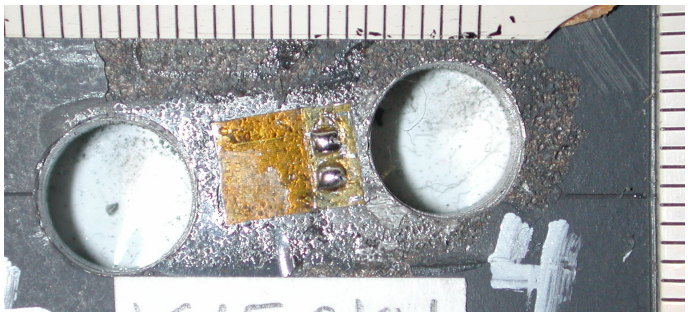

Figure 7.9: Measurement with severe inaccuracies.

After the completion of the residual stress measurements high resolution photographs are taken of every strain gauge. These photographs can be used to perform further image analyses to determine the exact relative positions of the strain gauges and the corresponding through-holes. Such image analyses are more commonly used in medical imaging but they can also be successfully employed in a wide range of other applications. The software Digimizer [90] is selected to perform the image analyses. As an example, some results of the image analysis of the gauge shown in Figure 7.9 are presented in Figure 7.10.

Every photograph includes a ruler, as shown in Figure 7.9, therefore it is a very straightforward process to calibrate the measurements of distances. The ruler provides a known distance and that distance needs to be divided by the corresponding number of pixels to determine the scale of the photo. Once such a unit of measurement is established the software provides a wide selection of tools (including: search for the centre of a circle, draw perpendicular lines, etc.) to mark the points of interest in the image and perform the necessary measurements of both distances and angles. Figure 7.10 shows the most important parameters that are necessary to evaluate each residual stress measurement:

- the angle of the gauge relative to the axis of the girder,

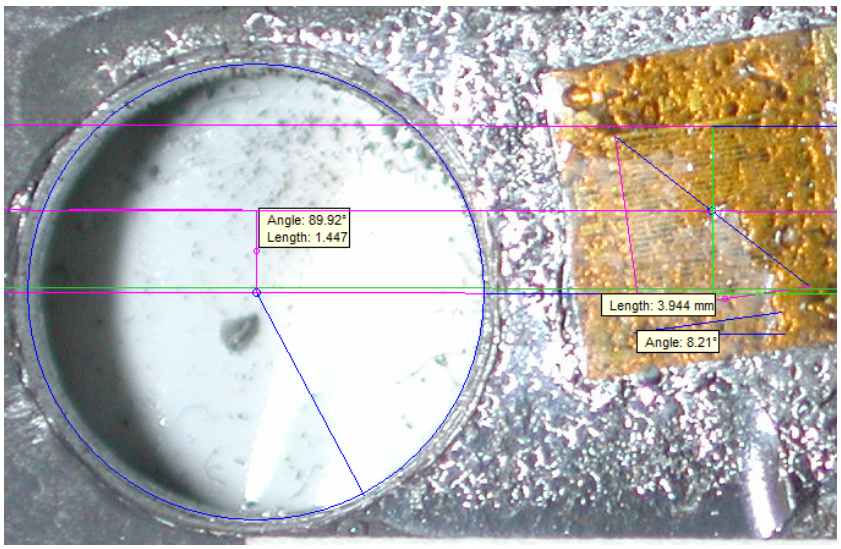

Figure 7.10: Measurement of inaccuracies using high-resolution photographs.

- the vertical distance between the centre of the through-holes and the centre of the gauge, and
- the horizontal distance between the edge of the through-holes and the centre of the gauge.

Altogether there are twelve locations (six each) in the flanges of specimen S1 and S2 that need to be analysed. The distances between the gauge centre and the through-hole centres are summarised in Figure 7.11 for both specimens. The scales of the horizontal (X) and vertical (Y) axis are different. Each data point in the chart represents the centre of a through-hole, while the rectangle at the centre of the image represents the active grid of the strain gauge. The two points enclosed in circles correspond to the case shown in Figure 7.9 which is the most severe case of the twelve measurements considering the inaccuracies in the execution. The numbers next to some of the points mark the extreme values of the vertical (Y) and horizontal (X) distances from the centre of the gauge. The numbers in the grey boxes are explained in Section 7.3.4.

The gauge angle is in the range of 0° to 8.21° (the latter corresponds to the gauge shown in Figures 7.9 and 7.10). Figure 7.12 shows the angle for each one of the twelve measurements in ascending order. Most of the angle values (7 out of 12) fall in the range of ±3°, one third of them (4 out of 12) is within ±5° and only a single case outside of that marked with a circle.

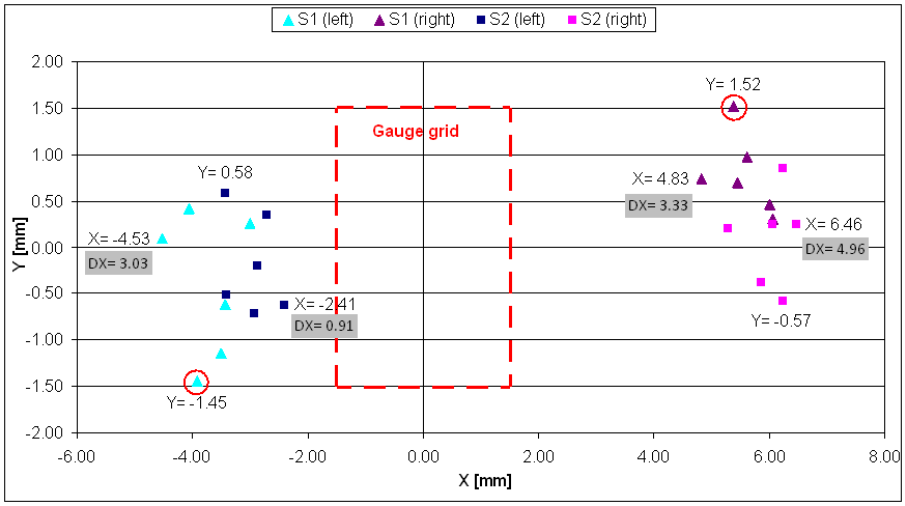

Figure 7.11: Inaccuracies in the drilling of through-holes. The data points represent the centre of the through holes.

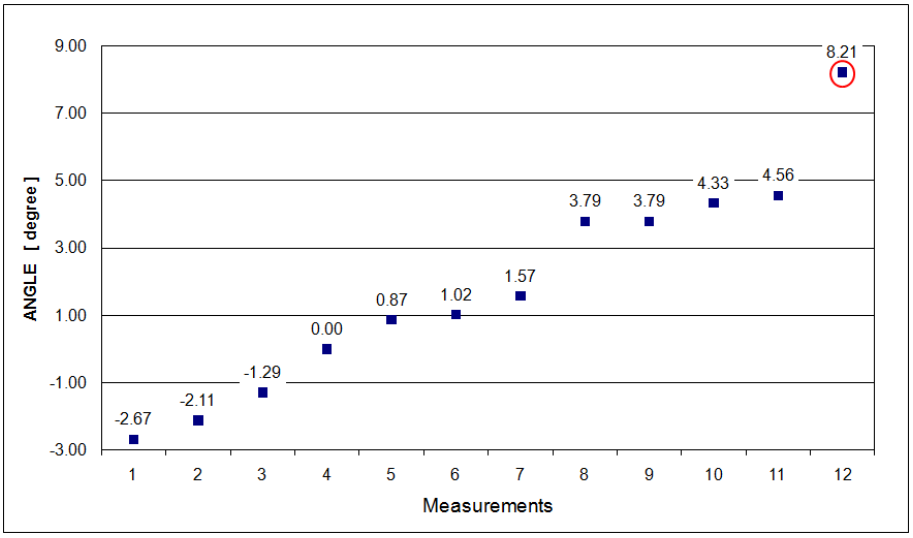

Figure 7.12: Angular inaccuracies in the placing of strain gauges (shown in ascending order).

A series of numerical tests is developed to determine how these inaccuracies can influence the results of the residual stress measurements. Details of the numerical models and the results of the numerical analyses are presented in the following sections.

7.3.2 Numerical model

The numerical model is developed in two steps. An initial numerical model is used to study the accuracy of such a model and to calibrate it by comparing the numerical results to analytical ones. Once the reliability of the numerical model is demonstrated, it is further developed in order to reproduce the actual residual stress measurements and study the effects of the inaccuracies.

The analytical solution of the stress distribution around a drilled hole in a thin infinite plate subjected to uniform stress was published by Kirsch in 1898. His solution can also be found in [93, 94]. Figure 7.13 taken from [93] shows the variation of radial (ϵ_r) and tangential (ϵ_θ) strains both in the direction of the uniform stress σ and in the direction perpendicular to it.

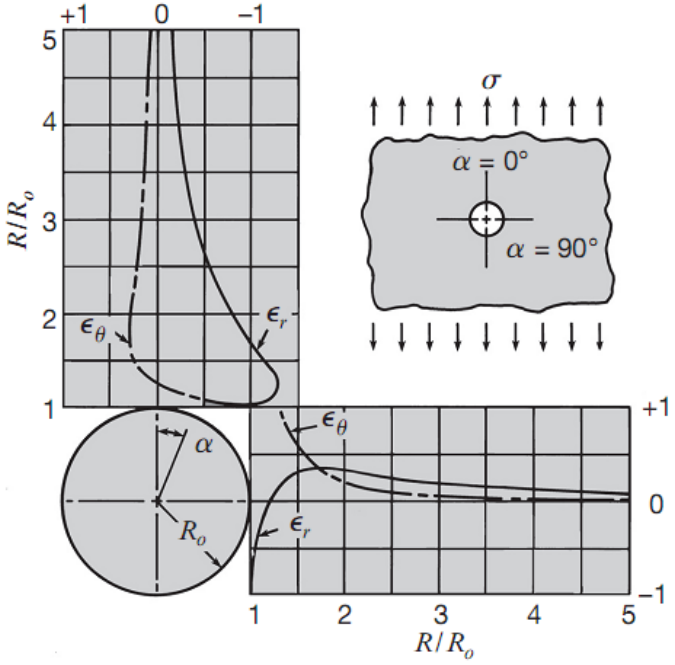

Figure 7.13: The variation of radial (ϵ_r) and tangential (ϵ_θ) strains around a drilled hole taken from [93].

Figure 7.14 shows the finite element model that is used to calibrate the numerical model. The general purpose finite element software ANSYS [84] is used. The thickness of the plate is $6mm$ and both the width and length of it are $60mm$. The symmetry of the problem is taken into account and only one quarter of the plate is modelled. In the two planes of symmetry and in the planes of the outer face of the plate the axial displacements are constrained as shown in Figure 7.15 and one

of the corner nodes is also supported in the vertical (Z) direction. A linear isotropic steel material is used with standard material property values of $E = 210kN/mm^2$ and $\nu = 0.3$ for Young's modulus and Poisson's ratio, respectively. The plate is subjected to a uniform stress of $100N/mm^2$ in the X direction. Using common finite element techniques this could be achieved either by subjecting the outer face of the plate to a uniformly distributed load or prescribing a constant displacement boundary condition at each node of the face. However, ANSYS also permits the definition of an initial stress state (ISTRESS command [84]) in the model simply by defining the desired stress level in each direction. All the analyses presented in this paper use this initial stress method.

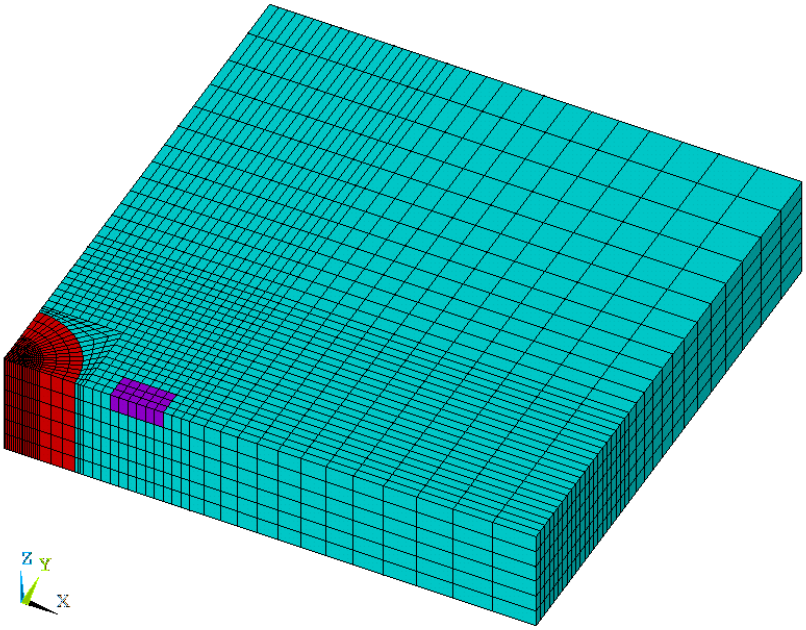

Figure 7.14: The three dimensional finite element model.

The elements highlighted in red, Figure 7.14, represent the hole to be drilled. The radius of the hole is $4mm$. The so called element birth and death technique is used to simulate the drilling process by deactivating ("killing") elements of the hole using the EKILL command of ANSYS [84].

The elements highlighted in purple, Figure 7.14, represent the active grid of the strain gauge. The distance between the edge of the hole and the edge of the grid of the gauge is $2mm$. Figure 7.16 shows the details of the strain gauge used in the

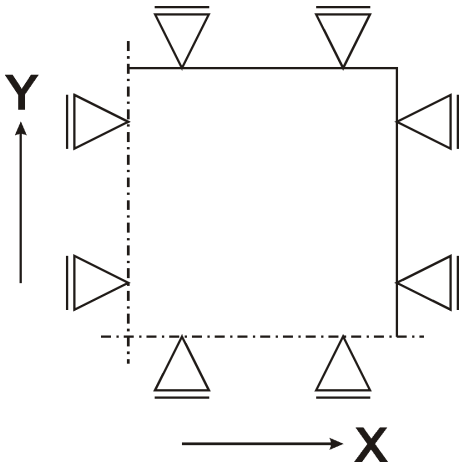

Figure 7.15: Boundary conditions.

measurements and Table 7.2 shows the dimensions of it. The important parameters are the width ($3mm$) and the length ($3mm$) of the active grid. The strain value that the gauge provides does not correspond to a discrete point but it is an average value of the strain field over the active grid area of the gauge [94]. Therefore the numerical model also needs to include the exact geometry of the active grid of the gauge in order to calculate the average strain over the area. In the discussion of the results the term strain gauge is often used to refer only to the active grid of the strain gauge and not to the full carrier.

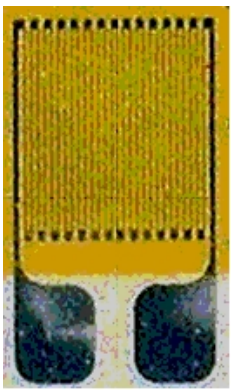

(a) Gauge photo.

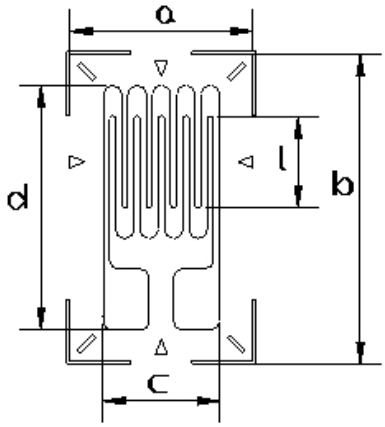

(b) Gauge dimensions.

Figure 7.16: Uniaxial strain gauge KMT-LIAS-06-3-3505E manufactured by Kaliber Ltd. [95].

Dimension	Description	mm
a	width of carrier	5
b	length of carrier	8
l	active length of grid	3
c	width of grid	3
d	full length of grid	6

Table 7.2: Strain gauge dimensions [95].

A sensitivity study of the finite element model is performed by analysing the following parameters of the model:

- the mesh density (element size),
- the plate size, and
- the number of drilling steps.

Four different meshes are studied as shown in Figure 7.17. The length of the active grid of the gauge is $3mm$ and the element sizes to be studied are chosen to result in 2, 4, 6 and 10 elements along the length of the grid.

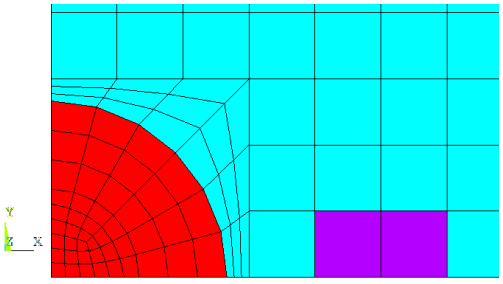

(a) Element size: $1.50mm$.

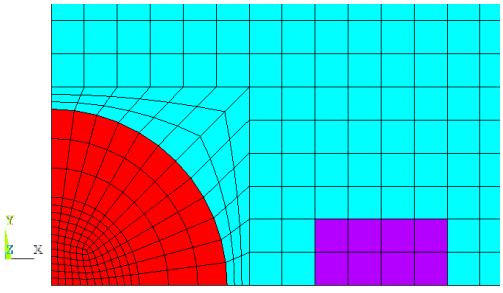

(b) Element size: $0.75mm$.

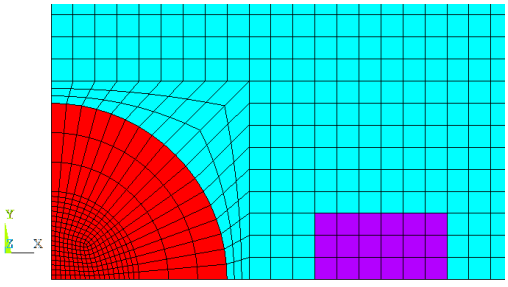

(c) Element size: $0.50mm$.

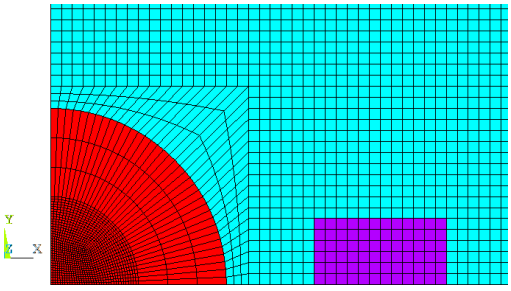

(d) Element size: $0.25mm$.

Figure 7.17: Details of mesh near the hole and the strain gauge.

Figure 7.18 shows the comparison of the analytical result (solid line) with the finite element analyses using different element sizes. The two vertical dashed lines at $6mm$ and $9mm$ represent the position of the active grid of the strain gauge. It can be seen that the numerical results are very close to the analytical one but slightly underestimate it. To be able to judge better the effect of the mesh density, Figure 7.19 shows the same results but only between the edge of the hole ($4mm$) and the far end of the strain gauge ($9mm$). Even though within the strain gauge area the results are practically identical, relatively large differences can be observed near the edge of the hole. Therefore the finite element mesh using elements of $0.5mm$ in length, as shown in Figure 7.17(c), are used in the rest of the numerical analyses.

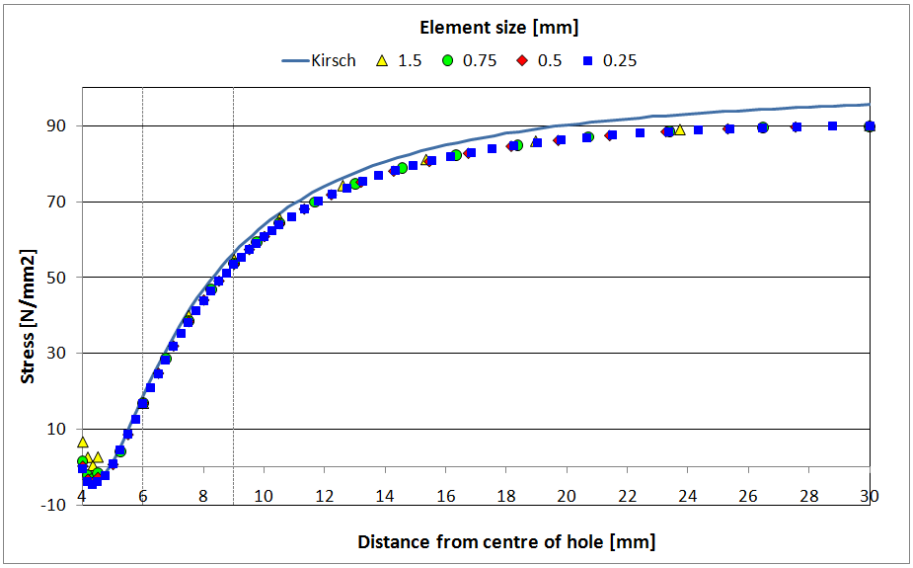

Figure 7.18: Effect of element size on the calculated stresses (full length of plate).

To make sure that the underestimation of stresses observed in Figures 7.18 and 7.19 are not caused by any modelling error the same calculations using the selected element size ($0.5mm$) are repeated with different plate sizes. Since the analytical solution assumes an infinite thin plate increasing the size of the plate should result in better agreement between the numerical and analytical stress distribution. Plate sizes of $40mm$, $60mm$, $80mm$, $120mm$ and $200mm$ with the same thickness ($6mm$) and boundary conditions are studied. Figure 7.20 shows that increasing the plate size moves the numerical results significantly closer to the analytical ones. This demonstrates that the numerical model is capable of reproducing the analytical

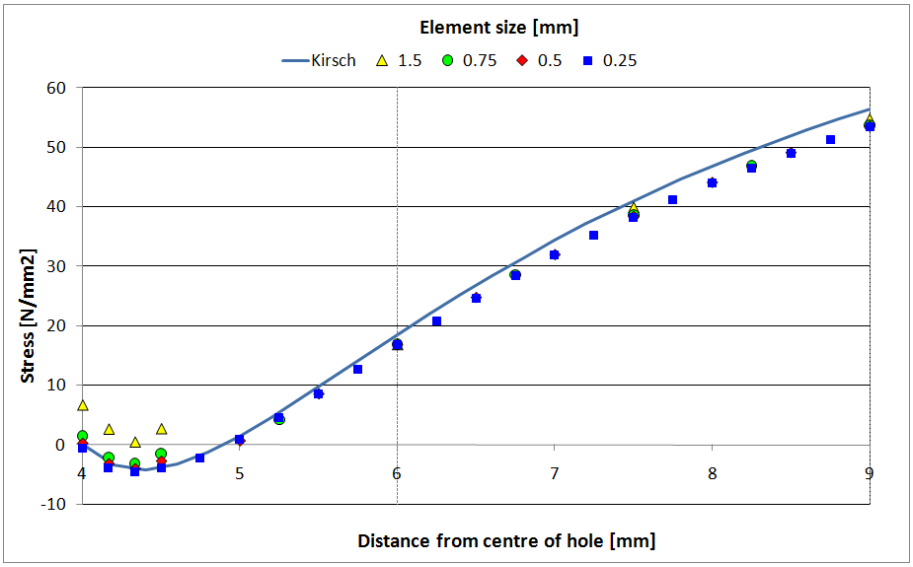

Figure 7.19: Effect of element size on the calculated stresses (zone of the strain gauge).

solution. However, the sensitivity analysis of the model can be performed on models of any size therefore there is no need to repeat the above analysis on the effect of the element size and the following study of the drilling steps can also be performed with the model based on the plate size of $60mm$.

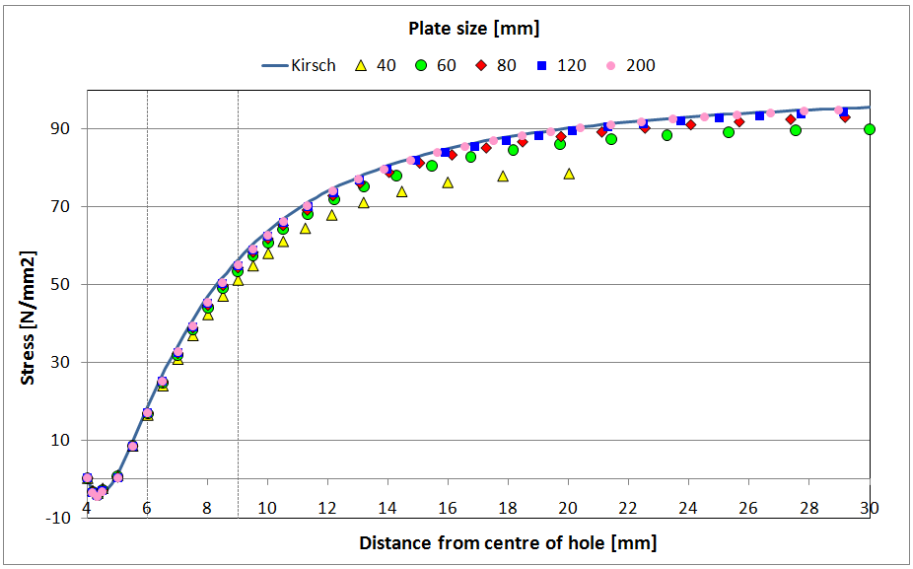

Figure 7.20: Effect of plate size on the calculated stresses.

Until now the element size along the thickness of the plate has not been mentioned. This is because this is studied together with the number of drilling steps.

In reality when a hole is being drilled into the plate the process takes a few seconds. In the numerical analysis this progression of the drilling can be taken into account by deactivating the elements of the hole layer by layer instead of deactivating all of them together. The drilling steps and the element size along the plate thickness are not independent. Table 7.3 shows the summary of all the different combinations of drilling steps and number of elements.

Number of steps	1	1	1	1	1	1	2	2	2
Elements per step	2	4	6	8	10	12	1	2	3
Total elements	2	4	6	8	10	12	2	4	6
Element size	3.00	1.50	1.00	0.75	0.60	0.50	3.00	1.50	1.00
Number of steps	3	4	6	8	10	12			
Elements per step	2	1	1	1	1	1			
Total elements	6	4	6	8	10	12			
Element size	1.00	1.50	1.00	0.75	0.60	0.50			

Table 7.3: The cases of drilling steps studied.

Unlike in the previous two studies, the results of the numerical analyses is not compared to the analytical solution but the average stresses calculated over the area of the active grid of the strain gauge are compared to each other. The average stress is calculated from the average strain by multiplying it by the Young's modulus. The average strain is obtained from the weighted average of strain values at the nodes of the active grid of the gauge. Figure 7.21 shows the elements and nodes of the active grid of the gauge and the weights associated with the nodes. Since the area of the elements is the same the weights follow a simple pattern:

- corner nodes: 0.25,
- edge nodes: 0.50, and
- internal nodes: 1.00.

The average stresses are calculated for every case listed in Table 7.3 and are displayed in Figure 7.22. The differences among the cases enclosed by the red box are within 0.021%. Clearly there is no advantage in reducing the element size beyond $1mm$, *i.e.* increasing the element number within the thickness of the plate beyond

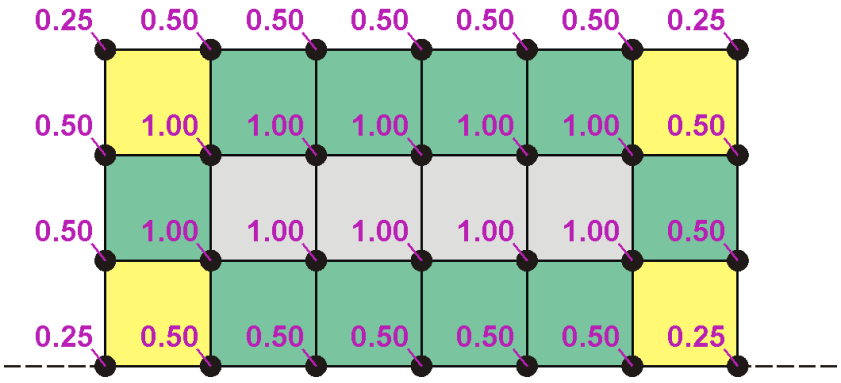

Figure 7.21: Weights at the nodes of the active grid of the gauge.

six elements. The points marked with green circles correspond to the four cases with an element size of $1mm$ but with a different number of drilling steps. The fact that the stress values of these four cases are identical indicates that once the element size is fixed the number of drilling steps has no influence on the results.

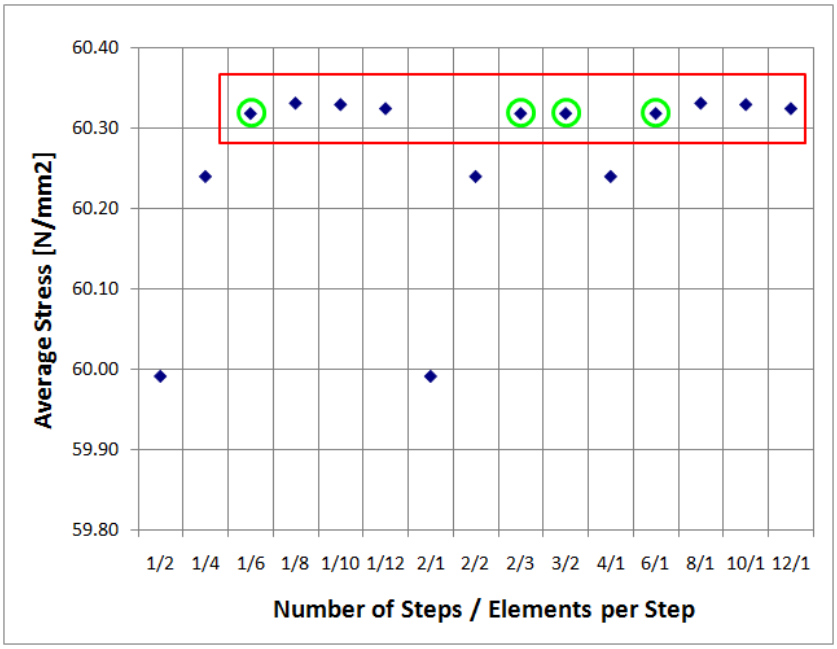

Figure 7.22: Effect of the number of elements and drilling steps on the average stress over the area of the active grid of the strain gauge.

Based on these results a new finite element model is built to study further the residual stress measurements of this project. The following parameters are used in the work presented in the next sections:

- element size in the zone of the gauge: $0.5mm$,

- number of elements along the thickness of the plate: 6, and
- number of drilling steps: 1.

In Section 7.3.3 the twelve actual measurements are reproduced numerically to determine how the experimental residual stress values need to be corrected to compensate for the inaccuracies in the execution of the measurements. In Section 7.3.4 a parametric study is presented to evaluate the overall effects of inaccuracies in the execution of the measurement technique used in this research and to develop a general calibration method for future measurements of this type.

7.3.3 Numerical simulation of the actual measurements

The inaccuracies in the execution of the measurements have three components that are shown in Figure 7.23. A parametrised numerical model was developed using APDL (ANSYS Parametric Design Language) where these components are defined as variables. This allows the generation of numerical models with the exact same geometry of the holes and gauge as in the actual measurements.

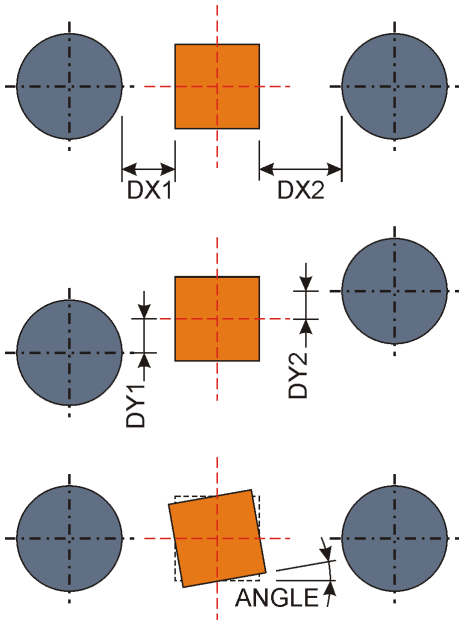

Figure 7.23: Types of inaccuracies.

Two kinds of model are required: one to simulate the measurements near the edge of the plate and one for measurements far from the edge. Examples of each of these two models are shown in Figure 7.24. The length and width of the plate are

60mm and the thickness is 6mm similarly to the initial numerical model presented in the previous section. The thickness of 6mm corresponds to that of the flanges of specimens S1 and S2 (see Table 7.1). Figure 7.25(a) shows a close-up of the zone of the gauge of the model in Figure 7.24(a), which corresponds to the measurements shown in Figure 7.9. The elements highlighted in pink represent the hole and the purple ones represent the active grid of the strain gauge. The elements in red have the same size as the elements of the grid. These elements are included in the model to make sure that the strain values calculated at each node of the active grid, including the nodes on its edge and at its corners, are calculated from elements of the same dimensions.

Figure 7.25(b) shows the image of the same numerical model overlaid on the top of the photograph of the actual measurement. It can be seen that using the image analysis technique explained in Section 7.3.1 to determine the parameters shown in Figure 7.23 can assist in the generation of accurate numerical models. In a similar fashion a numerical model can be prepared for each of the twelve measurements of specimens S1 and S2.

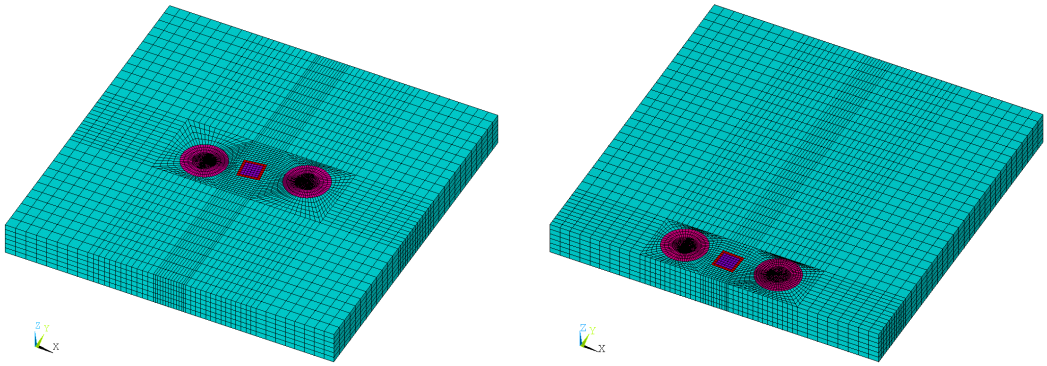

(a) Far from the edge. (b) Near the edge.

Figure 7.24: Finite element model of the actual residual stress measurements.

In the previous section the numerical results are compared with the analytical ones therefore it is necessary to maintain the assumptions of the analytical solution, such as linear behaviour. However, when the actual measurements are simulated numerically the model needs to be more realistic. Therefore in the following calculations large displacements and a bilinear material model with isotropic hardening are also considered. The following non-linear steel properties derived from tensile tests are used:

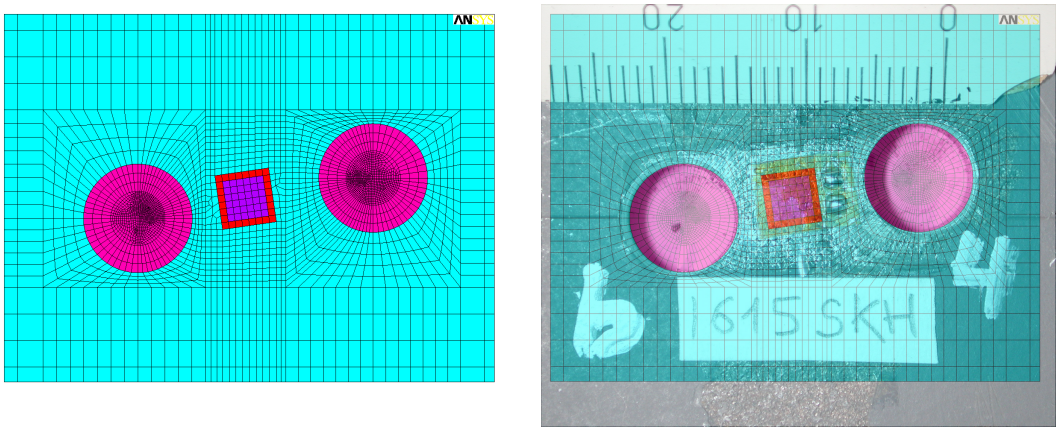

(a) Finite element mesh.

(b) Finite element mesh + photograph.

Figure 7.25: Finite element mesh details and its comparison to the actual measurement.

- yield strength: $f_y = 374N/mm^2$,
- ultimate strength: $f_u = 484N/mm^2$, and
- ultimate strain: $\varepsilon_u = 0.2$.

The boundary conditions of the two types of numerical model are shown in Figure 7.26. For the measurements far from the edge, at the four edges of the plate the axial displacement of the nodes is restricted. For the measurements near the edge, similar restrictions are applied at three of the four edges.

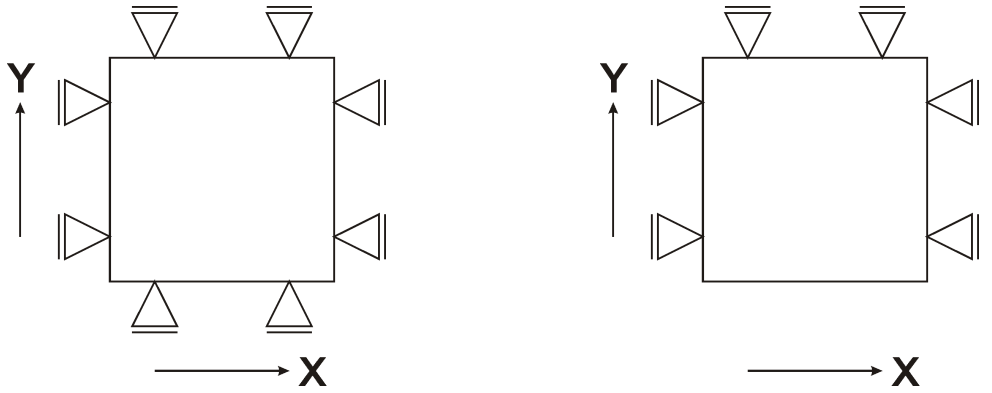

(a) Far from the edge.

(b) Near the edge.

Figure 7.26: Boundary conditions.

The initial stress state of the plate is defined using the ISTRESS command of ANSYS. While the primary interest of this investigation is the longitudinal residual

stresses during the calibration of the measurements, the transverse residual stresses cannot be ignored even if they are only a fraction of the longitudinal ones [18]. The transverse stresses will affect the measurements so several stress states are investigated varying the ratio of the transverse stress (SY) and longitudinal stress (SX) in the range of $SY/SX = 0, 0.25, 0.5, 0.75, 1.0$. The longitudinal stress is maintained constant ($SX = 100N/mm^2$) while the transverse stress is varied from $SY = 0N/mm^2$ to $SY = 100N/mm^2$ in steps of $25N/mm^2$. If this was a linear analysis it would not be necessary to perform calculations with several SY values since with only the results of the case of $SY = 0$ and another case with arbitrary level of SY would be sufficient to extrapolate the effect of the transverse stress to any SY value. Actually, despite the use of non-linear analysis, it is not expected to see significant non-linear behaviour since the stress level of $SX = 100N/mm^2$ is not going to cause any plasticity not even at the perimeter of the holes and the effects of large displacements are not significant either as a result of the boundary conditions on the edges of the plate. Naturally this investigation of the effect of transverse stress is not applied to the measurements near the edge of the plate where the transverse stress is approaching zero. Moreover the actual distribution of transverse residual stresses is such that it exhibits significant values only very near the weld and even those values are just a fraction of the longitudinal stresses [18].

The steps of the analysis are:

- apply initial stress state,
- perform the simulation of the drilling process by deactivating the elements of the holes,
- calculate the weighted average of the strain values at the nodes of the active grid of the strain gauge, and
- calculate the residual stress from the average strain and compare it to the initially applied SX to determine the stress ratio of the measurements.

The weighted average of strains is calculated in the same way as in the previous section (see Figure 7.21) with the only difference that in the present model the full area of the grid is considered as opposed to only half of it.

One example of the results is presented in Figure 7.27 that corresponds to the measurement shown in Figure 7.9. The stress ratio value of 0.77 means that if there

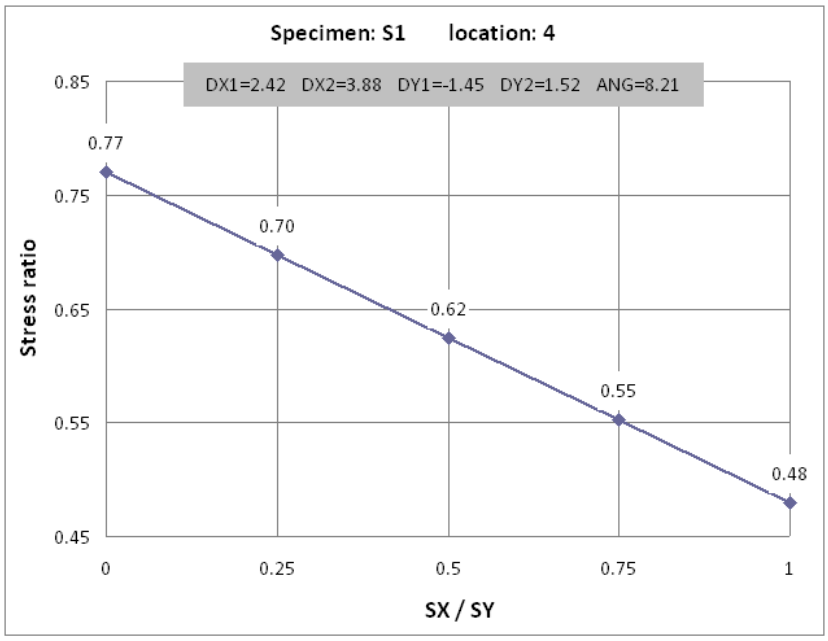

Figure 7.27: Variation of measurement stress ratio with SX/SY.

are no transverse stresses ($SY/SX = 0$) the measurements with the given inaccuracy parameters of $DX1 = 2.42mm$, $DX2 = 3.88mm$, $DY1 = -1.45mm$, $DY2 = 1.52m$ and $ANGLE = 8.21$ (see Figure 7.23) returns 77% of the actual residual stress value. In this case $SX = 100N/mm^2$ is applied to the model and the average stress over the area of the active grid is $77N/mm^2$. The same calculation is repeated for different SY values and the results are shown in the same figure. It can be observed, as it is expected, that there is a linear relationship between the transverse stress and the measurement's stress ratio. This relationship remains linear for any combination of inaccuracy parameters but the slope of the curve depends on those parameters. More details of this are presented in Section 7.3.4.

The same calculation is performed for all the twelve measurements of specimens S1 and S2. Once the stress ratio of each measurement is determined the original measurement results shown in Figure 7.8 can be re-evaluated. The only uncertainty that remains is the value of the transverse stress to be considered at each of the measurement locations. Once the numerical simulation of the fabrication is completed at a later stage of the project, a more exact relationship between the longitudinal and transverse residual stresses can be established for plate girders with a single sided fillet weld and the evaluation of the measurements can be revised. For the moment the general notion of the transverse stresses being significantly lower than

the longitudinal ones [18] are used to evaluate the results. At the measurements nearest to the weld (gauges #3 and #4 in Figure 7.6) it is assumed that the transverse stress level is about 25% of the longitudinal ones, *i.e.* $SY/SX = 0.25$. At the measurements closest to the edge of the flanges (gauges #1 and #6 in Figure 7.6) the transverse stress is assumed to be zero. Since the transverse stress level drops very quickly with the distance from the weld it is probably fair to assume that it is also approaching zero at gauges #2 and #5 in Figure 7.6. Tables 7.4 and 7.5 show the original measurements (see also Figure 7.8), the assumed SY/SX values, the corresponding measurement stress ratios and the corrected residual stress values.

Gauge ID	1	2	3	4	5	6
Orig measurement	-1.73	-23.81	-6.10	38.65	-51.34	-34.53
SY/SX	0	0	0.25	0.25	0	0
Stress Ratio	0.94	0.81	0.74	0.70	0.77	0.94
Corrected measurement	-1.84	-29.49	-8.26	55.41	-67.00	-36.65

Table 7.4: Corrected measurements: Specimen S1.

Gauge ID	1	2	3	4	5	6
Orig measurement	-66.83	-6.67	105.72	94.92	8.73	-20.27
SY/SX	0	0	0.25	0.25	0	0
Stress Ratio	0.87	0.90	0.79	0.75	0.83	0.96
Corrected measurement	-77.03	-7.44	133.07	126.98	10.59	-21.18

Table 7.5: Corrected measurements: Specimen S2.

Figures 7.28 and 7.29 show how the measurement stress ratios change the original measurement results for specimens S1 and S2, respectively.

Figure 7.30 shows the comparison of the corrected residual stress values for the two specimens. While the tendency is not changed relative to the comparison of the original measurement values shown in Figure 7.8, the difference between the residual stress levels is more pronounced. The highest value of the measured longitudinal residual stress in the girder with a double sided fillet weld (S2) is 2.4 times larger than in the girder with single a sided fillet weld (S1) which seems a very significant difference. Nevertheless it does not mean that there is such a big difference in

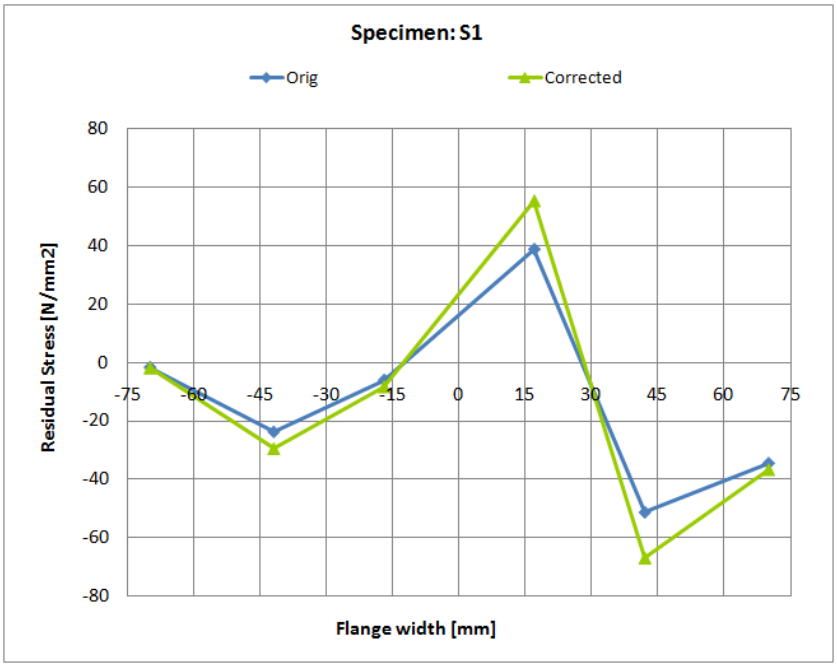

Figure 7.28: Original and corrected residual stress measurements: Specimen S1.

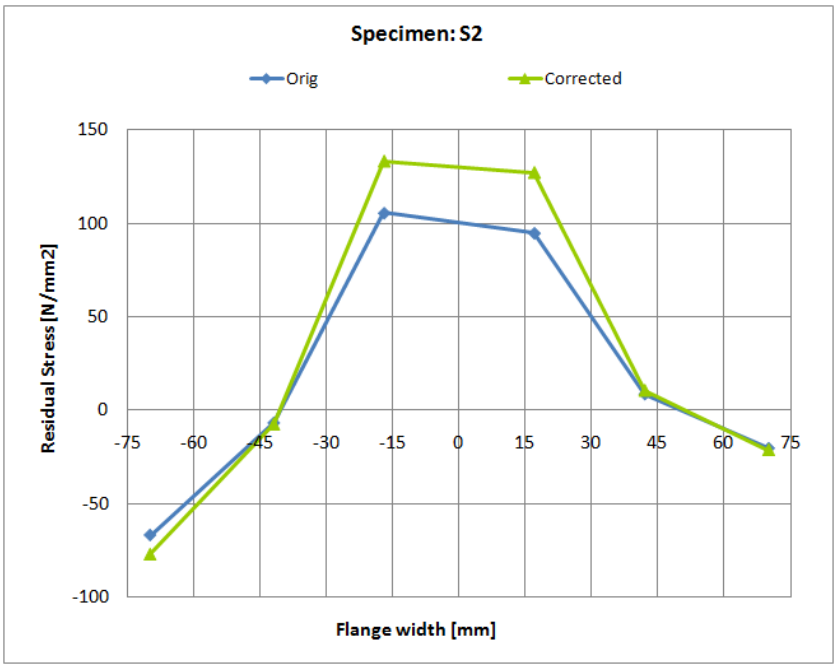

Figure 7.29: Original and corrected residual stress measurements: Specimen S2.

the maximum residual stress values of the two specimens. In fact the maximum values are probably of the same order and they are around the yield strength of

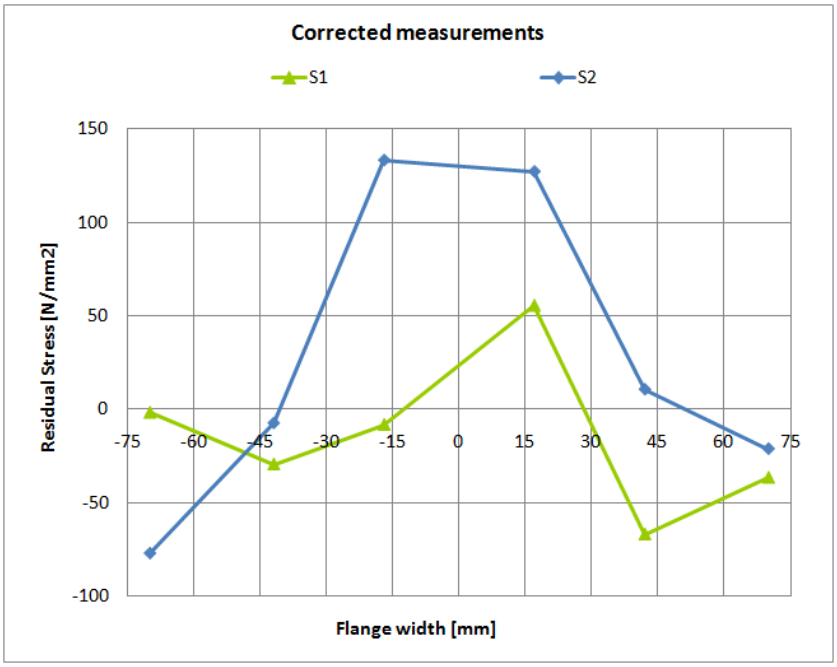

Figure 7.30: Comparison of corrected residual stress measurements for specimens S1 and S2.

the material. Figure 7.31 shows the same results as Figure 7.30 with a hypothetical extension of them between the two measurement locations nearest to the centre of the flange. The two vertical lines represent the edges of the fillet welds on both sides of the web. In the case of specimen S1 only the weld on the right side exists.

The reason for the significant difference in the measurements is that while the measurement locations are the same in both specimens, the zone of high residual stresses is likely to be wider in the specimen with a double-sided fillet weld. The residual stress values change rapidly near the weld which also contributes to the differences in the measurements. While it cannot be said that the residual stress values are much lower if a single-sided fillet weld is used, it is important to point out that the zone affected by high residual stresses is significantly smaller than in a girder with a double-sided fillet weld.

It is demonstrated that generating specific numerical models for every different measurement scenario can be used with great success to determine the errors introduced into the measurements by the inaccuracies in its execution. However, a better understanding of the sensitivity of such measurements can provide a more efficient way of evaluating future measurements based on the same "one-gauge two-hole" methodology. In the next section a detailed investigation concerning the sensitivity

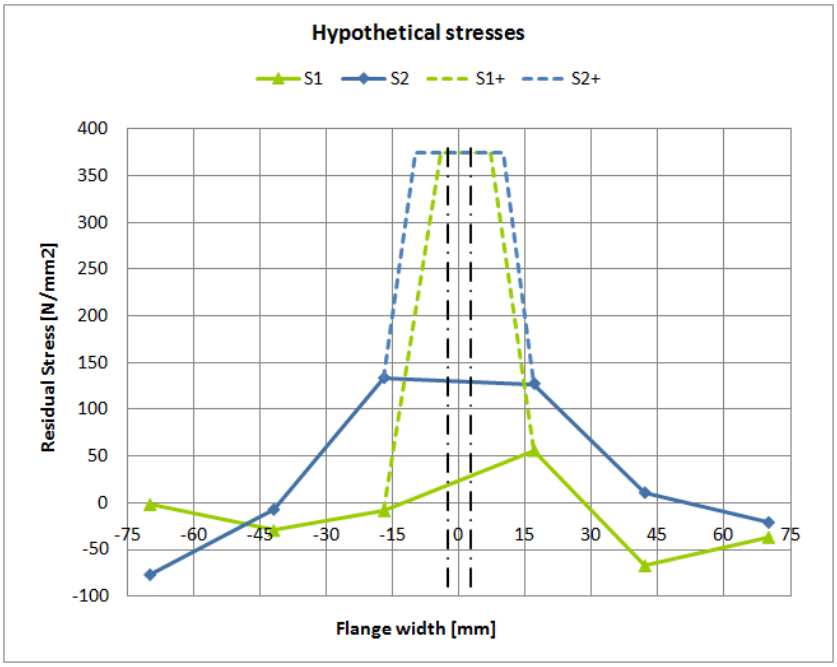

Figure 7.31: Comparison of hypothetical residual stress distributions for specimens S1 and S2.

of this measurement technique is performed in order to develop calibration tables that are easy to use for evaluating residual stress measurements.

7.3.4 A sensitivity study of residual stress measurement

The parameters of inaccuracy are defined in Figure 7.23. The basis for selecting the values of interest for these parameters is the set of actual measurements performed in this project. A summary of the actual eccentricities and rotation angles was presented previously in Figures 7.11 and 7.12, respectively. In Figure 7.11 the numbers in the grey boxes represent the extreme values of DX1 and DX2. In this study the effects of the eccentricity of the two holes (DX1, DX2, DY1 and DY2) and the rotation angle (ANGLE) of the strain gauge are investigated separately. In the first part of the study it is assumed that the rotation angle is zero and only the other parameters vary. Table 7.6 lists the values considered for the inaccuracy parameters.

The range of DX1 and DX2 is not the same as a result of the design of the strain gauge. The active grid of the strain gauge is not located at the centre of the carrier as shown in Figure 7.16 therefore the position of the two holes cannot be symmetric

DX1 [mm]	DX2 [mm]	DY1 [mm]	DY2 [mm]
1,2,3	3,4,5	0,0.75,1.5	-1.5,-0.75,0,0.75,1.5

Table 7.6: Inaccuracy parameter ranges (ANGLE=0°).

when they are close to the gauge. Fortunately the symmetry of the model in the transverse direction can be taken into account and therefore there is no need to analyse the full range $\pm 1.5mm$ for both DY1 and DY2 parameters. For one of them it is sufficient to include only half of the range. Altogether there are $3x3x3x5 = 135$ cases for every SY/SX ratio. The longitudinal stress is kept at $SX = 100N/mm^2$ and several SY/SX ratios are studied: 0, 0.25, 0.5, 0.75 and 1.0.

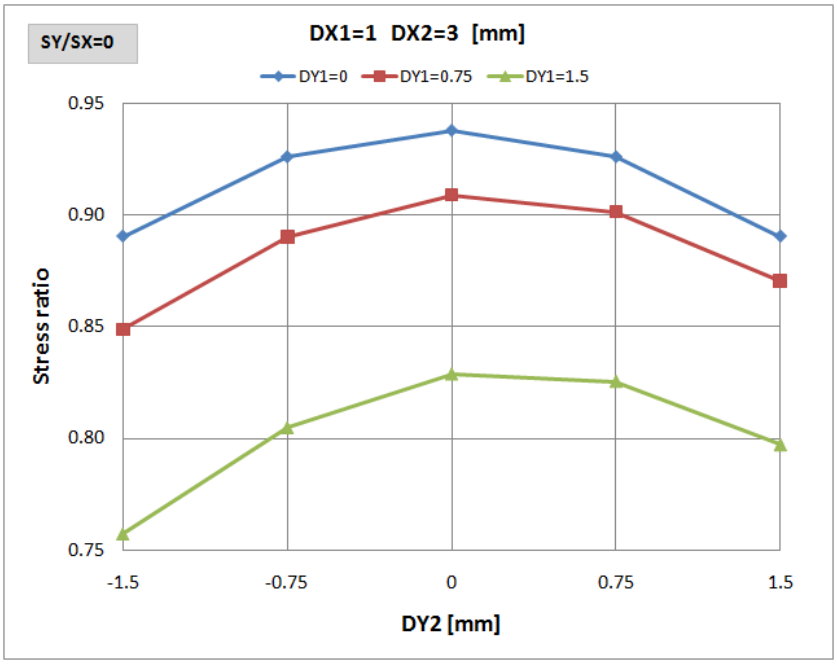

Figure 7.32: Inaccuracy sensitivity of the stress ratio: DX1 and DX2 are constant, DY1 and DY2 are variable.

Figure 7.32 shows a typical set of results. It demonstrates how much influence the transverse eccentricity (DY1 and DY2) has on the readings of the strain gauge. In order to better understand the full extent of the influence of these parameters the envelope of the results is presented in Figure 7.33. The curve on the top contains the highest value of measurement stress ratios while the bottom curve contains the lowest. The highest value (0.94) corresponds to the case when the holes are located closest to the strain gauge in the axial direction ($DX1 = 1$ and $DX2 = 3$) and in the

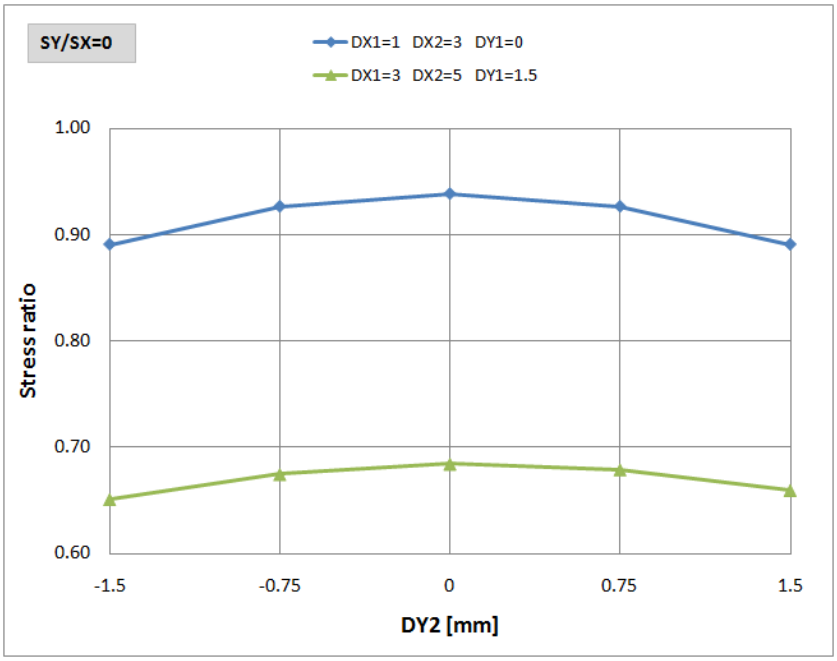

Figure 7.33: Envelope of the inaccuracy sensitivity of the stress ratio.

transverse direction the holes are perfectly aligned with the strain gauge ($DY1 = 0$ and $DY2 = 0$). The high stress ratio means that as a result of drilling the two holes a high percentage of the residual stress has been relaxed. Figure 7.34 shows the stress field over the area of the active grid of the gauge after the drilling. The original $SX = 100N/mm^2$ has been reduced significantly which shows how effective this method can be to relax stresses.

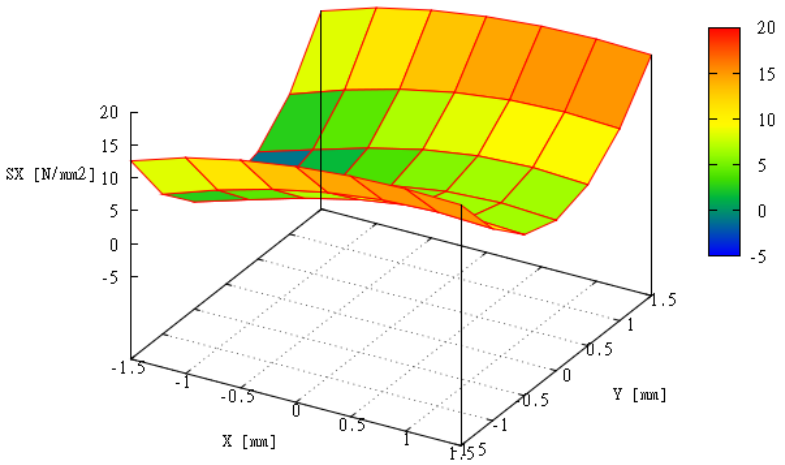

Figure 7.34: Stress field after drilling: max stress relaxation.

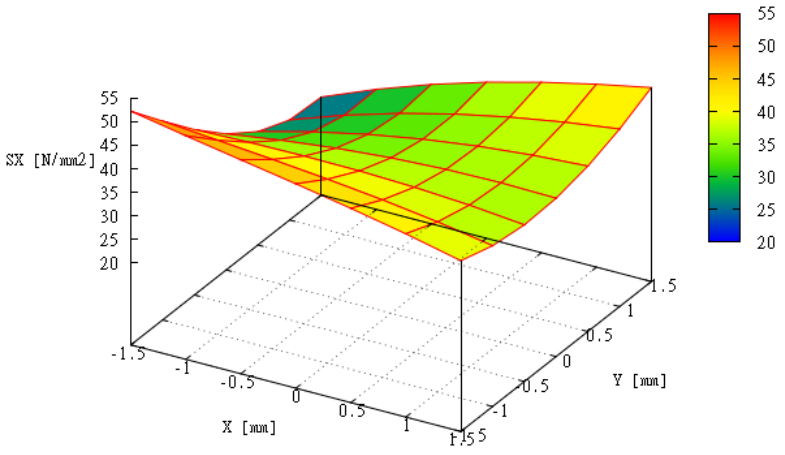

Figure 7.35: Stress field after drilling: min stress relaxation.

The lowest value (0.65) corresponds to the case when the holes are located furthest from the strain gauge in the axial direction ($DX1 = 3$ and $DX2 = 5$) and in the transverse direction the two holes are located on the opposite sides of the strain gauge ($DY1 = 1.5$ and $DY2 = -1.5$). Figure 7.35 shows the stress field over the area of the active grid of the gauge after the drilling. The original $SX = 100N/mm^2$ has been reduced to a much lesser extent which demonstrates how important the accuracy of the execution of the measurements can be.

Instead of using a large number of graphs, such as the one in Figure 7.32, the results of the complete study can be summarised in the table shown in Figure 7.36.

The first four columns correspond to the inaccuracy parameters shown in Figure 7.23. The SX_Ratio is the measurement ratio that corresponds to the combination of the inaccuracy parameters in the same row. The strain gauge reading needs to be divided by the SX_Ratio to obtain the real value of the measured axial stress (SX). The last column (SY_Slope) shows the influence of the transverse stress SY.

The same 135 cases are analysed with different levels of SY/SX. As seen in the numerical analysis of the actual measurements in the previous section, the influence of the transverse stress level is linear. After analysing the results of all the cases only two of them are shown in Figure 7.37: the one influenced most by SY (the line with higher slope) and the one that is the least influenced by SY (the line with lower slope).

The variation of the measurement stress ratio with the transverse stress is the

DX1	DX2	DY1	DY2	SX_Ratio	SY_Slope
1.00	3.00	0.00	-1.50	0.890	0.259
1.00	3.00	0.00	-0.75	0.926	0.284
1.00	3.00	0.00	0.00	0.938	0.293
1.00	3.00	0.00	0.75	0.926	0.284
1.00	3.00	0.00	1.50	0.890	0.259
1.00	3.00	0.75	-1.50	0.849	0.238
1.00	3.00	0.75	-0.75	0.890	0.265
1.00	3.00	0.75	0.00	0.909	0.277
1.00	3.00	0.75	0.75	0.901	0.270
1.00	3.00	0.75	1.50	0.870	0.246
1.00	3.00	1.50	-1.50	0.757	0.189
1.00	3.00	1.50	-0.75	0.805	0.220
1.00	3.00	1.50	0.00	0.829	0.233
1.00	3.00	1.50	0.75	0.825	0.228
1.00	3.00	1.50	1.50	0.797	0.205
1.00	4.00	0.00	-1.50	0.871	0.266
1.00	4.00	0.00	-0.75	0.896	0.284
1.00	4.00	0.00	0.00	0.904	0.290
1.00	4.00	0.00	0.75	0.896	0.284
1.00	4.00	0.00	1.50	0.871	0.266
1.00	4.00	0.75	-1.50	0.831	0.245
1.00	4.00	0.75	-0.75	0.860	0.265
1.00	4.00	0.75	0.00	0.874	0.273
1.00	4.00	0.75	0.75	0.869	0.269
1.00	4.00	0.75	1.50	0.848	0.252
1.00	4.00	1.50	-1.50	0.739	0.196
1.00	4.00	1.50	-0.75	0.773	0.218
1.00	4.00	1.50	0.00	0.790	0.229
1.00	4.00	1.50	0.75	0.789	0.225
1.00	4.00	1.50	1.50	0.770	0.209
1.00	5.00	0.00	-1.50	0.852	0.266
1.00	5.00	0.00	-0.75	0.869	0.279
1.00	5.00	0.00	0.00	0.874	0.283
1.00	5.00	0.00	0.75	0.869	0.279
1.00	5.00	0.00	1.50	0.852	0.266
1.00	5.00	0.75	-1.50	0.813	0.245
1.00	5.00	0.75	-0.75	0.834	0.260
1.00	5.00	0.75	0.00	0.843	0.266
1.00	5.00	0.75	0.75	0.841	0.263
1.00	5.00	0.75	1.50	0.826	0.251
1.00	5.00	1.50	-1.50	0.720	0.196
1.00	5.00	1.50	-0.75	0.745	0.212
1.00	5.00	1.50	0.00	0.758	0.220
1.00	5.00	1.50	0.75	0.758	0.218
1.00	5.00	1.50	1.50	0.745	0.207
DX1	DX2	DY1	DY2	SX_Ratio	SY_Slope

DX1	DX2	DY1	DY2	SX_Ratio	SY_Slope
2.00	3.00	0.00	-1.50	0.833	0.296
2.00	3.00	0.00	-0.75	0.872	0.324
2.00	3.00	0.00	0.00	0.885	0.333
2.00	3.00	0.00	0.75	0.872	0.324
2.00	3.00	0.00	1.50	0.833	0.296
2.00	3.00	0.75	-1.50	0.804	0.279
2.00	3.00	0.75	-0.75	0.847	0.308
2.00	3.00	0.75	0.00	0.865	0.319
2.00	3.00	0.75	0.75	0.854	0.311
2.00	3.00	0.75	1.50	0.818	0.284
2.00	3.00	1.50	-1.50	0.738	0.237
2.00	3.00	1.50	-0.75	0.785	0.268
2.00	3.00	1.50	0.00	0.806	0.281
2.00	3.00	1.50	0.75	0.798	0.273
2.00	3.00	1.50	1.50	0.763	0.247
2.00	4.00	0.00	-1.50	0.807	0.300
2.00	4.00	0.00	-0.75	0.835	0.320
2.00	4.00	0.00	0.00	0.843	0.327
2.00	4.00	0.00	0.75	0.835	0.320
2.00	4.00	0.00	1.50	0.807	0.300
2.00	4.00	0.75	-1.50	0.780	0.284
2.00	4.00	0.75	-0.75	0.810	0.305
2.00	4.00	0.75	0.00	0.822	0.313
2.00	4.00	0.75	0.75	0.815	0.306
2.00	4.00	0.75	1.50	0.789	0.287
2.00	4.00	1.50	-1.50	0.713	0.242
2.00	4.00	1.50	-0.75	0.746	0.264
2.00	4.00	1.50	0.00	0.761	0.273
2.00	4.00	1.50	0.75	0.755	0.267
2.00	4.00	1.50	1.50	0.731	0.248
2.00	5.00	0.00	-1.50	0.783	0.298
2.00	5.00	0.00	-0.75	0.802	0.312
2.00	5.00	0.00	0.00	0.808	0.317
2.00	5.00	0.00	0.75	0.802	0.312
2.00	5.00	0.00	1.50	0.783	0.298
2.00	5.00	0.75	-1.50	0.756	0.281
2.00	5.00	0.75	-0.75	0.777	0.296
2.00	5.00	0.75	0.00	0.786	0.302
2.00	5.00	0.75	0.75	0.781	0.298
2.00	5.00	0.75	1.50	0.764	0.284
2.00	5.00	1.50	-1.50	0.688	0.239
2.00	5.00	1.50	-0.75	0.712	0.255
2.00	5.00	1.50	0.00	0.723	0.262
2.00	5.00	1.50	0.75	0.720	0.258
2.00	5.00	1.50	1.50	0.703	0.245
DX1	DX2	DY1	DY2	SX_Ratio	SY_Slope

DX1	DX2	DY1	DY2	SX_Ratio	SY_Slope
3.00	3.00	0.00	-1.50	0.776	0.299
3.00	3.00	0.00	-0.75	0.818	0.328
3.00	3.00	0.00	0.00	0.831	0.338
3.00	3.00	0.00	0.75	0.818	0.328
3.00	3.00	0.00	1.50	0.776	0.299
3.00	3.00	0.75	-1.50	0.757	0.287
3.00	3.00	0.75	-0.75	0.801	0.317
3.00	3.00	0.75	0.00	0.818	0.328
3.00	3.00	0.75	0.75	0.805	0.318
3.00	3.00	0.75	1.50	0.765	0.289
3.00	3.00	1.50	-1.50	0.710	0.255
3.00	3.00	1.50	-0.75	0.757	0.287
3.00	3.00	1.50	0.00	0.776	0.299
3.00	3.00	1.50	0.75	0.765	0.289
3.00	3.00	1.50	1.50	0.726	0.261
3.00	4.00	0.00	-1.50	0.745	0.301
3.00	4.00	0.00	-0.75	0.774	0.322
3.00	4.00	0.00	0.00	0.783	0.329
3.00	4.00	0.00	0.75	0.774	0.322
3.00	4.00	0.00	1.50	0.745	0.301
3.00	4.00	0.75	-1.50	0.726	0.289
3.00	4.00	0.75	-0.75	0.757	0.311
3.00	4.00	0.75	0.00	0.769	0.319
3.00	4.00	0.75	0.75	0.760	0.311
3.00	4.00	0.75	1.50	0.732	0.291
3.00	4.00	1.50	-1.50	0.679	0.257
3.00	4.00	1.50	-0.75	0.712	0.280
3.00	4.00	1.50	0.00	0.726	0.288
3.00	4.00	1.50	0.75	0.718	0.282
3.00	4.00	1.50	1.50	0.691	0.261
3.00	5.00	0.00	-1.50	0.717	0.297
3.00	5.00	0.00	-0.75	0.737	0.312
3.00	5.00	0.00	0.00	0.743	0.317
3.00	5.00	0.00	0.75	0.737	0.312
3.00	5.00	0.00	1.50	0.717	0.297
3.00	5.00	0.75	-1.50	0.698	0.285
3.00	5.00	0.75	-0.75	0.720	0.300
3.00	5.00	0.75	0.00	0.729	0.306
3.00	5.00	0.75	0.75	0.722	0.301
3.00	5.00	0.75	1.50	0.703	0.286
3.00	5.00	1.50	-1.50	0.651	0.253
3.00	5.00	1.50	-0.75	0.674	0.269
3.00	5.00	1.50	0.00	0.684	0.276
3.00	5.00	1.50	0.75	0.679	0.271
3.00	5.00	1.50	1.50	0.659	0.256
DX1	DX2	DY1	DY2	SX_Ratio	SY_Slope

Figure 7.36: Calibration table for residual stress measurement using a strain gauge with an active grid size of $3mm$ and two through-holes with a diameter of $4mm$.

most pronounced when the two holes are arranged in perfect symmetry on the two sides of the strain gauge ($DX1 = 3$, $DX0 = 3$, $DY1 = 0$, $DY0 = 0$). The transverse stress has the least significant influence when the two holes located closest to the strain gauge in the axial direction ($DX1 = 1$ and $DX2 = 3$) and in the transverse direction the two holes are located on the opposite sides of the strain gauge ($DY1 = 1.5$ and $DY2 = -1.5$). The slope of the linear relationship is determined for all the 135 cases and listed in the last column (SY_Slope) of the table shown in Figure 7.36. Using the following equation the SX_Ratio can be

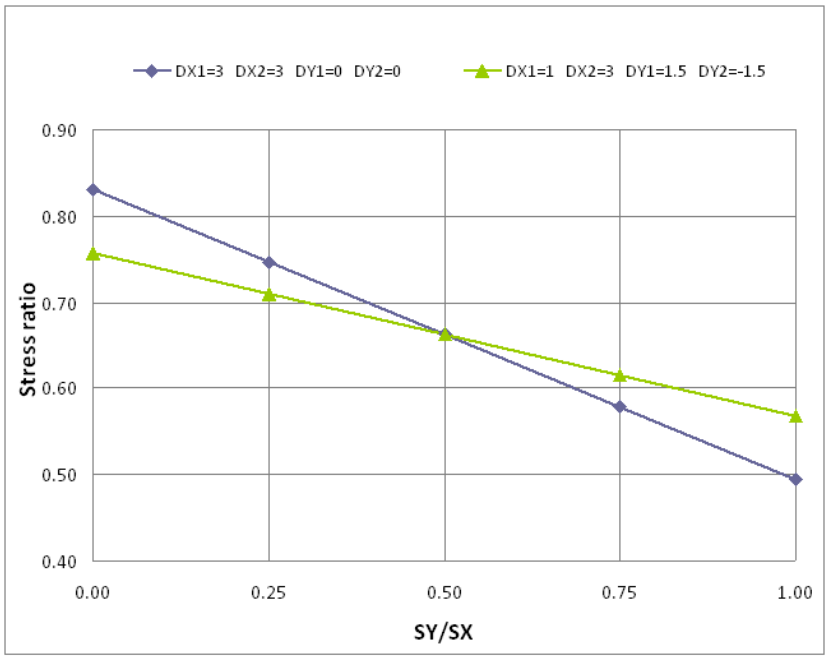

Figure 7.37: Influence of transverse stress (SY) on the stress ratio.

adjusted to any SY/SX value:

$$SX\_Ratio_{SY} = SX\_Ratio - SY\_Slope * (SY/SX) \tag{7.1}$$

To study the effect of not perfectly aligning the strain gauge with the direction of the stress of interest, a reduced set of cases are also analysed. The ANGLE values and the reduced set of the other parameters are listed in Table 7.7. For the rotation angles with one exception all the actual measurements (see Figure 7.12) are covered by the $\pm 5°$ range.

DX1 [mm]	DX2 [mm]	DY1 [mm]	DY2 [mm]	ANGLE [°]
2,3	3,5	0,1.5	-1.5,0,1.5	-5,-3,0,3,5

Table 7.7: Inaccuracy parameter ranges.

Figure 7.38 shows the cases where the holes are perfectly aligned with the gauge in the transverse direction ($DY1 = 0$ and $DY2 = 0$) and only the axial distance is varied (marked with a red box in the legends of the chart). It is clear that independently of the axial distance of the holes, the angle of the gauge has little influence. In the range of $\pm 3°$ and $\pm 5°$ the variation of the stress ratio is within 0.00318

and 0.00915, respectively. Which are equivalent to a variation of $0.318N/mm^2$ and $0.915N/mm^2$ in the case of $SX = 100N/mm^2$.

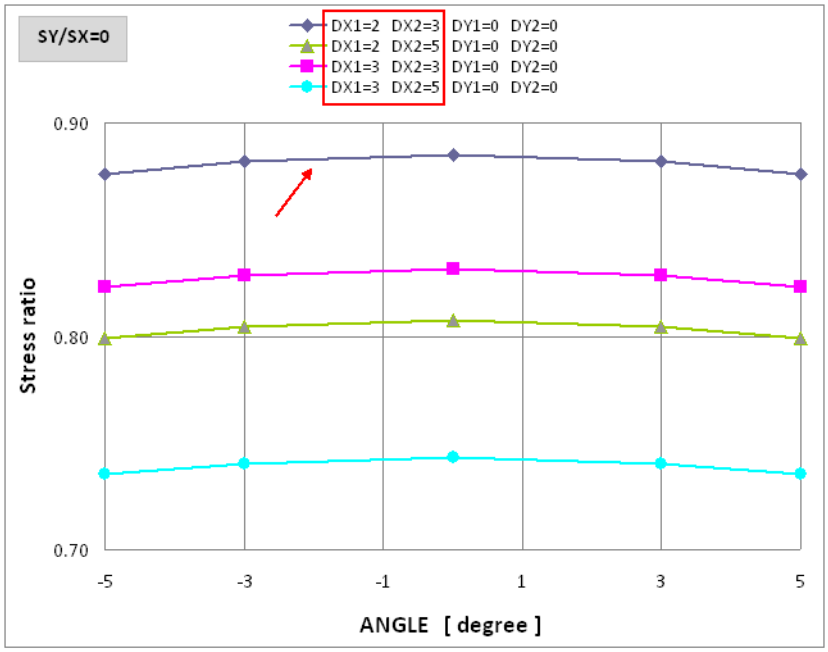

Figure 7.38: Influence of ANGLE on the stress ratio with variable DX1 and DX2, and constant DY1 and DY2.

Figure 7.39 shows the cases where the axial distances of the holes are kept constant ($DX1 = 2$ and $DX2 = 3$) and only the transverse eccentricities are varied (marked with a red box in the legends of the chart). The results show that transverse eccentricity has a very strong influence on how the angle of the gauge affects the stress ratio. The case with the most severe eccentricity ($DY1 = 1.5$ and $DY2 = -1.5$) shows the largest variation with ANGLE. In the range of $\pm 3°$ and $\pm 5°$ the variation of the stress ratio is within 0.03907 and 0.06802, respectively. Which are equivalent to a variation of $3.907N/mm^2$ and $6.802N/mm^2$ in the case of $SX = 100N/mm^2$.

In Figures 7.38 and 7.39 one of the curves is marked with a red arrow. These two cases represent the two extremes: one with the smallest and one with the largest variation with the value of ANGLE. Therefore these two cases are selected to demonstrate how the effect of ANGLE is influenced by the transverse stress (SY) level in the plate. Figures 7.40 and 7.41 demonstrates that the effect of the rotation angle of the strain gauge is not significantly influenced by the transverse stress level. In fact, the higher level of transverse stress slightly reduces the variation in the

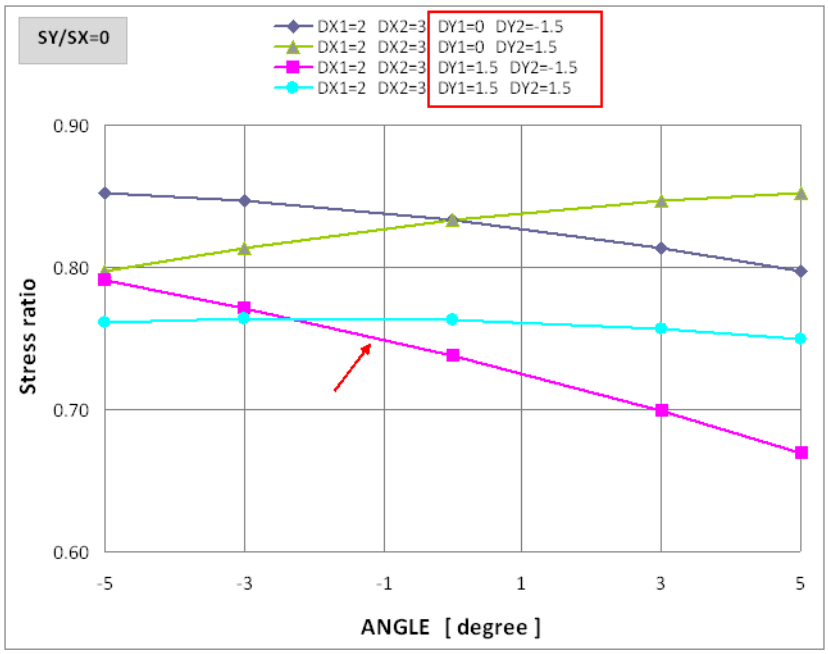

Figure 7.39: Influence of ANGLE on the stress ratio with constant DX1 and DX2, and variable DY1 and DY2.

measurement stress ratio.

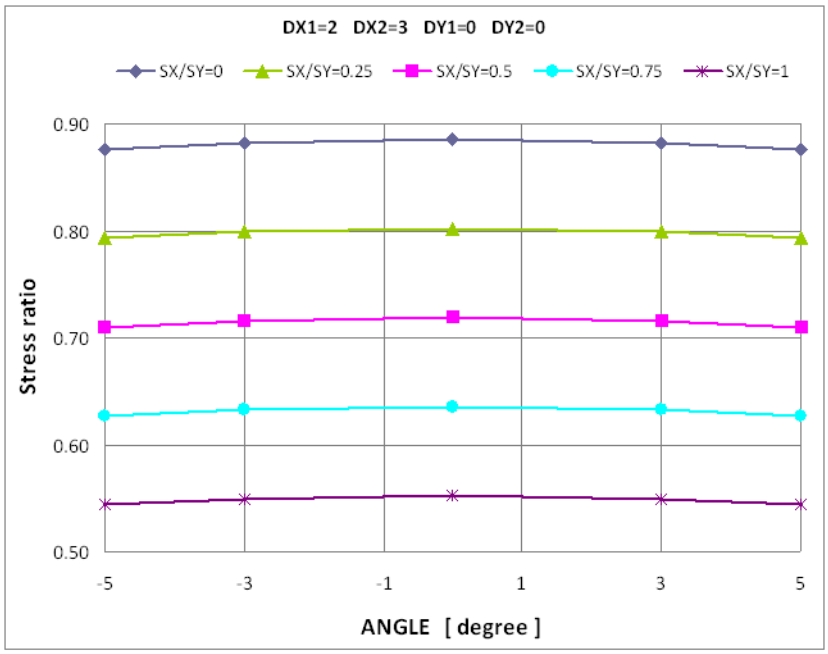

Figure 7.40: Combined effect of ANGLE and transverse stress (SY): no transverse eccentricities ($DY1 = 0$ and $DY2 = 0$).

Clearly the effect of the rotation angle of the strain gauge is highly dependent on

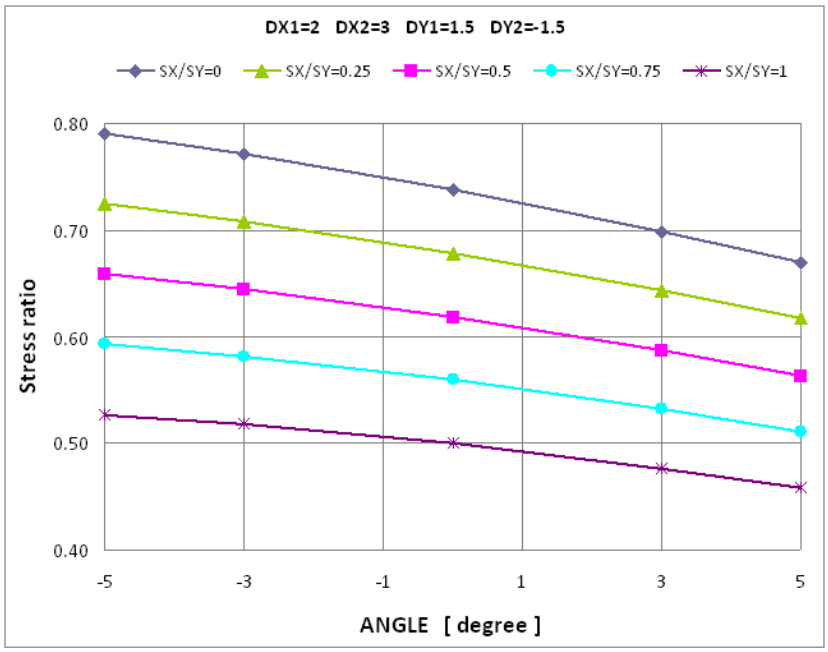

Figure 7.41: Combined effect of ANGLE and transverse stress (SY): severe transverse eccentricities ($DY1 = 1.5$ and $DY2 = -1.5$).

the eccentricity of the two holes. Nevertheless its influence is far less than that of the position of the holes. Considering the zero transverse stress level, the inaccuracies in the positions of the two holes alone can result in a measurement stress ratio as low as 0.65 (see Figure 7.33), *i.e.* a "loss" of $35N/mm^2$ in the case of $SX = 100N/mm^2$. Since in most of the actual measurements of this project the rotational angle did not exceed $\pm 3°$, it can be assumed that with some care in the placement of the strain gauges such an inaccuracy limit can be observed in practice. The results of this study shows that if the rotation angle stays within this limit the maximum variation of the measurement ratio is less than 0.04 ($4N/mm^2$ in the case of $SX = 100N/mm^2$) and it is further reduced by the presence of transverse stresses. Although tables similar to the one shown in Figure 7.36 could be generated for any values of ANGLE if necessary, it is relatively safe to assume that considering only the eccentricities of the holes on both sides of the strain gauge in the evaluation of the readings given by the gauge results in a very good approximation of the actual stress level in the structure under investigation.

7.4 Summary and conclusions

In this chapter it has been shown that the chosen "one-gauge two-hole" technique to measure residual stresses is much easier to execute and less sensitive to inaccuracies than the traditional hole-drilling method using a strain gauge rosette and a blind hole. This permits the use of very simple equipment to execute the measurements and has the additional advantage that it can be used in situations where other methods would be difficult to employ. The same techniques can be used in other applications such as determining stress levels in tension/compression members of existing structures as long as the drilling does not cause significant structural damage. Reducing the hole diameter in order to limit the structural damage would increase the sensibility of the technique to inaccuracies. Nevertheless calibration tables similar to the one presented in Figure 7.36 can be easily developed for different hole diameters and active grid sizes.

The current laboratory measurements of residual stresses are performed on two specimens to compare the longitudinal residual stress distribution in the flanges of plate girders with single-sided and double-sided fillet welds. The simulation of the actual measurements using parametrised finite element models is found to be an efficient method to evaluate and correct the readings of the strain gauges. Both the original and corrected values of the measurements indicate that the fabrication with single-sided fillet welds results in a considerably lower level and a non-symmetric distribution of longitudinal residual stresses at the measurement locations. This indicates that the zone of high residual stresses is much narrower in girders fabricated with single-sided fillet welds.

As a result of further numerical studies of the measurement method calibration tables for different degrees of inaccuracies have been developed. It is demonstrated that an inaccurately placed strain gauge (*i.e.* not perfectly aligned with the direction of the stress of interest) introduces much less error in the measurement than the eccentricities of the two through-holes on the two sides of the gauge.

In the next chapter the thermal stress analysis of welding is discussed in detail.

Chapter 8

Thermal stress analysis of plate girder fabrication

8.1 Introduction

In Chapter 6 the thermal analysis of welding was presented. The next step in the simulation of welding is the thermal stress analysis. In this chapter the details of the numerical model development and a series of studies are presented. Studies conducted on relatively small models are used to demonstrate the capabilities of the numerical model and to investigate how certain parameters affect the development of residual stresses and deformations in a welded plate girder. Finally, the welding simulation of full size plate girders is presented.

8.2 Numerical model

The aim of the thermal stress analysis is to calculate the residual stresses and deformations that develop as a result of the fabrication process (welding).

Using explicit time integration is very efficient even if the welding simulation is treated as a coupled thermomechanical analysis. In fact there are no advantages in doing a decoupled analysis even if the characteristics of welding would permit it because the heat generated by the deformation of the material is negligible compared to the heat input of welding. However, when implicit time integration is used it is advantageous to perform a decoupled analysis.

In Chapter 6 the thermal analysis of welding is studied separately. In a decoupled

thermomechanical analysis the stress analysis is performed after the thermal analysis. They can be performed either in a staggered approach or completely separately. The staggered solution means that after completing one thermal analysis step the corresponding stress analysis step is performed to calculate the deformation of the model. Using this deformation the thermal analysis model is updated and therefore the effect of the deformation is taken into account in the thermal analysis as well even though there is a one load step delay in the process. This is useful when the updated geometry might significantly alter the boundary conditions of the thermal analysis model. This is discussed in Section 6.2 when the interface between the surface of the flange and the end face of the web plate is investigated. As a result of the deformations of the plates the contact conditions between the two plates might change and therefore the nature of heat transfer might also change. However, the studies in Section 6.2 demonstrated that even if perfect contact could develop between the two plates, ignoring this would overestimate the weld surface temperature by less then 10°C. Not only is this relatively small compared to the high range of temperatures of welding but also adjusting the length of the proposed equivalent prismatic heat source model to match the temperature measurement data would compensate for this simplification. Therefore in the present study the thermal and the stress analyses are performed completely separately.

8.2.1 Material properties

The objective of this research is to develop a procedure to simulate the fabrication of welded plate girders that are relatively easy to implement and the necessary input data can be obtained also relatively easily for. Two major difficulties of welding simulation are the modelling of the heat input and the complex material behaviour. For the heat input the temperature measurements devised with this objective in mind were presented in Chapter 5. The methodology is easy to set up and execute in a factory setting and does not disturb the normal fabrication procedures. In Chapter 6 the use of these simple measurements to calibrate the heat source model for the thermal analysis is discussed. Unfortunately no easy to implement solution exists to obtain data that accurately describes the complex material behaviour of steel subjected to welding. The mechanical properties are not only influenced by the changes in temperature but also by the changes in the microstructure of the

material which in turn are also governed by the temperature history.

Only material properties that are directly available in Eurocode 3 (EC3) are used. While the current EC3 does not include any specific information regarding welding and other fabrication processes it does consider material behaviour under fire conditions in Eurocode 3, Part 1-2, EN 1993-1-2: Structural fire design [85]. In the case of the mechanical properties, EC3 defines temperature dependent reduction factors that need to be applied to the corresponding property values at 20°C. Figure 8.1 shows the reduction factors for effective yield strength (k_y), for proportional limit (k_p) and for Young's modulus (k_E). The reduction factors are specified up to 1200°C where they all have a value of zero. In the simulation such zero values would cause numerical problems therefore in the analyses presented here constant non-zero values are considered for the reduction factors at and above 1200°C. These constant values are equal to half of the EC3 values at 1100°C (the curves of Figure 8.1 are the modified ones not the original EC3 curves). Considering constant material properties above a certain cut-off temperature is common practice in computational welding mechanics as explained in Section 6.2. Moreover, if the overall residual stress distribution in the structure is of interest, rather than in the weld and its close vicinity, then a simplified material model also gives satisfactory results [35].

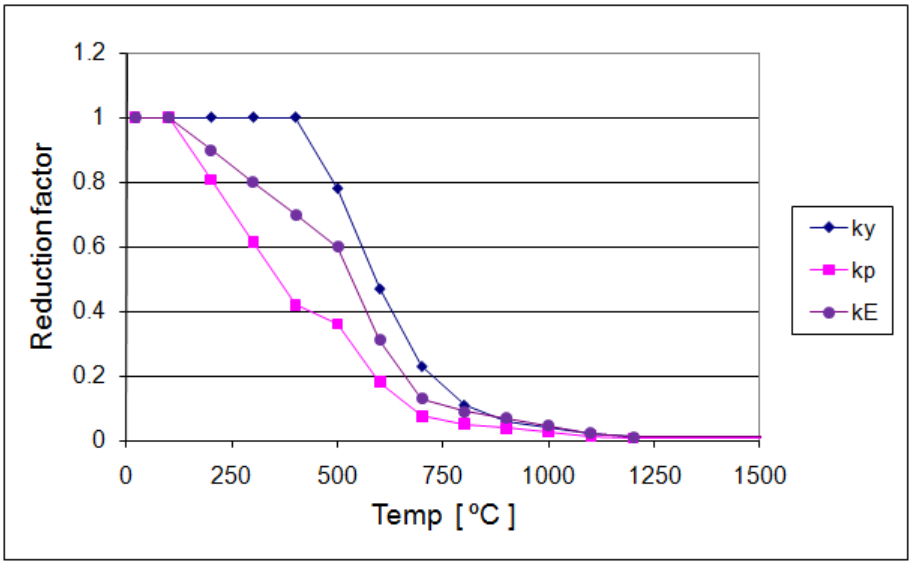

Figure 8.1: EC3: reduction factors for material properties at elevated temperatures.

The stress-strain relationship at elevated temperatures for the S355 material

shown in Figure 8.2 has been calculated using the reduction factors and the formulae given in EC3. EC3 also allows the consideration of strain-hardening below temperatures of 400°C. Figure 8.3 shows the stress-strain relationship at elevated temperatures for S355 material considering strain-hardening as well.

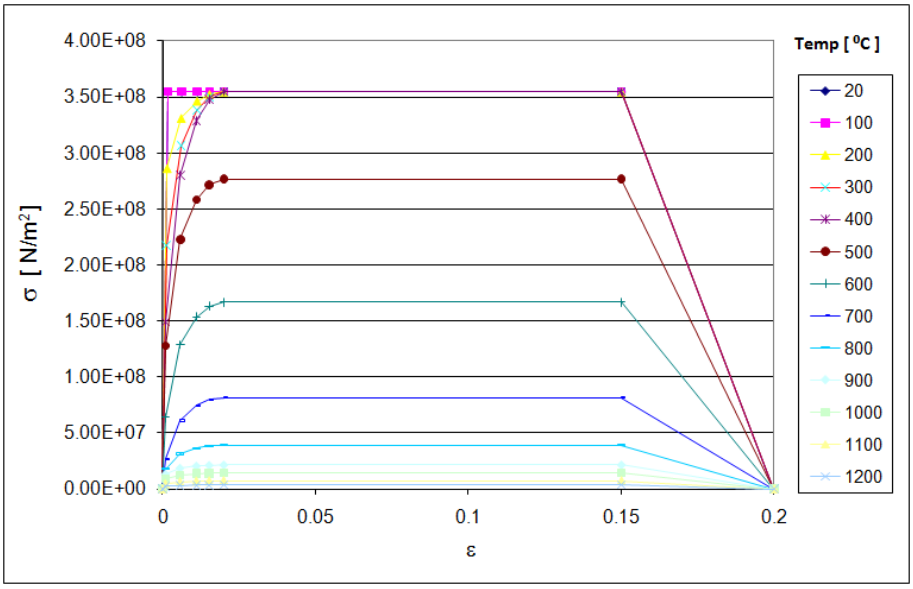

Figure 8.2: Stress-strain relationship of steel S355 without strain hardening.

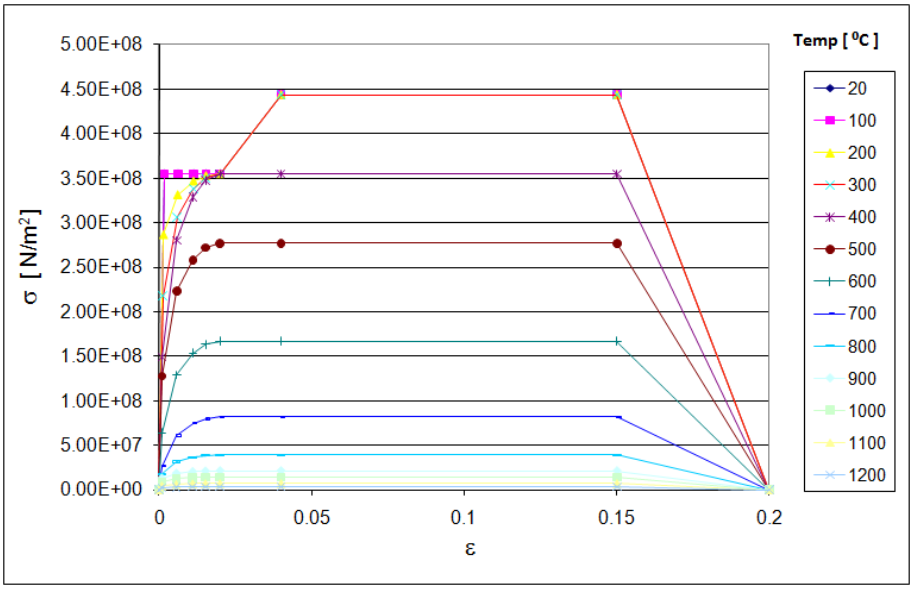

Figure 8.3: Stress-strain relationship of steel S355 with strain hardening.

Tensile tests of the actual materials of the plates used in the fabrication of the specimens have also been performed. The results are shown in Table 2.2 in

Section 2.3.2. Using the actual yield strength of the materials similar stress-strain curves can be calculated (the curves are not shown here) and used in the analyses.

The thermal elongation of steel is shown in Figure 8.4 (the curve is extended to 1500°C considering a constant slope above 1200°C). The use of a single curve assumes that the thermal elongation is the same during heating and cooling. However, as a result of the phase change and the metallurgical changes of the material the thermal elongation during cooling can be different. It is determined by the peak temperature and the cooling rate [87]. There are more advanced thermo-metallurgical-mechanical models that can take this into account by using mixture rules. Each phase has its own temperature dependent material properties defined and by using the mixture rules the macroscopic material properties can be estimated. Nevertheless, the simplest and most common solution is to ignore microstructural changes [86] and use a single curve as shown in Figure 8.4.

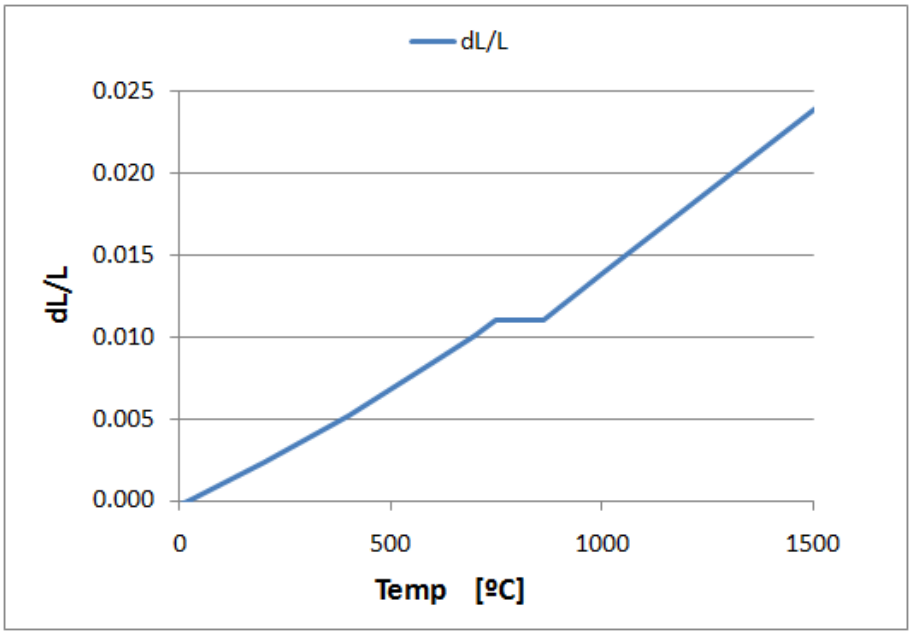

Figure 8.4: EC3: thermal elongation at elevated temperatures.

The density of steel and the Poisson's ratio is considered temperature independent and values of $7850 kg/m^3$ and 0.3, respectively, are used according to EC3.

8.2.2 Rod model

Before the analysis of plate girder can start it is necessary to investigate how ANSYS handles the resetting of plastic strains when the material reaches the melting tem-

perature. It is necessary to follow a more complicated procedure than in ABAQUS where a simple definition of the annealing temperature in the material properties takes care of everything (see Section 4.3 for more details). In ANSYS the same effect can be achieved by using the so called element birth and death technique [84]. When an element is deactivated ("killed" using the EKILL command) and then reactivated ("reborn" using the EALIVE command), the element does not keep a record of strain history. Furthermore it is necessary to redefine the reference temperature of the material properties of the reactivated element otherwise the thermal strains are calculated using the old reference temperature (e.g. room temperature). This can be avoided by specifying the melting temperature as the reference temperature. This results in a stress free state at the melting temperature and the stress in the element increases as the temperature decreases. It is also necessary to activate the large deformation option (NLGEOM,ON command) of the solver to obtain meaningful results.

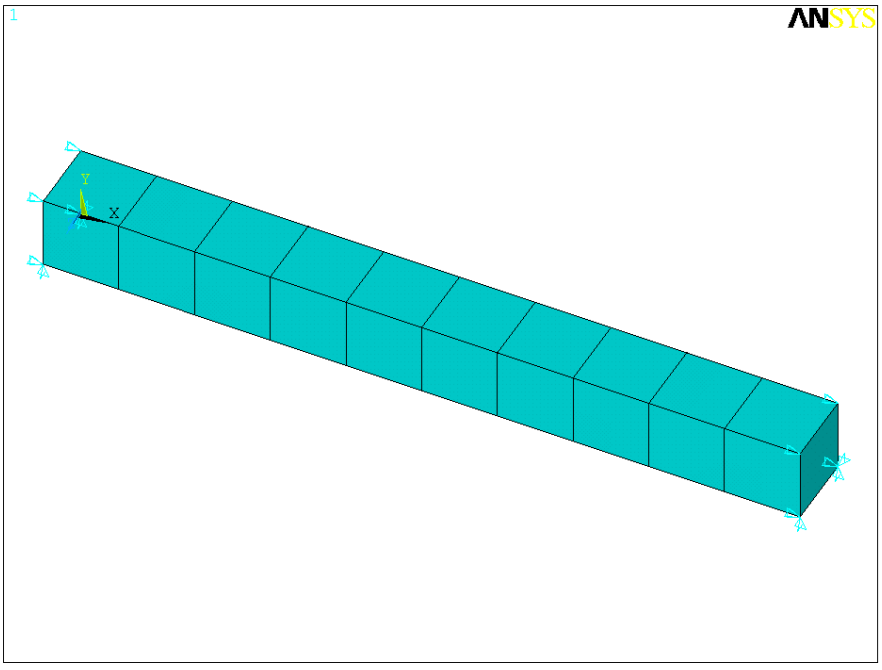

Figure 8.5: Rod model (ANSYS).

Figure 8.5 shows the simple rod model used to demonstrate how plastic strains are affected by the above procedure. The element type is SOLID185 (more information about this element is given in the next section). The boundary conditions do not allow the model to expand in the axial (X) directions but it is free to expand in

the lateral and vertical directions. The temperature of all the nodes are gradually increased to the melting temperature by the end of the first load step (at 1s) and it is gradually decreased to the initial temperature by the end of the second load step (at 2s). The equivalent plastic strain history is shown in Figure 8.6 for the two cases with and without employing the element birth and death procedure. If the reference temperature is not changed to the melting temperature but it is kept at its initial value the plastic strain would immediately jump back to its original level when the elements are reactivated and would follow the blue curve.

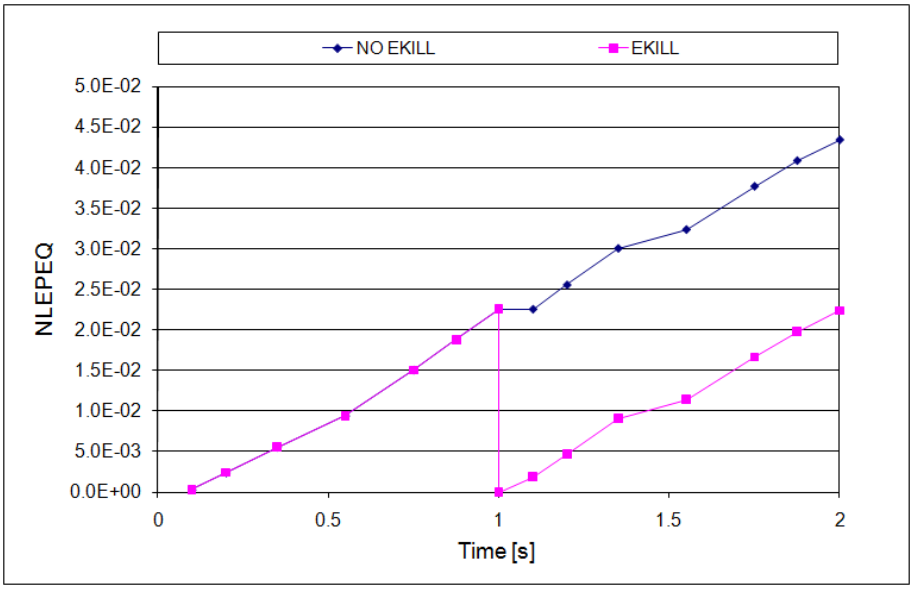

Figure 8.6: Effect of EKILL.

The same procedure is used in the model of the plate girder where the elements of the welding seam are reactivated when the welding heat source passes them. After the reactivation the elements are stress free and they develop residual stresses during cooling.

8.2.3 Plate girder model

The geometry and the mesh of the plate girder model is identical in both the thermal and the stress analyses. Figure 8.7 shows the mesh and the main dimensions of the model (in some of the analyses below different lengths are also considered). The thickness of the flange (vertical plate) and the web (horizontal plate) are $6mm$ and $4mm$, respectively.

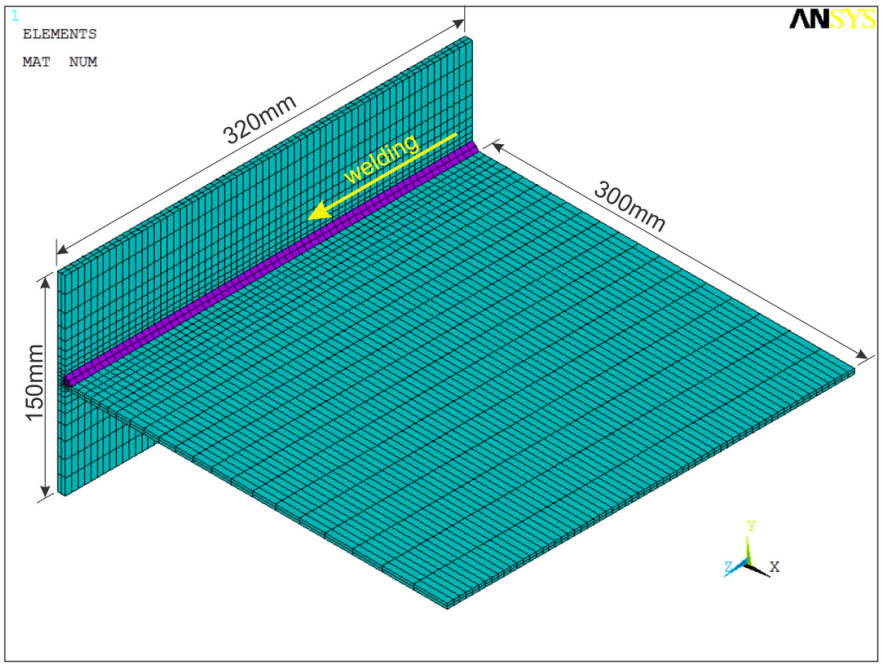

Figure 8.7: Finite element model of the plate girder.

The element type and the boundary conditions need to be changed when switching from the thermal analysis to the stress analysis. The element type employed is SOLID185 element of ANSYS. This is a three dimensional structural solid element with eight nodes and three DOFs at each node. The element permits the use of different element technologies that best suit the analysis. In the present model this element is used with an enhanced strain formulation that prevents volumetric locking in nearly incompressible cases (which is not a concern in this work) and, more importantly, shear locking in bending dominated problems [84]. This formulation uses additional internal DOFs which makes the analysis more computationally expensive than other formulations.

The mechanical boundary conditions are shown in Figure 8.8. As only half of the plate girder is modelled, on the face of the centre of the web symmetry boundary conditions (X direction) are specified. All the nodes of the face of the bottom edge of the flange are supported vertically (Y direction) and at mid length a node at the centre of the flange and at the centre of the web are supported axially (Z direction). In the welding machine there were rollers supporting both the web and the flange plates. The effect of those extra supports is also studied but unless otherwise stated only the supports shown in Figure 8.8 are applied to the model.

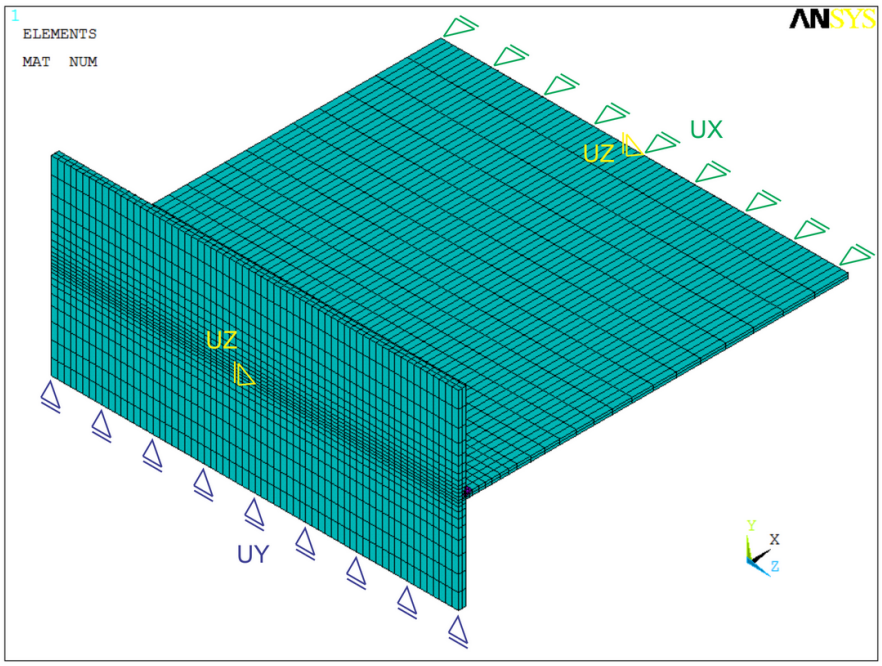

Figure 8.8: Constraints boundary conditions.

Figure 8.9 shows the finite element mesh around the weld. The nodes below the weld seam are not connected but have the same initial position. How this affects the thermal analysis is discussed in Section 6.2 and how the interaction between those nodes are treated in the stress analysis is studied below as it is one of the subjects of the parametric studies of Section 8.3.

The weld seam is divided into three layers. They are shown with different colours in Figure 8.9 along with their ID number. At the end of each welding step when the heat source moves on to its next position the elements of the welds in the preceding section need to be brought alive again (*i.e.* activated). When all the elements of the weld seem are activated at once it leads to convergence problems. To improve the stability of the analysis the weld seam region is divided into three zones or three layers. When it comes to the activation of these elements it is done layer by layer in the order of the numbers shown in Figure 8.9.

Considering the activation of these layers the number of load steps within each welding step is shown in Figure 8.10 (The length of the cells in the figure are not proportional; the length simply implies that load steps 2, 7 and 12 are much longer than the others). The temperature increasing step (brings the temperature of the nodes of the weld seam gradually up to melting temperature) and the temperature

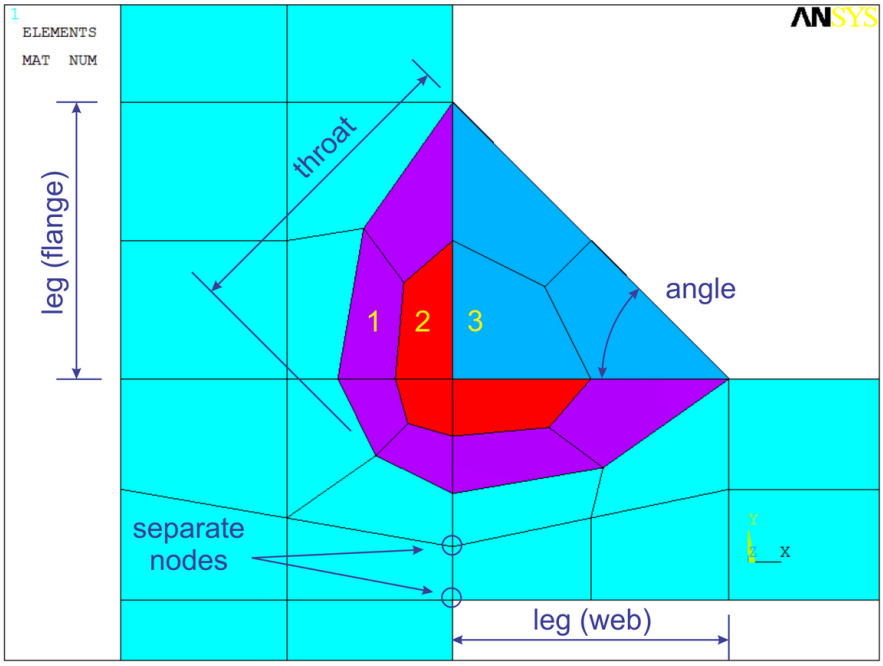

Figure 8.9: Finite element mesh around the weld seam.

maintaining step (maintains the temperature of the nodes of the weld seam at melting temperature) are explained in detail in Section 6.2 and illustrated in Figure 6.6. In the first welding step after the increasing step there are only two maintaining steps because there are no weld seam layers to be activated from the previous welding step. In the second welding step, however, during the temperature maintaining phase of the step three extra load steps need to be included because of the activation of the elements in the three layers of the weld seam of the previous welding step. This brings the total number of load steps to five within the temperature maintaining phase. For this chart it is assumed that there are only three welding steps in total, which makes step three the last welding step. Since there is no need to gradually increase the temperature of the elements of the weld seam of the next welding step there are only four steps in total within the temperature maintaining phase. In total there are always five load steps per welding steps. This is important when the possibility of speeding up the analysis is studied later.

In the next section the results of a series of parametric studies on reduced size models are presented.

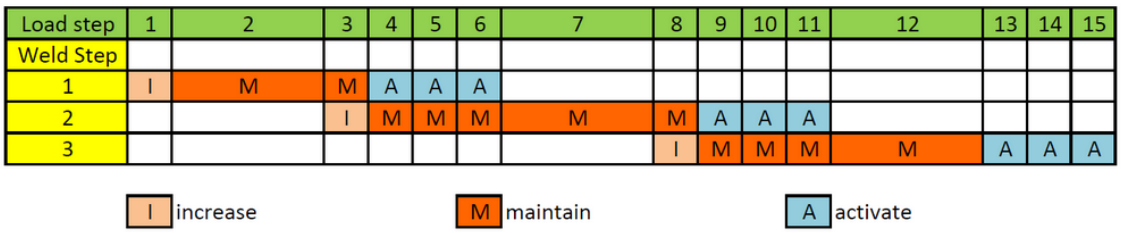

Figure 8.10: Number of loads steps in each welding step.

Parameter / Feature	Range / Characteristic
Length of the model	0.12, 0.20, 0.32, 0.40, 0.52, 0.60 [m]
Gravity	without gravity, with gravity
Contact between plates	no contact, constraint equations, contact
Material models	EC3 properties, measured properties
Angle of weld seam	40°, 45°, 50°
Welding speed	20, 22, 24 [mm/s]
Preheating	without preheating, with preheating
Fully constrained model	–
Length of plate supporting rollers	20, 40, 60, 80 [mm]
Reduction of welding steps	factor of 1, 2, 3, 5, 6, 10, 15, 30
Calibrated heat source models	–

Table 8.1: Parameters and features studied.

8.3 Parametric studies

The aims of the parametric studies are to demonstrate the capabilities of numerical welding simulation based on the proposed equivalent prismatic heat source model and to study the importance of the selected parameters in the development of residual stresses and deformations in a plate girder with single-sided fillet weld. Some of the parameters are the same as the ones already studied in the thermal analysis in Chapter 6 and there are additional ones such as contact between the plates and displacement constraints, among others. Table 8.1 lists the parameters or features studied and their ranges if applicable. Unless otherwise stated the length of the equivalent prismatic heat source is $20mm$ as in the studies of Section 6.2.

The axial and the transverse residual stresses in the flange and the deformations

of the web and the flange of the girder are the primary results to be used in the evaluation of the analyses. Figure 8.11 shows the locations of the paths that are used to present the results. The residual stresses on the top face of the flange are shown along path F1 and FC1. Path FC1 is located at the half length of the model and it is used to show the distribution of residual stresses across the flange. Path F1 is slightly off-centre of the flange (located at 86mm from the lower edge of the flange) and it is used to show the variation of the residual stresses along the length of the girder. The deformations of the flange and the web of the girder are shown along path W1 and F2, respectively. Even though all of these results are calculated for all the cases, only the results that show the influence of the investigated parameter are included here.

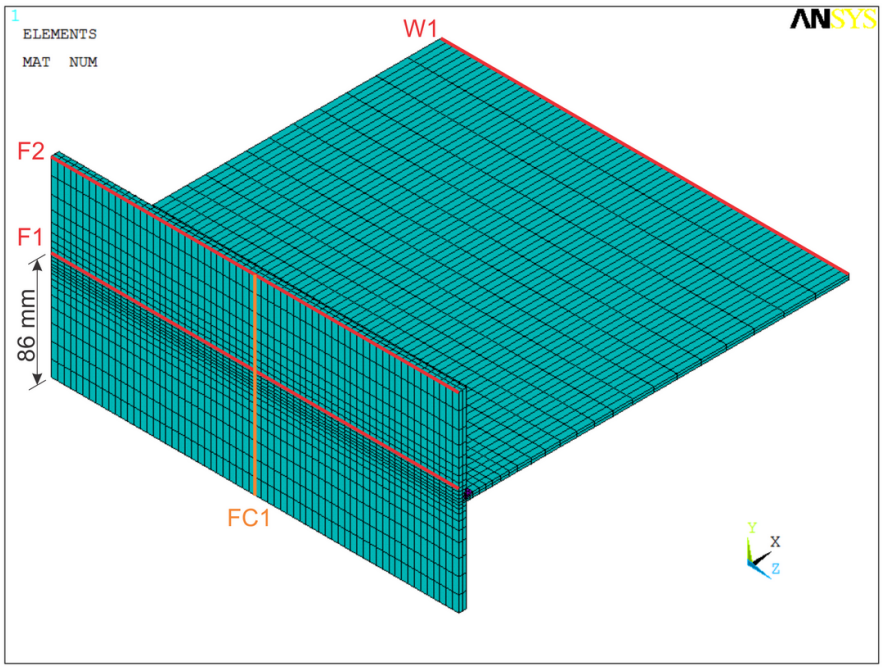

Figure 8.11: Path definitions for post-processing.

In the following sections the results of each parametric study are summarised and evaluated.

8.3.1 Length of the numerical model

A series of analysis is performed on numerical models that are identical in every aspects apart from their total length. The aim is to determine an optimal length for the numerical model that is used in the rest of the parametric studies. Since

the computational cost of these calculations is rather high it is beneficial to reduce the model size as much as possible without significantly influencing the results of interest.

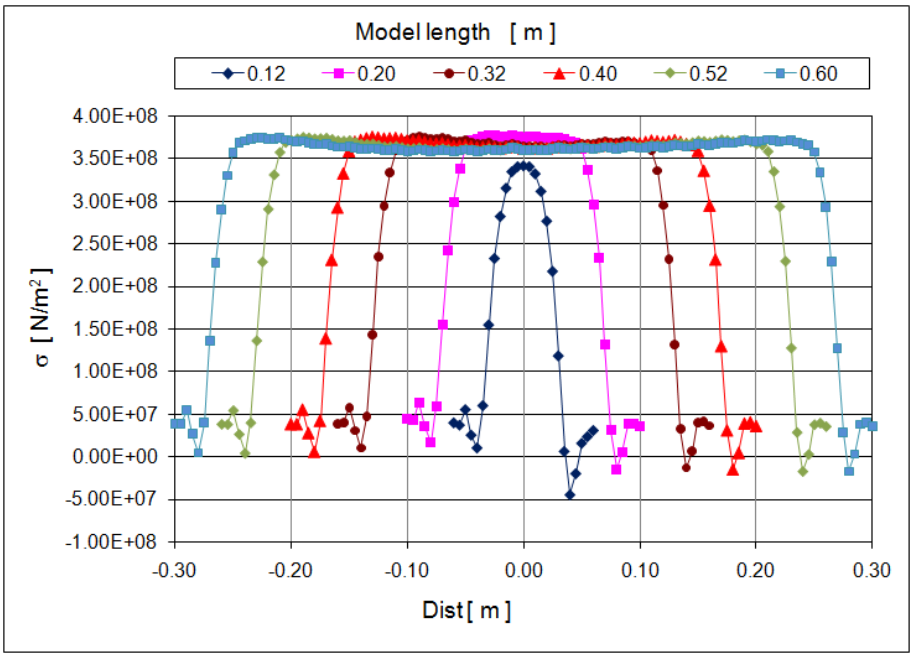

Figure 8.12: Axial residual stress (SZ) along the length of the flange (path F1): effect of the length of the numerical model.

Figures 8.12 and 8.13 show the effect of the length of the model on the axial (SZ) residual stresses on the top surface of the flange along the length of the girder (path F1). The former one shows the full length of the models, while the latter only shows the result near the centre of them to provide a better comparison. The origin of the horizontal axis is positioned at half length of the models. It can be seen that only the two shortest ones (length of $120mm$ and $200mm$) give significantly different residual stress values at the centre of the model. The rest of the models produce results that are very close to each other. This suggests that using a model with a length of $320mm$ is sufficient in order to compare residual stresses at the centre of the model.

Similar conclusion can be drawn from Figure 8.14 that shows the effect of the length of the model on the transverse (SY) residual stresses.

Figures 8.15 and 8.16 show the variation of the axial (SZ) and transverse (SY) residual stresses across the width on the top surface of the flange at the centre of the girder (path FC1), respectively. These results also show that apart from the two

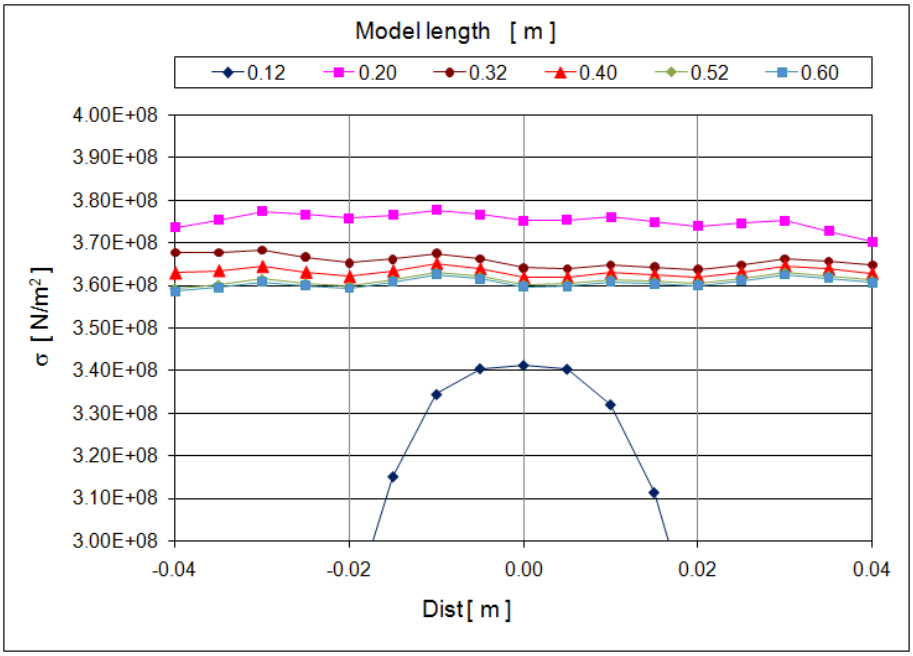

Figure 8.13: Axial residual stress (SZ) along the length of the flange (path F1): effect of the length of the numerical model.

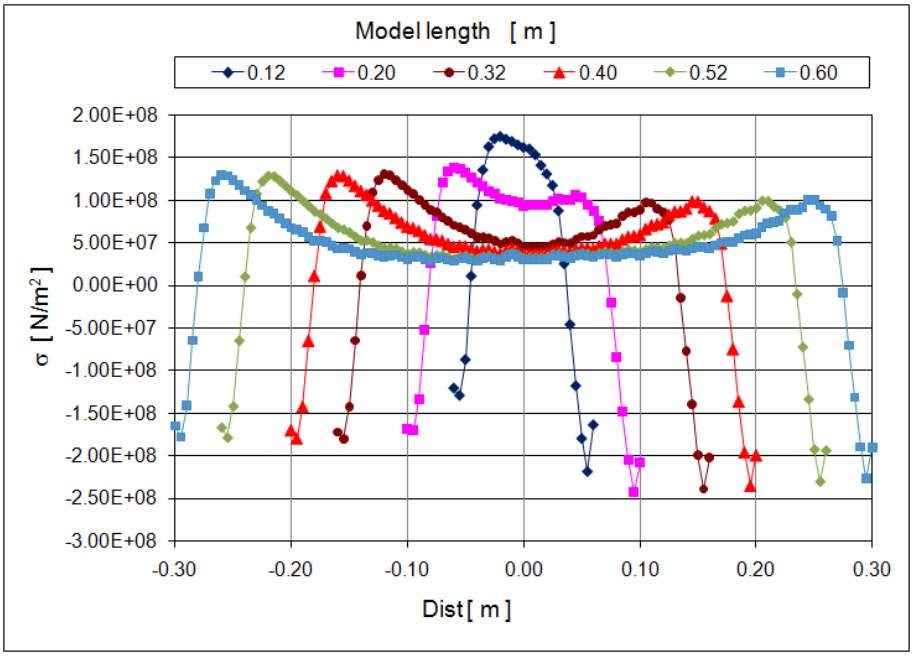

Figure 8.14: Transverse residual stress (SY) along the length of the flange (path F1): effect of the length of the numerical model.

shortest models the rest give very similar residual stress distributions. Figure 8.16 also explains the off-centre location of path F1 shown in Figure 8.11. The transverse

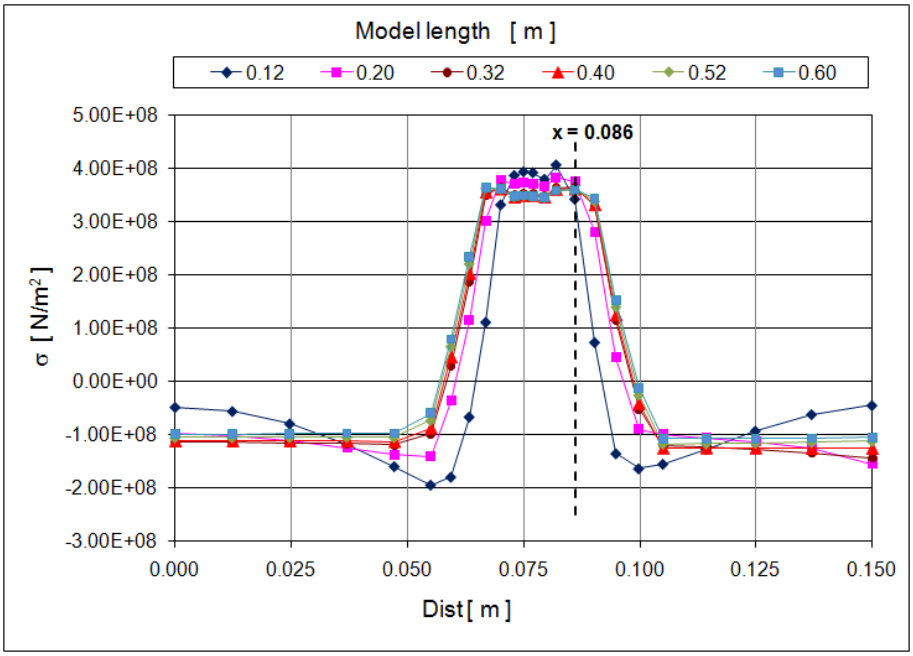

Figure 8.15: Axial residual stress (SZ) across the width of the flange (path FC1): effect of the length of the numerical model. The dashed line represents the location of Path F1.

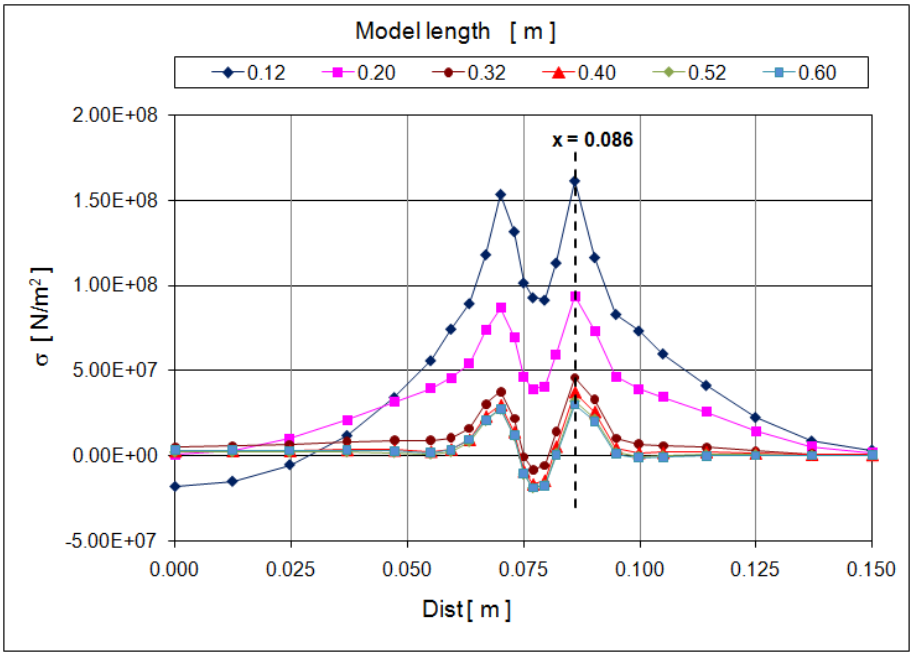

Figure 8.16: Transverse residual stress (SY) across the width of the flange (path FC1): effect of the length of the numerical model. The dashed line represents the location of Path F1.

residual stress (SY) is the highest at this node of the flange cross-section therefore it is better suited to show the variation of stresses along the length of the girder. Figure 8.15 shows that there are little differences in the maximum axial residual stress (SZ) values near the centre of the flange therefore the same location can be used to show the variation of the axial residual stress along the length of the girder (path F1). This also explains why in Figure 8.13 the axial stress in the model with a length of $120mm$ appears much lower. In the case of this model the width of the maximum residual stress zone is narrower than that of the rest of the cases resulting in a lower stress value at the location of path F1 even though its overall maximum stress value is the highest among the studied cases. Again, the only two models that show different values are the two shortest ones.

In Figure 8.16 the transverse residual stresses at the bottom edge of the flange (at 0.0 distance in the chart) are different from zero as a result of the boundary conditions shown in Figure 8.8. However, as long as they remain near zero the assumptions of the boundary conditions are acceptable. Only the case of the shortest model results in relatively high values.

Figures 8.17 and 8.18 show the effect of the length of the model on the vertical deflection (UY) of the centre line of the web (path W1) and the horizontal deflection (UX) of the top edge of the flange (path F2), respectively. The deformations of the flange are similar in all cases but clearly there are very significant differences in the calculated web deformations. It is, however, the combined effect of the length of the model and the self weight of the web which also increases with the length of the model. After eliminating the effect of gravity the deformations of the web are shown in Figures 8.19. The variation of the web deformations is similar to that of the residual stresses: apart from the two shortest cases the rest of the models give the same deformation values near the centre of the girder.

While the effect of gravity cannot be ignored, for the purpose of the present studies it can be assumed that a model with a length of $320mm$ is sufficient to investigate the effects of the chosen parameters on the development of residual stresses and deformations induced by welding. Therefore the majority of the following analyses are performed on models limited to this length.

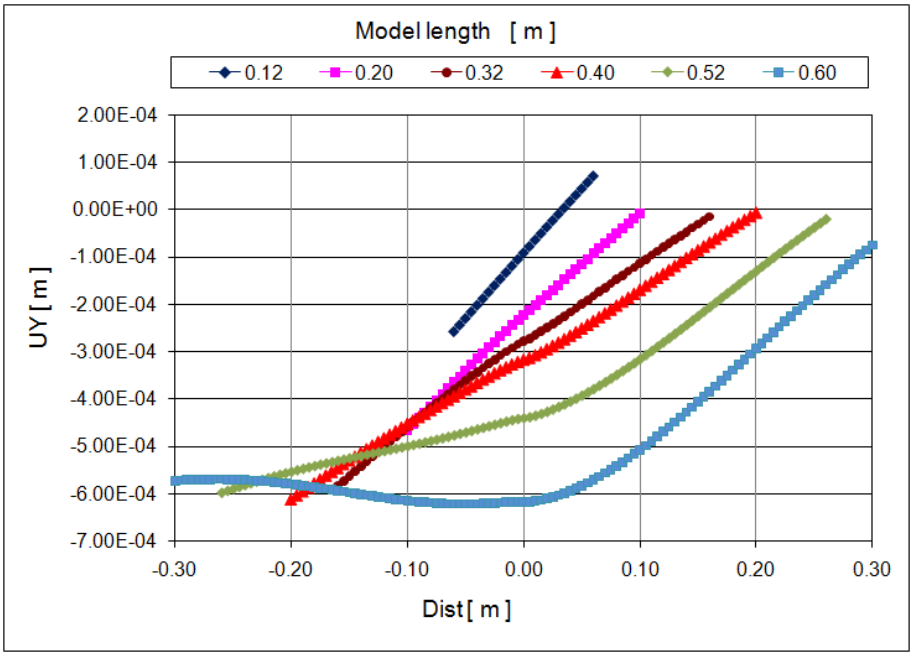

Figure 8.17: Vertical deflection (UY) of the centre line of the web (path W1): effect of the length of the numerical model.

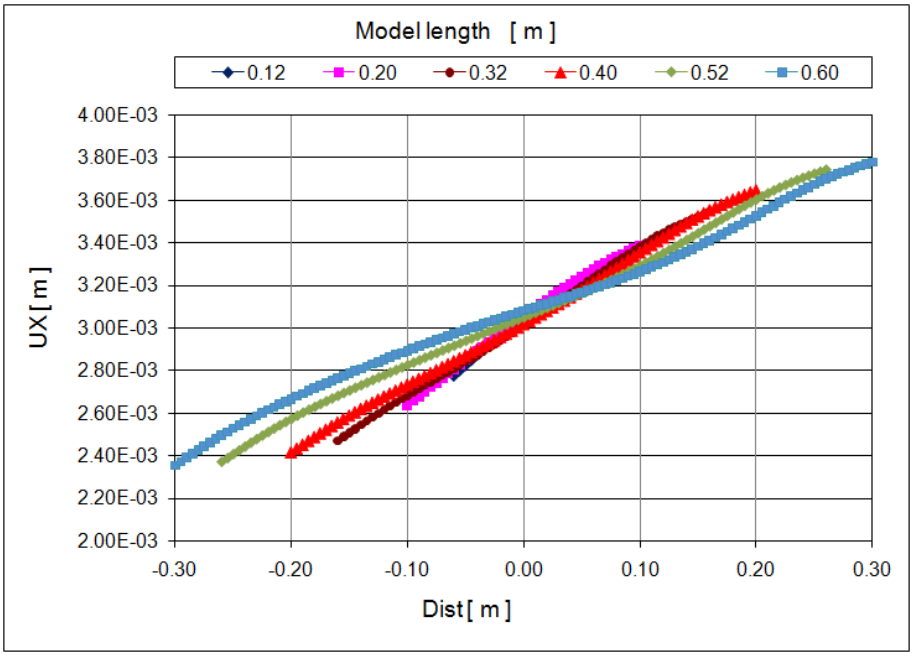

Figure 8.18: Horizontal deflection (UX) of the top edge of the flange (path F2): effect of the length of the numerical model.

8.3.2 Gravity

It has been demonstrated previously that considering gravity in the simulation significantly influences the deflection of the web plates. It is because the position of the

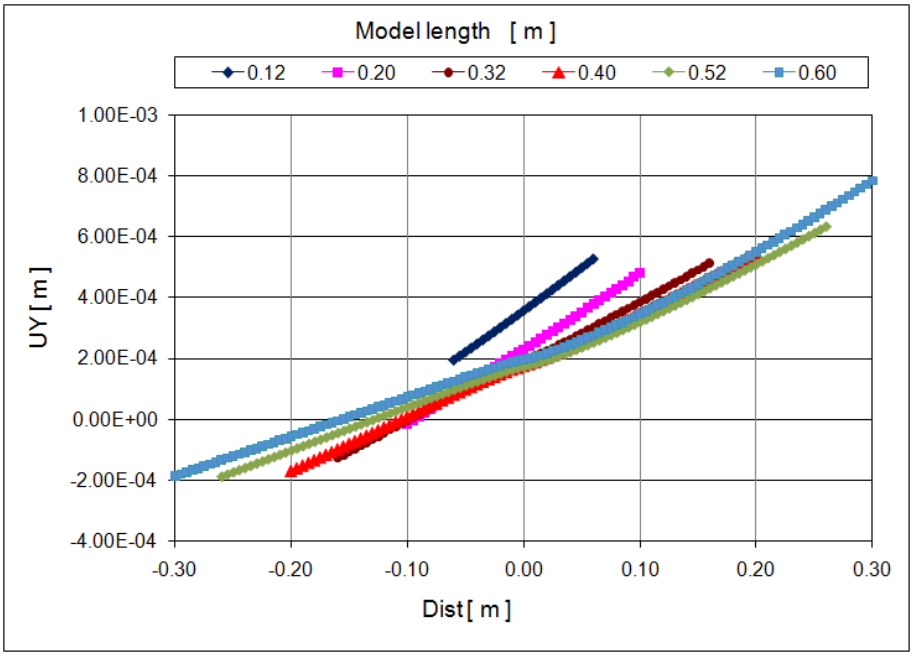

Figure 8.19: Vertical deflection (UY) of the centre line of the web (path W1): effect of the length of the numerical model (without gravity).

girders during the fabrication is such that the web plate is horizontal therefore its self weight produces significant deflections. It is also important to point out that, unless otherwise stated, the models of these parametric studies ignore additional constraints such as the rollers supporting the web and the flange near the welding head (the effects of such constraints are also studied separately). Not including such extra supports of the web further amplifies the deflections produced by the self weight of the structure.

Figure 8.20 shows the effect of gravity on the axial (SZ) residual stresses across the width on the top surface of the flange at the centre of the girder (path FC1). The residual stresses are not influenced by the self weight of the structure. The same can be said about the transverse residual stresses therefore the results are not shown here.

The horizontal deflections of the flange (not shown) are not influenced by the self weight while the web deformations, as expected, are strongly altered by it as shown in Figure 8.21.

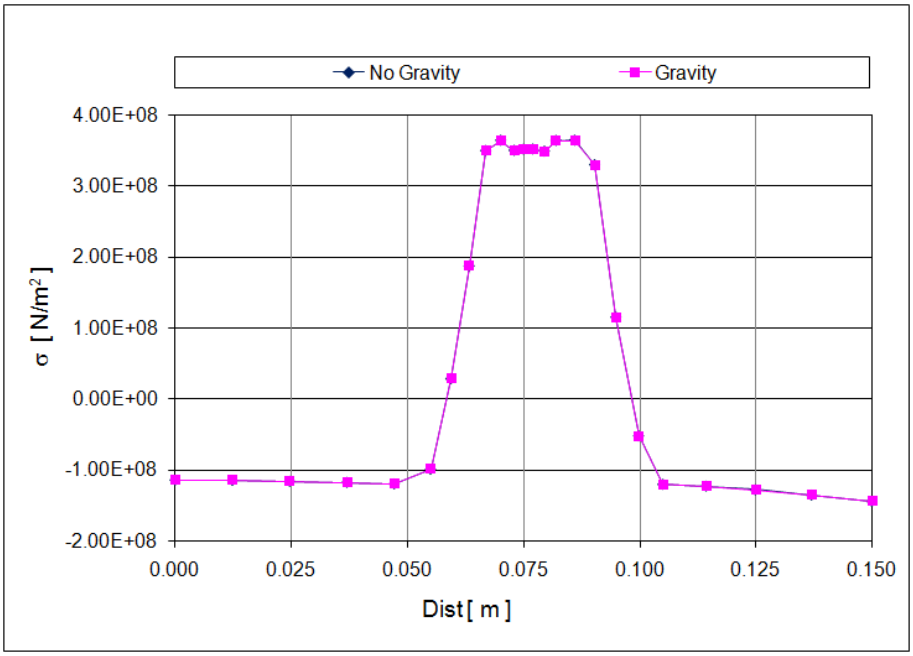

Figure 8.20: Axial residual stress (SZ) across the width of the flange (path FC1): effect of gravity.

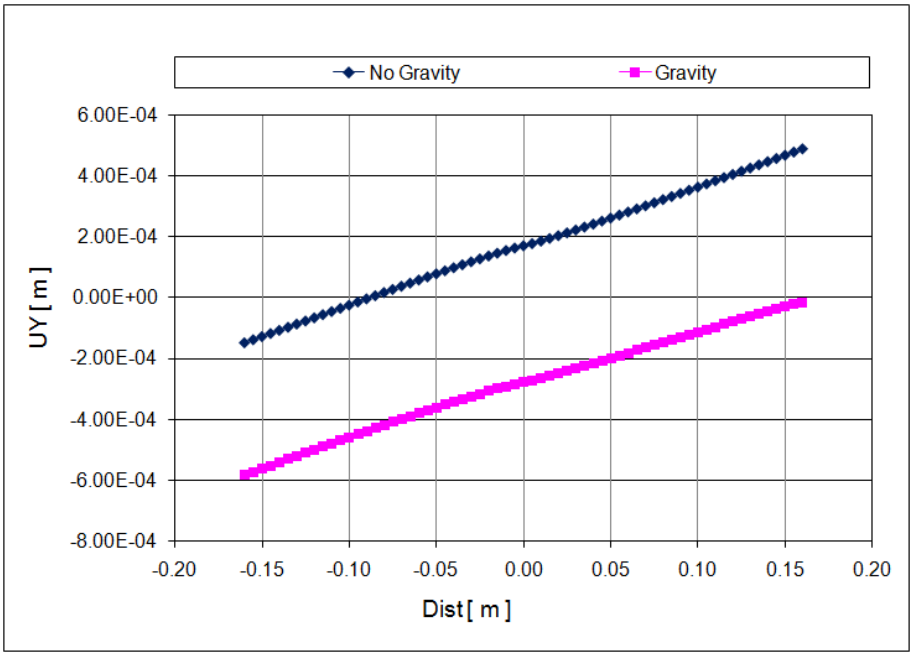

Figure 8.21: Vertical deflection (UY) of the centre line of the web (path W1): effect of gravity.

8.3.3 Contact between the plates of the web and the flange

The flange and the web plates are connected only by the elements of the weld seam and the nodes below the weld seam are separated as shown in Figure 8.9. Several

solutions concerning the displacements of these nodes are investigated in this section. The simplest solution is not to do anything and let them move freely. While this allows the opening of the gap between the two plates, this could however, result in unrealistic displacements if the elements penetrate into each other. The next solution is to employ constraint equations (CE) between each pair of coincident nodes. Only the movements in the X direction (*i.e.* the direction parallel to the plane of the web) are specified to be equal at both nodes while in the other directions they are free to take up any position independently from one another. While this solution prevents any penetration of the elements it also prevents the opening of the gap between the two plates.

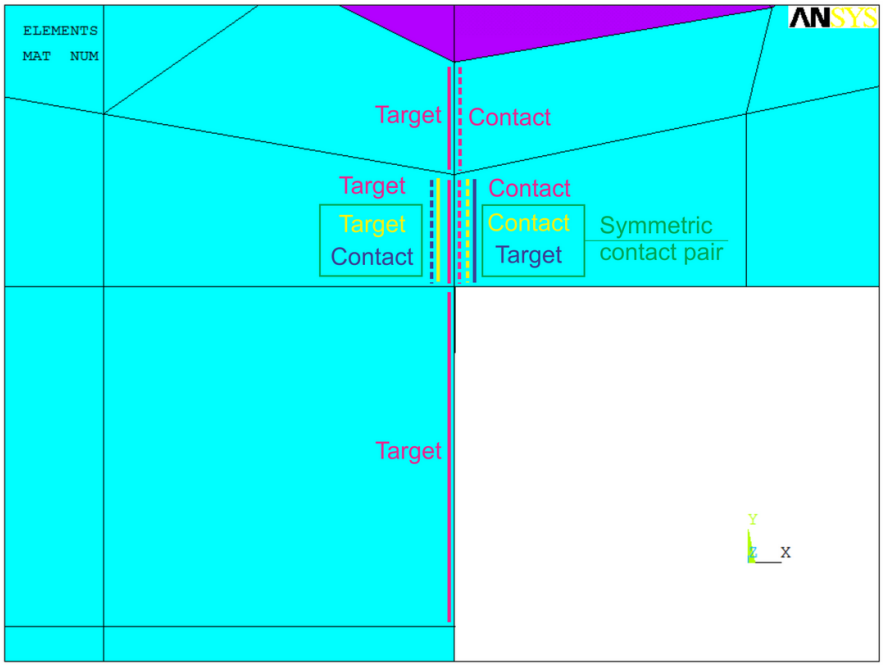

Figure 8.22: Surface-to surface contact elements below the weld seam.

The most sophisticated and most computationally expensive solution is to use contact elements on the faces of the solid elements connected to the coincident nodes. The contact elements are employed in two different ways as shown in Figure 8.22. Originally, in order to minimise the computational cost, contact elements were placed only at the faces marked with yellow and blue lines. The solid lines represent the target elements (TARGET170 3D target segment element of ANSYS) and the dashed lines represent the contact elements (CONTA173 3D four-node surface-to-surface contact element of ANSYS). To compensate for the reduction of the contact

area to one element face only, a symmetric contact pair is used. This means that both separated faces are at the same time contact and target faces therefore the contact algorithm is forced to check the contact conditions in both directions (that is why this type of contact is also known as "two-pass contact" [84]). Symmetric contact requires more computational effort but reduces the possibility of undetected penetrations. The reason for this is that the contact algorithm tries to prevent contact elements from penetrating target elements, however, target elements can freely penetrate contact elements.

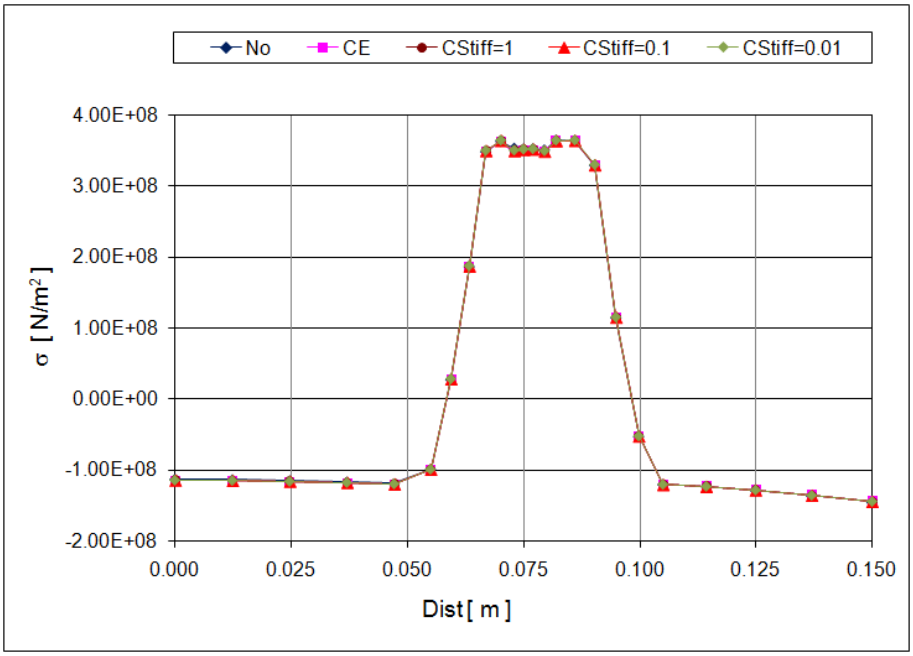

Figure 8.23: Axial residual stress (SZ) across the width of the flange (path FC1): effect of contact between the plates of the web and the flange (No: no contact; CE: constraint equations; CStiff: contact stiffness factor).

Two important characteristics of simulating contact are the friction between the surfaces in contact and the contact stiffness. In the present calculations friction is ignored as the nodes of the contact elements are expected to displace perpendicular to the plane of the contact surface (*i.e.* no sliding on top of each other is expected) as a result of the movements of the plates. By default the contact stiffness is determined by the stiffness of the material of the elements under the contact surfaces. One of the properties of the contact elements is the normal contact stiffness factor that is used to alter the default contact stiffness. Its default value is 1.0 but can be as

low as 0.01. In general, the higher the contact stiffness the less penetration can occur, however, it comes at a price of higher computational cost and can even result in convergence problems. Values of 0.01, 0.1 and 1.0 are studied to determine an optimal value for the rest of the analyses.

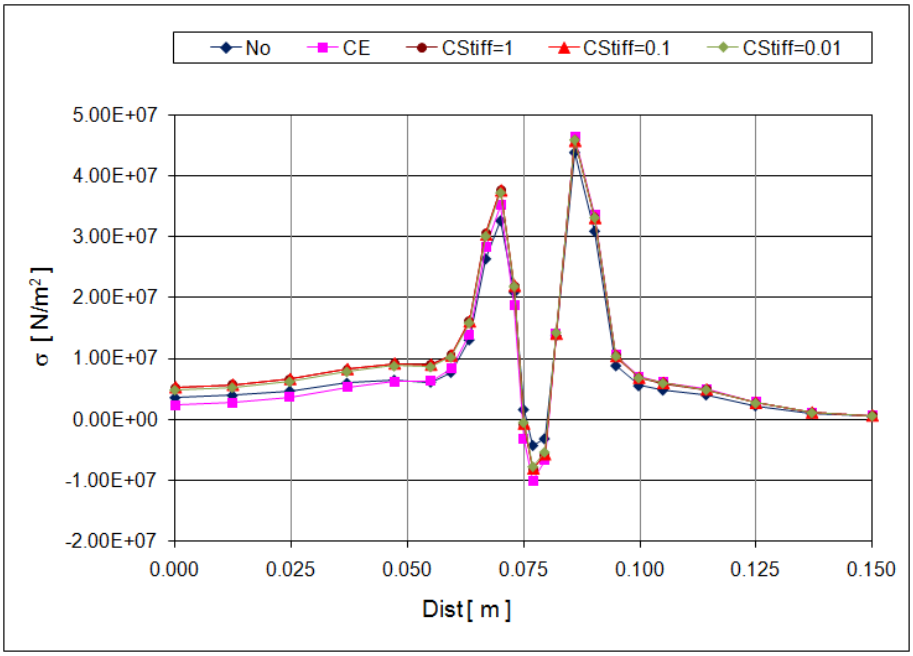

Figure 8.24: Transverse residual stress (SY) across the width of the flange (path FC1): effect of contact between the plates of the web and the flange (No: no contact; CE: constraint equations; CStiff: contact stiffness factor).

Figures 8.23 and 8.24 show the effect of contact between the plates of the web and the flange on the axial (SZ) and transverse (SY) residual stresses across the width on the top surface of the flange at the centre of the girder (path FC1), respectively. The axial stresses are not affected neither by the different solutions of contact nor by the contact stiffness of the symmetric surface-to-surface contact. This is the expected outcome since the contact between the web and the flange only influences the deformations in the transverse directions. That is why the transverse residual stresses are influenced by the type of the contact. It can be seen that in the zone of the weld, where the stress values are the highest, the case with neither contact nor constraint equations produces the lowest stress values since the plates can move without any restriction. By a very small margin the case with constraint equations produces the highest stress values on the right side of the weld. This solution limits

the movements of the plates most since neither penetration nor opening of the gap is allowed. Comparing the three cases of the contact elements no influence of the contact stiffness value can be observed.

The deflections of the flange (not shown) are not affected by the different contact solutions but there are significant differences in the deflections of the web shown in Figure 8.25. During welding the zone of the weld seam expands which pushes the web downwards and during cooling the zone of the weld seam contracts which pulls the web upwards. If no contact of any kind is considered the web can be pushed downwards much more than in any of the other cases therefore even after cooling this is reflected in the magnitude of the final deformations. When constraint equations are employed the web cannot be pushed down as much as in the previous case but at the same time when the weld zone contracts and pulls the web upwards, no gap between the plates can develop which results in a final deformation somewhere between the case of the free plates and the cases of surface-to-surface contact. While the contact stiffness has no influence on the residual stresses it does affect slightly the deformations of the web plate. A lower stiffness means that the contact algorithm permits a greater penetration therefore when finally during cooling the web plate is pulled upwards it does not reach the same position as in the cases of higher stiffness. The difference between the cases of stiffness factor 0.01 and 0.1 is relatively large, however, it is negligible between the cases of 0.1 and 1.0.

In some cases the use of symmetric contact pairs have resulted in numerical difficulties. Therefore an alternative surface-to-surface contact solution is devised using asymmetric contact (or "one-pass contact"). In this case target elements cover the element faces of the flange only and contact elements are defined only on the faces of the web elements. This modelling solution is also shown in Figure 8.22 using purple colour. The target and contact surface areas are extended by including the faces of the elements above and below of the two coincident nodes. Calculations with the same contact stiffness factors give practically identical results (not shown) to that of the symmetric contact.

Comparing the different contact solutions it can be concluded that if deformations are also of interest it is very important to consider realistic contact conditions between the two plates. If the aim of the analysis is only to obtain residual stress distributions then contact can be either ignored or simplified by the use of constraint equations in order to reduce the computational cost.

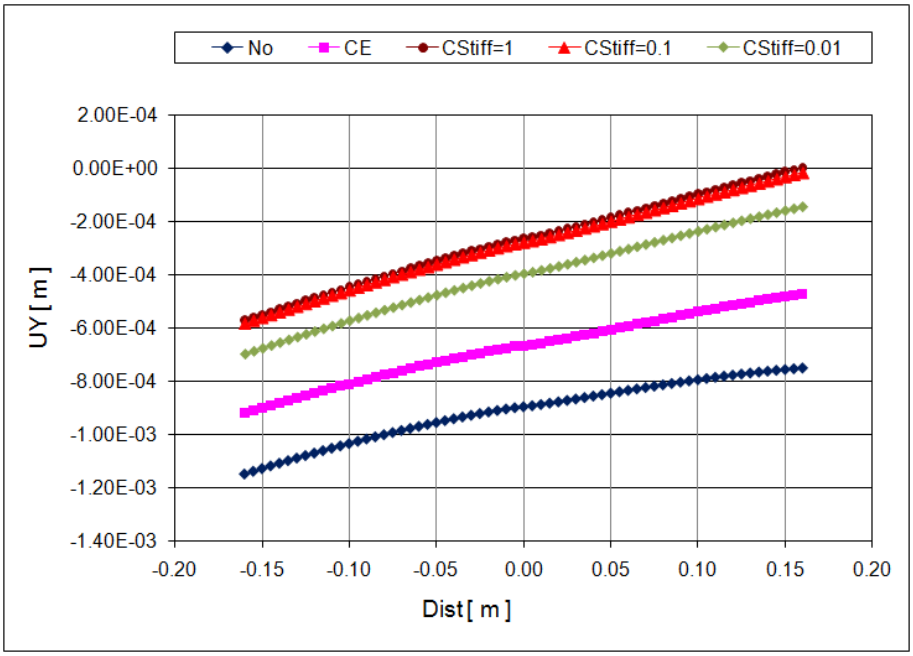

Figure 8.25: Vertical deflection (UY) of the centre line of the web (path W1): effect of contact between the plates of the web and the flange (No: no contact; CE: constraint equations; CStiff: contact stiffness factor).

Considering the contact stiffness of the surface-to-surface contact elements it has been demonstrated that the use of a normal contact stiffness factor of 0.1 gives almost identical results to that of factor 1.0. Since using a lower stiffness results in significant reduction of the computational cost the analyses presented here use a factor of 0.1.

8.3.4 Material models

In this section the effect of strain hardening and the yield strength of the materials are studied. First the results with the material properties shown in Figures 8.2 and 8.3 are compared. These are the properties defined in EC3 with no strain hardening and with strain hardening considered below 400°C, respectively.

Figure 8.26 shows the axial (SZ) residual stresses across the width on the top surface of the flange at the centre of the girder (path FC1). It can be seen that strain hardening affects the stresses closest to weld but do not affect the overall stress distributions. A similar observation can be made regarding the transverse

stresses (results not shown). The deformations of the flange and the web is also compared but no influence of strain hardening can be observed (results are not shown).

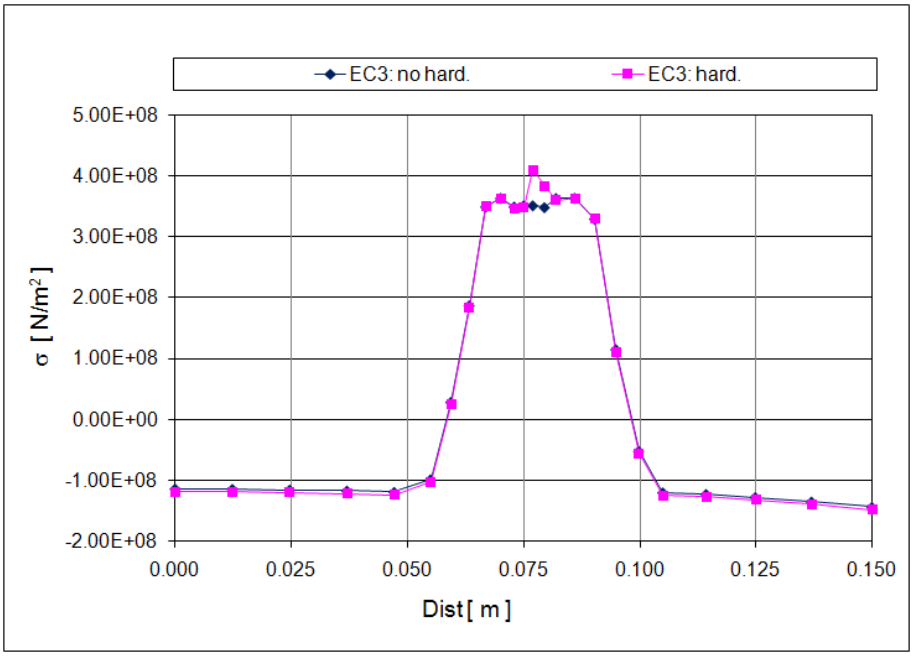

Figure 8.26: Axial residual stress (SZ) across the width of the flange (path FC1): effect of strain hardening.

Yield strength values based on tensile tests are considered in the next set of analyses. The material properties of the flange and the web plates are determined using the formulae of EC3 and the yield strength obtained from the tensile tests (Table 2.2 in Section 2.3.2). These cases are referred to as Test cases in the following discussion. For the material properties of the weld seam the following three cases are studied:

- (f): same as the material of the flange,
- (w): same as the material of the web (highest yield strength), and
- (EC3): standard EC3 properties (lowest yield strength).

The letters in brackets are used to identify the cases in the following figures. The results of these three Test cases are compared to the case of using the EC3 properties for the entire model. All these cases are evaluated with and without strain hardening. Since similar conclusions can be drawn from both only the results considering strain hardening are shown here.

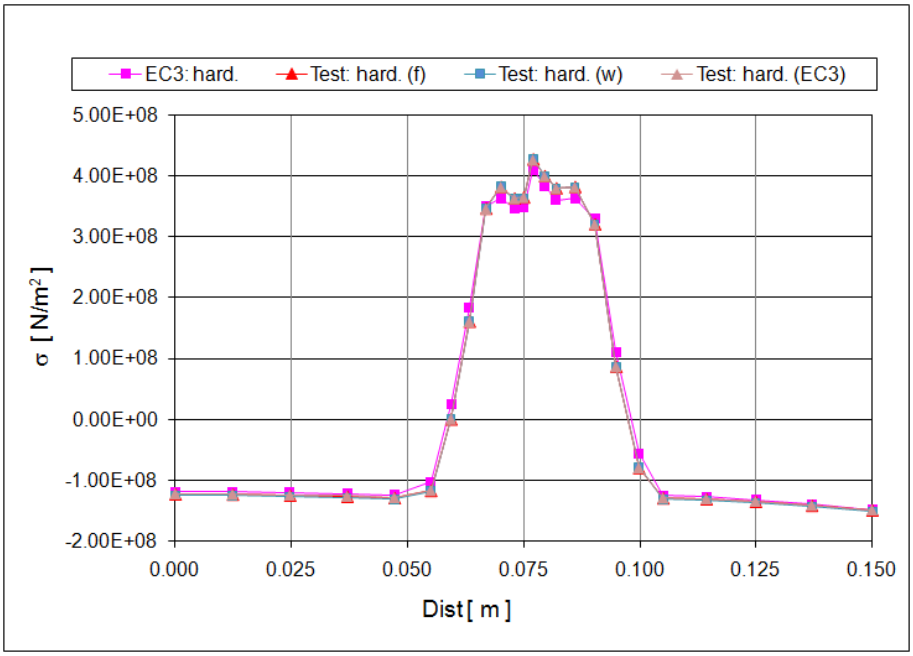

Figure 8.27: Axial residual stress (SZ) across the width of the flange (path FC1): effect of yield strength with strain hardening.

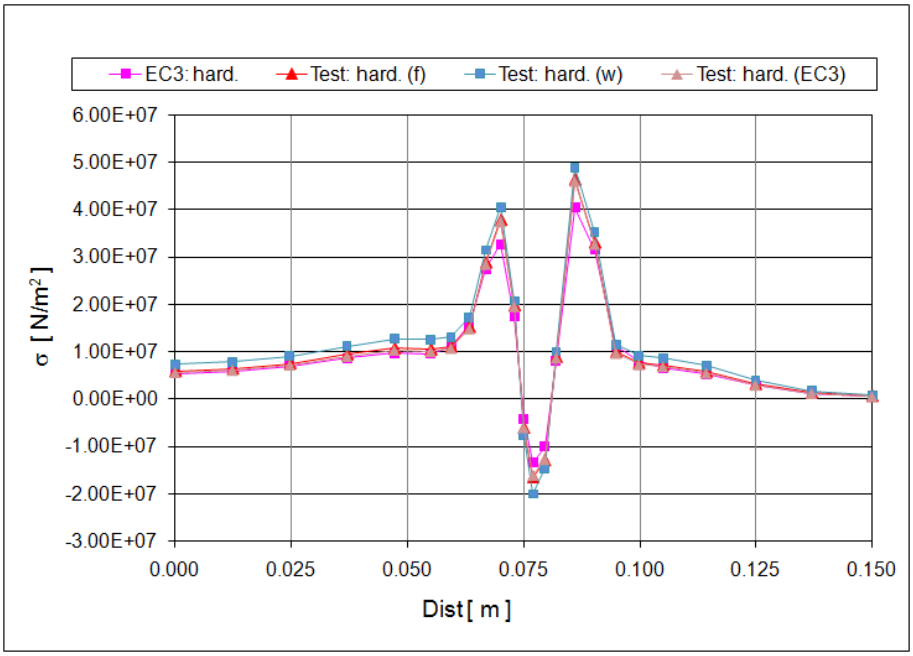

Figure 8.28: Transverse residual stress (SY) across the width of the flange (path FC1): effect of yield strength with strain hardening.

Figure 8.27 shows the comparison of the axial (SZ) residual stresses. The three Test cases (*i.e.* with the measured yield strengths) give slightly higher maximum

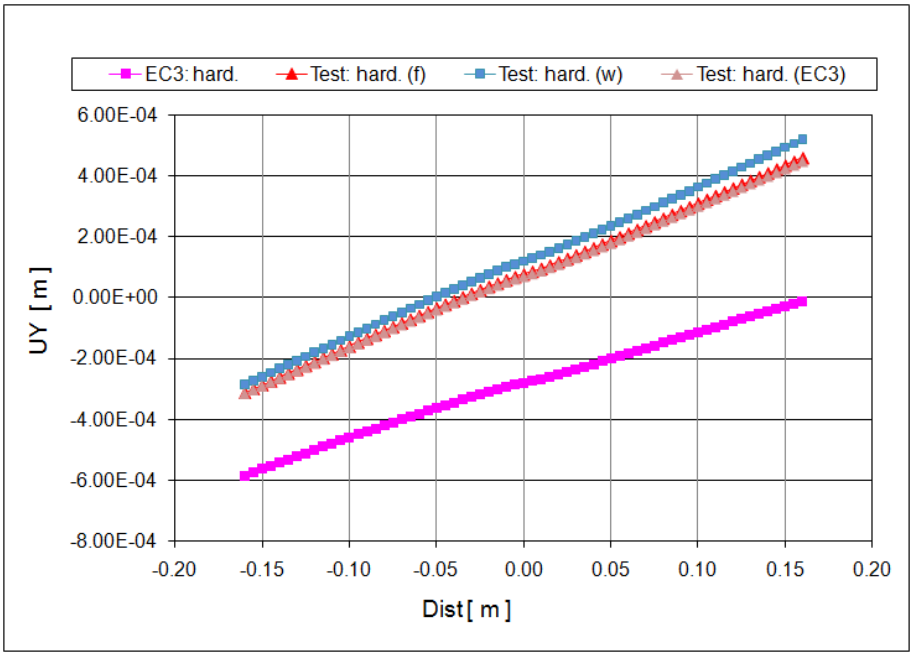

Figure 8.29: Vertical deflection (UY) of the centre line of the web (path W1): effect of yield strength with strain hardening.

stress values and slightly narrower zone of high stresses compared to the case of EC3 material. No differences among the three Test cases can be observed.

Similarly, the transverse (SY) stresses presented in Figure 8.28 show that the Test cases give higher stresses as well. However, this time some differences among them can also be observed. The highest stress values come from the case where the weld seam has the same material as the web, *i.e.* the highest yield strength. Between the other two Test cases there are very little differences.

Figure 8.29 shows how the vertical deflection (UY) of the centre line of the web (path W1) is influenced by the different material properties. It is clear that the model with EC3 properties produces rather different deflections. The reason for this is that the materials with higher yield strengths have more capacity for elastic deformations that can be "recovered" during cooling when the web plate is pulled upwards resulting in higher final positions. In the case of the deformations of the flange (results not shown here) similar tendencies can be observed but the scale of the differences is much smaller.

Comparing the three Test cases it can be seen that when the weld seam is made of the material of the flange (highest yield strength) the final position of the web is the highest for the same reason as above. While the differences are not very big,

the results indicate that the material properties in the weld and HAZ (heat affected zone) could play an important role in the development of deformations.

Since no experimental data is available about the actual material properties of the weld seam, whenever an analyses is done with the measured yield strengths of the plates it is assumed that the weld seam has the standard material properties defined in EC3.

8.3.5 Angle of the weld seam surface

The angle of the weld seam surface is also studied in Section 6.2. Figure 6.20 shows that depending on the angle more heat goes either into the flange or into the web. This phenomenon also influences the residual stresses and deformations.

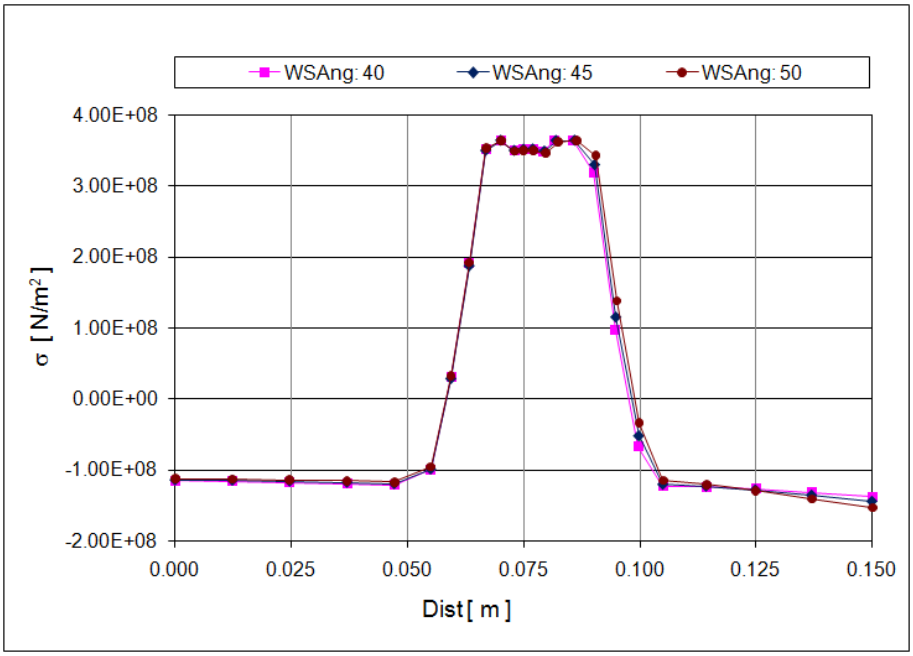

Figure 8.30: Axial residual stress (SZ) across the width of the flange (path FC1): effect of the angle of the weld seam.

Figure 8.30 shows the effect of the angle of the weld seam on the axial (SZ) residual stresses across the width on the top surface of the flange at the centre of the girder (path FC1). A higher angle (*i.e.* the weld is orientated more towards the flange) results in slightly higher stress values in the flange on the side of the weld, as expected.

The deflection of the web shown in Figure 8.31 is significantly affected by the

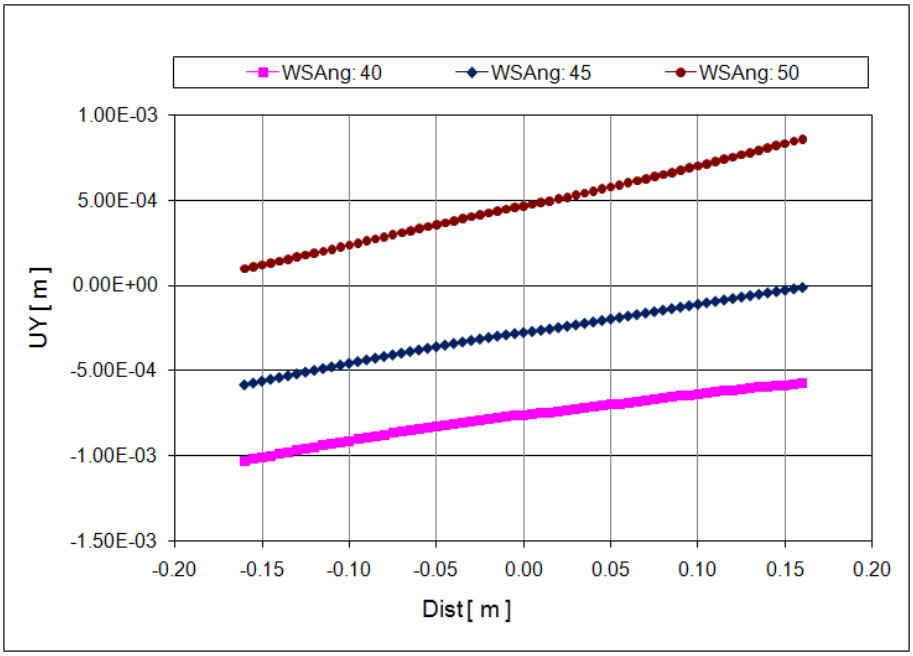

Figure 8.31: Vertical deflection (UY) of the centre line of the web (path W1): effect of the angle of the weld seam.

angle of the weld seam. A lower angle results in more heat going into the web which causes a more pronounced deflection during welding which is also reflected in the final position of the web.

8.3.6 Welding speed

The welding speed is also studied in Section 6.2. Figures 6.15 to Figures 6.17 show that a higher welding speed increases the cooling rate. This is the exact opposite of the aim of preheating that reduces the cooling rate and the deformations. Therefore the expected effect of an increase in the welding speed is also an increase in the deformations.

Figure 8.32 show the axial (SZ) residual stresses and it can be seen that a 10% change in the welding speed has very little effect on them.

What is more interesting is the deformations of the web and the flange which are shown in Figures 8.33 and 8.34, respectively. Both results show that the case with the highest welding speed results in the larger deflections. In the case of the flange the absolute deflections are clearly larger, while in the case of the web the difference between the deflection at the start and at the end of the model is larger, *i.e.* the web is more distorted. Since the welding speeds are of similar values the

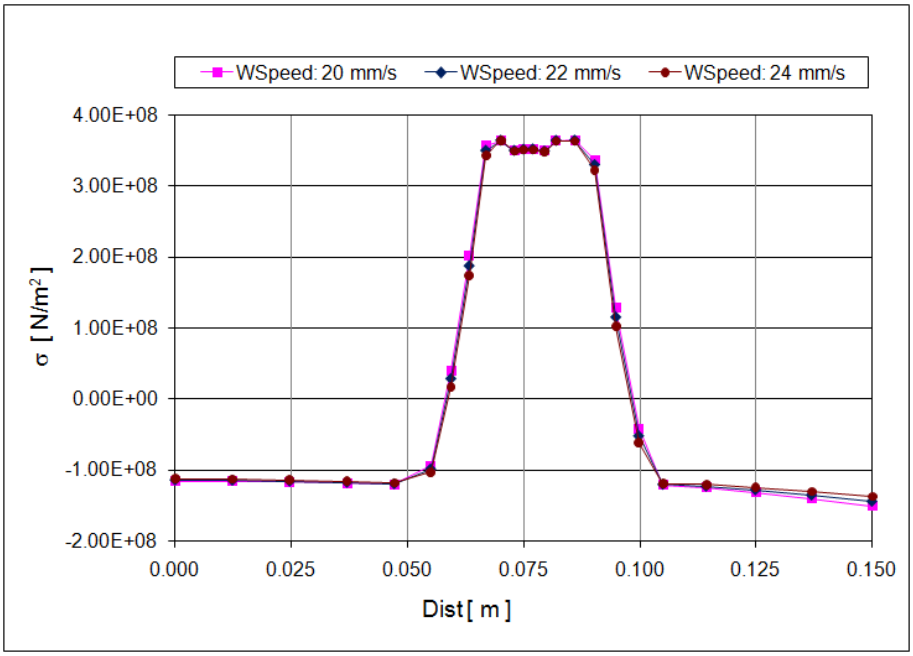

Figure 8.32: Axial residual stress (SZ) across the width of the flange (path FC1): effect of the welding speed.

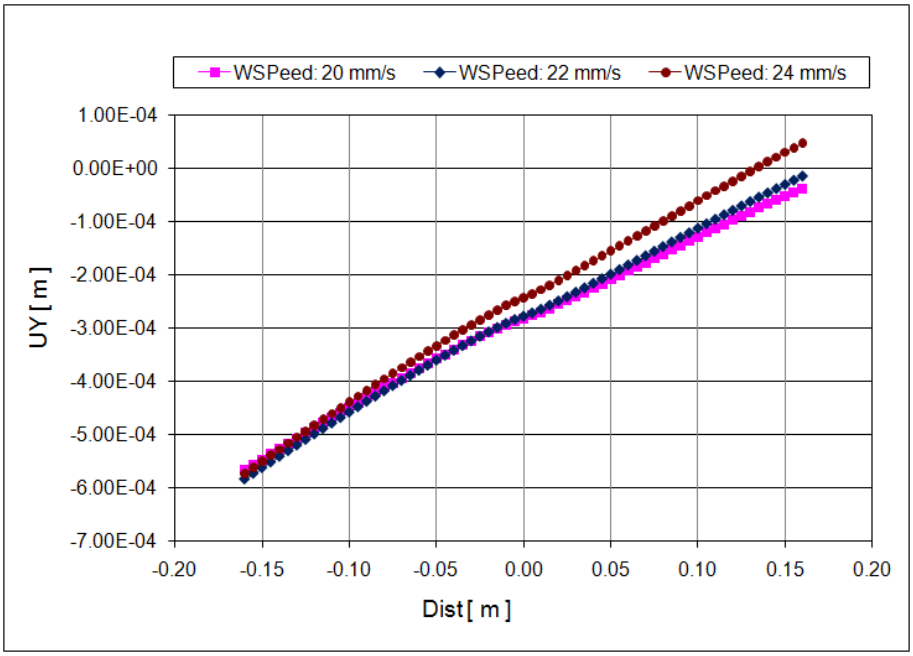

Figure 8.33: Vertical deflection (UY) of the centre line of the web (path W1): effect of the welding speed.

deflection differences are not very significant. However, the results demonstrate well that welding simulation based on the equivalent prismatic heat source model and

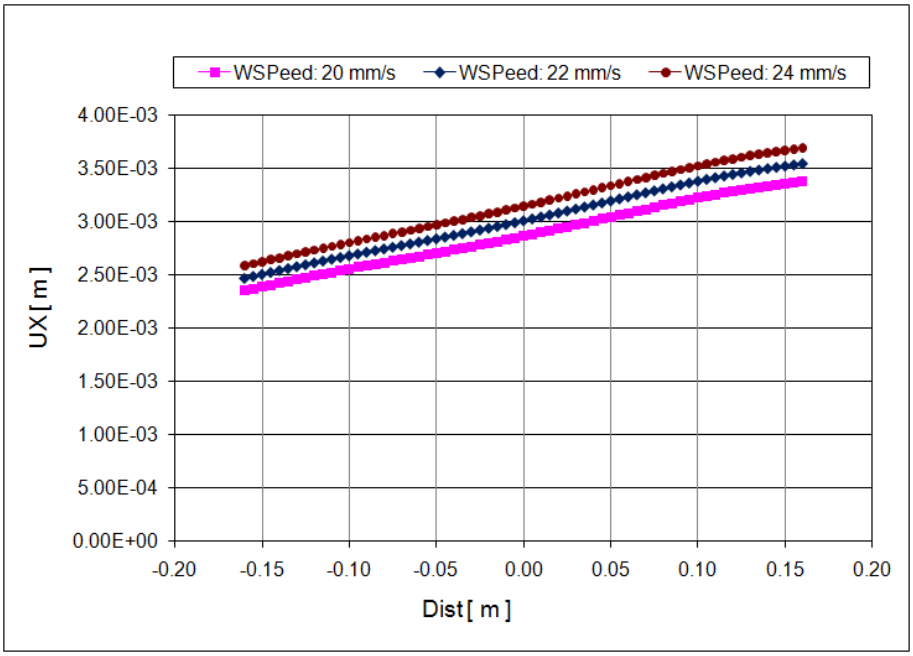

Figure 8.34: Horizontal deflection (UX) of the top edge of the flange (path F2): effect of the welding speed.

simplified material models (*i.e.* material properties taken from EC3) can capture such phenomena.

8.3.7 Preheating

Preheating is also studied in Section 6.2. Figure 6.19 shows how the length of the preheated zone influences the weld seam surface temperature. In the present study it is assumed that the nodes on the top surface of the web are preheated to 150°C in a 200mm long zone in front of the welding heat source. No direct preheating is applied to the flange. The general aim of preheating is to reduce the cooling rate around the weld and therefore to reduce the deformations in the plates.

Figure 8.35 shows how preheating affects the axial (SZ) residual stresses across the width on the top surface of the flange at the centre of the girder (path FC1). The positive stresses near the weld are slightly reduced as a result of the preheating, however, the negative stresses further away from the weld seam are increased.

The most interesting aspect of preheating is how it affects the deformations of the plates and if the present numerical model can reproduce the results expected. Figures 8.36 and 8.37 show the effect of preheating on the vertical deflection (UY)

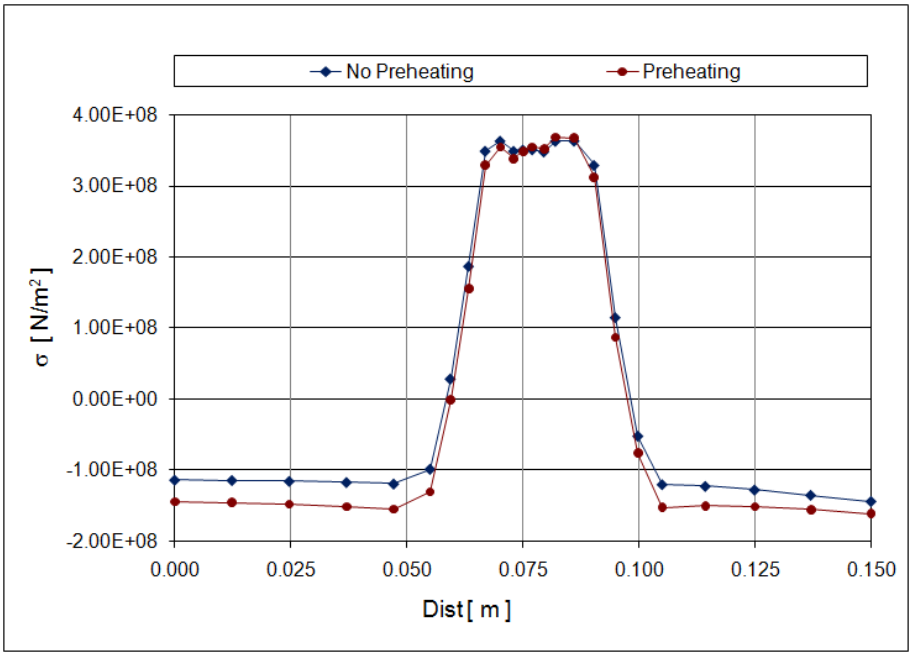

Figure 8.35: Axial residual stress (SZ) across the width of the flange (path FC1): effect of preheating.

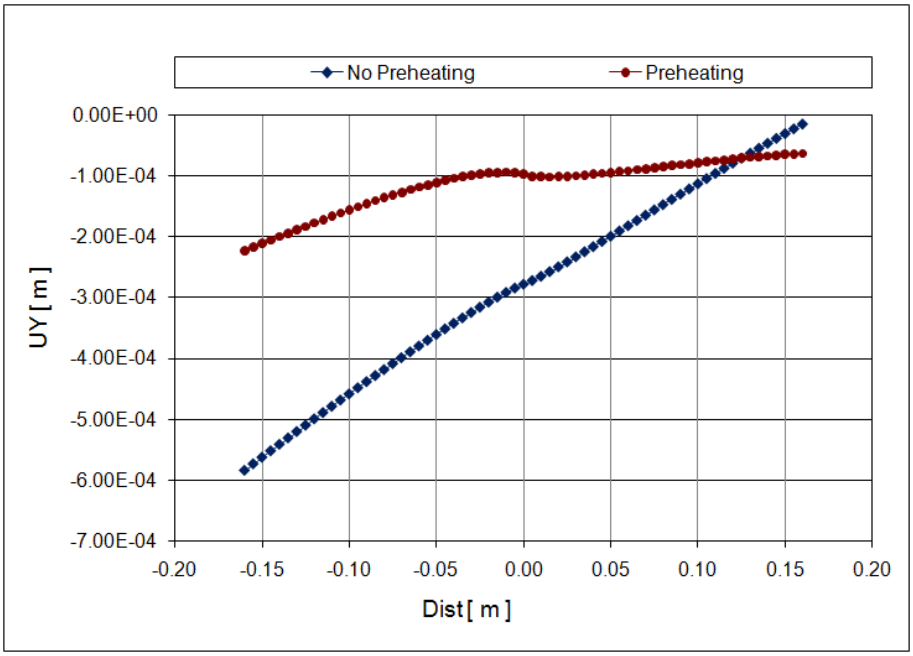

Figure 8.36: Vertical deflection (UY) of the centre line of the web (path W1): effect of preheating.

of the centre line of the web (path W1) and the horizontal deflection (UX) of the top edge of the flange (path F2), respectively. In the case of the web there is a

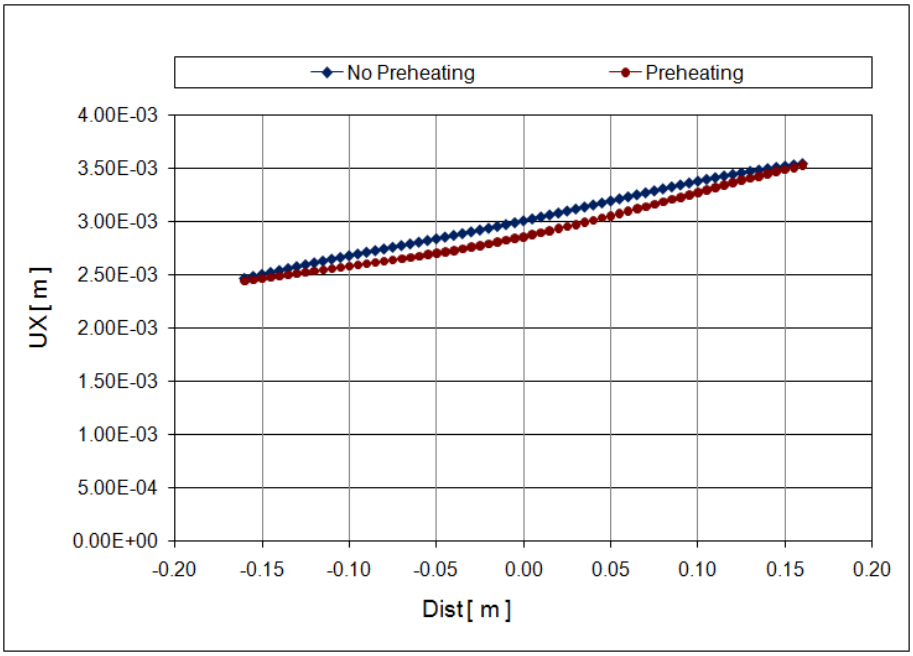

Figure 8.37: Horizontal deflection (UX) of the top edge of the flange (path F2): effect of preheating.

very significant improvement regarding deflections. Not only the absolute deflection values are smaller but also the difference between the deflections at the start and at the end of the web plate is reduced. The distortion of the web is significantly reduced as a result of preheating. Since the preheating is applied only to the web it has much less influence on the deflection of the flange. Nevertheless a slight improvement can also be observed in the flange.

8.3.8 Fully constrained plates

The case studied in this section is not practical but it is intended to demonstrate that the numerical model developed can be used to study the effects of displacement constraints on the development of residual stresses and deformations. The nodes of the bottom of the web (-Y side) and the nodes on the left side of the flange (-X side) are fully constrained during the welding and cooling. The constraints are additional to the ones shown in Figure 8.8. This means that practically the plates of the model can not deform during the analyses. This would result in an accumulation of stresses in the structure. The balance between residual stresses and deformations are governed by the constraints and the flexibility of the structure. On the one hand, if

a structure is very flexible and free to deform very small amounts of residual stresses develop in it. On the other hand, if a structure is very rigid or a lot of constraints are applied to it and therefore deformations are very limited, high residual stresses develop in the structure.

The following figures show the results of three cases. In the FREE case only the constraints shown in Figure 8.8 are applied to the model. The FIXED results refers to the model with all the additional constraints described above. The FREED results are actually derived from the same calculation as the FIXED ones. At the end of the cooling the results of the FIXED model are gathered and shown here. However, one additional calculation step is also performed on the same model. All the additional constraints are removed (the ones shown in Figure 8.8 stay active) and the structure is allowed to redistribute the accumulated stresses and develop deformations.

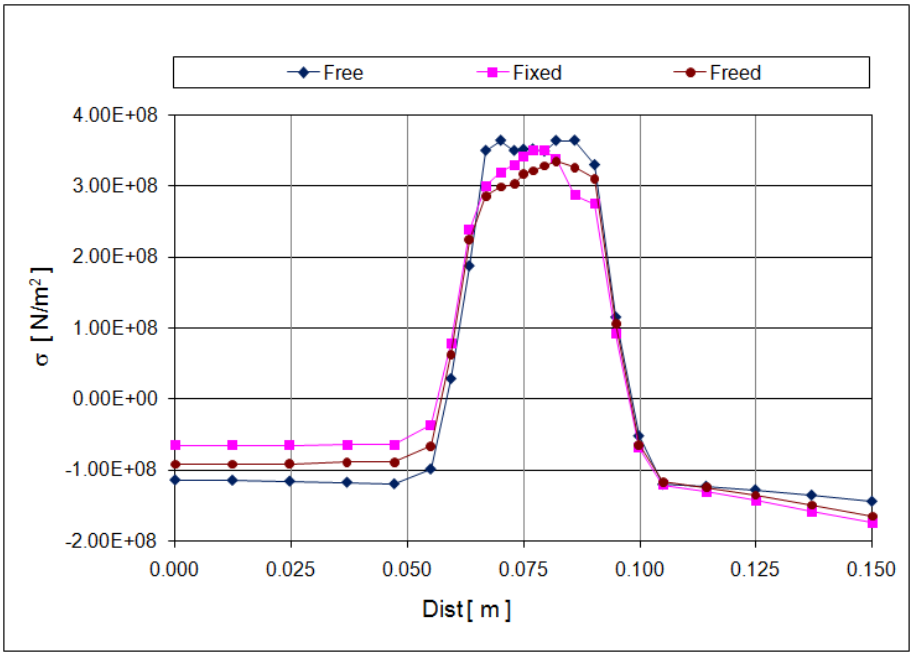

Figure 8.38: Axial residual stress (SZ) across the width of the flange (path FC1): effect of displacement constraints.

Figures 8.38 and 8.39 show the effect of displacement constraints on the axial (SZ) and transverse (SY) residual stresses across the width on the top surface of the flange at the centre of the girder (path FC1), respectively.

The additional constraints of the web and the flange do not limit directly the axial deformations of the model therefore no increase in the axial stresses can be

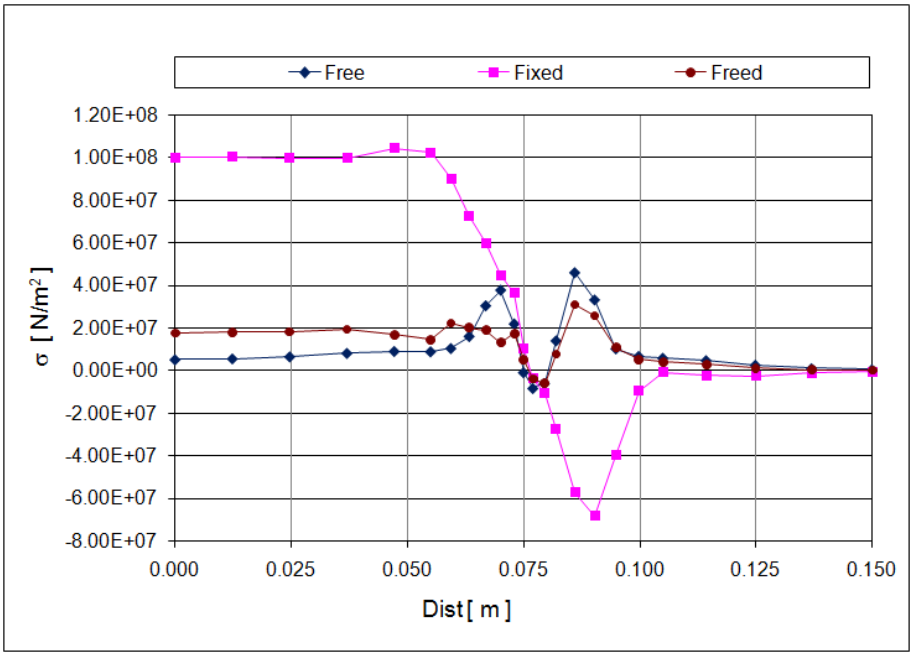

Figure 8.39: Transverse residual stress (SY) across the width of the flange (path FC1): effect of displacement constraints.

observed. In fact the stresses are slightly reduced at the centre of the flange and on the left side of it (this is where the UY supports are applied as shown in Figure 8.8). Only on the right side are the negative stresses slightly increased. The stresses are further reduced when the additional constraints are removed. As expected, the transverse residual stresses are much more strongly influenced. On the left side very large stresses develop as a combined result of the additional constraints and the original UY constraints at the edge of the flange. After removing the additional constraints the stresses change dramatically.

Applying additional constraints during welding can be advantageous since it can reduce the overall deformations in the structure as shown in Figures 8.40 and 8.41. The same tendencies can be observed in both sets of results: the final deformations after the removal of the additional constraints are significantly smaller both in the flange and the web.

This demonstrates that the model can be used for the evaluation of different support conditions during welding. This is of great interest since this allows the investigation of different support systems as distortion control techniques. This has the advantage that no further energy consuming technique needs to be used unlike in other mitigation methods [96].

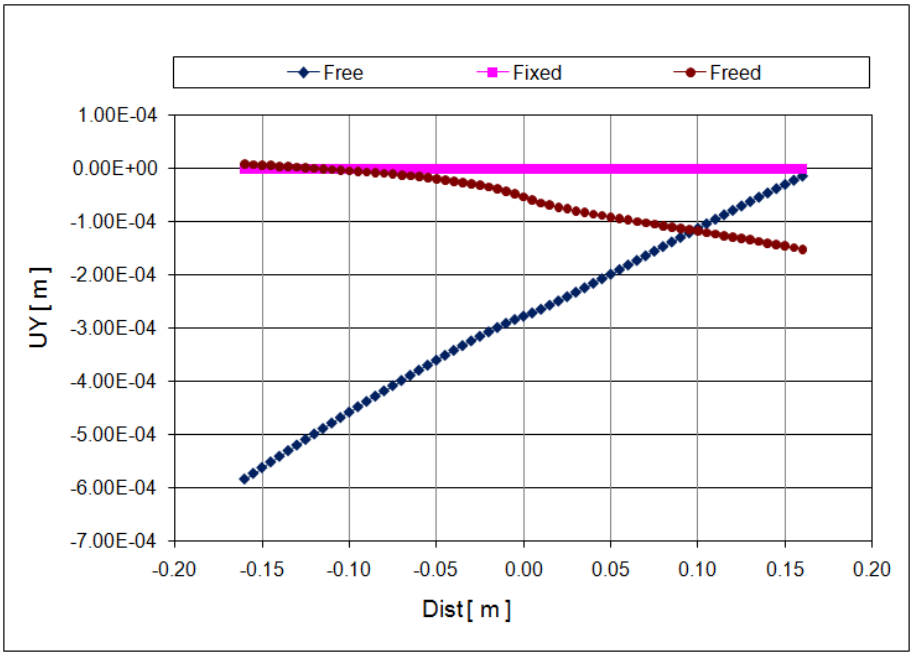

Figure 8.40: Vertical deflection (UY) of the centre line of the web (path W1): effect of displacement constraints.

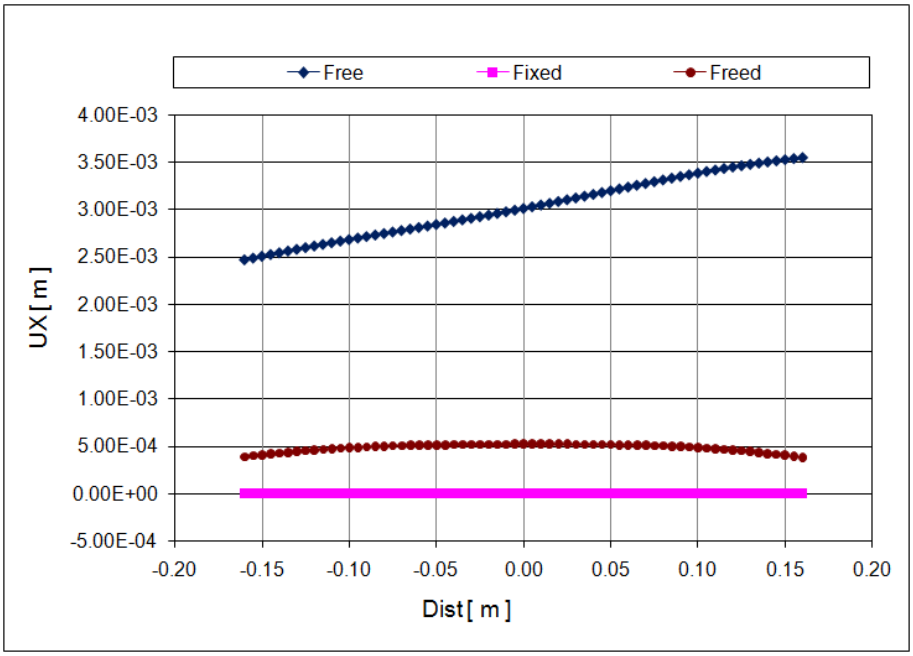

Figure 8.41: Horizontal deflection (UX) of the top edge of the flange (path F2): effect of displacement constraints.

The next study is a more practical application of this.

8.3.9 Length of the plate supporting rollers

Apart from the constraints shown in Figure 8.8 additional supports of the flange and web plates are considered in this study. These constraints represent the rollers that support the plates near the welding head in the welding machine. In the case of the web the use of displacement constraints closely resembles the actual support conditions in the welding machine since a series of rollers supports both sides of the web to make sure that the plate is kept at the correct position during welding and it cannot displace neither downwards nor upwards. The situation of the flange is different. There are rollers supporting the flange only on the external face of it. Therefore a more exact solution would be to use contact elements with rigid targets that allows the deformation of the flanges towards the webs but prevents any displacement in the opposite direction. Nevertheless the use of displacement constraints at the nodes of the flange is a realistic solution since the constraints are only applied near the actual position of the weld pool, which means that at that moment the zone of the weld is expanding, pushing the web and the flange in the opposite direction. The constraints advance together with the weld pool and by the time the weld zone starts contracting and pulling the web and the flange towards each other, those constraints are not there any more to prevent such deformations of the flange.

Figure 8.42 shows the position of the rollers during welding. The web is supported within a $20mm$ wide zone located $20mm$ from the face of the flange (in the figure the zone is marked as a transparent band on the top of the web - the actual constraints are at the nodes on the bottom face of the web). Within this zone the position of the actual support depends on the location of the welding heat source (*i.e.* the welding head) and changes from one welding step to another. The zone of the support is defined by the length of the equivalent prismatic heat source (LWPool) and an additional parameter (LRoller) that specifies the extra length of the support outside the heat source. The support of the flange is defined in the same way. The figure only shows the edge of the support zone (orange line) which starts $40mm$ below the top face of the web and terminates $60mm$ above it.

The extra support length (LRoller) varies from zero to $80mm$ and the results are also compared to the case without any additional support of the plates. The roller supports have negligible effects on the residual stresses therefore only the

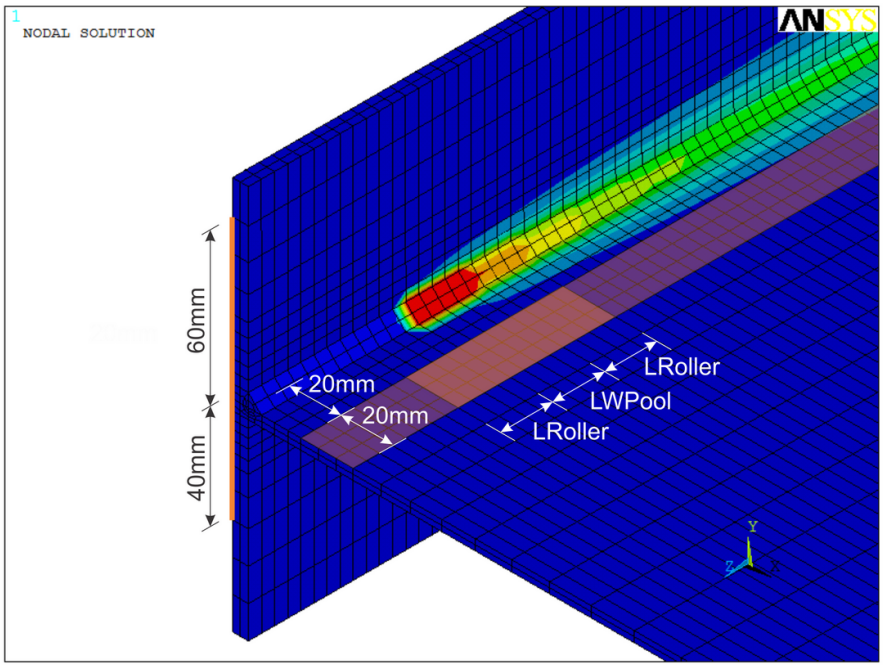

Figure 8.42: Roller supports of the web and the flange during welding.

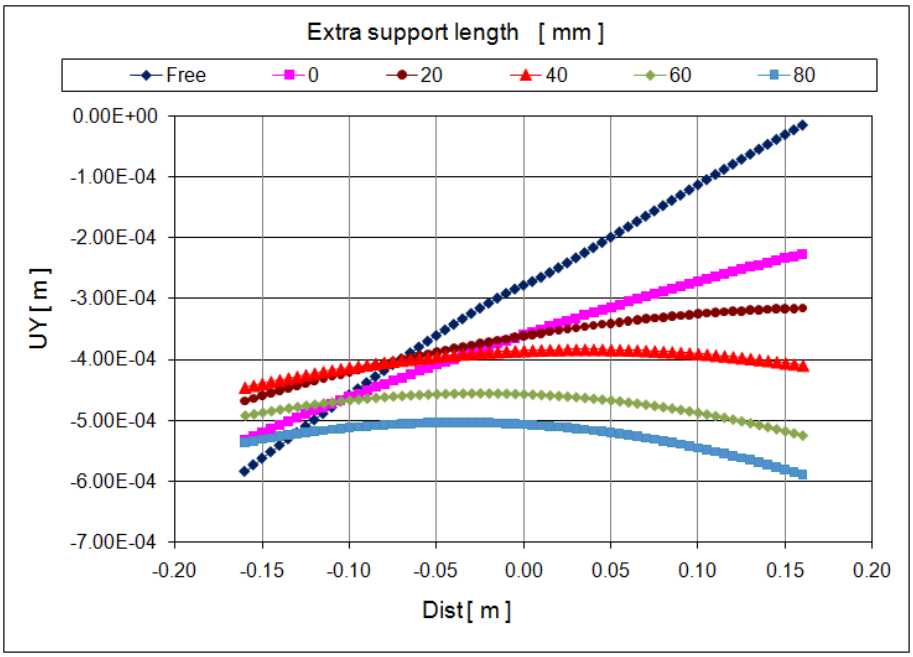

Figure 8.43: Vertical deflection (UY) of the centre line of the web (path W1): effect of plate support length.

displacements of the plates are discussed here. Figures 8.43 and 8.44 show the effect of plate support length on the vertical deflection (UY) of the centre line of the web (path W1) and the horizontal deflection (UX) of the top edge of the flange (path

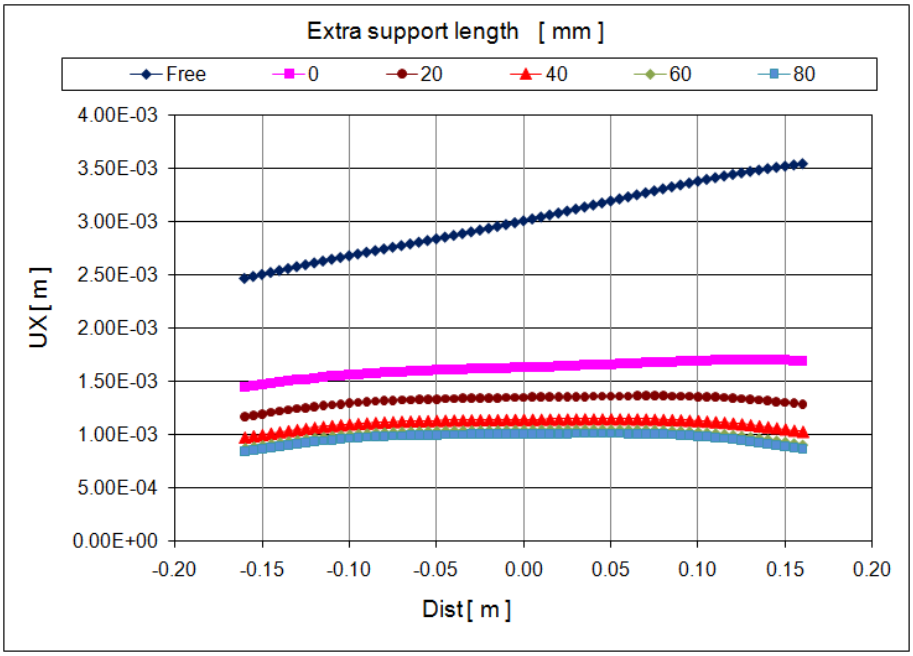

Figure 8.44: Horizontal deflection (UX) of the top edge of the flange (path F2): effect of plate support length.

F2), respectively. Both results clearly indicate that even the smallest support during welding can significantly alter the deformation of the plates. In the case of the web, while the maximum deflection is also reduced, what is more significant is the way the nature of the deformation changes. The longer the support the closer the deformed shape is to horizontal. It seems that the supports do not eliminate the deflection but they reduce the distortion of the web. In the case of the flange both the deflection amount and the distortion are reduced by the rollers.

8.3.10 Reduction of welding steps

In this section a technique to speed up the analysis is investigated. In Chapter 6 it was decided that in the thermal analysis the welding process advances one full weld pool length in each welding step. The same assumption is used in the calibration of the equivalent heat source model in Section 6.3. While this is a very reasonable assumption there are other possibilities as well. One can decide to "Speed Up" the calculation and double the length of the weld pool and at the same time double the welding speed as well. As a result of this each node of the weld pool is maintained at welding temperature for the same period of time as in the original calculation, *i.e.*

the total amount of heat introduced into the model is the same. This is not to say that the two solutions are identical but both of them seem a valid approximation. In the above example the so called Speed Up factor would take the value of two. A somewhat similar technique called "variable length heat source" is used in [44] for the simulation of multi-pass circumferential welding using different heat source lengths in each weld pass up to half of the circumference, *i.e.* two welding steps.

The possible values for the Speed Up factor is limited by the ratio of the length of the model and the weld pool length. In the previous studies the length of the model is limited to $320mm$, however, in this investigation it is extended to $600mm$ in order to study more cases. Since the size of the weld pool (*i.e.* the length of the equivalent prismatic heat source model) is $20mm$ the maximum value of the Speed Up factor is 30. Using this factor means that the full length of the weld is done in a single welding step. Several factors between 1 and 30 are investigated.

Apart from the mechanical boundary conditions shown in Figure 8.8 additional support of the plates is considered similarly to the study in the previous section. It is assumed that the length of the rollers is equal to the size of the weld pool, *i.e.* the parameter LRoll in Figure 8.42 is set to zero. When applying a Speed Up factor the length of the weld pool is increased artificially. This in turn also increases the length of roller support zone.

Figure 8.45 shows the effect of the Speed Up factor on the axial (SZ) residual stresses on the top surface of the flange along the length of the girder (path F1). The stresses are very similar at the two ends of the girder but in middle part a clear oscillation of the stresses can be observed. Figure 8.46 shows the same results near the centre of the model. It can be seen that the larger the Speed Up factor is the larger is the difference between the peaks and troughs of the curves. The difference is about $30MPa$ in the case of factor 15 (*i.e.* analysis with two welding steps) but it goes down to $7MPa$ with a factor of 2. This variation in the stresses is caused by the transition ("jump") of the heat source between two welding steps. Increasing the Speed Up factor makes the analysis steps less smooth. The results also demonstrate that the original assumption to advance a single weld pool length in the analysis in each welding step (*i.e.* Speed Up factor 1) is a good approximation since the axial stress values show very little variation between two steps. There is one curve that shows no such a variation: Speed Up factor 30. Since in this case the full length of the weld is done in a single step the distribution of the residual stresses is

very smooth along the length of the model. The variation of the transverse stresses along the length of the model in function of the Speed Up factor show very similar characteristics therefore the results are not shown here.

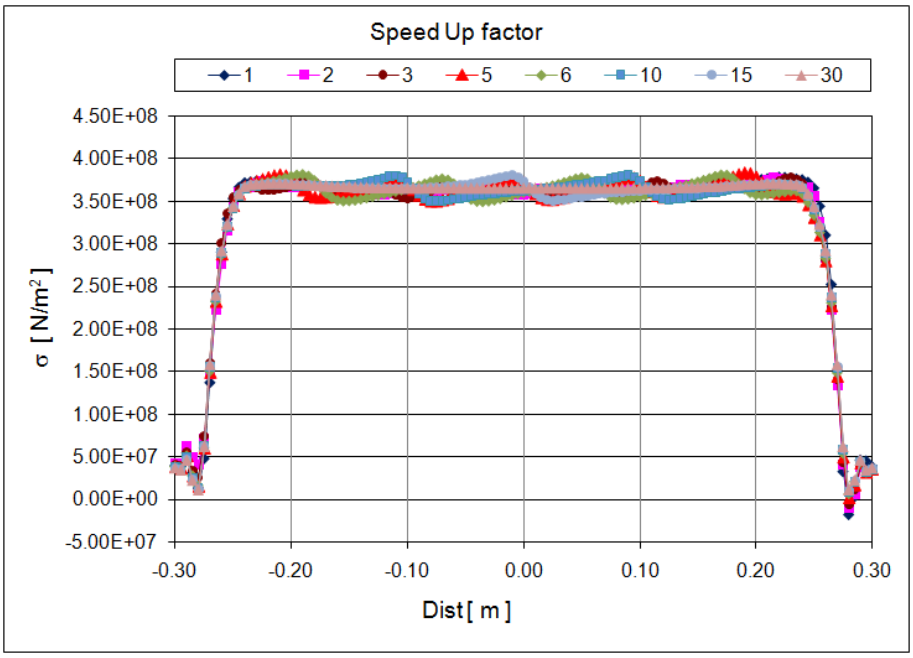

Figure 8.45: Axial residual stress (SZ) along the length of the flange (path F1): effect of analysis "Speed Up" factor.

In Figure 8.46 an arrow marks the location where all the curves come together and have very similar stress values. In every case this location is half way between the peaks and the troughs of the curves. The axial (SZ) and transverse (SY) residual stresses in that section of the model are compared in Figures 8.47 and 8.48, respectively. The axial residual stresses show very little variation. This suggest that even if a high Speed Up factor is used in the analysis the residual stress values taken from the cross-section of the model located halfway between the peaks and troughs of the longitudinal stress variation are very good approximations of the actual stresses. It also demonstrates that even if the full length of the weld is completed in a single step the axial residual stresses can be accurately approximated. Additional advantage of this method is that it gives a very smooth stress distribution along the full length of the model.

The transverse stresses show somewhat more variation. The higher values come from the cases of 3, 5, 15 and the lower values from 2, 6, 10. A clear pattern can be observed here. The odd factors result in an even number of welding steps while the

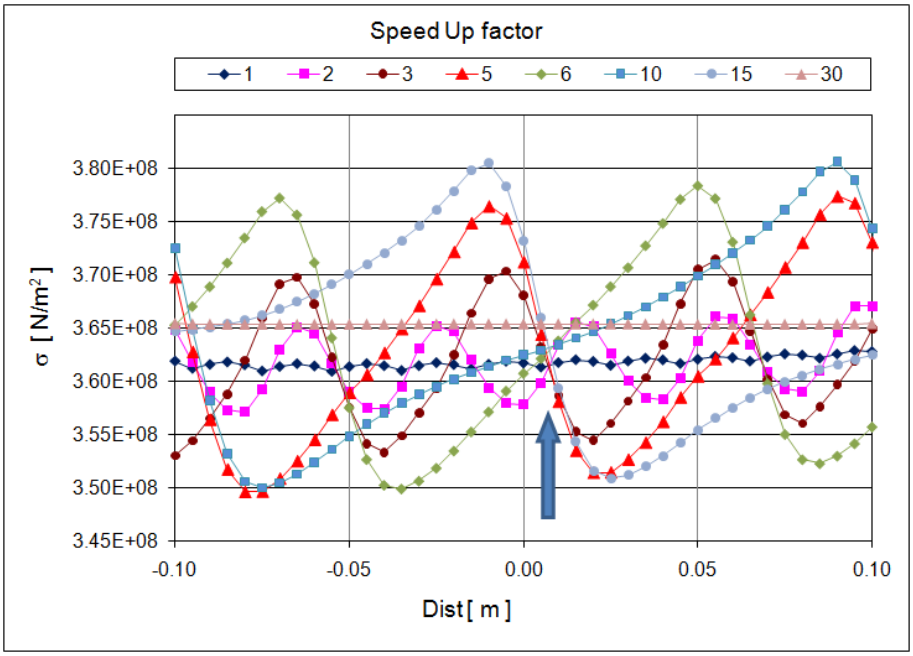

Figure 8.46: Axial residual stress (SZ) along the length of the flange (path F1): effect of analysis "Speed Up" factor.

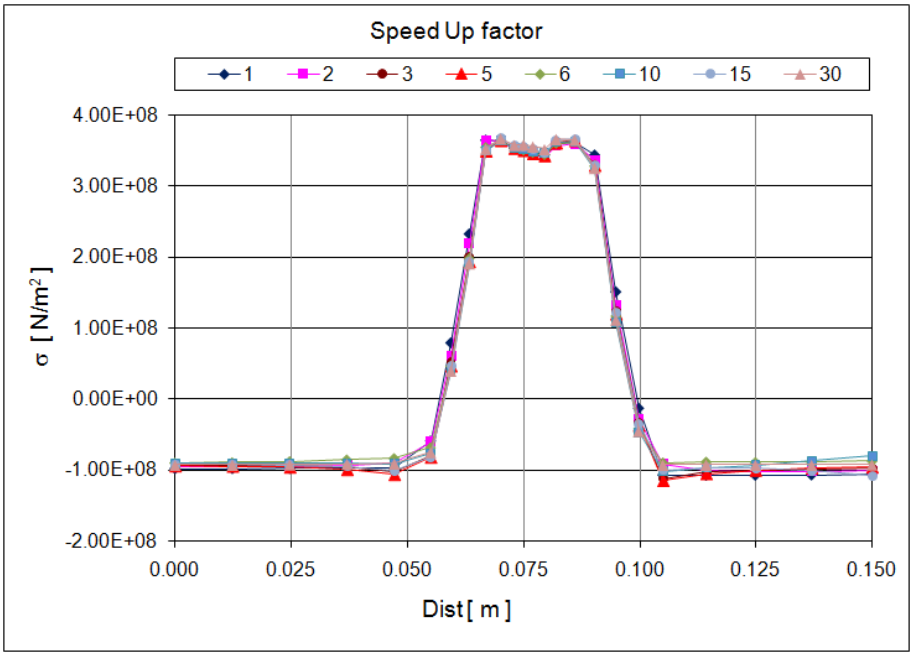

Figure 8.47: Axial residual stress (SZ) across the width of the flange: effect of analysis "Speed Up" factor.

even factors result in an odd number of welding step. In the case of the even welding steps the section at the centre of the model is a place where the transition from one

welding step to another takes place. In the case of the odd welding steps, however, the section at the centre of the girder is in the middle of a welding steps. This can also be observed in Figure 8.46. At the centre of the model (0.00 on the horizontal axis) the curves of factor 3, 5, 15 are decreasing in value, while curves of factor 2, 6, 10 are increasing in value. A more exact comparison would be to use the same (ascending or descending) part of each curve but in the case of the higher factors that would mean that a cross-section far from the centre of the model would need to be used which would make the comparison equally difficult. Nevertheless, these stresses are an order of magnitude less than the axial stresses which are usually the main interest of the analyst therefore the variations observed here have little importance.

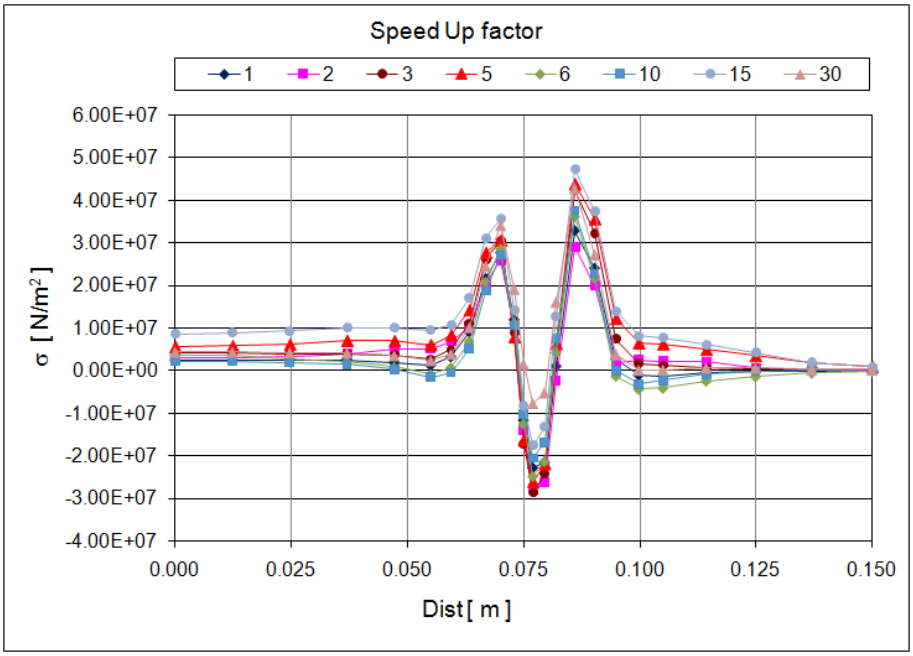

Figure 8.48: Transverse residual stress (SY) across the width of the flange: effect of analysis "Speed Up" factor.

The Speed Up factors have much a stronger influence on the deformations of the plates as shown in Figures 8.49 and 8.50. The deformed shapes of the web are very similar up to a factor of three even though the magnitudes of the deflections are slightly different. However, higher factors can change the shape of the web completely. In fact, in the case of a factor of 30 the shape of the web is the exact opposite of the shape calculated with factor 1. The deformations of the flange are also strongly affected even though such a significant change in the shape of the flange

cannot be observed.

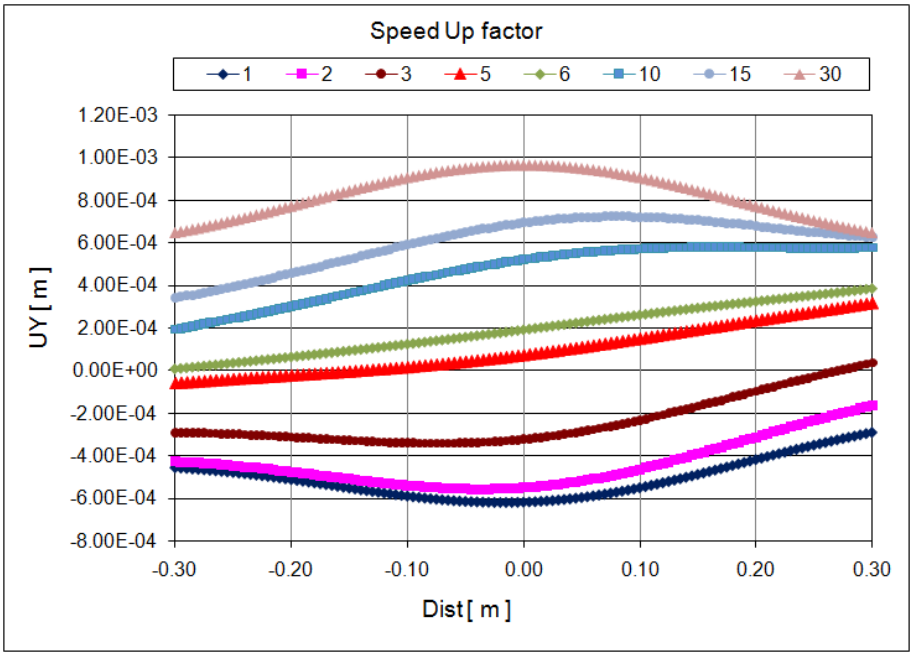

Figure 8.49: Vertical deflection (UY) of the centre line of the web (path W1): effect of analysis "Speed Up" factor.

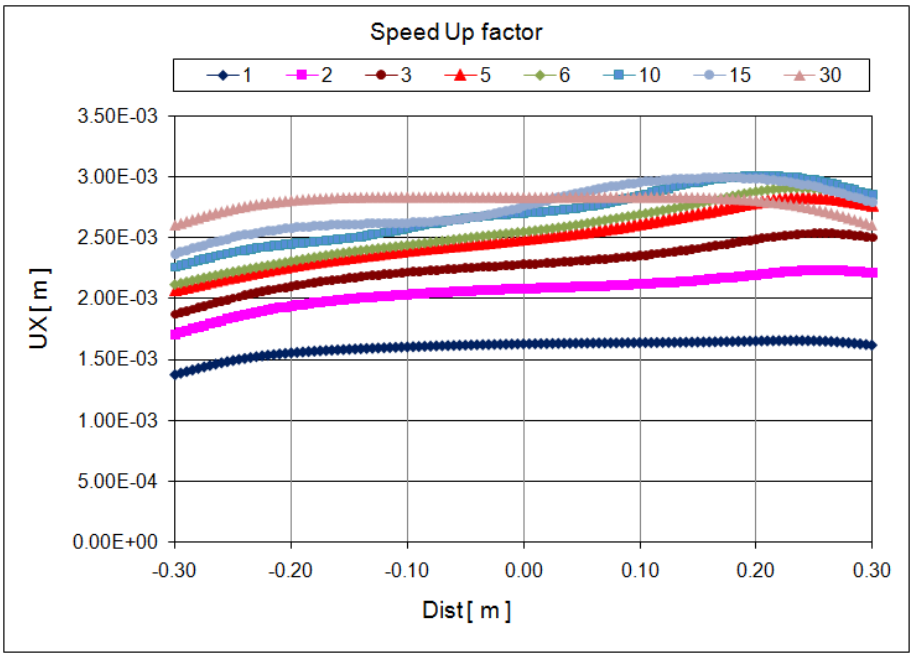

Figure 8.50: Horizontal deflection (UX) of the top edge of the flange (path F2): effect of analysis "Speed Up" factor.

It is important to point out that the support conditions of the plates are also

governed by the Speed Up factor in this example as explained above. The combined effect of reducing the welding steps and at the same time changing the support conditions is what causes such dramatic changes in the deflections. One of the challenges of using this Speed Up method is to ensure that the support conditions remain valid during the analysis. This needs to be carefully considered when this method is employed to reduce the number of welding steps.

Speeding up the analysis by reducing the number of welding steps is a very efficient way to make the analysis less expensive computationally. In Section 8.2.3 the number of load steps in each welding step is discussed. Figure 8.10 shows that for every welding step there are five load steps in an analysis. This means that reducing the welding steps significantly reduces the number of load steps to be solved. The complete analysis includes load steps during the cooling down of the model which is not affected by the Speed Up factor. The number of load steps in the cooling down phase is practically independent from the length of the model (*i.e.* the length of the weld) since cooling always starts after the last welding step and the temperatures range always from melting temperature to ambient temperature. The longer the model is the smaller is the ratio of the load steps during cooling and the load steps during welding. This makes this technique particularly advantageous for very long welds. In Section 8.4 models of much larger size are studied and the subject of Speed Up factors is also revisited.

8.3.11 Calibrated heat source models

In Chapter 6 the results of the temperature measurements are used to calibrate the equivalent prismatic heat source model. Considering two weld cross-sections and preheating, altogether four different heat source models are determined. Their characteristics are summarised in Table 6.3. This last study in the series of parametric studies compares the residual stresses and deformations produced by these four cases. The following labels are used to identify the results:

- L5 $\Rightarrow$ weld leg: $5mm$, no preheating,
- L5_PH $\Rightarrow$ weld leg: $5mm$, with preheating,
- L52 $\Rightarrow$ weld leg: $5.2mm$, no preheating, and
- L52_PH $\Rightarrow$ weld leg: $5.2mm$, with preheating.

In the analyses both the measured yield strengths of the plates and strain hardening are considered. The material properties of the weld seam are taken from EC3 with strain hardening as discussed in Section 8.3.4. No additional roller support of the web and flange is included, only boundary conditions shown in Figure 8.8 are considered.

Figure 8.51 show the variation of the axial (SZ) residual stresses. The size of the weld does not affect the stress levels while preheating has the exact same effects as discussed in Section 8.3.7.

Figure 8.52 shows the effect of the heat source models based on the temperature measurements on the vertical deflection (UY) of the centre line of the web (path W1). Preheating significantly reduces the deflections and distortions of the web. The effect of the size of the weld is negligible in the cases without preheating. In the case of preheating the larger weld seems to produce slightly less deflection in the web. The deflections of the flange show very little variations (not shown).

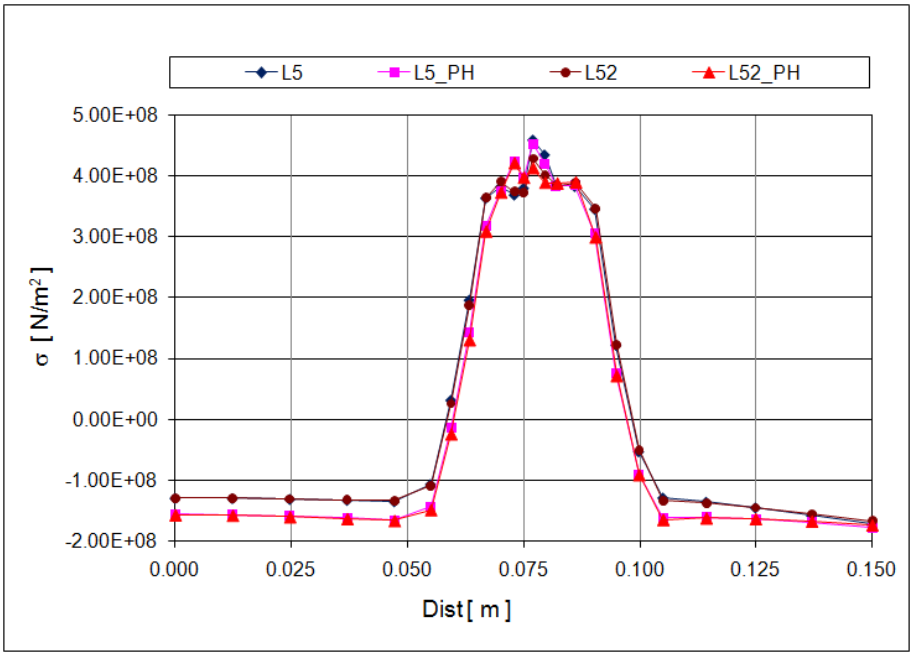

Figure 8.51: Axial residual stress (SZ) across the width of the flange (path FC1): effect of the heat source models based on the temperature measurements.

It is important to take into account that all these studies have been performed on models of relatively short length. While many conclusions can be extrapolated to larger models there are certain phenomena, such as the buckling of plates during

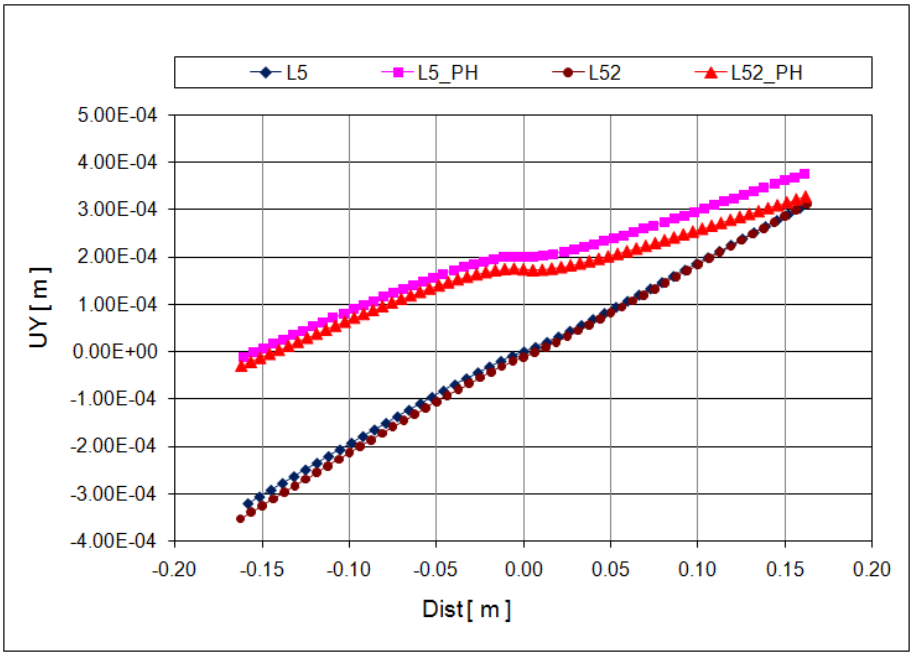

Figure 8.52: Vertical deflection (UY) of the centre line of the web (path W1): effect of the heat source models based on the temperature measurements.

welding, that can only be investigated with larger models. In the next chapter results of welding simulations performed on models with a length of $3000mm$ and $6000mm$ are presented.

Since there are no experimental data to confirm the efficiency of preheating during the fabrication of the specimens, preheating is ignored in the analyses of the full size models. The weld size of $5.2mm$ is chosen for the remaining analyses since this is the weld geometry that was obtained from the macrograph images of three weld cross-sections.

8.4 Full size girders

In Section 8.3.10 it has been investigated how the computational cost can be reduced by using a Speed Up factor to reduce the number welding steps and therefore the number of load steps in the analysis. It has been demonstrated that if residual stress values are of interest then such technique can be used successfully. However, the deformations of the plates have been very significantly altered when a high Speed Up factor was applied. In this section a similar study is performed but with models

of full size plate girders where buckling of the plates might occur as a result of the welding process.

First a girder with a length of $3000mm$ is studied with the assumption that at the two ends of the girder there are $300mm$ long sections without welding. This corresponds to the actual fabrication conditions of the specimens shown in Table 2.1 in Section 2.2. As a result of the positions of the rollers supporting the plates in the welding machine it was impossible to start the welding at the very start of the girder and finish it at the very end of it. At the start of the girder tack weld was also used to keep the plates in place. This is also considered in the numerical model by merging the nodes of the web and the flange along a $30mm$ long section at the start of the model. No such tack weld was used at the end of the girder therefore in the model the plates are also free to deform separately.

The boundary conditions are the same as shown in Figure 8.8 with additional supports of the plates being also considered in the analyses in the same way as in Section 8.3.10. The length of the zone with additional support is equal to the weld pool length and scaled up by the Speed Up factor. The material properties of the plates are based on the tensile test measurements, while the weld seam has the standard properties of S355 steel defined in EC3 . Strain hardening is also considered below 400°C. No preheating is employed and the equivalent prismatic heat source model with a weld pool length of $25mm$ and weld cross-section with a leg of $5.2mm$ are used as explained in Section 8.3.11.

The total length of the weld is $2400mm$ which results in 96 ($2400mm/25mm$) welding steps if no Speed Up factor is applied. The Speed Up factors considered are shown in Table 8.2. The table also shows the corresponding welding steps and load steps (five per each welding step) during the welding phase of the analysis. The studies of Section 8.3.10 demonstrate that up to a Speed Up factor of 3 even the deflection results show a reasonable agreement with the calculations without Speed Up. Therefore no factors below 3 are studied here.

Speed Up factor	3	6	12	24	48	96
Welding steps	32	16	8	4	2	1
Welding load steps	160	80	40	20	10	5

Table 8.2: Speed Up factors.

The longitudinal variation of the residual stresses show the same characteristics as seen in Figures 8.45 and 8.46 in Section 8.3.10 therefore these results are not shown. The residual stresses across the face of the flange are shown near the centre of the girder at the location half way between the peak and the trough of the stress curves as shown in Figure 8.46.

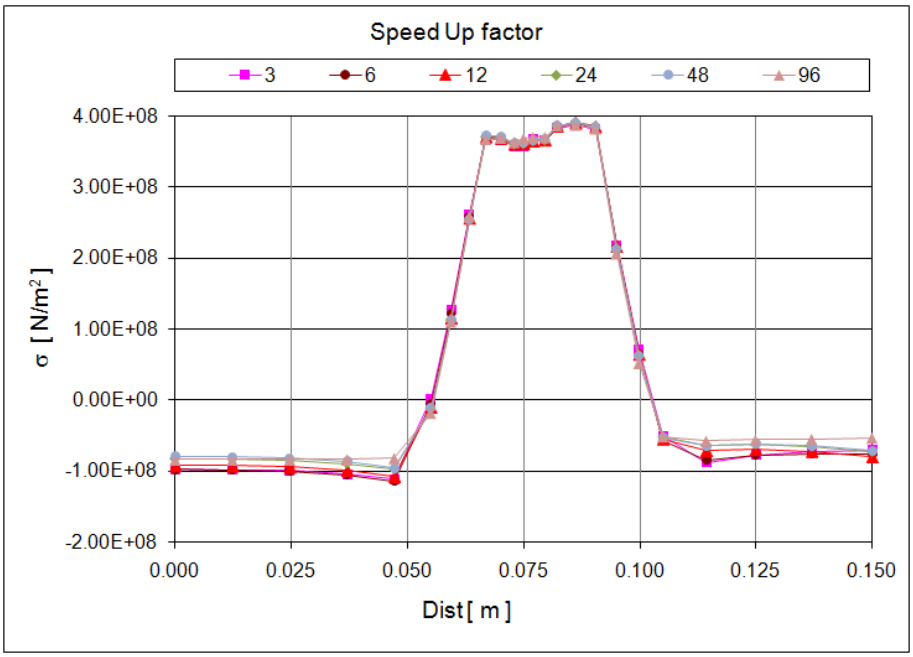

Figure 8.53: Axial residual stress (SZ) across the width of the flange: full UY support.

Figures 8.53 and 8.54 show the axial (SZ) and transverse (SY) residual stresses across the width on the top surface of the flange, respectively. The axial stresses do not display significant variation with the Speed Up factor, just as in Figure 8.47. However, comparing Figures 8.54 and 8.48 there is a very significant difference, which has nothing to do with the Speed Up factors. The girders of this study are much longer and are therefore much more flexible. According to the boundary conditions shown in Figure 8.8 every node at the bottom face of the flange is supported vertically. While there are no horizontal supports, all the three nodes in one section are fixed in the vertical direction which means that the rotation of the edge of the flange is constrained. This does not seem to have significant importance in the case of the shorter model since the transverse stresses near the edge remain close to zero. However, in the case of a much longer girder these stresses are significantly higher as seen in Figure 8.54. This issue is addressed by additional calculations that follow

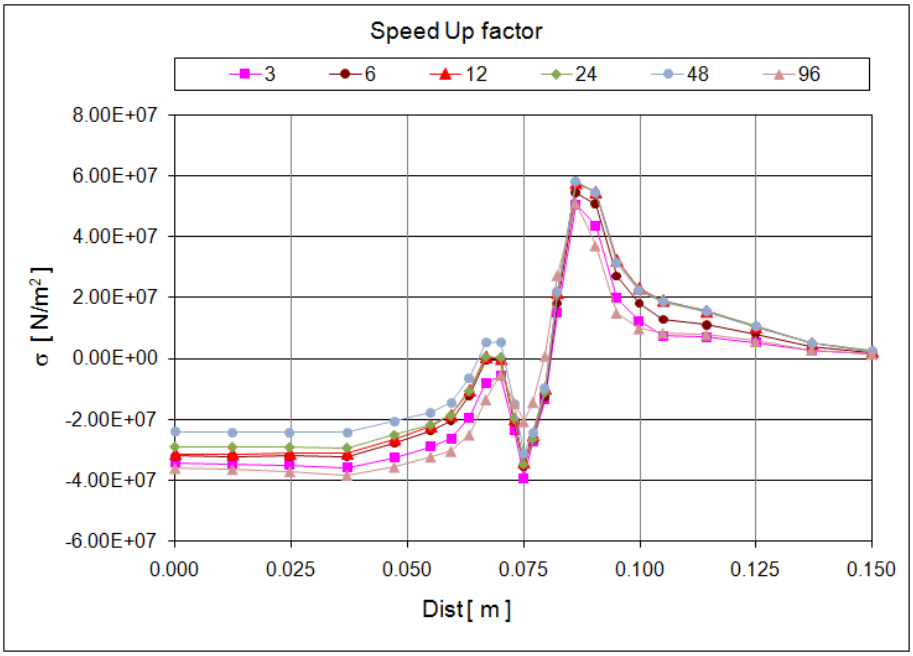

Figure 8.54: Transverse residual stress (SY) across the width of the flange: full UY support.

the discussion of the present results. Even if the model seems over-constrained it is useful to analyse the effect of the Speed Up factor on the deflections of the plates of such a long model and see how it differs from that of the short models.

Figures 8.55 and 8.56 show the vertical deflection (UY) of the centre line of the web (path W1) and the horizontal deflection (UX) of the top edge of the flange (path F2), respectively. It can bee seen immediately that there is a much better agreement among the results than in the case of the short model. The reason for this can be deduced from the deformed shape. Clearly the stresses introduced by welding forced the plate of the web to buckle. This seems to reduce significantly the role of the Speed up factor.

When a smaller Speed Up factor is used the stresses accumulate more gradually especially if compared to the case of the highest factor when the full weld is done in one step and the cooling introduces the compressive stresses outside of the weld along the full length of the girder. It can be seen at the beginning of the girder (the negative side of the chart) that the smaller the Speed Up factor is the more the curves are shifted towards the end of the girder (right side). When the welding slowly advances at the beginning the accumulated stress are not high enough to provoke buckling. By the time the stress level is high enough the start of the girder

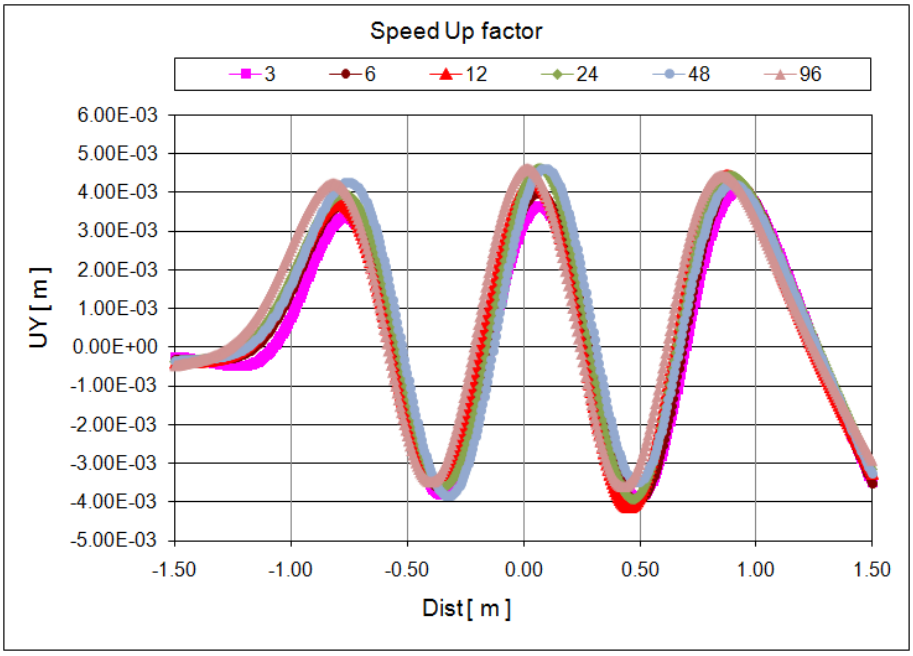

Figure 8.55: Vertical deflection (UY) of the centre line of the web (path W1): full UY support.

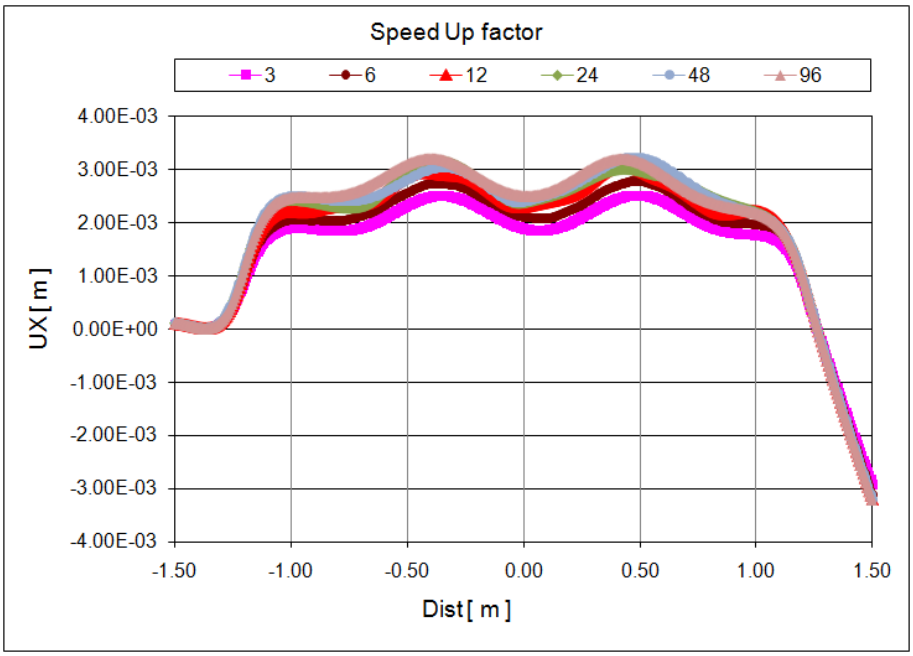

Figure 8.56: Horizontal deflection (UX) of the top edge of the flange (path F2): full UY support.

is more stiff since the connection between the two plates are stronger than in the rest of the structure. This is not the case when the full weld is done in one step since there is no difference between the start and the end of the weld. The results also

very clearly demonstrate the effect of the tack weld at the start of the girder and the lack of it at the other end. The deflections of the flange (Figure 8.56) show very similar results. In the next example the support condition of the flange is changed in order to eliminate the high transverse stresses at the edge of the flange.

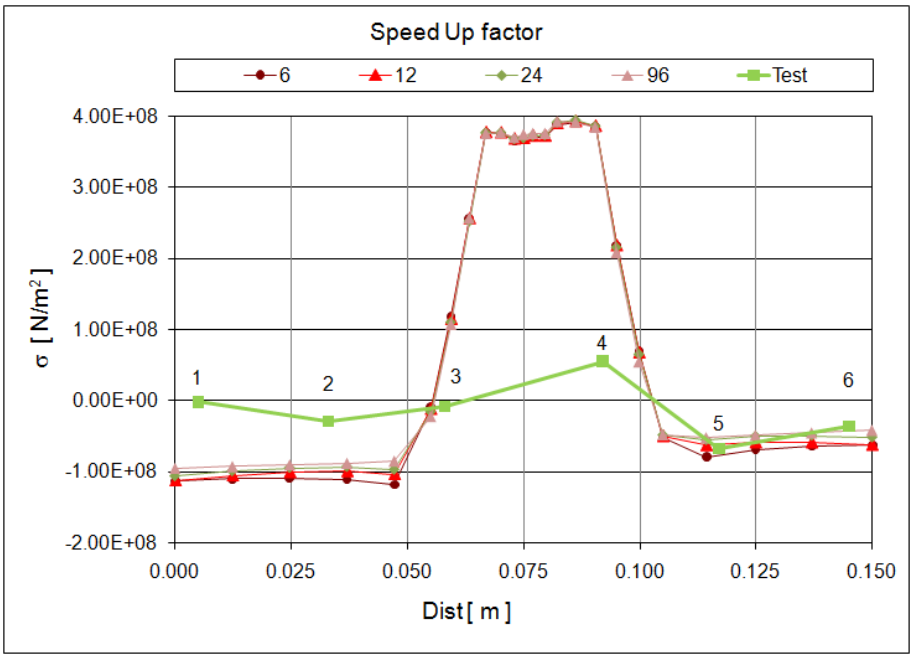

Figure 8.57: Axial residual stress (SZ) across the width of the flange (path FC1): UY support every 500mm. Residual stress measurement result.

In the factory when a girder leaves the welding machine it is supported by a series of rollers that are placed at a regular distance of approximately $500mm$. In this example instead of supporting every single node on the bottom face of the flange only sections at every $500mm$ are supported. The positions of the supports do not change during the analysis and they are placed in such a way that there are no supports at half length of the model. The location of the first section is $250mm$ from the start of the girder. As a result of the good agreement among the previous results, only a reduced number of cases are studied with Speed Up factors of 6, 12, 24 and 96.

No important changes in the axial stresses can be observed in Figure 8.57. However, the figure also includes the results of the residual stress measurements shown in Figure 7.28 in Section 7.3.3. This objective of the simplified measurement method was to focus on the comparison of the two fabrication methods (double-sided fillet

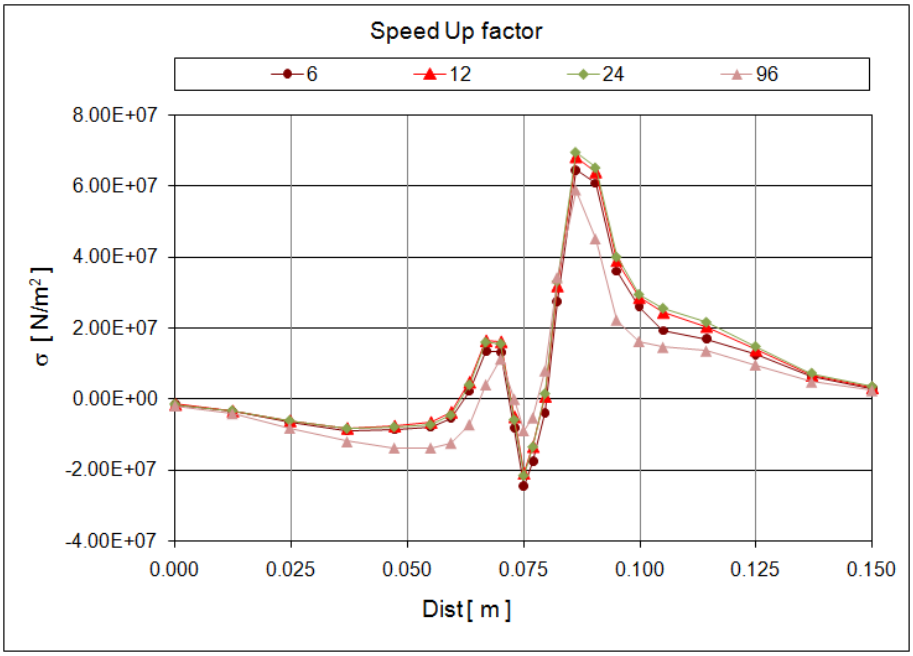

Figure 8.58: Transverse residual stress (SY) across the width of the flange (path FC1): UY support every 500mm.

weld vs. single-sided fillet weld) and not on the exact residual stress values. Nevertheless, it is worthwhile to compare the measurements with the simulations. The measured stress values on the left side of the chart (gauge No. 1 and 2) are far from the calculated ones but they show much better agreement at the other locations. The near zero value at gauge No. 3 is very close to the calculated stress. The value at No. 4 correctly shows the increase of the stress but predicts a narrower zone of high stresses. Finally the values at gauges No. 5 and 6 are in very good agreement with the simulation results.

The transverse stresses, as expected, are rather different and are shown in Figure 8.58. On the left side stress values are at zero which also causes the redistribution of the stresses in the rest of the flange. While the overall shape of the distribution remains similar, there is a general shift towards the positive stress values.

Figure 8.59 shows the vertical deflection (UY) of the centre line of the web (path W1). The results show similar tendencies to the results of the case with full support of the flange edge, the differences in the magnitudes of the deflections are also very similar. However, the curves are much more similar as there are no differences in their wave lengths. The horizontal shift of the curves at the start of the girder, which can be clearly observed in Figure 8.55 seems to have disappeared. However, there

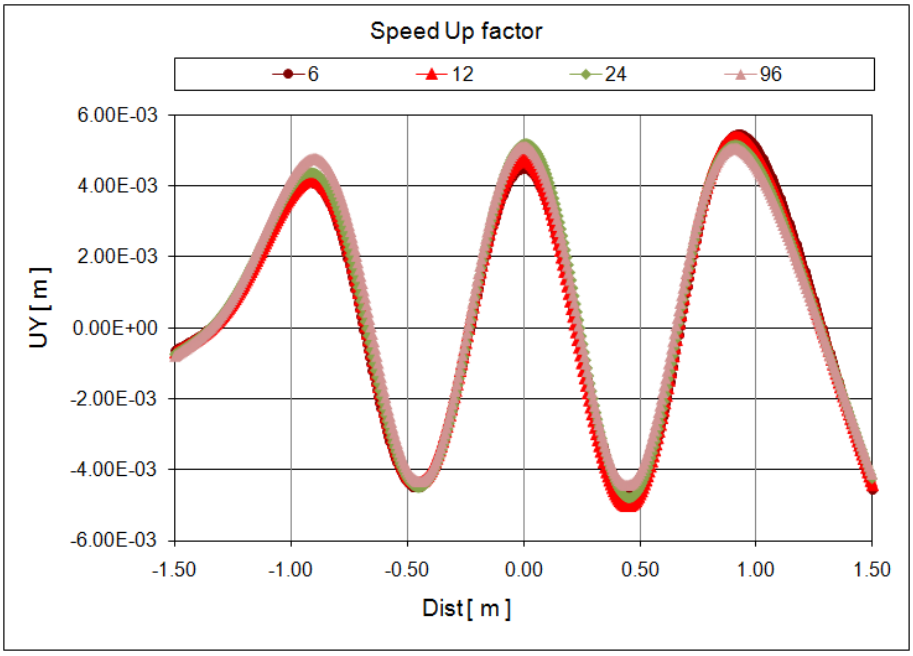

Figure 8.59: Vertical deflection (UY) of the centre line of the web (path W1): UY support every 500mm.

is another phenomenon to be noticed. In the cases with lower Speed Up factors the amplitude of the curves are getting gradually larger closer to the end of the girder. In the case of Speed Up factor 96 (*i.e.* single welding step) this cannot be observed. Nevertheless the web deflections of the different Speed Up factors appear very similar and they all seem a reasonable approximation of imperfections in a virtual experiment. As a result of the less rigid support conditions the horizontal deflections of the flange are significantly larger than in the previous case but the shape is very similar. All the results are not show here but one case can be seen in Figure 8.61.

The results of the different support conditions are compared in Figures 8.60 and 8.61 for the cases of the maximum Speed Up factor. The magnitude of both the deflections of the web and the flange are amplified as a result of the new support conditions. The number of waves is the same, while the wave lengths are slightly longer when the flange is not supported completely along its edge. The same conclusion can be drawn from the comparison of the calculations with other Speed Up factors therefore those results are not shown.

In Section 2.3.3 the imperfection measurement results of a type S1 specimen are shown in Figures 2.2 and 2.3. The deflections in the middle of the web (at

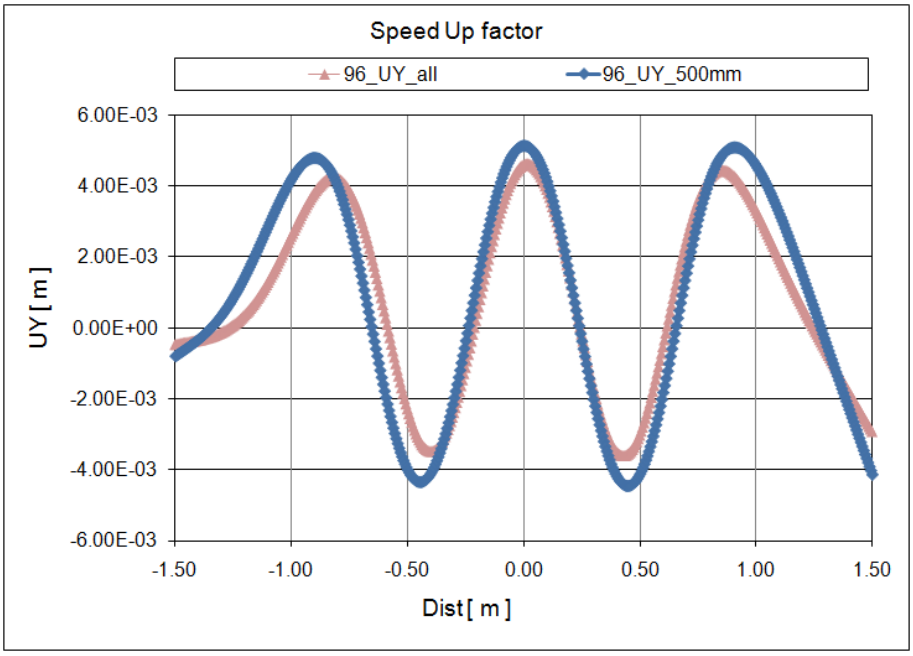

Figure 8.60: Vertical deflection (UY) of the centre line of the web (path W1): Speed Up 96; different flange support conditions.

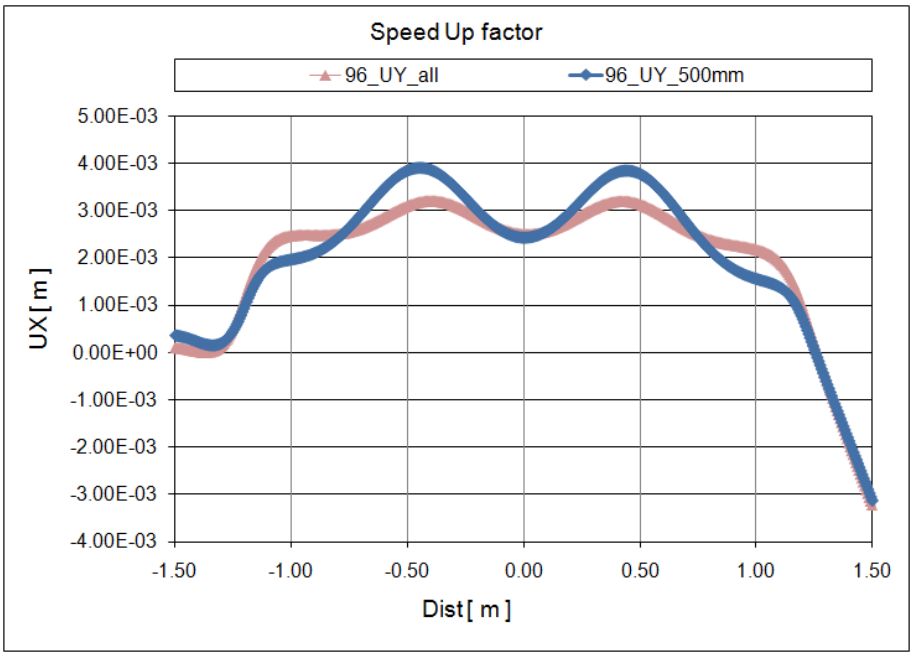

Figure 8.61: Horizontal deflection (UX) of the top edge of the flange (path F2): Speed Up 96; different flange support conditions.

height of b/2) are compared with the results of the simulation in Figure 8.62 (the simulation result is the same as the curve for Speed Up factor of 6 in Figure 8.59 and the notion "short" refers to the fact that the length of the weld is shorter than

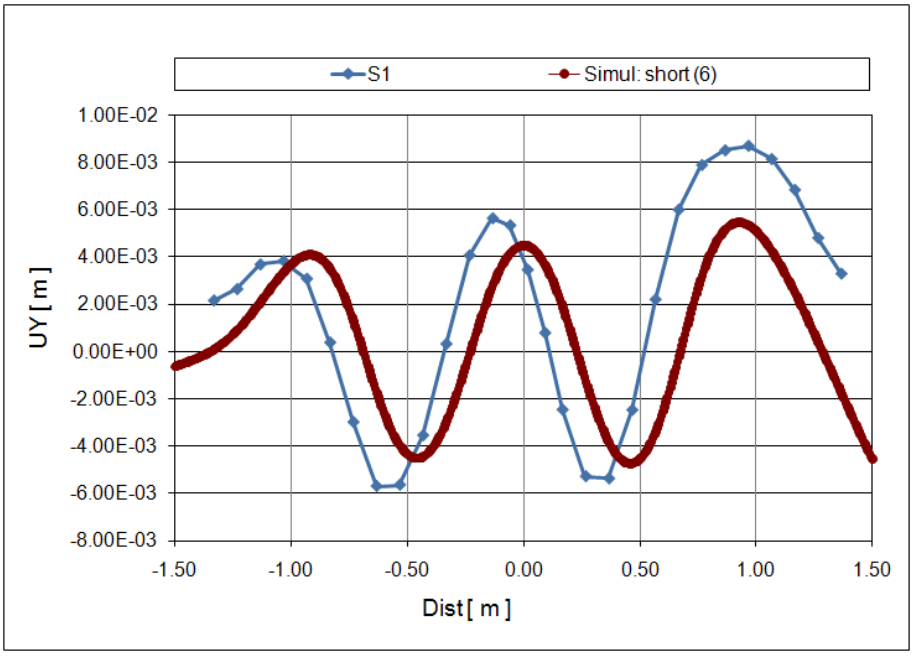

Figure 8.62: Vertical deflection (UY) of the centre line of the web (path W1): comparison of measurement and simulation results.

the length of the girder). The wave lengths of the curves are the same even though there is a horizontal shift of about $135mm$ between the two curves. Both curves feature the same tendency of increasing deflection amplitudes towards the end of the girder (right side of the chart). While the curves are very similar, the amplitudes of the deflections in the measured values are higher than in the numerical results especially near the end of the girder. As discussed before the welding machine could not complete the weld from the start to the end of the girder and the same conditions are assumed in the simulation. However, in the factory once the automatic welding is completed the welding at two ends of the girder is finished by manual arc welding using double-sided fillet welds. The imperfection measurements were performed on the specimen in its completely welded state. While no experimental or numerical results are available to support this idea it is likely that the additional welds at the ends of the girder cause the differences between the curves. This is also discussed during the evaluation of the results of the next example.

The results of the calculations on a girder of length of $3000mm$ suggest that when bucking becomes the driving force behind the deformations the role of Speed Up factors becomes less important. In the next step girders of $6000mm$ are studied to see if the above statement remains valid. In these examples the chosen Speed Up

factors are equivalent to completing the welding either in eight welding steps or in a single welding step (*i.e.* the maximum value of the factor). The actual values of the factors depend on the full length of the welding.

There are two types of girder to be studied: short and full weld length. The first type (short weld model) is fabricated with a 300mm long section without welding at the start and the end of the girder with a tack weld at the start (same case as for the girder of 3000mm). Figure 8.63 shows the vertical deflection (UY) of the centre line of the web (path W1).

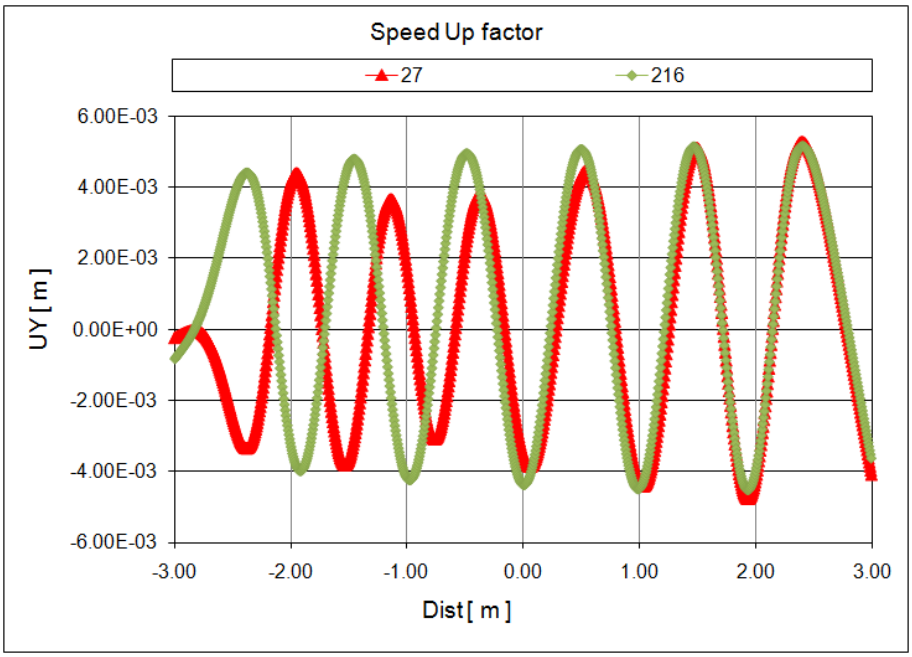

Figure 8.63: Vertical deflection (UY) of the centre line of the web (path W1): 300mm long section without welding.

It can be seen that the deflections are very similar in the second half of the girder but they are rather different at the start. Even though there is no doubt that the deflections are dominated by the buckling of the web, it cannot be said that the Speed Up factor does not significantly alter the deformed shape of the web unlike in the previous studies on a girder with a length of 3000mm.

In the real fabrication when the automatic welding is finished they use manual arc welding to complete the welds at the two ends of the girder. While the numerical model in its present development state is not capable to simulate such case, an analysis assuming that the full length of the weld is done in the welding machine can be performed. This is the second type of girder (full weld model) in the study.

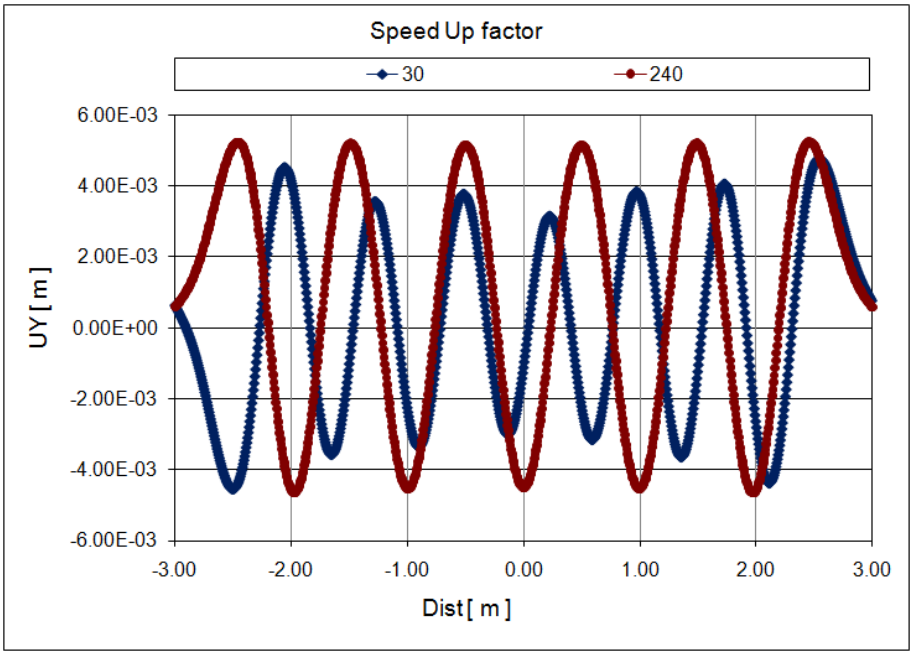

Figure 8.64: Vertical deflection (UY) of the centre line of the web (path W1): full length of girder welded.

Figure 8.64 shows the vertical deflection (UY) of the centre line of the web (path W1). The differences between the two cases of Speed Up factors are even more pronounced.

Figure 8.65 shows the comparison of the web deflection measurements and the results of the numerical simulation of the fabrications. The measurements on specimens L3 and L4 (the same specimens that have been used for the calibration of the heat source model in Section 6.3) are presented (same results as in Figure 2.4). The first thing to notice is that the results of the two measurements are rather different especially at the right side (end of the weld) of the chart even though the specimens have identical characteristics and they were fabricated one after the other under the same conditions. However, both show that the deflections at the two ends are greater than in the centre of the girder.

The numerical results are the one with eight welding steps for both types of model with full weld length and with shorter weld length (same results as the curve for Speed Up factor of 27 in Figure 8.63 and the curve for Speed Up factor of 30 in Figure 8.64). It can be seen immediately that the result of the simulation with the shorter weld (red curve) is much more similar to the measurements, especially to the deflection of specimen L3. The number of waves is the same and the wave lengths

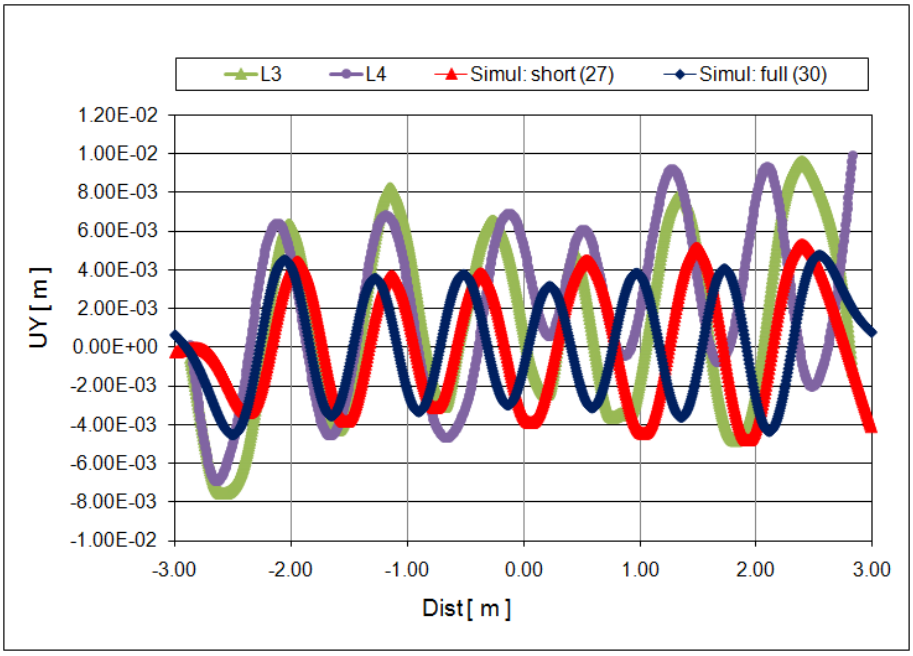

Figure 8.65: Vertical deflection (UY) of the centre line of the web (path W1): comparison of measurement and simulation results.

are also very close. The reason for this is that doing the analysis with a shorter weld (*i.e.* with a section of $300mm$ at both ends of the girder without welding) resembles much more the real fabrication conditions. During automatic welding only this part of the girder is welded and that is when the initial deformations develop in the web. Finishing the welds between the web and the flange at the two ends by manual arc welding would affect these initial deformations but very likely would not change significantly their nature (no experimental or numerical results are available at this stage to support this supposition). However, the case of the model with full weld length represents a practically different fabrication procedure which results in different web deflection pattern with one more wave.

Nevertheless, the tendency of the deflections being smaller in the centre of the girder can also be observed in both simulation results even though the variations of the deflections along the length of the girder are much less pronounced than in the measured deflections. In the centre of the girder both the amplitude of the waves (*i.e.* not the actual deflection values) and the wave lengths are comparable between the measurements and the simulations. Further away from the centre the wave lengths are somewhat similar but there are big differences in the amplitudes of the waves.

For the evaluation of the comparison it is important to point out some significant differences between the real specimens and the simulation, some of which have already been discussed. In the two simulations it is assumed that the welding is conducted in the same way from the start of the weld to the end of it in one continuous welding. In the fabrication the welding at the two ends of the specimens are finished off by manual arc welding on both sides of the web (*i.e.* with double-sided fillet welds) after the girder is removed from the welding machine. At the two ends of the specimens vertical stiffeners were also welded to the web with double-sided fillet welds using manual arc welding. In the simulations no welding of stiffeners is considered. In the numerical model it is assumed that the welding process and the girder is symmetric therefore only half of the girder is modelled. In the welding machine the two welding heads at the opposite edges of the web were not perfectly aligned, there was about a $3cm$ difference in their axial position. While this does not seem significant at first, the welding engineer of the factory assumed that this difference was the reason for many long girders becoming notably curved during fabrication.

8.5 Summary and conclusions

The development of the thermal stress analysis model of welding is presented in this chapter. Details of the modelling strategy such as the importance of contact between the plates, and details of solution strategies such as the gradual activation of the elements in the weld seam are discussed here. It is also demonstrated that the numerical simulation based on the equivalent prismatic heat source model and a simplified material model using material properties specified in EC3 for analysing structural response in fire is capable of reproducing and therefore studying successfully a number of phenomena (e.g. effect of material properties, preheating, displacement constraints) during welding.

A technique of using a so called "Speed Up" factor to reduce the computational cost is proposed for long girders. In the case of the short models this factor can alter the deflections very significantly which makes the method very unreliable unless the main interest is the residual stress development in the girders in which case it can be employed successfully. However, in the case of long girders (*i.e.* girders in which the deformations are dominated by the buckling of plates provoked by the thermal

stresses of welding) the use of Speed Up factors is much more promising. This is not to say that they do not influence the deflections in the girder. There are differences but the main characteristics of the deformed shape of them are very similar which can make such an approximation acceptable depending on the use of the results.

The advantage of using the maximum Speed Up factor (*i.e.* the full length of the weld is done in a single welding step) is the smooth residual stress distribution along the length of the girder. However, at the same time it is also its main disadvantage since the differences in the deflections are also smoothed out. The disadvantage of using a lower factor is that the residual stress distribution can be slightly rough. On the other hand, in this way the variations in the deflections along the length of the girder can be also captured. Of course using a very low value or even one for the Speed Up factor overcomes these unwanted side effects but it comes at a very high price in terms of computational cost. One need to consider the aim of the analysis (residual stresses or deflections or both) and the available computational power and time to find the optimal simulation parameters.

The calculated web deflections in girders of $3000mm$ and $6000mm$ in length are also compared to the measurements of similar specimens. Even though there are some differences between the assumptions of the simulations and the actual fabrication conditions (e.g. welding at the two ends of the specimens), the deformed shapes produced by virtual fabrication show reasonable agreement with the measurements.

In the next chapter the numerical model development for the simulation of the fabrication of plate girders are reviewed step by step and the virtual fabrication of a full plate girder is presented as well. Finally, this virtually fabricated specimen is also used in a virtual experiment.

Chapter 9

From virtual fabrication to virtual experiments

9.1 Introduction

In the previous chapters the development steps of the numerical model for the simulation of fabrication of full size welded steel plate girders are discussed in detail. In this chapter all these are put together to demonstrate that with the model developed it is possible to virtually fabricate specimens for virtual experiments. Very briefly the most important aspects of the simulation are summarised and a complete example is presented with results not seen in the previous parametric studies. The geometry of specimens L3 and L4 is selected from Table 2.1 in Section 2.2 for the example. Since the simulation of the fabrication is followed by a virtual load bearing test the full girder needs to be modelled unlike in the previous examples, in Chapter 8, where only half of the girder with symmetry boundary conditions was considered.

9.2 Thermal analysis

9.2.1 Heat source

The heat source model is the single most important feature of the simulation. It is the main driving force behind the temperature distribution in the structure which in turn determines the material behaviour and the development of imperfections (stresses and deformations) in the structure. Since phenomena inside the weld pool

are of no interest a heat source model based on prescribed temperatures is recommended. These models require the knowledge of the weld pool shape since the temperature values need to be defined on the interface separating the solid and liquid phase of the welded material. In this research the "equivalent prismatic heat source model" has been developed that is based on the idea that the volume of the weld pool can be approximated by the cross-section of the weld (using either actual values obtained from macrograph images or design values) and a fictitious weld pool length (for details see Section 6.2). The prescribed temperature value is equal to the liquidus temperature of the material (1520°C for mild carbon steel). The fictitious weld pool length is the only unknown parameter that are very easy to calibrate even with limited temperature data. To obtain such temperature date during the fabrication of plate girders a temperature measurement method has been developed that are easy to set up in a factory environment with minimal disturbance of the fabrication process (for details see Section 5.2).

In the example: Weld leg: $5.2mm$; weld throat: $5.5mm$; length of equivalent prismatic heat source model: $25mm$; welding speed: $22mm/s$

9.2.2 Material properties

Apart from the heat source model the other critical parameter of the simulation is the material properties at elevated temperatures. As a result of intense research in fire engineering and in welding simulation more and more data are available, however, they are still not easy to obtain. A good starting point is Eurocode 3, Part 1-2, EN 1993-1-2: Structural fire design [85] that contains steel material properties up to 1200°C. Even though welding involves higher temperature ranges, it is common practise to ignore material property changes above a certain cut-off temperature. The 1200°C limit is an acceptable cut-off temperature since lower temperature ranges play more important role in the development of residual stresses. The properties remain constant above the cut-off temperatures (for details see Section 6.2).

In the example: all properties are taken from EC3 (Figure 6.3).

9.2.3 Boundary conditions

The usual thermal boundary conditions are free convection and radiation to the ambient. The two can be combined into a single combined heat transfer coefficient to avoid solving the non-linear equations of radiation boundary conditions. The actual value of the combined heat transfer coefficient has very little effect on the cooling rate and the temperature distribution during welding and at the beginning of the cooling since in the high temperature ranges the heat transfer in the welded plates is dominated by heat conduction. It is only in the last stage of the cooling closer to room temperature when the heat transfer coefficient strongly influences the final cooling time (for details see Section 6.2). Even a constant coefficient gives acceptable results, however, the use of a temperature dependent coefficient is recommended since it does not increase the computational cost and is more realistic.

In the example: a temperature dependent combined heat transfer coefficient is used (curve Var_2 in Figure 6.7).

9.2.4 Solution control

Only implicit time integration is considered here (for a detailed discussion on the use of explicit and mixed time integration schemes see Chapter 4). The thermal analysis usually does not result in any numerical difficulty or convergence problems. The time steps are governed by the accuracy of the analysis (for details see Section 3.3.6). The temperature difference between the ambient temperature and the welding temperature (*i.e.* the liquidus temperature) is very large therefore at the beginning of cooling the temperature gradient (*i.e.* the cooling rate) is very steep. Even in a very short time step it is easy to jump several hundreds of degrees. Even if convergence can be easily achieved the time step size needs to be limited by the maximum allowable temperature change in one step. It is recommended that no more than a few tens of a degree change is present in a single step. In the examples presented such a limit is set to 50°C, however, in most steps the actual change is much less (using ABAQUS it is very easy to comply with such a criterion since the temperature change limit per time step can be defined as one of the solution control parameters, however, in ANSYS such control does not exist therefore the results need to be revised and the time step control parameters might need to be adjusted accordingly).

In the example: the maximum temperature change per time step is limited to 50°C.

9.3 Thermal stress analysis

9.3.1 Material properties

Material properties not only depend on the actual temperature of the material but also on the microstructural changes of it. Such changes on the other hand not only depend on the actual temperature but on the entire temperature history (details are included in Sections 3.3.3 and 8.2.1). As a result of this properties such as thermal elongation cannot be represented by a single curve but several curves are necessary that take into account the peak temperature and the cooling rate. Working with the mechanical material properties at elevated temperatures obtained from Eurocode 3, Part 1-2, EN 1993-1-2: Structural Fire Design [85] means that the material model is simplified and the same material behaviour is assumed regardless if the temperatures are increasing or decreasing (*i.e.* a single curve is used for thermal elongation). As with the thermal properties, data are available up to 1200°C where the strength properties all have zero values specified. This leads to numerical problems in the analysis therefore a small but non-zero values need to be used at and above 1200°C. It is recommended that half of the values specified at 1100°C should be used (for details see Section 8.2.1).

It is important to take into account the effect of melting on the development of stresses in the structure. When the material reaches melting temperature it becomes completely stress free. In the numerical model this means that the accumulated plastic strains need to be reset to zero. In ABAQUS this can be achieved by simply specifying the annealing temperature (set to be equal to the melting temperature) in the material properties. In ANSYS it requires several actions to be taken. To make sure that the elements that reaches melting temperature become stress free they need to be deactivated ("killed") and reactivated ("born") to lose their stress/strain history. In the material properties the reference temperature that is used to calculate thermal stresses needs to be set to the melting temperature too (for details see Sections 4.3 and 8.2.2).

In the example: all properties of S355 steel are calculated according to EC3 (from Figures 8.1 to 8.4) with the measured yield strengths of the plates being taken into

account (Table 2.2). The material properties of the weld seam are the standard S355 properties. Strain hardening below 400°C is also considered.

9.3.2 Boundary conditions

Unlike in the thermal analysis, the mechanical boundary conditions need careful considerations. The applied displacement constraints can significantly alter the distribution of residual stresses and the deformations of the plates. As a general rule more constraints result in higher residual stresses and smaller deformations (for details see Section 8.3.8). Depending on the welding process simulated, it is very likely that the support conditions are constantly changing with the progress of the welding (for details see Section 8.3.9). The correct application of the boundary conditions requires a detailed knowledge of the welding equipment, however, often such information is not available when the simulation is done. It that case it is important to study several possible scenarios to make sure that the numerical model is not overconstrained for the deformations to develop.

Welding simulation has a special feature that can be discussed together with the boundary conditions. With the progress of the welding the relationship between the plates being welded changes constantly. Plates that were separated before become connected and therefore their movements become more restricted as well. In the simulations this is achieved by the activation of the elements of the weld seam once the welding heat source has passed those elements which also makes sure that the elements are stress free as explained in the previous section (for details see Section 8.2.3).

In the example: the bottom edges of flanges are permanently supported at every $500mm$ as explained in Section 8.4; displacement constraints following the position of the welding heat source are shown in Figure 8.42 with LRoller set to zero.

9.3.3 Decoupled solution options

In a decoupled thermomechanical analysis the thermal and the mechanical analyses are solved separately (for details see Section 8.2). One option is to run the two analyses completely separately. Once the thermal part has finished during the stress analysis for each load step the corresponding temperature distribution is read from

the result file of the thermal analysis and applied to the structure as nodal loads. There is only a one-way interaction between the thermal and the mechanical parts of the simulation.

The other option is to employ a staggered solution procedure in which the two analyses are solved alternating, one step at a time. One solution step of the thermal analysis is followed by a mechanical analysis step. The advantage of this procedure is that after the mechanical step the geometry of the thermal model can also be updated to take into account any deformations that might alter the thermal boundary conditions (*i.e.* there is a two-way interaction between the thermal and the mechanical parts of the simulation). This is something to consider in the case of complex geometries such as a welded joint with several welds.

In the example: the two analyses are run completely separately.

9.3.4 Solution control

When the elements are activated their temperature is at near melting temperature which means that their mechanical properties such as the Young's modulus are near zero. If inside the weld seam there are several layers of elements they need to be activated layer by layer to minimise numerical problems and avoid the risk of the failure of the analysis. At any given load step of the stress analysis the temperatures are read from the results file of the thermal analysis and applied as loads in the stress analysis. If there are no temperature results saved at the exact time of the load step of the stress analysis the software can interpolate between the available results. However, it is better if the load steps are synchronised between the two analyses (if a staggered solutions is followed this is done by default) and the extra load steps required by the activation of the layers of elements in the weld seam in the stress analysis should also be included in the thermal analysis even though it would not be necessary from a numerical point of view (for details see Section 8.2.3).

In the example: within the weld seam there are three layers of elements as shown in Figure 8.9 and they are activated in separate loads steps of very short time duration (0.01s).

9.3.5 Reduction of welding steps

The number of load steps in the analysis can be reduced by increasing the length of the heat source and the welding speed by the same factor. The total amount of heat introduced during welding is not affected by the use of such a Speed Up factor nevertheless it influences the results of the analyses. The use of a Speed Up factor should be carefully evaluated since under certain circumstances it can significantly alter the results (for details see Section 8.3.10). If the geometry of the plate girder is such that the welding induced stresses produce buckling in the plates, the influence of the Speed Up factor on the calculation results are greatly reduced. The maximum value of the Speed Up factor is determined by the ratio of the total weld length and the length of the heat source model. The use of the maximum value means that the full length of the weld is completed in a single welding step. This is a very fast solution but can not account for the variation of residual stresses and deformations along the length of the girder as a results of the actual gradual progress of the welding (for details see Section 8.4).

In the example: two cases are considered. In the first one the full length of the weld is completed in one welding step (Speed Up factor of 240). In the second one the full length of the weld is completed in eight welding steps (Speed Up factor of 30).

9.4 Results of the virtual fabrication

The purpose of the following series of figures is to link the evolution of the temperature distribution during the fabrication process to the evolution of the web deflections in the welded plate girder. The temperature distribution is always shown on the deformed shape of the girder. The deformations are magnified by a factor of 10. The results cover the full fabrication process from welding to the end of cooling.

In the figures the girder is shown at a low viewing angle which helps to visualise the variation of the deformations along the length of the girder. Only the results of the case with a Speed Up factor of 30 are shown here. The end of the girder closer to the viewer is where the welding terminates.

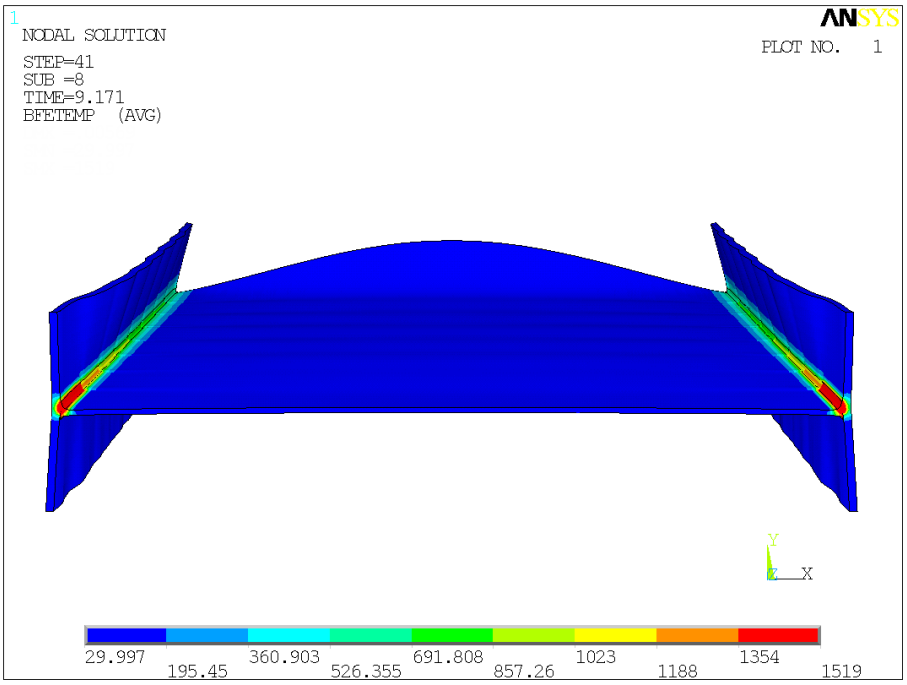

Figure 9.1: Temperature distribution shown on the deformed shape of the girder after the last welding step. Maximum temperature: 1519°C.

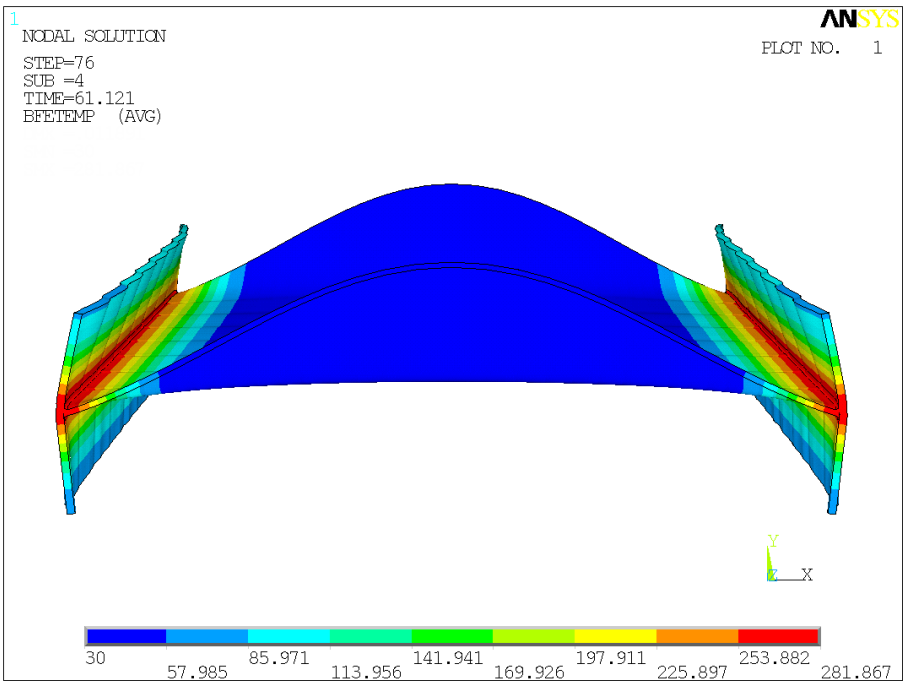

Figure 9.2: Temperature distribution shown on the deformed shape of the girder. Maximum temperature: 282°C. Maximum deflection in the web at the two ends of the girder.

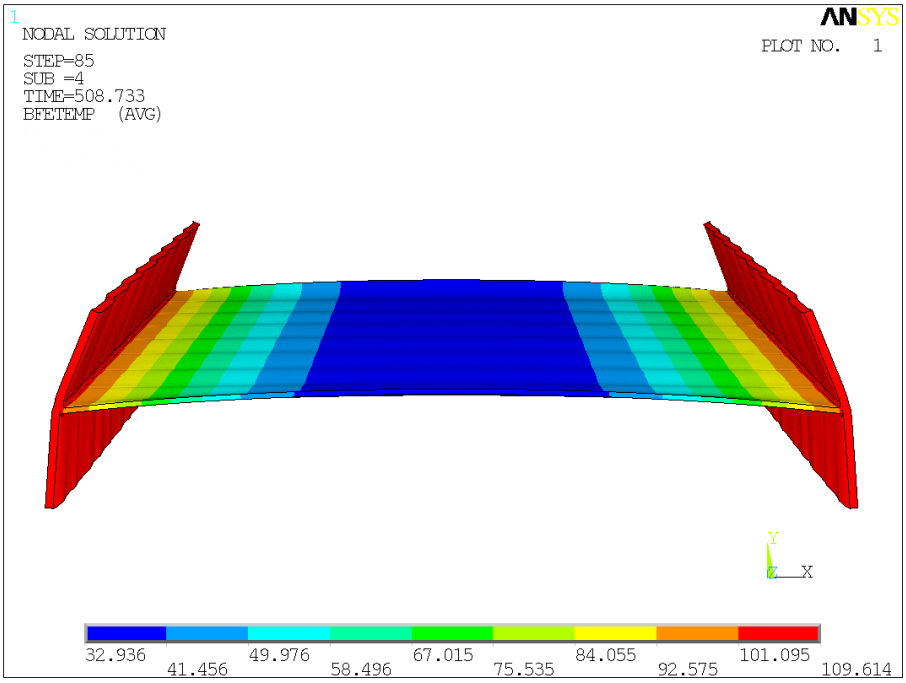

Figure 9.3: Temperature distribution shown on the deformed shape of the girder. Maximum temperature: 110°C. The deflections in the web have almost disappeared.

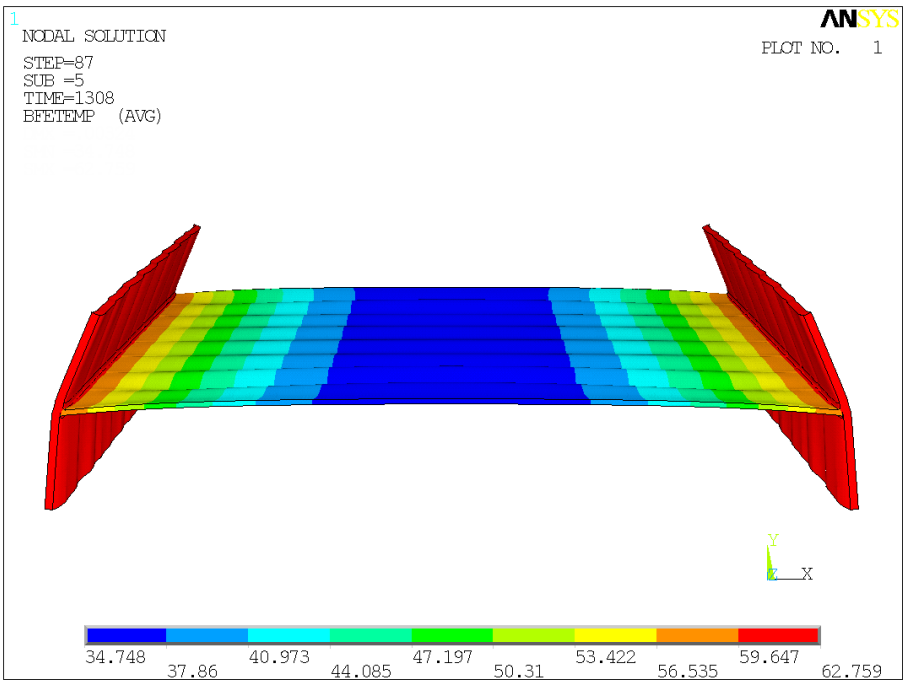

Figure 9.4: Temperature distribution shown on the deformed shape of the girder. Maximum temperature: 63°C. Buckling starts to develop in the web at the two ends of the girder.

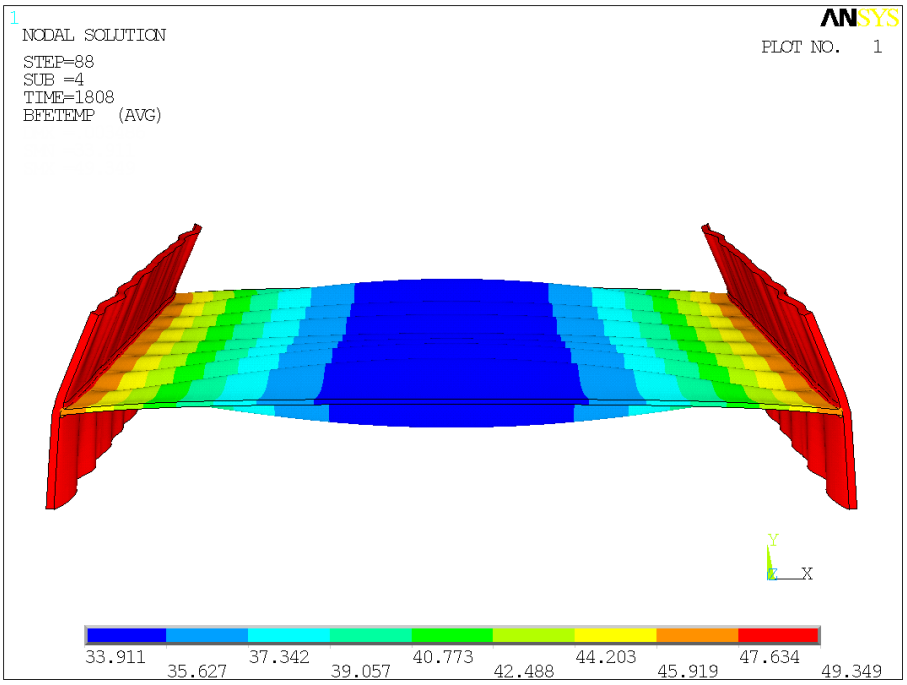

Figure 9.5: Temperature distribution shown on the deformed shape of the girder. Maximum temperature: 49°C. Buckling of the web is developed along the full length of the girder.

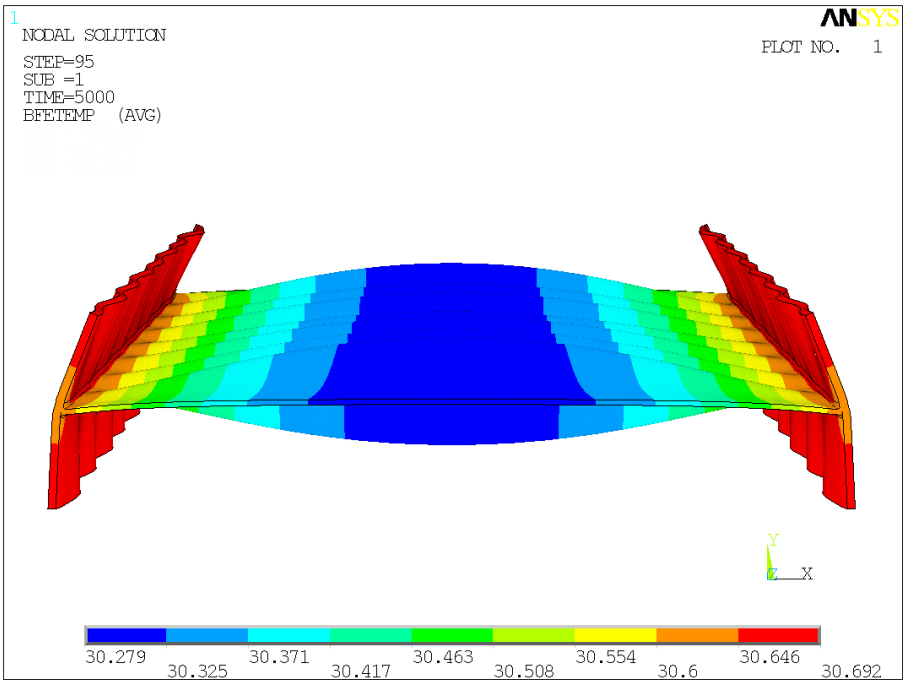

Figure 9.6: Temperature distribution shown on the deformed shape of the girder at the end of the cooling process. Maximum temperature: 30°C.

Figure 9.1 shows the temperature distribution just after the last welding step. Significant deformations in the web can be observed only at the very start of the girder (far from the viewer). Angular distortion of the flange is visible along the full length of the girder apart from the length of the segment of the last welding step. This is the result of the displacement constraints that simulate the rollers supporting the plates in the vicinity of the welding arc.

Figure 9.2 shows the temperature distribution in the load step when the deflections in the web at the two ends of the girder are the largest and the highest temperature value is around 280°C. The web does not exhibit any significant deformations in the centre part of the girder. This figure also demonstrates that only a very narrow zone around the weld seam is affected by relatively high temperatures.

Figure 9.3 shows the temperature distribution when the highest temperature value is around 110°C and the deflections in the web have been significantly reduced to almost its original pre–fabrication state.

The girder continues to cool down and when the maximum temperature is as low as around 63°C clear signs of the beginning of buckling in the web can be observed as shown in Figure 9.4. At this stage only the two ends of the girder exhibit more significant deflections.

By the time the highest temperature in the girder drops to around 50°C the waves of buckling can be clearly observed along the full length of the web as shown in Figure 9.5.

The last figure, Figure 9.6, shows the deformed shape of the girder at the end of the cooling when temperatures practically reach the ambient temperature of 30°C.

9.5 Virtual experiment

Numerical analysis of civil engineering structures are commonplace both in structural design and research. With the advancement of both software and hardware technology more realistic simulations can be performed that require also more realistic input including imperfections. For design purposes the standards provide guidelines on what level of imperfections should be considered. Eurocode 3 uses the concept of equivalent geometric imperfections. It is equivalent because it does not include only actual geometrical imperfections but takes into account other factors such as residual stresses, among others. Both global and local imperfection types

are considered and their magnitudes are provided in terms of other geometrical data (e.g. a fraction of the height of a panel). The global and local imperfections can be combined and as a result complex imperfection shapes can be applied to the numerical model of the structure designed.

In research, where actual structural behaviour is to be reproduced in a virtual environment these imperfections need to be as realistic as possible in order to obtain a realistic structural response. There are two main methods to consider imperfection in a virtual experiment:

- measurements and
- imperfections sensitivity analysis.

Measurements of geometrical imperfections can be easily performed and there are also several methods, including non-destructive ones, to measure residual stress level in a structure. Measurements provide the most reliable imperfection data for a particular specimen, however, it cannot always be applied in everyday work.

In an imperfection sensitivity analysis a number of different imperfections are studied based on previous experience with similar specimens, the eigenmodes of the model or if the shape of the failure mode is known a similar shape can be considered as initial imperfection as well. Different distributions of residual stresses can also be included in the analysis. While this method does not reproduce the exact imperfections it gives a very good idea concerning the importance of imperfections in the structural behaviour studied.

With the emergence of computational welding mechanics there is a now a third option: virtual fabrication. The actual fabrication of a welded plate girder can be simulated and the imperfections can be calculated. Such virtual fabrication of specimens can provide both geometrical and residual stress imperfections. Moreover, any plasticity that occurs during fabrication is carried forward and included in the virtual experiment, something that none of the other two options can be achieved with.

In the present example the virtual experiment follows the test set-up shown in Figure 2.5 in Section 2.3.5. When the virtual fabrication is complete it is first necessary to change the boundary conditions which are very different to that of the experiment. It is important to make sure that the displacement boundary conditions are applied in such way that the supported nodes are kept at their current

positions (*i.e.* the deformations as a result of the fabrication are respected) and are not returned to their original (*i.e.* pre-fabrication) position. In ANSYS this can be achieved by specifying %_FIX% as the prescribed displacement value [84].

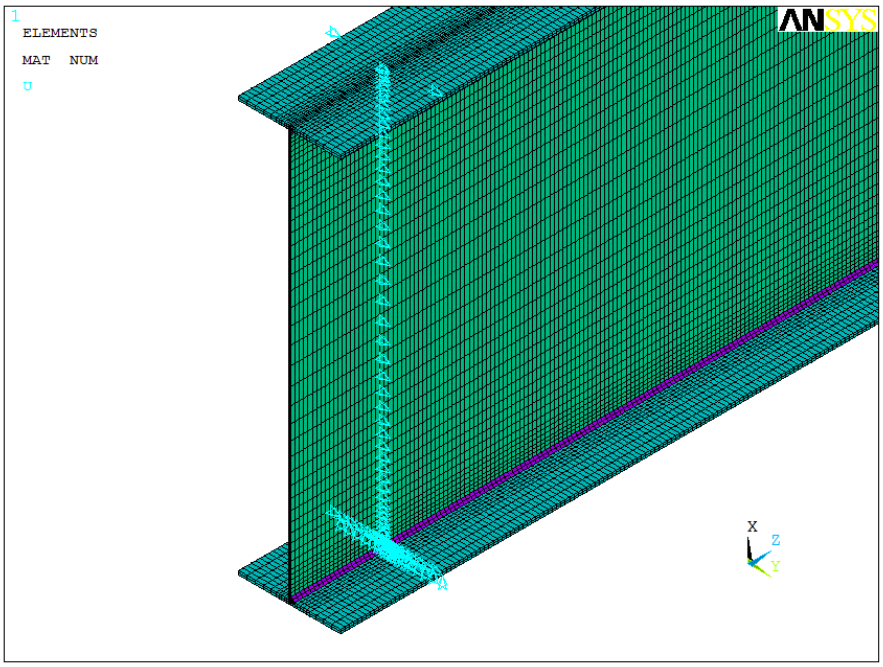

Figure 9.7: Displacement boundary conditions at the end of the girder.

Figure 9.7 show the displacement boundary conditions at the end of the girder. The bottom flange is supported both in the vertical (X) and transverse (Y) directions. At one end of the girder the centre of the flange is also supported in the axial (Z) direction. The two edges of the top flange are also supported in the transverse direction. These conditions represent a hinged fork support that prevents lateral deflection at the two ends of the girder. In the models of the numerical analyses [17] presented in Section 2.3.5, in the sections of the support there is a vertical stiffener welded to the web and to the flanges. This is considered in the present numerical model as lateral supports at the nodes of the web.

When the fabrication displacement constraints are removed and the ones of the experiment are applied the residual stresses are redistributed and the deformations might change too. The self weight of the specimen can also have an important effect as well since during fabrication the specimen is in a horizontal position unlike in the experimental set-up. The web deflections (UY) of the specimen with the boundary conditions of the experiment are compared to the deflections at the end

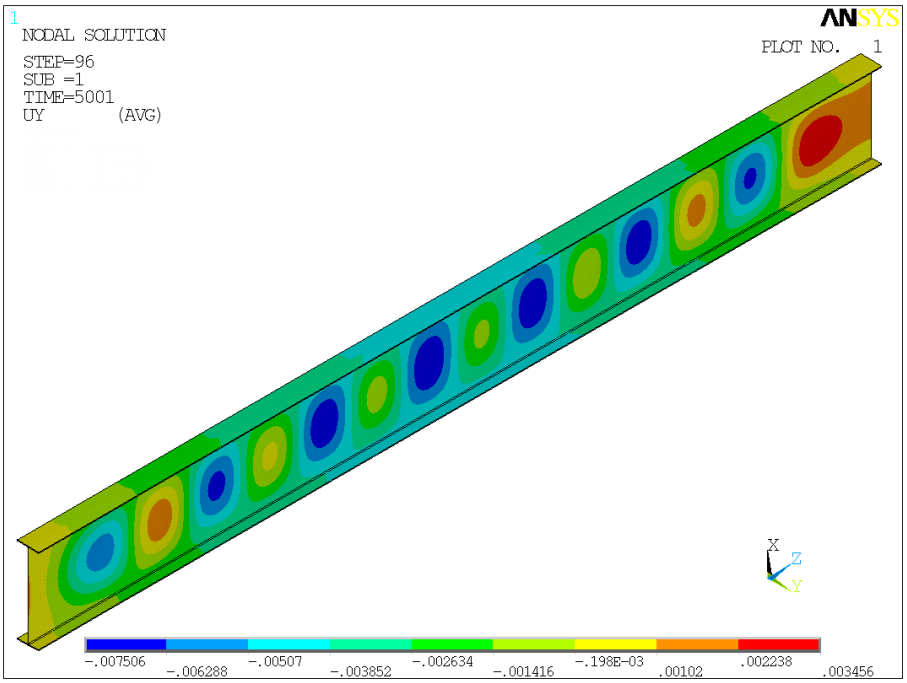

Figure 9.8: Web deflection before the experiment (Speed Up factor of 30).

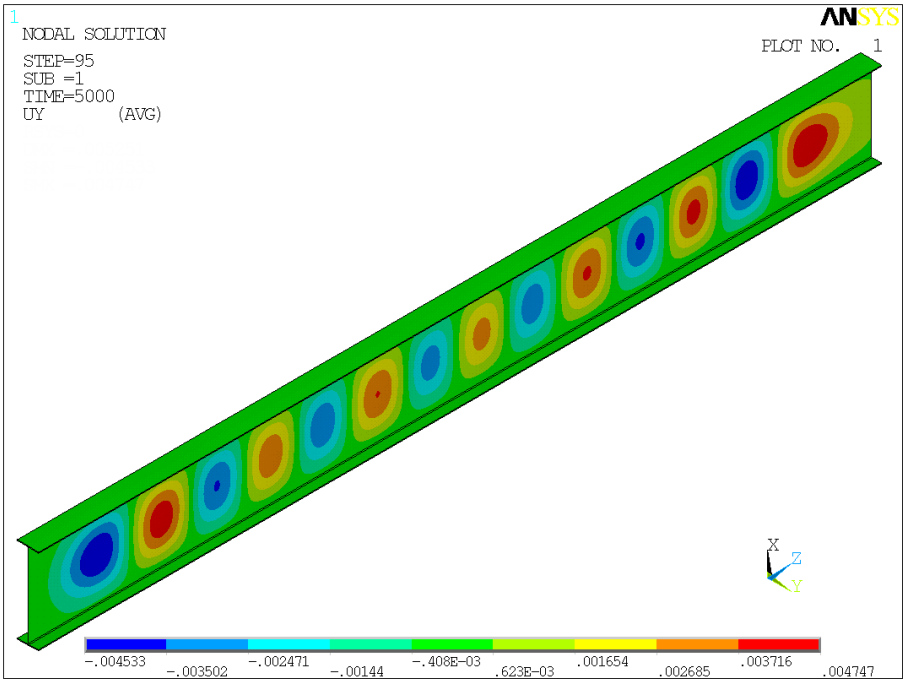

Figure 9.9: Web deflection at the end of the fabrication process (Speed Up factor of 30).

of the fabrication in Figures 9.8 and 9.9, respectively in the case with a Speed Up factor of 30. It can be seen that there is a shift towards the –UY direction. This is

because during fabrication the flanges are supported in the Y direction (*i.e.* vertical direction) at an interval of $500mm$ while in the experimental set-up only the two ends of the girder are restrained in the Y direction (*i.e.* lateral direction). Similar conclusions can be drawn from the results of the case with a Speed Up factor of 240 therefore those results are not shown here.

Figure 9.10 shows the part of the mesh where the loads are applied. A $100mm$ wide zone is considered for the load transmission which corresponds to the width of the rigid plate used in the experiment. During a real experiment when the flange undergoes severe deformations the load is transmitted only at the points where there is contact between the rigid plate and the flange. This effect is not considered in the numerical model in reference [17] therefore it is also ignored in the present model. The nodal forces are acting at each node throughout the whole analysis. This produces even more severe deformations in the flange that might reduce the calculated load bearing capacity of the specimen.

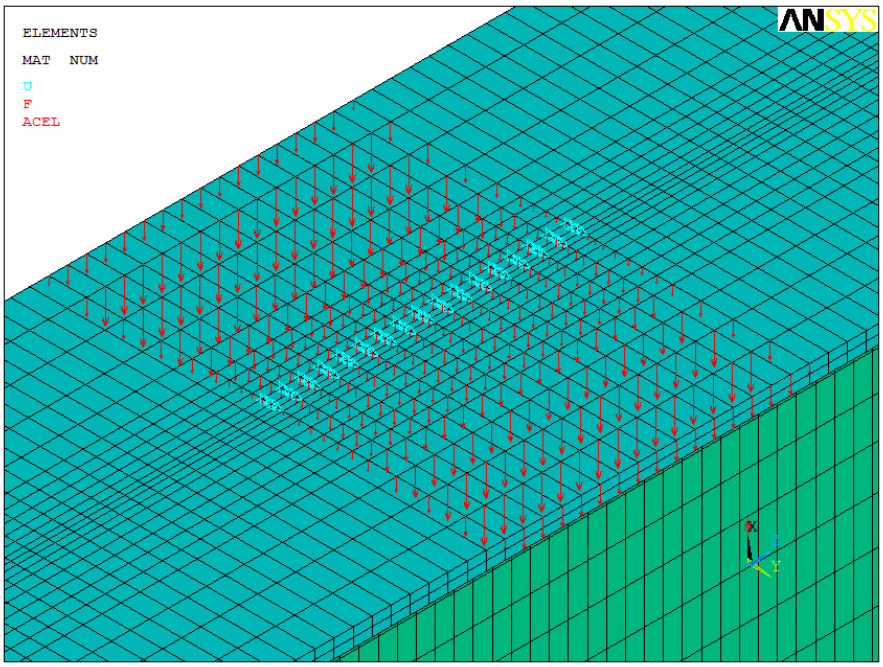

Figure 9.10: Load application on the top of the flange and lateral support.

The loading of the model is performed in two stages. The results of the numerical studies [17] on the same specimen presented in Section 2.3.5 suggest that the calculated ultimate load is in the region of $80kN$ per loading point. Therefore in the first stage a load controlled strategy is used up to $70kN$. From that point the

arc-length method is used to capture the post-failure part of the equilibrium path as well. Figure 9.11 shows the comparison of the calculated load deflection curves of the present analyses with the results of the shell models presented in Section 2.3.5. The deflection is measured at the bottom of the cross section at mid-span.

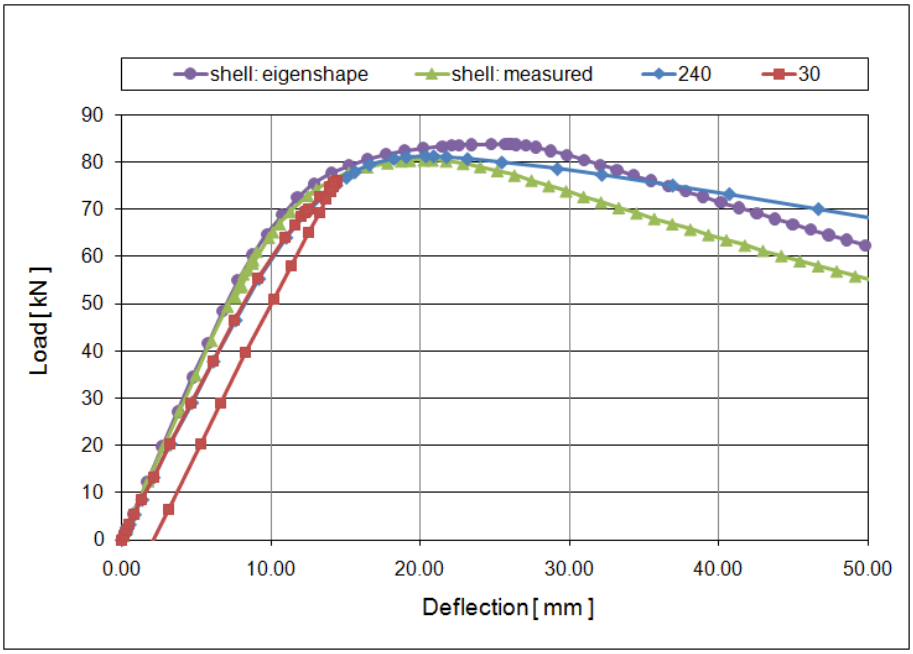

Figure 9.11: Load-deflection curves: comparison of numerical results of shell models [17] and numerical results of virtually fabricated specimens using solid elements with a Speed Up factor of 240 and 30.

The calculated ultimate loads in the cases with a Speed Up factor of 30 and 240 are $76.19kN$ and $81.34kN$, respectively. The calculated load bearing capacities of the shell model with measured imperfections and the virtually fabricated model with a Speed Up factor of 240 are practically identical.

Comparing the results of the two numerical analyses performed on the virtually fabricated specimens two main differences can be observed. First, there is a 7% difference in the calculated load bearing capacity. Second, the post–failure equilibrium paths found by the arc–length method are also very different. To understand these differences the deformed shape of the plate girders at the end of the load step corresponding to their ultimate load are shown in Figures 9.12 and 9.13.

In the case with a Speed Up factor of 240 the full length of the weld is assumed to be completed in a single welding step. As a result of this the variation in web

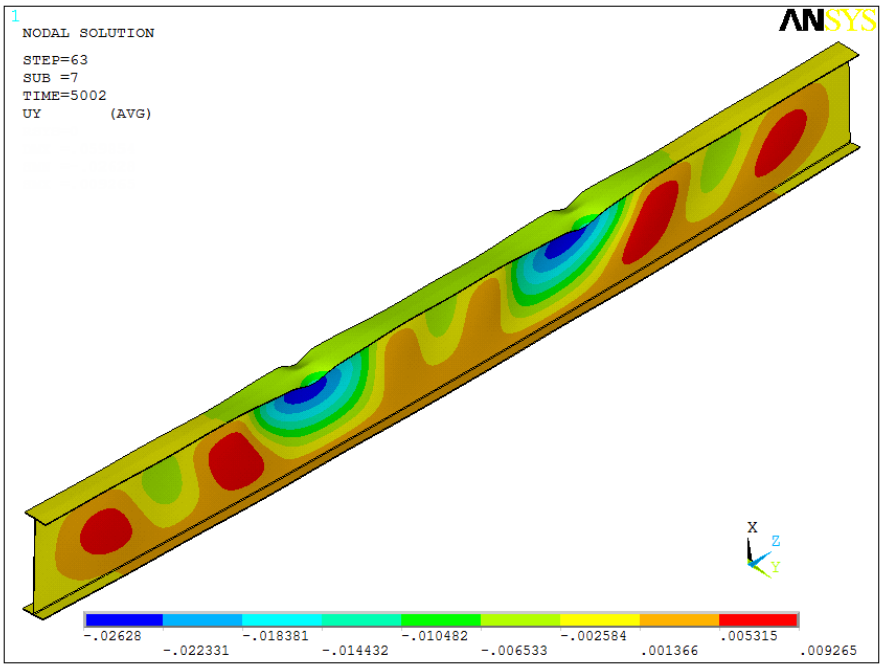

Figure 9.12: Lateral deflection (UY) shown on the deformed shape of the plate girder subjected to the ultimate load of 81.34kN (Speed Up factor of 240).

deflections along the length of the girder are smoothed as discussed in Section 8.4 and shown in Figure 8.64. Since the deformations are symmetric with respect to the plane at mid-span of the girder, the deflections of the girder at the two loading locations are the same. The loading points are located at a distance of 1m from the centre of the girder. It can be seen in Figure 8.64 that at -1.0m and 1.0m the web deflections are symmetric. This symmetry can also be observed in the deformed shape of the girder in Figure 9.12. Near the loading locations the web exhibits large deflections in the –UY direction while in the rest of the girder the +UY deflections are dominant. This helps to stabilise the girder when the load approaches the ultimate load value and also allows the development of a smooth post-failure equilibrium path.

In the case with a Speed Up factor of 30 the full length of the weld is assumed to be completed in eight welding steps. This results in an uneven web deflection along the length of the girder as shown in Figure 8.64 in Section 8.4. It can be seen in Figure 8.64 that at -1.0m and 1.0m, at the loading locations, the web deflections are very different, in fact they have the opposite sign. The same tendency can be

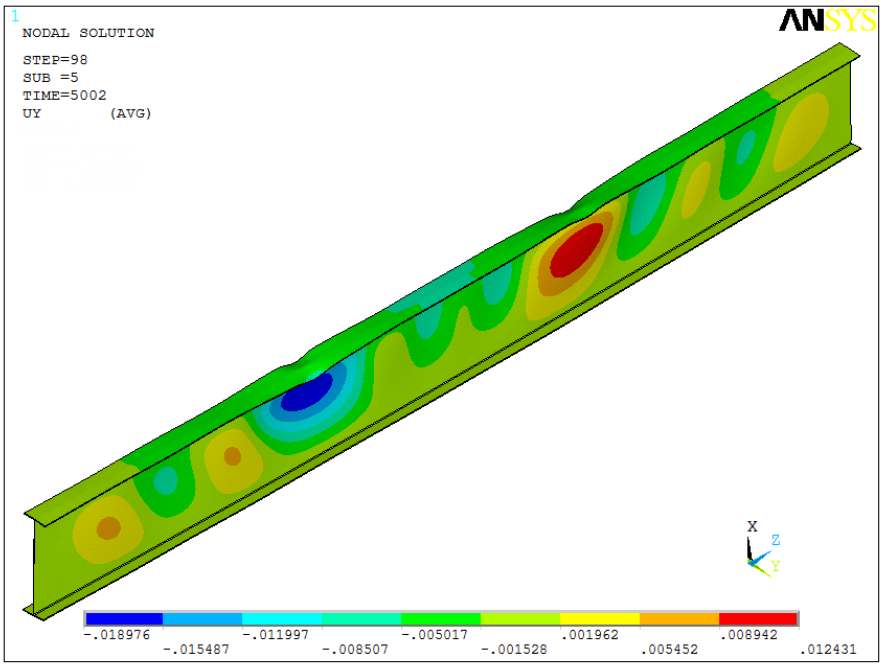

Figure 9.13: Lateral deflection (UY) shown on the deformed shape of the plate girder subjected to the ultimate load of 76.19kN (Speed Up factor of 30).

observed in the deformed shape of the girder in Figure 9.13 as well. Unlike in the case with a Speed Up factor of 240, as a result of the uneven initial deformations of the girder, a deformed shape that would help stabilising the girder during loading can not develop. This results in a lower ultimate strength and a more sudden failure.

9.6 Summary and conclusions

In the first part of the chapter every step in the development of a numerical model for the simulation of the welding of full size plate girders are summarised and a complete example is presented. The welding simulation results presented in this chapter demonstrate how the deflections of the web in a plate girder follow the evolution of the temperature distribution:

- Large deflections develop in the web initially (from the start of the welding until the maximum temperature drops to around 280°C) at the start and the end of the girder.

- As the temperatures in the girder continue to drop those initial web deflections almost disappear when the maximum temperature reaches around 110°C.
- The first signs of buckling appear at the two ends of the girder when the maximum temperature drops to around 63°C.
- By the time the maximum temperature drops further to around 49°C buckling can be observed along the full length of the web.
- When the girder finally reaches the ambient temperature of 30°C the shape of the web remains the same but with larger deflection values.

In the second part of the chapter two virtually fabricated specimens are used in virtual ultimate load tests. The use of the maximum Speed Up factor, *i.e.* completing the full length of the weld in a single welding step, produces symmetric initial deformations in the specimens. Such deformations can result in stabilising the girder near the ultimate load level. This leads to a higher calculated load bearing capacity and a smoother post-failure equilibrium path when compared to the results of another analysis with a lower Speed Up factor. Therefore the use of the maximum Speed Up factor should be carefully evaluated to make sure that it does not introduce unwanted stabilising deformations in the specimen. In order to preserve the longitudinal variation in the initial deformations it is necessary to use a lower value for the Speed Up factor. Such solution results in more realistic imperfections and therefore realistic structural response in the virtual experiment.

The next and final chapter of this thesis summarises the achievements and recommendations of this research project and sets out the directions for further research.

Chapter 10

Summary and conclusions

10.1 Summary of achievements and research outcomes

The major achievements of the research presented in this thesis are summarised as follows:

1. Computational welding mechanics (CWM) has been successfully applied to full size welded plate girders used in civil engineering.

2. A new robust welding heat source model has been developed that allows the accurate reproduction of the thermal effects of welding and at the same time it is easy to calibrate.

3. A temperature measurement methodology is developed using infrared temperature measurements that not only is easy to set up in a factory environment with minimal disruption of the fabrication process but also provides sufficient experimental data for both the calibration and the verification of the numerical model.

4. A mixed time integration solution method is proposed for the numerical simulation of welding that takes advantage of the different nature of the welding and the cooling processes in order to significantly improve the efficiency of the simulation.

5. It has been demonstrated that in large specimens where the deformations as a result of the welding process are governed by plate buckling, the computational

cost can be significantly reduced by artificially increasing the length of the heat source model and the welding speed by the same so called Speed Up factor.

6. The relationship between the evolution of the temperature distribution and the evolution of the deformations in a full scale welded plate girder has been established with the help of the virtual fabrication.

7. The behaviour of a virtually fabricated plate girder has been successfully studied in a virtual experiment.

8. A numerical strategy has been developed to evaluate the effect of the inaccuracies in the execution of the residual stress measurements using a single uniaxial strain gauge and two through-holes.

These achievements and their practical use are discussed in more detail in the following sections.

10.1.1 Computational welding mechanics in civil engineering

Computational welding mechanics (CWM) has been an intense area of research during the last few decades [97]. A large number of papers [35, 73, 98] and also a few books [82, 86, 87] have been published on the topic and very significant progress has been made. Nevertheless, even with the advancement of computational technology, most of the published works remain limited in size as a result of the very high computational cost. This is probably the main reason why CWM is not commonly seen in civil engineering applications. Simply the scale of welded structures used in civil engineering is so big that only a few have considered it as a practical field of application for CWM. The common way to cope with the high computational cost is to include simplifications in the model, however, the use of such models can be rather limited as discussed in Section 3.3.4.

In the present work no such simplifications have been employed, instead efficient numerical strategies such as the use of mixed time integration is proposed. This does not mean that this work does not contain important simplifications. However, those simplifications have not been introduced in the model in order to reduce computational cost. They are justified either by measurements or the results published

by other researchers. For example the use of the equivalent prismatic heat source model is a simplification since the real weld pool geometry is substituted by a prismatic volume. This method does not significantly affect the computational cost and its use is justified by the temperature measurements that were the basis of the calibration and validation of the heat source model.

Another important simplification used in this work is the material model that ignores the effects of phase transformation. This is justified by the work found in the literature where it has been demonstrated that the behaviour of mild steel used in this research can be simplified without significantly affecting the outcome of the simulation (for details see Sections 3.3.4 and 8.3.4). Moreover, the lack of reliable material properties data at elevated temperature also supports the use of a simplified material model.

It is the combination of efficient numerical solution methods, a robust numerical model and simple measurements techniques that has led to a successful application of CWM in the virtual fabrication of full size welded plate girders as explained in more detail in the following sections.

10.1.2 Equivalent prismatic heat source model

Adequate modelling strategy of the welding heat source is critical for the success of welding simulation. One of the most commonly used heat source model is the so called double ellipsoid model [86]. It has been successfully applied in many studies but it requires the knowledge of a number of parameters (e.g. weld pool shape, arc efficiency) that can be challenging to determine accurately [87]. There are other simplified models such as distributed heat input over an area of the surface of welded specimen. Studies have demonstrated that the shape of the heat source area has little influence on the calculated temperature filed as long as the heat input remains the same [88]. Combining these two approaches a modified welding heat source model based on prescribed temperatures has been developed for the simulation of the fabrication of plate girders. The equivalent prismatic heat source model presented in Chapter 6 has the following characteristics:

- Unlike traditional prescribed temperature models that require the knowledge of the shape of the weld pool the equivalent prismatic heat source model has only one variable parameter: the length of the prismatic weld pool (for details

see Section 6.2).

- The cross-section of the prismatic weld pool can be easily approximated either by the design values of the weld geometry or a macrograph image of the actual weld cross-section (for details see Section 6.3).

- Calibration of the length of the prismatic weld pool requires a single temperature reading such as the weld surface temperature which is the one used in the present research (for details see Section 6.3).

- The length of the prismatic weld pool can be freely adjusted to match any temperature data, which not only makes the calibration easy and accurate but it also allows for the compensation of other uncertainties in the numerical model (for details see Section 6.2).

The *equivalent prismatic heat source model* together with the *combined FIXED and MOVING temperature measurement method* (for details see Section 10.1.3) provide all the necessary tools to gather data in a factory environment and reproduce the fabrication process in a virtual environment. The methodology developed is robust, easy to implement and efficient.

In Section 6.3 it has been also demonstrated that as a result of the freely adjustable length of the weld heat source model even if no macrograph image of the weld seam is available the temperature measurements can be equally well reproduced assuming the design values of the weld dimensions. This greatly reduces the experimental part of the model development since only the results of simple temperature measurements are necessary to successfully calibrate the numerical model without the need for slicing up the specimens. This makes the heat source model and the calibration procedure especially attractive for manufacturers who wish to numerically analyse and improve their fabrication process without the need for destroying any girder, *i.e.* during normal operation the girders fabricated for paying clients can be used for such temperature measurements without generating any extra cost for the manufacturer.

A series of parametric studies were also performed during the model development. Parameters such as the combined heat transfer coefficient, thermal contact between the plates, weld pool length, welding speed, ambient temperature, preheating, the angle of weld seam surface and the area of weld cross section were investigated. The

main observations of these studies can be summarised as follows:

- in the high temperature range the combined heat transfer coefficient does not influence the temperature distribution because it is dominated by heat conduction but it does strongly influence the last phase of cooling down and therefore the total cooling time,
- thermal contact between the web and the flange has no significant influence on the overall temperature distribution,
- the length of the prismatic heat source, *i.e.* the length of the artificial weld pool, is a major driving force behind the temperature distribution which makes it the ideal parameter to be used in the calibration of the heat source model,
- higher welding speed results in higher cooling rate,
- higher ambient temperature reduces the cooling rate,
- applying preheating also reduces the cooling rate,
- changing the angle of the weld seam surface affects the temperature distribution within the weld seam, and
- the area of weld cross section also has a very strong influence on the temperature distribution but it is not considered as a parameter to be calibrated since the weld cross section is known.

These results also demonstrate that the developed numerical model can be used to study a wide range of phenomena related to the fabrication of welded structures.

10.1.3 Combined FIXED and MOVING temperature measurement method

Temperature measurements during welding are traditionally performed in a laboratory environment using thermocouples attached to the specimen prior the welding [99]. However, for the experiments of the research presented in this thesis the use of thermocouples was not suitable.

Using an infrared thermometer a combined FIXED and MOVING temperature measurement experimental set-up has been devised that are easy to install in a

factory environment with minimal disturbance of the normal fabrication process. During FIXED measurement the infrared thermometer is placed on a fully adjustable tripod on the floor next to the specimen being welded and therefore it is stationary. The instrument focuses on a point at a fixed distance from the welding arc. The measured point is fixed relative to the welding arc but continuously changing relative to the specimen.

During MOVING measurement the infrared thermometer is placed on the web of the welded specimen. The instrument travels with the girder and it focuses on a point of the girder that is moving relative to the welding arc but it is fixed relative to the specimen.

Based on the performed in-situ measurements presented in Chapter 5 the following has been established:

- The two kinds of measurement provide semi-independent sets of temperature data for the same experiment providing information about different aspects of the welding process: heat input (FIXED measurement) and cooling down (MOVING measurement) (for details see Section 5.2).

- The FIXED measurement method provides a large sample size of the same temperature data therefore it increases significantly the reliability of the results (for details see Section 5.3).

- Using two thermometers with different measurement ranges for concomitant FIXED (high temperature range thermometer) and MOVING (low temperature range thermometer) would increase the reliability of the results and reduce the number of specimens to be measured (for details see Section 5.4).

This methodology of temperature measurement provides sufficient data for the calibration and validation of a numerical model based on the equivalent prismatic heat source model. Additionally, using this methodology has a number of practical advantages over the traditionally used thermocouples, especially in a factory environment:

- the installation of the thermocouples are rather labour intensive and can significantly disturb the fabrication process therefore they are only suitable for laboratory measurements,

- thermocouples cannot be used to measure the surface temperature of the weld seam since they need to be installed before the fabrication starts, and
- thermocouples can only be used for measurements that give results similar to the MOVING measurements. The FIXED measurements cannot be reproduced with thermocouples.

Using infrared thermometers therefore gives manufacturers and researchers much more freedom to perform a large number of measurements with minimal set up effort.

10.1.4 Mixed time integration method for efficient welding simulation

The time discretisation strategy can greatly influence the computational time. Almost exclusively implicit time integration method is employed in computational welding mechanics. There are only very few examples of the use of explicit time integration [35, 78].

Mixed time integration is commonly applied to the analyses of sheet metal forming since the process can be divided into two very different phases: stamping and springback. Explicit time integration is more suitable for simulating stamping, while springback can be more efficiently analysed with implicit time integration [80]. The complete welding process also consists of two very distinct phases: welding and cooling.

In this thesis the use of explicit time integration with mass scaling has been thoroughly studied in order to propose a mixed time integration scheme as an efficient solution for coupled thermomechanical welding analysis. The numerical investigation using examples of increasing complexity presented in Chapter 4 has established the following:

- The stable time step limit for explicit analysis of the welding of steel like materials is governed by the mechanical part of the simulation independently of any practical mesh size (for details see Section 4.2).
- Explicit time integration appears to underestimate the deformations calculated using the implicit method, however, the calculated residual stresses demonstrate very good agreement (for details see Sections 4.4 and 4.5).

- To minimise the calculation time of a mixed time integration scheme the time integration method should be switched from explicit to implicit soon after the welding phase of the simulation is over. For a better agreement between the explicit and implicit analyses results the time of the switch can be delayed. A simple method to estimate the upper time limit of the switch has been developed and it has been demonstrated that it gives a conservative estimate of the time limit (for details see Section 4.6).

- The use of the mixed time integration method can significantly reduce the calculation time. The rate of reduction increases as the size of the model increases (for details see Sections 4.3 and 4.5).

When the main objective of the analysis is to obtain the distribution of residual stresses, the mixed time integration scheme is a computationally cost effective solution. However, if accurate deformations are also of interest a more cautious approach is required because the explicit method has the tendency to underestimate the deformations when compared to the implicit method. Techniques such as applying damping to the model or the use of variable mass scaling could improve the agreement between the two types of analysis.

10.1.5 Welding simulation of full size plate girders

The numerous failures in welded ship hulls [18] and the collapse of several welded steel bridges [100] highlighted the importance of understanding the effects of welding and the role of residual stresses and geometrical imperfections in structural behaviour. Intense research lead to the understanding of the development of residual stresses [101], numerical methods were also developed and eventually computational welding mechanics was born [97]. However, it is only in recent years that the advancement in computer hardware and software has allowed researchers to consider more realistic structures for welding simulation. Nevertheless, large scale models of civil engineering structures have been considered impractical until now.

The numerical model developed for the thermal stress analysis of welding in Section 8.2 has been successfully used for the virtual fabrication of full size plate girders. The web deflections calculated with the proposed numerical model has shown a reasonable agreement with the imperfection measurements despite a number of differences in the assumptions of the simulation and the real fabrication conditions. To

increase the efficiency of the simulation the use of a "Speed Up" factor is proposed that reduces the number of welding steps while maintaining the total heat input. The following have been established as a result of the investigations in Chapter 8:

- The numerical simulation of welding based on the equivalent prismatic heat source model and simplified material model taken from EC3 can successfully reproduce the effects of welding (for details see Section 8.3).

- The Speed Up factor method can be used both in short and long girders if the main interest of the analysis is residual stress distribution (for details see Sections 8.3.10 and 8.4).

- If plate deformations are also of interest Speed Up factors should be used with care in short models. However, it can greatly reduce the computational cost with relatively little loss of accuracy in the case of long girders where the deflections of the plates are dominated by buckling provoked by the compressive thermal stresses of welding (for details see Sections 8.3.10 and 8.4).

- The maximum value of the Speed Up factor (*i.e.* a single welding step) produces a very smooth residual stress distribution along the length of the girder but at the same time does not capture the longitudinal variations in the deflections of the plates (for details see Section 8.4).

- A lower value of a Speed Up factor might produce a slightly rougher residual stress distribution along the length of the girder but successfully captures longitudinal variations in the deflections of the plates (for details see Section 8.4).

It is important to consider the aim of the analysis (residual stresses or deflections or both) and the available computational power and time to determine the optimal Speed Up factor for the simulation.

A series of parametric studies were also performed during the model development on small scale models before the analysis of a full size specimen was attempted. Parameters such as contact between the plates, material properties, angle of weld seam surface, welding speed, preheating and displacements constraints were investigated. The main observations of these studies can be summarised as follows:

- in general it can be said that the parameters investigated have relatively little influence on the development of residual stresses,

- it is very important to consider the contact between the web and flange if the deformations of the plates are also of interest,
- the yield strength of the material can significantly influence the final deformations of the plates,
- changing the angle of the weld seam surface can help to reduce the deformations of the web,
- a 10% variation in the welding speed has little influence on the deformations of the plates,
- preheating the web not only reduces the absolute deflection of the web but it also reduces its distortion, and
- applying displacement constraints during welding is an efficient way to reduce deformations in the plates without additional energy consumption unlike other mitigation techniques.

These studies also demonstrate that the numerical model developed can be used to investigate a wide range of phenomena related to the fabrication of welded structures. While these models have not been calibrated and verified by experiments, the results are what one would expect and show similar characteristics to what can be found in the work of others (e.g. in references [18, 101, 102]).

10.1.6 Evolution of temperatures and deformations in full scale plate girders during fabrication

Traditional experimental methods can be used to determine the effects of welding, such as deformations, only after the welding process is completed and the specimen has cooled down to ambient temperature. One of the major advantages of using numerical simulation is that the development of deformations can be followed during the entire fabrication process. However, as a result of the high computational cost, until now such simulation has not been attempted for specimens of large scale.

The numerical model described in this thesis is capable of establishing the relationship between the evolution of the temperature distribution and the deformations during fabrication of a full scale plate girder. It has been found that the deflections

in the web undergo several transformations during the welding and cooling processes in the girder studied (for details see Section 9.4):

- During welding and in the early part of the cooling large deflections develop at the two ends of the girder.
- The above deflections disappear as the cooling continues.
- The final deflections are dominated by the buckling of the web that develops in the final part of the cooling process.

Visualising how the deformations in the girder evolve during and after the welding process can help manufacturers to understand and therefore deal with unwanted imperfections in their product. This information can be used, for example, to develop a clamping system of the plates to reduce such deformations.

10.1.7 Virtual experiments on virtually fabricated specimens

Welding simulation of specimens of limited scale, which are still common, does not permit the analyses of models that are needed to perform virtual experiments [43]. The results obtained with those small scale models could be extrapolated to a full size specimen but the more complex the specimen is the less reliable such approximation becomes. For the generation of realistic virtual specimens it is necessary to simulate the fabrication of full size girders.

With the help of the numerical model developed in this thesis, the complete life cycle of a full size welded steel plate girder has been studied in a virtual environment from fabrication to failure. A virtually fabricated plate girder has been placed in a virtual experiment set-up to investigate its ultimate behaviour. The following has been found in relation to the use of Speed Up factors:

- Using the maximum value of the Speed Up factor (*i.e.* a single welding step) can produce initial deformations that can stabilise the girder near failure. This can result in higher load bearing capacity and smoother post-failure equilibrium path. Therefore such analysis should be reviewed carefully (for details see Section 9.5).

- The use of a low Speed Up factor value is recommend for the calculation of realistic initial deformations and realistic structural response in a virtual experiment (for details see Section 9.6).

The real importance of this achievement is the fact that fabrication and experiment have been successfully combined in a single virtual environment. This opens the door to a wide range of applications in the analysis of welded structures since such tool allows researchers to use more realistic numerical models in their virtual experiments.

10.1.8 Uniaxial stress measurement method

The hole drilling method with a strain gauge rosette is a commonly used semi-destructive procedure to measure residual stresses. As a result of the very small blind hole diameter the method is very sensitive to eccentricities of the drilling. The effects of eccentricity have been widely studied including numerical investigations [94].

In this research the "one-gauge two-hole" method has been used to measure the uniaxial residual stress level in steel plate girders. It is based on the same principle of removing material from the specimen (drilling two through-holes in this case) and measuring the released stress using a uniaxial strain gauge. For the evaluation of the measurements a combination of high resolution images, image analysis and advanced finite element models were used. The experimental and numerical investigations of the measurement method presented in Chapter 7 have established the following:

- Using high resolution digital photographs the geometry of the measurements can be evaluated with great accuracy with the help of image analysis software (for details see Section 7.3.1).

- The parameters of possible inaccuracies in the measurements and their range have been established (for details see Section 7.3.1).

- A numerical model has been developed to simulate the measurement process. The model can take into account the inaccuracy parameters and study their effects. It has been demonstrated that the eccentricities of the holes play a more important role in influencing the readings than the inaccurate placing of the gauge (for details see Sections 7.3.3 and 7.3.4).

- Calibration tables have been developed for a given hole diameter and gauge geometry. The same numerical model and methodology can be used to develop similar tables for any other measurement conditions (for details see Section 7.3.4).

- With the help of the calibration tables the readings of the gauge can be corrected depending on the exact position of the holes and the estimated stress value in the perpendicular direction (for details see Section 7.3.4).

The same technique can also be used in structural members in service that are dominantly loaded uniaxially and have a constant stress distribution through the thickness of their plates.

10.2 Virtual fabrication model development steps

In this section the most important aspects of the numerical model development are summarised and links are provided to the relevant section of the thesis for further details. The purpose of this section is to provide a quick reference for researchers and manufacturer who wish to use the methodology developed in this thesis. A more detailed guide of the steps of the numerical analyses (from virtual fabrication to virtual experiments) can be found in Chapter 9.

Temperature measurements:

For the calibration of the equivalent prismatic heat source model (for details see Section 6.2) only a single temperature data is needed. It is recommended that the so called FIXED temperature measurements (for details see Section 5.2) is used to determine the temperature of the weld seam surface at a fixed distance from the welding arc. This single temperature data is sufficient to calibrate the numerical model (for details see Section 6.3) but it is recommended that further measurements are taken in order to be able to verify the model and adjust other parameters such as thermal boundary conditions if necessary.

For the model verification it is recommended to use the so called MOVING measurement (for details see Section 5.2) that produces the temperature history of a given location on the specimen.

Thermal analysis:

The main goal of the thermal analysis is the calibration of the heat source model and the verification of the calculated temperature history. The cross section of the heat source model can be estimated with the design values of the weld seam dimensions or using macrograph images of the weld seam. The length of the heat source model needs to be calibrated using the temperature data obtained from the FIXED measurement. The calibration can be done in just a few steps starting with two arbitrary lengths and then using linear interpolation to find a better length to match the temperature data. If necessary this step can be repeated to improve the agreement.

Using the calibrated heat source model the thermal history of any point of the girder can be calculated. If additional temperature data is available from a MOVING measurement then the calculated and measured temperature history can be compared (for details see Section 6.3) to verify the model.

More details of the modelling strategy such as material properties, boundary conditions and solution control can be found in Sections 6.2 and 9.2. The calibration and verification process are explained in detail in Section 6.3.

Stress analysis:

With the calibrated and verified thermal analysis model the full fabrication process can be simulated and the temperature history of the welded structure can be calculated and used as thermal load in the stress analysis. One key element of the stress analysis is the material properties. If no other material data is available the material properties at elevated temperature given in Eurocode 3, Part 1-2, EN 1993-1-2: Structural fire design [85] serves as a good reference. More details concerning material properties and material behaviour can be found in Sections 3.3.3, 3.3.4 and 8.2.1.

It is also very important that correct displacement boundary conditions are considered. While they might not significantly affect residual stresses they play a key role in the development of geometrical imperfections. Therefore contact between the plates and support conditions that take into account the advancement of the plates in the welding machine need to be carefully defined (for more details see Sections 8.3.3 and 8.3.9.

More details of the modelling strategy, solution control and how the computa-

tional time can be reduced can be found in Sections 8.2, 8.3.10 and 8.4.

Based on the above temperature measurements techniques and the equivalent prismatic heat source model the numerical model development is a straightforward process. Following the additional guidelines for the thermal and stress analyses laid down in this work, virtual fabrications of welded specimens can be successfully achieved even at the scale of civil engineering structures.

10.3 Further studies

It has been demonstrated that the numerical model developed is already capable of providing meaningful results in many practical cases for the fabrication of steel plate girders. Nevertheless, there are a number of areas where the model can be further improved in order to cover a wider range of fabrication scenarios and to take into account certain physical phenomena that cannot always be ignored.

In its current state the numerical model can be used to simulate the fabrication of steel plate girders with the following limitations:

- only single-sided fillet weld is allowed,
- only welds between the web and the flanges are allowed,
- only a single welding sequence can be simulated, and
- effects of phase transformation are ignored.

The first three items require relatively simple changes to the model that are mainly related to the geometrical representation of the model and the control of the solution steps.

In order to be able to simulate double-sided fillet weld as well there are two options depending on the actual fabrication technology. Certain automatic welding machines allow simultaneous welding on both sides of the web. To simulate such a fabrication method it could be sufficient to consider the model to be symmetric about the middle plane of the web if the support conditions of the plates are also symmetric in the welding machine.

Other automatic welding machines can only weld one side of the web at the same time and require that the plate girder is turned up-side down after finishing

the welding on one side (the welding machine used in the fabrication of the specimens of this research was of this kind). In this case no symmetry can be considered in the numerical model and it is necessary to allow for the definition of two independent weld seams on both sides of the web. This also requires an improvement of the numerical time step control to allow for the simulation of an additional welding sequence.

Usually welded plate girders have additional structural elements such as stiffeners, gusset plates and doubler plates welded to their web and flanges. The simulation of the welding of these additional plates require a more versatile model definition than the current implementation of the numerical model since at the moment only welds between the web and the flanges are allowed. While such improvement is a straightforward process the actual implementation of the geometry definition that permits the connection of additional plates at arbitrary locations on the plate girder with either single-sided or double-sided fillet welds is a complex task. To achieve this the internal logic of the numerical model definition needs to be completely revised and, practically, it is necessary to go back to the very basics of the geometry definition. Once the geometry definitions is sorted the solution control procedure also needs to be adapted to handle the more complex geometry. However, this is can be a much simpler task if the geometry is generated with careful numbering of the different structural elements (plates and welds) and their meshes. This numbering can serve as the basis of an efficient solution control algorithm.

Another limitation of the current model is that at the present only a single continuous segment of weld is permitted. This means that the welding is simulated between the two ends of the weld seam in a continuous series of welding steps that cannot be interrupted and no additional sequences can be simulated. By removing this limitation it would be possible to simulate intermittent welding and also the actual welding steps that were used in the fabrication of the specimens of this research. The design of the welding machine did not allow the welding head to reach the ends of plate girder where the welding had to be completed using manual arc welding. As a result, three individual welding sequences were necessary to complete the welding of the web to each flange. Similarly to the previous point this issue can also be resolved with the redesign of the geometry definition and solution control.

The previous three limitations do not require any modification in the simulation strategy of the physics of welding. They are only geometry related issues that can be

relatively easily resolved even if the actual implementation within the finite element software can be complex. However, there is another feature in the current model that limits its application for certain material types. It has been assumed that the properties of both the base material and the weld material are not influenced by the phase transformation of steel that takes place at high temperatures, *i.e.* the material behaviour is the same during heating and cooling independently of the maximum temperature and the temperature gradient. While this assumption is common and in most cases valid as well, there are certain material types (e.g. ferritic steel materials) where this can have significant influence on the outcome of the analysis. A number of studies investigating the effects of phase transformations [55, 103] have been published already but with one aspect in common: the use of small scale specimens. The influence of more advanced material models must also be investigated in specimens of civil engineering scale which require the improvement of the present model used in this research. The main difficulty of this is not the actual implementation of such material model but to find reliable material properties data that are both temperature and micro-structure dependent.

While the numerical model developed in this thesis provides a powerful tool to simulate the fabrication of plate girders, with the implementation of the above improvements a truly versatile virtual fabrication simulation environment can be created. Such a virtual environment could be used in a wide range of numerical studies where the imperfections of welded structures need to be accurately considered. It can also be applied to a reverse problem where the aim is not to determine the structural behaviour considering imperfections but the aim is to optimise the parameters of the fabrication in order to alter the imperfections of the welded structure to achieve more favourable structural behaviour. With the help of the numerical simulation of welding the relationship between fabrication technology, imperfections and ultimate behaviour of plate girders can be successfully established.

Bibliography

[1] J. Néző, L. Dunai, I. Okura, and M. Iványi, "Influence of local and global phenomena in the ultimate behaviour of plate girders," in *Proceedings of the 2nd European Conference on Steel Structures*, Prague, Czech Republic, 26-29 May 1999, pp. 39–43.

[2] I. Okura and J. Néző, "Effects of stiffener-end-gaps on local strains at stiffener-ends," in *Proceedings of the 5th Korea-Japan Joint Seminar on Steel Bridges*, 1999.

[3] L. Dunai and J. Néző, "Interaction of stiffener-end-gap and stiffener size in the ultimate strength of thin-walled girders," in *Proc. 6th International Colloquium on Stability and Ductility of Steel Structures*, Timisoara, Romania, 9-11 September 1999.

[4] L. Dunai and J. Nézö, "Hosszborda kialakításának hatása gerinclemezes tartó teherbírására," in *VIII. MAMEK*, Miskolc, 1999.

[5] I. Okura, J. Néző, L. Dunai, and M. Iványi, "Finite element analysis of local strains in plate girders," in *Proceedings of the 5th International Conference on Computational Structures Technology and the Second International Conference on Engineering*, M. Iványi, J. Muzeau, and B. Topping, Eds. Leuven, Belgium: Civil-Comp Press, Edinburgh, UK, September 2000, pp. 27–34.

[6] J. Néző, L. Dunai, and M. Iványi, "Nonlinear finite element analysis of plate girders with stiffener-end-gaps," in *Proceedings of the 5th International Conference on Computational Structures Technology and the Second International Conference on Engineering*, M. Iványi, J. Muzeau, and B. Topping, Eds. Leuven, Belgium: Civil-Comp Press, Edinburgh, UK, September 2000, pp. 35–42.

[7] J. Néző and L. Dunai, "Effect of steel material on the ultimate behaviour of plate girders," in *3rd International Conference on Coupled Instabilities in Metal Structures, CIMS 2000*, Lisbon, Portugal, September 2000, pp. 571–578.

[8] L. G. Vigh and L. Dunai, "Finite element modelling and analysis of bolted joints of 3d tubular structures," *Computers & Structures*, vol. 82, no. 23-26, pp. 2173 – 2187, 2004, computational Structures Technology.

[9] L. G. Vigh, "Influence of flange-to-web connection ont he patch load resistance of I beams." in *Proc. SDSS 2010 International Colloquium on Stability and Ductility of Steel Structures*, E. Batista, P. Vallesco, and L. de Lima, Eds., Rio de Janeiro, Brazil, 8-10 September 2010.

[10] L. G. Vigh, *Virtual and real test based analysis and design of non-conventional thin-walled metal structures.* Budapest University of Technology and Economics (BME), 2006, PhD thesis.

[11] L. G. Vigh and L. Dunai, "Advanced stability analysis of regular stiffened plates and complex plated elements." in *Proc. SDSS 2010 International Colloquium on Stability and Ductility of Steel Structures*, E. Batista, P. Vallesco, and L. de Lima, Eds., Rio de Janeiro, Brazil, 8-10 September 2010, keynote lecture.

[12] Y. C. Kim, J. U. Park, Y. Nakanishi, I. Imoto, and K. Horikawa, "Effects of initial imperfections on out-of-plane deformation and residual stress produced by welding," *Transactions of JWRI*, vol. 26 (2), pp. 75–80, 1997.

[13] C. Rasche and U. Kuhlmann, "Investigations on longitudinal fillet welded lap joints of HSS," in *Nordic Steel Construction Conference NSCC2009*, Malmo, Sweden, 2-4 September 2009, pp. 462–469.

[14] L. Dunai, G. Jakab, J. Néző, and B. Topping, "Experiments on welded plate girders: Fabrication, imperfection and behaviour," in *First International Conference on Advances in Experimental Structural Engineering*, Nagoya, Japan, 19-21 July 2005.

[15] G. Jakab, L. Dunai, and R. Macdonald, "Behaviour of plate girders with single-sided fillet welds," in *Proceedings of the Eurosteel 2005 Conference on Steel and Composite Structtures*, Maastricht, The Netherlands, 2005.

[16] L. G. Vigh and L. Dunai, "Imperfections and ultimate behaviour of multi-stiffened welded plate girders," in *Proc. 22nd Danubia - Adria Symposium on Experimental Methods and Solid Mechanics*, Parma, 2005, pp. 218–219.

[17] G. Jakab, G. Szabó, and L. Dunai, "Imperfection sensitivity of welded beams: experiment and simulation," in *ICMS 2006 Conference*, Brasov, Rumania, 20-22 September 2006.

[18] K. Masubuchi, *Analysis of Welded Structures*. Pergamon Press, 1980.

[19] *Open Visualisation Data Explorer, Version 4.1.3*, 2002, www.opendx.org.

[20] J. Néző, B. Topping, and L. Dunai, "Virtual fabrication of steel welded plate girders," in *Proceedings of the Eighth International Conference on Civil and Structural Engineering Computing*, B. Topping and Z. Bittnar, Eds. Stirling, United Kingdom: Civil-Comp Press, Stirlingshire, UK, 2002, paper 101.

[21] D. Radaj, *Heat Effects of Welding*. Berlin Heidelberg: Springer-Verlag, 1992.

[22] L. Wikander, L. Karlsson, M. Näsström, and P. Webster, "Finite element simulation and measurement of welding residual stresses," *Modelling and Simulation in Materials Science and Engineering*, vol. 2, no. 4, pp. 845–864, 1994.

[23] T. Zacharia, J. M. Vitek, J. A. Goldak, T. A. DebRoy, M. Rappaz, and H. K. D. H. Bhadeshia, "Modeling of fundamental phenomena in welds," *Modelling and Simulation in Materials Science and Engineering*, vol. 3, no. 2, pp. 265–288, 1995.

[24] K. Masubuchi, "Prediction and control of residual stresses and distortion in welded structures," in *International Symposium on Theoretical Prediction in Joining and Welding*. JWRI Osaka University, 1996, pp. 71–88.

[25] Y. V. L. N. Murthy, G. V. Rao, and P. K. Iyer, "Numerical simulation of welding and quenching process using transient thermal and thermo-elasto-plastic formulations," *Computers and Structures*, vol. 60, no. 1, pp. 131–154, 1996.

[26] P. Michaleris and A. DeBiccari, "Prediction of welding distortion," *Welding Journal*, vol. 75, pp. 172s–181s, April 1997.

[27] A. S. Oddy and L.-E. Lindgren, *Modeling in Welding, Hot Powder Forming and Casting*. ASM International, 1997, ch. Mechanical Modelling and Residual Stresses, pp. 31–59.

[28] Y. Dong, J. K. Hong, C. L. Tsai, and P. Dong, "Finite element modeling of residual stresses in austenitic stainless steel pipe girth welds," *Welding Journal*, vol. 76, no. 10, pp. 442s–449s, 1997.

[29] R. C. Reed, H. J. Stone, S. M. Roberts, and J. M. Robinson, "The development and validation of a model for the electron beam welding of aero-engine components," *Proceedings of the Institution of Mechanical Engineers, Part G: Journal of Aerospace Engineering*, vol. 211, pp. 421–428, 1997.

[30] G. Little and A. Kamtekar, "The effect of thermal properties and weld effciency on transient temperatures during welding," *Computers and Structures*, vol. 68, pp. 157–165, 1998.

[31] M. Mochizuki, M. Hayashi, and T. Hattori, "Comparison of five evaluation methods of residual stress in a welded pipe joint," *JSME International Journal, Series A: Solid Mechanics and Material Engineering*, vol. 42, no. 1, pp. 104–110, 1999.

[32] A. Bachorski, M. J. Painter, A. J. Smailes, and M. A. Wahab, "Finite-element prediction of distortion during gas metal arc welding using the shrinkage volume approach," *Journal of Material Processing Technology*, vol. 92–93, pp. 405–409, 1999.

[33] H. Runnemalm and S. Hyun, "Three-dimensional welding analysis using adaptive mesh scheme," *Computer Methods in Applied Mechanics and Engineering*, vol. 189, pp. 515–523, 2000.

[34] S. Sarkani, V. Tritchkov, and G. Michaelov, "An efficient approach for computing residual stresses in welded joints," *Finite Elements in Analysis and Design*, vol. 35, pp. 247–268, 2000.

[35] L.-E. Lindgren, "Finite element modeling and simulation of welding, part 1: Increased complexity," *Journal of Thermal Stresses*, vol. 24, pp. 141–192, 2001.

[36] X. Lu, *Influence of Residual Stress on Fatigue Failure of Welded Joints.* North Carolina State University, 2002, PhD thesis.

[37] A. Lundback, *Finite Element Modelling and Simulation of Welding of Aerospace Components.* Lulea University of Technology, 2003, PhD thesis.

[38] P. Astrom, *Simulation of Manufacturing Processes in Product Development.* Lulea University of Technology, 2004, PhD thesis.

[39] D. Camilleri and T. G. F. Gray, "Computationally efficient welding distortion simulation techniques," *Modelling and Simulation in Materials Science and Engineering*, vol. 13, pp. 1365–1382, 2005.

[40] P. Ferro, H. Porzner, A. Tiziani, and F. Bonollo, "The influence of phase transformations on residual stresses incluced by the welding process – 3d and 2d numerical models," *Modelling and Simulation in Materials Science and Engineering*, vol. 14, pp. 117–136, 2006.

[41] D. E. Katsareas, C. Ohms, and A. G. Youtsos, "Finite element simulation of welding in pipes: A sensitivity analysis," in *Fracture of Nano and Engineering Materials and Structures*, E. E. Gdoutos, Ed. Springer Netherlands, 2006, pp. 1311–1312.

[42] E. M. Van Der Aa, *Local Cooling during Welding: Prediction and Control of Residual Stresses and Buckling Distortion.* Delft University of Technology, 2007, PhD thesis.

[43] D. Deng, H. Murakawab, and W. Liang, "Prediction of welding distortion in a curved by means of elastic finite element method," *Journal of Materials Processing Technology*, vol. 203, pp. 252–266, 2008.

[44] S. Kiyoshima, D. Deng, K. Ogawa, N. Yanagida, and K. Saito, "Influences of heat source model on welding residual stress and distortion in a multi-pass j-groove joint," *Computational Materials Science*, vol. 46, pp. 987–995, 2009.

[45] W. Perret, C. Schwenk, and M. Rethmeier, "Comparison of analytical and numerical welding temperature field calculation," *Computational Materials Science*, vol. 47, pp. 1005–1015, 2010.

[46] A. Barroso, J. Canas, R. Picon, F. Paris, C. Mendez, and I. Unanue, "Prediction of welding residual stresses and displacements by simplified models. Experimental validation." *Materials and Design*, vol. 31, pp. 1338–1349, 2010.

[47] J. Goldak, "Distortion and residual stress in welds: The next generation," in *Trends in Welding Research, Proceedings of the 8th International Conference*. Pine Mountain, Georgia, USA: ASM International, 1-6 June 2009, pp. 45–52.

[48] J. Ronda and G. J. Oliver, "Consistent thermo-mechano-metallurgical model of welded steel with unified approach to derivation of phase evolution laws and transformation-induced plasticity," *Computer Methods in Applied Mechanics and Engineering*, vol. 189, pp. 361–417, 2000.

[49] D. Deng and H. Murakawa, "Finite element analysis of temperature field, microstructure and residual stress in multi-pass butt-welded 2.25cr-1mo steel pipes," *Computational Materials Science*, vol. 43, pp. 681–695, 2008.

[50] J. A. Goldak, *Modeling in Welding, Hot Powder Forming and Casting*. ASM International, 1997, ch. Thermal Analysis of Welds, pp. 17–29.

[51] S. B. Brown and H. Song, "Implications of three-dimensional numerical simulations of welding of large structures," *Welding Journal*, vol. 71, pp. 55s–62s, February 1992.

[52] A. Capriccioli and P. Frosi, "Multipurpose ansys fe procedure for welding processes simulation," *Fusion Engineering and Design*, vol. 84 (2-6), pp. 546–553, 2009.

[53] Y. J. Chao and X. Qi, "Thermo-mechanical computer modeling of residual stress and distortion during welding process," in *9th International Conference on Computer Technology in Welding*, 1999, pp. 109–119.

[54] S. E. Chidiac, F. A. Mirza, and D. S. Wilkinson, "A simplified welding arc model by the finite element method," *Computers and Structures*, vol. 53, no. 5, pp. 1235–1241, 1994.

[55] D. Deng, "Fem prediction of welding residual stress and distortion in carbon steel considering phase transformation effects," *Materials and Design*, vol. 30, pp. 359–366, 2009.

[56] M. R. Frewin and D. A. Scott, "Finite element model of pulsed laser welding," *Welding Journal*, vol. 78, pp. 15s–22s, January 1999.

[57] M. Kassner and H. Wohlfahrt, "Analysis of distortion and residual stresses in welded steel structures with finite element method and comparison with experimental results," in *8th International Conference on Computer Technology in Welding*. Woodhead Publishing Ltd., 1998, pp. 227–238.

[58] N. X. Ma and Y. Umezu, "Analysis of thermal distortion and residual stresses in welding using ls-dyna," in *5th International LS-DYNA Users Conference*, 1998.

[59] A. M. Malik, E. M. Qureshi, N. U. Dar, and I. Khan, "Analysis of circumferentially arc welded thin-walled cylinders to investigate the residual stress fields," *Thin-Walled Structures*, vol. 46, pp. 1391–1401, 2008.

[60] P. Tekriwal and J. Mazumder, "Finite element analysis of three-dimensional transient heat transfer in gma welding," *Welding Journal*, vol. 67, pp. 150s–156s, July 1988.

[61] J. Wang, Y. Ueda, H. Murakawa, M. G. Yuan, and H. Q. Yang, "Improvement in numerical accuracy and stability of 3-d fem analysis in welding," *Welding Journal*, vol. 75, pp. 129s–134s, April 1996.

[62] J. H. Argyris, J. Szimmat, and K. J. Willam, "Computational aspects of welding stress analysis," *Computer Methods in Applied Mechanics and Engineering*, vol. 33, no. 1–3, pp. 635–666, 1982.

[63] L.-E. Lindgren, H. Runnemalm, and M. O. Näsström, "Simulation of multipass welding of a thick plate," *International Journal for Numerical Methods in Engineering*, vol. 44, pp. 1301–1316, 1999.

[64] P. Michaleris and X. Sun, "Finite element analysis of thermal tensioning techniques mitigating weld buckling distortion," *Welding Journal*, vol. 76, pp. 451s–457s, November 1997.

[65] T. D. Michaleris P, Dantzig J, "Minimization of welding residual stress and distortion in large structures," *Welding Journal*, vol. 78, pp. 361s–366s, November 1999.

[66] Y. Shim, Z. Feng, S. Lee, D. Kim, J. Jaeger, J. C. Papritan, and C. L. Tsai, "Determination of residual stresses in thick-section weldments," *Welding Journal*, vol. 71, pp. 305s–312s, September 1992.

[67] W. W. Wilkening and J. L. Snow, "Analysis of welding-induced residual stresses with the adina system," *Computer and Structures*, vol. 47, no. 4–5, pp. 767–786, 1993.

[68] J. Caňas, R. Picón, F. París, A. Blazquez, and J. C. Marín, "A simplified numerical analysis of residual stresses in aluminium welded plates," *Computers and Structures*, vol. 58, no. 1, pp. 59–69, 1996.

[69] M. Jonsson, L. Karlsson, and L.-E. Lindgren, "Simulation of tack welding procedures in butt joint welding of plates," *Welding Journal*, vol. 64, pp. 296s–301s, October 1985.

[70] E. Kannatey-Asibu Jr., N. Kikuchi, and A.-R. Jallad, "Experimental finite element analysis of temperature distribution during arc welding," *Transactions of the ASME: Journal of Engineering Materials and Technology*, vol. 111, pp. 9–18, January 1989.

[71] N. S. Prasad and T. K. S. Narayanan, "Finite element analysis of temperature distribution during arc welding using adaptive grid technique," *Welding Journal*, vol. 75, pp. 123s–128s, April 1996.

[72] L. Yu-Ning and E. Kannatey-Asibu Jr., "Finite element analysis of heat flow in dual-beam laser welded tailored blanks," *Transactions of the ASME: Journal of Manufacturing Science and Engineering*, vol. 120, pp. 272–278, May 1998.

[73] L.-E. Lindgren, "Finite element modeling and simulation of welding, part 2: Improved material modeling," *Journal of Thermal Stresses*, vol. 24, pp. 195–231, 2001.

[74] T. Belytschko, W. K. Liu, and B. Moran, *Nonlinear Finite Elements for Continua and Structures*. Chichester: John Wiley & Sons Ltd., 2000.

[75] T. J. R. Hughes and T. Belytschko, "Nonlinear finite element analysis," A short course, 1992.

[76] K. Bathe, *Finite element procedures*. Prentice Hall, 1996.

[77] Y. Jaluria and K. E. Torrance, *Computational Heat Transfer*, ser. Series in Computational Methods in Mechanics and Thermal Science. Hemisphere Publishing Corp., 1986.

[78] Y. U. Ninshu Ma, "Application of explicit fem to welding deformation," *Welding International*, vol. 23(1), pp. 1–8, 2009.

[79] J. Néző, B. Topping, and L. Dunai, "Use of mixed time integration for efficient welding simulation of steel plate girders," in *Proceedings of the Twelfth International Conference on Civil, Structural and Environmental Engineering Computing*, B. Topping, L. C. Neves, and R. Barros, Eds. Civil-Comp Press, Stirlingshire, UK, 2009, paper 87.

[80] N. Narasimhan and M. Lovell, "Predicting springback in sheet metal forming: an explicit to implicit sequential solution procedure," *Finite Elements in Analysis and Design*, vol. 33, no. 1, pp. 29–42, 1999.

[81] *Abaqus Analysis User's Manual, Version 6.7*, 2007, www.simulia.com.

[82] D. Radaj, *Welding residual stresses and distortion: Calculation and measurement*. DVS-Verlag, 2003.

[83] *LAND UNO Stand Alone Radiation Thermometers*, LAND Instruments International, Dronfield S18 1DJ, UK, www.landinst.com.

[84] *ANSYS User's Manual, Release 10.0*, ANSYS Inc., 2005, www.ansys.com.

[85] *EN 1993-1-2 : 2003, Eurocode 3 : Design of steel structure, Part 1.2 : General rules, Structural fire design.*

[86] J. A. Goldak and M. Akhlaghi, *Computational welding mechanics*. Springer, 2005.

[87] L.-E. Lindgren, *Computational welding mechanics: Thermomechanical and microstructural simulation*. Woodhead Publishing Ltd., 2007.

[88] P. Gilles, W. El-Ahmar, and J.-F. Jullien, "Robustness analyses of numerical simulation of fusion welding net-tg1 application: single weld-bead-on-plate," *International Journal of Pressure Vessels and Piping*, vol. 86, pp. 3–12, 2009.

[89] E. A. Bonifaz, "Finite element analysis of heat flow in single-pass arc welds," *Welding research supplement, Welding Journal*, pp. 121s–125s, 2000.

[90] *Digimizer, Version 3.7.0*, 2010, www.digimizer.com.

[91] *ASTM E837 - 08e1 Standard Test Method for Determining Residual Stresses by the Hole-Drilling Strain-Gage Method*, American Society for Testing and Materials (ASTM) International.

[92] G. Schajer, "Hole-drilling residual stress measurements at 75: Origins, advances, opportunities," *Experimental Mechanics*, vol. 50, no. 2, pp. 245–253, 2010.

[93] *Measurement of Residual Stresses by the Hole-Drilling Strain Gage Method, Tech Note TN-503*, Vishay Precision Group, 2007.

[94] E. G. Sobolevski, *Residual stress analysis of components with real geometries using the incremental hole-drilling technique and a differential evaluation method*. Kassel University Press GmbH, 2007.

[95] *Fémfólia nyúlásmérő ellenállás KMT-LIAS-063-350-5E*, Kaliber Ltd., www.kaliberkft.hu.

[96] T. Schenk, I. Richardson, M. Kraska, and O. S., "A study on the influence of clamping on welding distortion," *Computational Materials Science*, vol. 45, pp. 999–1005, 2009.

[97] Y. Ueda, H. Murakawa, K. Nakacho, and N. Ma, "Establishment of computational welding mechanics," *Transaction JWRI*, vol. 24 (2), pp. 73–86, 1995.

[98] L.-E. Lindgren, "Finite element modeling and simulation of welding, part 3: Efficiency and integration," *Journal of Thermal Stresses*, vol. 24, pp. 305–334, 2001.

[99] J. Pan, *Processes and mechanisms of welding residual stress and distortion*. Woodhead Publishing Ltd., 2005, ch. Measuring temperature during welding, pp. 126–174.

[100] B. Akesson, *Understanding Bridge Collapses*. Taylor & Francis, 2008.

[101] W. Zinn and B. Scholtes, "Residual stress formation processes during welding and joining," *Handbook of Residual Stress and Deformation of Steel*, pp. 391–396, 2002.

[102] N. X. Ma, Y. Ueda, H. Murakawa, and H. Maeda, "Fem analysis of 3-d welding. residual stresses and angular distortion in T-type fillet welds," *Transaction JWRI*, vol. 24 (2), pp. 115–122, 1995.

[103] H. Murakawa, M. Beres, A. Vega, S. Rashed, C. M. Davies, D. Dye, and K. M. Nikbin, "Effect of phase transformation onset temperature on residual stress in welded thin steel plates," *Transactions of JWRI*, vol. 37 (2), pp. 75–80, 2008.